Development of Nanotherapeutic platforms for the treatment and management of solid cancer

Atul Dev

A thesis submitted for the partial fulfilment of
the degree of

Doctor of Philosophy

Institute of Nano Science and Technology, Mohali, India

Indian Institute of Science Education and Research, Mohali, India

March 2021

Dedicated to my Loving Daughter…

Declaration

The work carried out in this thesis is carried out by me under the supervision of Dr. Surajit Karmakar at the Institute of Nano Science and Technology, Mohali. This work has not been submitted in part or full for a degree, diploma or a fellowship to any other University or Institute. Wherever contributions of others are involved, every effort has been made to indicate this clarity, with due acknowledgement of collaborative research and discussions. This thesis is a bonafide record of original work done by me and all the sources listed within have been detailed in bibliography.

Place: Mohali

Date: 30/03/2021 Atul Dev

In my capacity as the supervisor of the candidate's Ph.D. thesis work, I certify that the above statements by the candidate are true to the best of my knowledge.

Place: Mohali

Date: 30/03/2021

Dr. Surajit Karmakar
Scientist-F/Professor
Institute of Nano Science and Technology, Mohali

Acknowledgments

I thank my supervisor Dr. Surajit Karmakar for his guidance and immense support throughout the duration of my thesis work. I express my gratitude towards him for being a great mentor, a great friend and an inspirational personality.

I am thankful to Prof. Amitava Patra (Director), Prof. Ashok K. Ganguly (Former Director) and Prof. H.N. Ghosh (Former officiating Director) INST Mohali for their support and encouragement. I would like to express my sincere gratitutde to Dr. Subhasree Roy Choudhury (INST, Mohali), Prof. Prasenjit Guchhait (Regional Centre for Biotechnology, Faridabad, India) for their supportive collaboration for the thesis work.

I am grateful to the doctoral committee members Dr. Sharmistha Sinha and Dr. Prakash P. Neelakandan for their suggestions and timely review of the progress of my Ph.D. work. I am grateful to my lab mates Avinash, Jignesh, Babita, Nadeem, Anup, Dr. Madhunika, Dr. Sanjeev, Dr. Arpit, Dr. Ankur for their unconditional love and support throughout this journey. This work won't be possible without the immense support of my parents, my in-laws, my wife and my loving daughter.

I would like to thank everyone who helped me reach this goal. I thank my funding agency UGC for providing Junior research Fellowship (JRF) and senior research fellowship (SRF) to complete my Ph.D. research work. I am highly thankful to the whole INST family for their love and support during this journey.

Atul Dev

List of Publications

Relevant to thesis

- **Dev, A**.; Sardoiwala, M. N.; Kushwaha, A. C.; Karmakar, S.; Choudhury, S. R., Genistein nanoformulation promotes selective apoptosis in oral squamous cell carcinoma through repression of 3PK-EZH2 signalling pathway. *Phytomedicine : international journal of phytotherapy and phytopharmacology* **2021,** *80*, 153386.

- **Dev, A**.; Mohanbhai, S. J.; Kushwaha, A. C.; Sood, A.; Sardoiwala, M. N.; Choudhury, S. R.; Karmakar, S., kappa-carrageenan-C-phycocyanin based smart injectable hydrogels for accelerated wound recovery and real-time monitoring. *Acta biomaterialia* **2020,** *109*, 121-131.

- **Dev, A**.; Sood, A.; Choudhury, S. R.; Karmakar, S., Paclitaxel nanocrystalline assemblies as a potential transcatheter arterial chemoembolization (TACE) candidate for unresectable hepatocellular carcinoma. *Materials science & engineering. C, Materials for biological applications* **2020,** *107*, 110315.

- **Dev, A**.; Srivastava, A. K.; Choudhury, S. R.; Karmakar, S., Nano-curcumin influences blue light photodynamic therapy for restraining glioblastoma stem cells growth. *RSC advances* **2016,** *6* (97), 95165-95168.

- **Other Publications**

- Kushwaha, A. C.; Kaundal, B.; **Dev, A.**; Srivastava, A. K.; Mohanbhai, S. J.; Karmakar, S.; Choudhury, S. R., PRT4165 nanocomposite promoting epigenetic retardation through proteasomal depletion of polycomb in acute myeloid leukemia. *Applied Materials Today* **2020,** *21*, 100847.

- Sardoiwala, M. N.; Kushwaha, A. C.; **Dev, A**.; Shrimali, N.; Guchhait, P.; Karmakar, S.; Roy Choudhury, S., Hypericin-Loaded Transferrin Nanoparticles Induce PP2A-Regulated BMI1 Degradation in Colorectal Cancer-Specific Chemo-Photodynamic Therapy. *ACS biomaterials science & engineering* **2020,** *6* (5), 3139-3153.

- Kaundal, B.; Srivastava, A. K.; **Dev, A**.; Mohanbhai, S. J.; Karmakar, S.; Roy Choudhury, S., Nanoformulation of EPZ011989 Attenuates EZH2–c-Myb Epigenetic Interaction by Proteasomal Degradation in Acute Myeloid Leukemia. *Molecular pharmaceutics* **2020,** *17* (2), 604-621.

- Sood, A.; **Dev, A**.; Mohanbhai, S. J.; Shrimali, N.; Kapasiya, M.; Kushwaha, A. C.; Roy Choudhury, S.; Guchhait, P.; Karmakar, S., Disulfide-Bridged Chitosan-Eudragit S-100 Nanoparticles for Colorectal Cancer. *ACS applied nano materials* **2019,** *2* (10), 6409-6417.

- Singh, P. K.; Srivastava, A. K.; **Dev, A.**; Kaundal, B.; Choudhury, S. R.; Karmakar, S., 1, 3beta-Glucan anchored, paclitaxel loaded chitosan nanocarrier endows enhanced hemocompatibility with efficient anti-glioblastoma stem cells therapy. *Carbohydrate polymers* **2018,** *180*, 365-375.

- Srivastava, A. K.; **Dev, A**.; Choudhury, S. R.; Karmakar, S., New insight into curcumin tethered lanthanum carbonate nanospheres and protein corona conferring fluorescence enhancement based sensitive detection of Amyloid-β aggregates. *Sensors and Actuators B: Chemical* **2018,** *262*, 687-695.

- Kumar Yadav, S.; Kumar Srivastava, A.; **Dev, A**.; Kaundal, B.; Roy Choudhury, S.; Karmakar, S., Nanomelatonin triggers superior anticancer functionality in a human malignant glioblastoma cell line. *Nanotechnology* **2017,** *28* (36), 365102.

- Srivastava, A. K.; **Dev, A.;** Karmakar, S., Nanosensors and nanobiosensors in food and agriculture. *Environmental Chemistry Letters* **2017,** *16* (1), 161-182.

- **Dev, A**.; Srivastava, A. K.; Karmakar, S., Nanomaterial toxicity for plants. *Environmental Chemistry Letters* **2017,** *16* (1), 85-100.

Book chapters

- New Generation hybrid nanobiocatalysts: The catalysis redefined, In: "Handbook of Nanomaterials for Industrial Applications": **Dev A**, Srivastava A, **(2018)** Elsevier Press, 1st Edition,eBook,

- Nano-toxicity and Plants. In Nanoscience in Food and Agriculture: **Dev A**, Srivastava A, **(2017)** 5: 169-204.

- Nanosensors and Nanobiosensors: Current trend and innovation in perspective of Food and Agriculture Sector.: Srivastava A, **Dev A, (2017)** In Nanoscience in Food and Agriculture, 5: 41-79.

Contents

Abstract

The present thesis is focussed on the development of novel therapeutic nanoplatforms to treat highly malignant solid tumours and unhealed wounds which used to develop post-surgical resection of the tumours. The nanoplatforms were developed to address multiple challenges in cancer therapeutics like low bioavailability of the highly efficient and poorly water-soluble drugs, high dose requirement of chemotherapeutic drugs and associated systemic toxicities along with providing solutions to the unhealed chronic wounds, failed to heal post resection of tumors. Protein-based nanocarrier systems were developed using albumin proteins viz; Bovine serum albumin, Human serum albumin and lactalbumin to load poorly water-soluble drugs curcumin, fenretinide (4-HPR) and Genistein respectively. In addition to the protein nanoparticles, a novel nanocrystal-based platform of Paclitaxel is prepared with nearly 100 per cent drug loading efficiency. The prepared formulation is termed as paclitaxel nanocrystalline assemblies (PNAS) which are true to type, highly fluorescent and Cremophor EL free formulation of Paclitaxel. Hydrogel based injectable nanoplatform was developed using natural polysaccharide κ-Carrageenan and a pigmented protein C-phycocyanin to accelerate wound healing and provide real-time monitoring of the wound recovery through *in vivo* fluorescence imaging. The therapeutic potential of nanoformulations was evaluated in the in-vitro and in-vivo models of various malignant solid tumours including, Glioblastoma multiforme, paediatric Neuroblastoma, Oral squamous cell carcinoma and Hepatocellular carcinoma. The wound healing potential of the injectable hydrogel was evaluated in the in-vivo wound healing mice models. All the platforms were designed to address the challenge faced by the clinicians during the treatment of the disease. Nanocurcumin platform, in combination with the blue light phototherapy, is designed to restrict the growth of glioma stem cells (GSCs), the main culprit in the tumour recurrence. The GSCs proliferate during the time lag between tumour resection and the onset of chemotherapy and radiotherapy. Therefore, the current platform is best suited to target this phase of the treatment and prevent cancer recurrence. The nanocurcumin platform has shown immense potential in restricting the growth of GSCs in a combination of the blue light phototherapy at a very minimal dose which is non-toxic to the healthy cells. Following bovine serum albumin-based nanocurcumin platforms, another platform using Lactalbumin and Genistein (GLNPs) was designed to address the oral squamous cell carcinoma (OSCC) and its epigenetic regulation. Lactalbumin (whey protein) and Genistein (a flavonoid present in the soybean) are highly consumed by the

people in their daily nutritional requirement. The idea was conceived to target OSCC through nutraceutical molecules. The developed nanoformulation was highly biocompatible and potent in restricting the growth of OSCC along with reversing the histone modifications caused by PRC-1 and PRC-2 complex proteins. GLNPs work through the reestablishment of the epigenetic modification (downregulating the expression of epigenetic gene silencer H3K27me3, UbH2AK119 along with EZH2 and Bmi-1) and the onset of critical apoptotic machinery (increased Bax: Bcl-2, caspase-3 activation) to halt the progress of OSCC. Following the successful results of BSA and lactalbumin based nanoformulations in Glioblastoma multiforme and OSCC, another essential albumin protein, Human serum albumin (HSA) was used to develop 4HPR loaded HSA nanoparticles (4HPRNPs) to target neuroblastoma. All these albumin protein nanoparticles have immense potential to be used to treat any form of solid cancer including Brain tumor, breast cancer, liver cancer, pancreatic cancer etc. The synthesized HSA nanoparticles were modified using acetylsalicylic acid to incorporate acetyl moieties on the surface. Thus, 4HPRNPs and acetyl modified particles (4HPRANPs) were targeted to the highly malignant paediatric neuroblastoma. The concept of acetyl modification was put forward to address the acetyl and methyl modifications of histones. These modifications work as the epigenetic regulators which are possibly responsible for the metastasis in neuroblastoma. The developed 4HPRANPs nanoformulation successfully restricted the growth and lymph node metastasis in the *in-vivo* xenograft model of neuroblastoma in nude mice. The acetyl modification found to be a contributing factor in downregulating the epigenetic gene repressor H3K27me3, along with significantly improving the acetylation at histone 3. After the successful results of protein-based nanoparticles, a nanocarrier free formulation of Paclitaxel was developed. This nanocarrier free formulation of Paclitaxel (PNAS) was designed for the TACE application in the HCC. It provides the advantage of increased payload and higher retention of a chemotherapeutic drug inside the tumour site for a prolonged period. The molecule showed unique morphology with sustained drug release behaviour along with multichannel fluorescence properties. The therapeutic efficacy of the molecules is successfully verified at a clinically significant dose of Paclitaxel through a significant reduction in the volume of the 3D spheroid model of hepatocellular carcinoma (HCC). In addition to the chemotherapy-based treatment, the surgical removal of tumours leaves behind the unhealed wound. These unhealed wounds always remain a healthcare challenge in the cancer patients. The further onset of chemotherapy and radiotherapy post-resection makes these wounds chronic and nearly impossible to heal. This

wound healing complication was addressed by an injectable hydrogel system based on ionic crosslinking of κ-carrageenan monomers along with C-phycocyanin. The synthesized hydrogel was nanoporous with hydrophilic surface and good mechanical stiffness. Hydrogel material provided haemostasis, reduced inflammation, along with the proliferation of dermal fibroblasts in *in vitro* and *in vivo* conditions. The hydrogel successfully demonstrated the potential for accelerating tissue repair and real-time monitoring of the wounds in the mice model system. All the developed nanotherapeutic platforms have shown tremendous potential in addressing the different challenges in cancer therapeutics and post-treatment management of solid cancers.

Synopsis

Development of Nano therapeutic platforms for the treatment and management of solid cancer

Cancer is always remaining the major health problem worldwide for a long time with millions of new cases and cancer-related death yearly. According to the International Agency for Research on Cancer (IARC), there were more than 16.0 million new cancer cases, and 9 million cancer deaths were reported worldwide in 2018. GLOBOCON predicted this global burden of cancer is expected to double by the year 2040.[1] The increasing knowledge of cancer pathophysiology and molecular biology has changed the paradigm of cancer treatment and management in the last decade. Development of chemotherapy and radiotherapy has provided new hopes for the treatment; unfortunately, no significant improvement has been reported in death rate and incidence rate of cancer. Among the solid and liquid forms of cancer, solid cancers are the most common with more than 90 per cent incident worldwide.[2] The development of solid malignancies in various body organs has significantly affected the efficacy of available cancer treatments. Development of post-surgical complications like wound healing,[3] multiple organ failure due to chemotherapy, chemo and radioresistance in cancer patients has raised concerns in recent years. Introduction of nanotherapies as novel drug delivery platforms provided promising therapeutic potential in recent time for cancer treatment and rehabilitation. Nanotechnology offers improvement in the solubility of drugs, increasing concentration at the tumour site, along with minimizing systemic toxicities to the healthy cells, overcoming chemoresistance and radioresistance. Multidimensional approaches like Photodynamic therapy, hyperthermia, immunotherapy, alongside nanotherapeutic platforms offer some novel solutions to the long last issues in cancer therapies.

The current thesis addresses several critical issues in current cancer therapeutics and provides some novel solutions and mechanistic insight into cancer treatment. The main focus of the current thesis is to develop highly efficient and biocompatible nano-drug delivery platforms to address drug solubility issues of some very known and potential chemotherapeutic drugs like curcumin, genistein, paclitaxel and fenretinide. Here, we have developed several drug delivery platforms using albumin (Bovine serum albumin, Lactalbumin and Human serum albumin) as a drug carrier. This nanocarrier provides new therapeutic solutions in cancer treatment. Additionally, we have developed a polymer-based injectable hydrogel platform to address the wound healing; one of the emerging concerns in recent time after surgical

resection of the tumour. The thesis is comprising of five major studies on cancer and wound healing. Each study has its hypothesis, which has been well addressed with relevant data and supportive proofs.

The first chapter of the thesis is based on the development of nanocurcumin mediated blue light photodynamic therapy for the treatment of glioblastoma multiforme. The study focused on the role of cancer stem cells in cancer relapse and presented a novel therapeutic approach, which could selectively restrict the growth of cancer stem cells keeping the non-cancerous cells unharmed and healthy. The nano curcumin is prepared using Bovine serum albumin as a drug carrier which helps increase the solubility and bioavailability of the drug along with improving the drug release profile in *in vitro* simulation conditions. The absorbance of curcumin (350 nm) provides a unique combination of blue light photodynamic therapy, which further improves the potential of therapeutic efficacy of the curcumin in glioma treatment. The study has successfully shown that nanocurcumin in the presence of blue light effectively destroys cancer stem cells at a minimal treatment dose of 6 µM compared to the curcumin. Several critical factors including the total time of blue light exposure and the time delay between nanoparticle treatment and the blue light treatment were assessed to get the best combination of the treatment conditions using *in vitro* models of glioblastoma multiforme. Possible mechanisms of improved efficiency of nanocurcumin are discussed in the study with underlined experimental proofs and supportive literature. Nanocurcumin induced excessive ROS production in the presence of blue light resulting in the activation of proteases like caspase 3, which causes apoptosis in the cancer stem cells. The nanocurcumin formulation and blue light combination treatment could be beneficial between surgical resection and the onset of chemoradiotherapy. The time lag between glioma surgery and the onset of chemoradiotherapy is probably the prime reason for the recurrence of glioma. The local delivery of the nanocurcumin directly at the tumour resection site and time-dependent shots of blue light could help minimize the glioma recurrence rate. The current therapy promises the potential to assist the recovery of the glioma resected patient and could help increase the survival time in comparison to the standard operation and treatment conditions.[4]

The second chapter of the thesis is focused on paediatric neuroblastoma. In the present chapter, we have synthesized 4 HPR loaded HSA nanoparticles and its acetate variant. The study is focussed on evaluating the therapeutic efficacy of the nanoparticles in restricting metastasis and improving cell killing in *in vitro* and *in vivo* neuroblastoma models. The idea

of the development of acetate variant was conceived to study the effect on histone 3 acetylation and methylation status in the development of neuroblastoma metastasis. Acetate is a known alternative source of energy, which works as an alternative fuel for uncontrolled cancer growth. Cancer cells scrap acetate from various sources like acetyl-CoA, histones and various other proteins to fulfil its energy requirement. This acetate scrapping possibly directs the cellular machinery to the epigenetic gene silencing of the critical cancer regulators through the management of acetylation and methylation equilibrium. The 4HPR loaded HASNPs were acetylated using the acetylsalicylic acid, and the modification was verified using the fluorescence change in Fluorescamine. Fluorescamine is a non-fluorescent compound that binds to the primary amine such as the terminal amino group of peptides and the e-amino group of lysine, to form highly fluorescent moieties. The change in fluorescence was quantified to measure the free amine group in the 4HPR loaded HSANPs post-modification. The results confirmed the acetyl modification of 4HPR loaded HSANPs.

The nanoparticles were successfully delivered to the neuroblastoma cells. Following their cellular uptake, the particles were analyzed for their in vitro cytotoxicity in the monolayer model system. The studies confirm the superior therapeutic efficacy of the 4HPRANPs compared to other groups. The cells were treated with the IC50 value of 4HPR drug, 4HPRNPs and 4HPRANPs to screen the molecular aspect of the treatment. The total RNA was isolated from the treated cells, and qPCR studies were performed to monitor the expression profile of various key genes involved in cancer metastasis. The qPCR result confirmed the efficacy of 4HPRANPs in altering the gene expression of E-cadherin and fibronectin, which are key molecules in the development of metastasis. To recapitulate the in vitro results in *In vivo* models, tumour xenograft model of neuroblastoma was developed in the nude mice and therapeutic efficacy was studied. Simultaneously, *in vivo*, whole-body biodistribution studies of the 4HPRANPs and 4HPRNPs were performed in balb/C mice. The studies confirmed that nanoparticles are very well distributed through the various body organs, and no specific accumulation was found in the body except low concentration in the highly fibrous and complex body organs like liver and kidney.

The therapeutic efficacy of the drug and nanoparticles was performed by optimizing the drug dose in mice. The dose optimization was performed in the nude mice by giving three prefixed doses (5,7,9 mg/kg/day) of the drug. The drug with multiple doses was administered intraperitoneally for 30 days, and depending upon the toxicity and death rate, the final dose of

5 mg/kg/day was selected. Once the tumour xenografts reached a minimum volume of 100mm^3 in size, the dosing of the drug and nanoparticles was started. All the animals were given the equivalent daily dose of the drug, 4HPRANPs and 4HPRNPs for 15 days with a gap of one day after 7 consecutive days of dosing. After completion of the treatment, the tumours and all major organs were surgically harvested and snap-frozen in liquid nitrogen for further analysis. The body weight of the animals was recorded every two days. All the tumours and organs were weighed after the necropsy of the animal. The *in vivo* therapeutic results verified the therapeutic efficacy of the 4HPRANPs compared to bare drugs and 4HPRNPs. We have further studied the molecular mechanism of the nanoparticles therapeutic action using western blotting, histology (H&E), Immunohistochemistry (IHC) of the tumour tissue and body organs. The histology and IHC showed that neuroblastoma cells metastasized to the mesenchymal lymph node, which is well restricted in the 4HPRANPs treatment groups.

The third chapter in the thesis is primarily based on oral squamous cell carcinoma, one of the significant contributors to cancer patients, especially in Asian countries. There are several factors which induce the OSCC, among these, consumption of tobacco and pollution are the major contributors.[5] Consumption of tobacco, and regular exposure to the environmental pollution result in epigenetic changes, which reversibly alter the genome and proteome of the individual and trigger the cancer development. This chapter addresses the role of epigenetic alterations in the development of OSCC. The study shed light on developing a nanotherapeutic platform which could help deal with the epigenetic alterations in OSCC along with providing therapeutic support to eliminate cancer. Here, we have utilized one of the primarily used nutritional protein source lactalbumin (whey protein) as a carrier molecule to load isoflavonoid molecule genistein. Genistein is a poorly water-soluble drug which has immense potential in targeting the multiple pathways in cancer.[6] We have synthesized highly biocompatible and therapeutically active genistein loaded lactalbumin nanoparticles which selectively kill OSCC cells while imparting no toxicity to the normal fibroblast cells. The particles were very well uptake by the OSCC cells both in monolayer and 3D multilayer raft model system, showing their potential of successful delivery in the loosely packed solid tumour like OSCC. The synthesized nanoparticles promise as an effective therapeutic alternative to target OSCC by regulating the altered epigenetic profile and diverting OSCC cells towards programmed cell death. Here we have primarily focussed on histone

modifications and the key players of this epigenetic alteration; the PRC1 and PRC-2 complexes. We have established that GLNPs reverse the altered expression of EZH2, Bmi-1 along with their possible targets H3K27me3 and UbH2AK119 in the in-vitro model of OSCC. The similar results were recapitulated in 3D multilayer raft model system of OSCC, through qPCR, western and IHC; showing therapeutic efficiency in complex systems. In critical experiments, we have shown that the vital regulator EZH2 is found physically linked to the 3PK (kinase), which possibly controls the expression of EZH2 and regulates gene silencing. Finally, the particles were analyzed for their whole-body distribution and possible toxicity in *In vivo* mice model. The intravenous delivery of the particles has shown that lactalbumin nanoparticles were well distributed in the body organs of mice. A timely body clearance with no specific accumulation was observed in the *in vivo* mice model system, showing compatibility and potential of using these nanoparticles for successful treatment of OSCC. [7]

The next study is focussed on Hepatocellular cell carcinoma and TACE procedure. Here we have developed a new therapeutic class as Nanocrystalline nano-assemblies using Cremaphor free paclitaxel. Different parameters viz. solvent and antisolvent ratios, the concentration of paclitaxel, were studied to optimize the size and morphology of the molecules. Time-dependent NMR studies were conducted to establish the mechanism of formation self-assemblies and generation of multichannel autofluorescence in the molecule. These assemblies are unique in their physical appearance, which provide a structural advantage to be used as a potential TACE agent to treat HCC. Currently, there is no such type of paclitaxel variant in the market which could be used in TACE procedures. The increased payload of the drug is highly warranted at the tumour site to keep tumour growth in check. The current form of paclitaxel is highly efficient in providing increased payload due to its structural uniqueness. Their unique structural form makes it suitable to be delivered through a catheter directly in the hepatic artery, which could provide embolization of the artery and required drug pool at the site. The synthesized nano-assemblies are highly fluorescent, which provide multichannel fluorescence in the blue-green and red channel. This potential provides an additional advantage to the physicians to track and monitor the authentic delivery of the drug molecules in the organ. We have verified our hypothesis in delivering the paclitaxel nano-assemblies in the in vitro 3D spheroid model of hepatocellular carcinoma. The drug molecules showed significant therapeutic efficiency in restricting the growth of the 3D

spheroid at the clinically effective dose; simultaneously the delivery of the nanocrystalline assemblies to the spheroids is verified using confocal and scanning electron microscopy of the treated spheroids.[8]

The last study of the thesis work is provided in the end as Appendix, which addresses wound healing complications post-surgical resection of solid cancer. Cancer resection works as an emergency treatment to minimize the load on the affected organs. However, rehabilitation after surgery is never easy. Surprisingly, post-surgical resection fatalities are very high.[9] The prime reason for such fatalities are severe medical complications like wound healing. Post resection wound healing is one of the significant issues that required serious attention. Chemotherapy and radiotherapy treatment following the surgical resection delay the wound healing, leading to tissue loss and chronic wounds. This wounded site needed biochemical and mechanical support for cellular growth and wound recovery. There is a constant search for the dressing matrix, which could help in the restructuring of the chronic wounds and help restore the tissue loss. Addressing this concern, we have synthesized self-healing, k-carrageenan and C-phycocyanin based injectable hydrogel matrix. The synthesized hydrogel promises rapid blood clotting and accelerated wound healing.

C-phycocyanin is a pigmented protein which shows unique pharmaceutical properties including anticancer, anti-inflammatory and antimicrobial. These properties make it a suitable candidate in the post-resection wound healing application. The hydrogel matrix is prepared using ionic crosslinking of k-carrageenan monomers along with the pigmented protein C-phycocyanin. The rheological properties of the hydrogels were measured with varying concentration of K-carrageenan and c phycocyanin. k-carrageenan and C-phycocyanin at 1% concentration work best in terms of rheological properties and pore size of the matrix. The hydrogel was further characterized using FTIR studies for the chemical changes during gelation. The In vitro cytotoxicity of the material was analyzed by performing MTT analysis in fibroblast cells. The results confirmed the highly biocompatible nature of the molecules at the 1% concentration. We have further assessed the potential of the hydrogel, whether it allows the growth of fibroblast cells inside the matrix or not. The live dead cell staining was performed after incubating the fibroblast cells inside the hydrogel matrix. The result confirmed the functional metabolic activity and cellular viability inside the cellular matrix. The matrix was finely chopped, and cross-section of the hydrogel was observed under the confocal microscope. The results validated the structural integrity and morphology of the

cells. The wound healing properties of the hydrogel was studied using In vitro wound healing scratch assay. The result indicates that k-carrageenan-c-phycocyanin hydrogel rapidly fills the scratched wound, showing immense potential in the wound recovery. Blood clotting is one of the prime mechanisms required in wound healing. Therefore, blood clotting analysis of the hydrogels was performed in in vitro and *in vivo* traumatic liver injury traumatic wound model in mice. The hydrogel has shown impeccable blood clotting, which minimizes the blood clotting time by nearly half compared to the controls. The blood compatibility of the hydrogel was further measured through per cent haemolysis in isolated RBCs. The material was high blood compatible with no significant haemolysis. The wound healing potential of the hydrogel was further validated using the *In vivo* mice model. A fixed-size wound was created on the dorsal side of the mice.

The wound was allowed to heal in the presence and absence of the prepared hydrogel along with the controls. After the completion of 14 days of the treatment, the mice were sacrificed. The skin was harvested to study wound healing. The hydrogel treated mice show some remarkable recovery, as complete restructuring was established in the wound. Picrosirius staining of the healed wound was performed to show the collagen restructuring of the wound. The biocompatibility of the hydrogel was studied *In vivo* by injecting the hydrogel in the subcutaneous site of the flank. The histopathological observation was carried out on the tissue samples of the collected skin tissue, which revealed no acute and chronic inflammation at the site of implants. Additionally, the synthesized hydrogel has shown *In vivo* fluorescence potential, which could help monitor the wound recovery by capturing the time-lapse images of the wound. Analysis of the Time-lapse images of the hydrogel filed wound help monitor the progress of the wound by analyzing the depth of the recovered wound.[10]

In summary, the present thesis has provided new insight into the molecular mechanism of cancer epigenetics along with providing novel therapeutic platforms for drug delivery in cancer therapeutics. The synthesized nanomaterials addressed the drug solubilities issues of highly effective but low water-soluble drugs like paclitaxel, genistein, curcumin and fenretinide (4-HPR). The developed nanoplatforms promise improved therapeutic efficacy compared to conventional cancer treatments.

References

1. Bray, F.; Ferlay, J.; Soerjomataram, I.; Siegel, R. L.; Torre, L. A.; Jemal, A., Global cancer statistics 2018: GLOBOCAN estimates of incidence and mortality worldwide for 36 cancers in 185 countries. **2018,** *68* (6), 394-424.
2. Dillekas, H.; Rogers, M. S.; Straume, O., Are 90% of deaths from cancer caused by metastases? *Cancer medicine* **2019,** *8* (12), 5574-5576.
3. Payne, W. G.; Naidu, D. K.; Wheeler, C. K.; Barkoe, D.; Mentis, M.; Salas, R. E.; Smith, D. J., Jr.; Robson, M. C., Wound healing in patients with cancer. *Eplasty* **2008,** *8*, e9.
4. Dev, A.; Srivastava, A. K.; Choudhury, S. R.; Karmakar, S., Nano-curcumin influences blue light photodynamic therapy for restraining glioblastoma stem cells growth. *RSC advances* **2016,** *6* (97), 95165-95168.
5. Pires, F. R.; Ramos, A. B.; Oliveira, J. B.; Tavares, A. S.; Luz, P. S.; Santos, T. C., Oral squamous cell carcinoma: clinicopathological features from 346 cases from a single oral pathology service during an 8-year period. *J Appl Oral Sci* **2013,** *21* (5), 460-7.
6. Spagnuolo, C.; Russo, G. L.; Orhan, I. E.; Habtemariam, S.; Daglia, M.; Sureda, A.; Nabavi, S. F.; Devi, K. P.; Loizzo, M. R.; Tundis, R.; Nabavi, S. M., Genistein and cancer: current status, challenges, and future directions. *Advances in nutrition* **2015,** *6* (4), 408-19.
7. Dev, A.; Sardoiwala, M. N.; Kushwaha, A. C.; Karmakar, S.; Choudhury, S. R., Genistein nanoformulation promotes selective apoptosis in oral squamous cell carcinoma through repression of 3PK-EZH2 signalling pathway. *Phytomedicine : international journal of phytotherapy and phytopharmacology* **2021,** *80*, 153386.
8. Dev, A.; Sood, A.; Choudhury, S. R.; Karmakar, S., Paclitaxel nanocrystalline assemblies as a potential transcatheter arterial chemoembolization (TACE) candidate for unresectable hepatocellular carcinoma. *Materials science & engineering. C, Materials for biological applications* **2020,** *107*, 110315.
9. Welch, H. G.; Black, W. C., Are deaths within 1 month of cancer-directed surgery attributed to cancer? *Journal of the National Cancer Institute* **2002,** *94* (14), 1066-70.
10. Dev, A.; Mohanbhai, S. J.; Kushwaha, A. C.; Sood, A.; Sardoiwala, M. N.; Choudhury, S. R.; Karmakar, S., kappa-carrageenan-C-phycocyanin based smart injectable hydrogels for accelerated wound recovery and real-time monitoring. *Acta biomaterialia* **2020,** *109*, 121-131.

Chapter 01

Introduction

Cancer is a diseased condition where cellular changes lead to the irregular growth of the cells. These alterations may cause rapid or restricted cell growth patterns. These uncontrollable changes in the cells' growth pattern led to the solid visible mass termed as solid tumour while others result in restricted growth of a particular cell type resulting in liquid cancer, better known as blood cancer (leukaemia). Every cell in our body has a specific function and limited life span. Cell death is a natural phenomenon which runs through a specialized programme known as apoptosis. A cell receives controlled signals to die to be replaced by a new cell that functions better. The cancer cell escapes this controlled mechanism and therefore keeps dividing. This uncontrolled division of the cells takes over the control of nutrition and growth factors required for normal cells' growth. The newly formed cancer cells escape the immune system of the body and remain unrecognizable. Their potential to migrate from one place to another in the body makes them even more lethal.

Cancer is one of the leading causes of global deaths, with an estimated 9.6 million deaths in 2018. Approximately 75% of the cancer-related deaths occur in low- and middle-income countries. Increasing pollution and consumption of cancer inducing foods like tobacco elevate cancer development risk; these factors are responsible for approximately 22% of cancer-related deaths.[1] Except for these factors, some cancer-causing viral infections like Human papillomavirus (HPV) are responsible for nearly 25% cancer cases in the low -and middle-income countries.[2] The economic burden of cancer is significant and is increasing at a very high rate. The total annual economic cost of cancer management in 2010 was estimated at approximately US$ 1.16 trillion. This cost is expected to rise to 40% by 2040 (4).[3] Among several reported cancer cases, solid cancer contributes more than 90% cases; CNS cancer, extracranial neuronal cancer like neuroblastoma, oral squamous cell cancer, liver cancer and breast cancer are the prime form of cancer worldwide.[4] Last decade has given several modalities in cancer prognosis and treatment, although the death rate and incidence rate has not significantly improved.

Development of post-treatment complications makes life difficult for cancer patients. Currently available conventional treatments like surgical resection, chemotherapy, and radiotherapy provide survival benefits to the cancer patients, although none of the treatment is entirely free from side effects and latent complications. The treatment available for cancer patients is highly variable and dependent on several factors, including the type, location, and progress of the disease, age, and patient's health status. The majority of the cancer patients'

treatments are designed to either directly kill/remove the cancer cells or to deprive them for survival signals. Immunotherapy has shown a new approach to target cancer by stimulating the body's defence mechanism against the cancer cells; although its full potential is still not explored so far.

The most common therapeutic approach clinicians use for treating the cancer patients is surgery, chemotherapy and radiotherapy. Each therapy's success rate depends on the tumour's location, origin, and progressive stage. Surgical resection is very common in the easily approachable solid cancer which followed by adjuvant chemo or radiotherapy. The adjuvant therapeutic approach has shown better survival compared to chemotherapy and radiotherapy alone.[5]In recent time, resistance against commonly used chemotherapeutic drugs and radiation has raised serious concern in cancer therapeutics. [6] Development of new therapeutics platforms to target several cancer types is the need of the time. In the series of therapeutic advances, nanotherapeutic platforms' introduction has shown new hope of the proper treatment.[7]

The major drawback in the cancer therapeutics is the inability of current platforms to deliver a specific amount of the drug to the target area, causing excessive drug requirement and added systemic toxicities. The available chemotherapeutic drugs are poorly water-soluble, which reduces their bioavailability in the system. The formulation of these drugs comes with some organic solvents[8] which improves the availability of the drug but cause some unknown toxicities in the system.[9]All these therapeutic efficacy barriers could be addressed by the invention of nanotherapeutic platforms. The nanomedicine improves the drug molecule's delivery to the target site, improving its specificity and tumour related barriers.[10]

In the current thesis, we have focused on developing several nanotherapeutic platforms using nanocarrier and carrier-free approach to target several critical aspects of currently available challenges in cancer therapies. Here, we have addressed solubility issues of some very potent chemotherapeutic drugs like Curcumin, Genistein and 4-HPR through the development of albumin-based nanoformulation. In addition to the nanocarrier based nanoplatforms, we have synthesized nanocrystalline based Cremaphor free nanoformulation of paclitaxel. Except for these chemotherapeutic platforms, the hydrogel-based injectable platform is developed to address post tumour resection wound healing complications. These developed nanoformulations are evaluated in several solid cancers like glioblastoma multiforme,

neuroblastoma, oral squamous cell carcinoma and hepatocellular carcinoma. The current thesis's prime focus is to provide a multidimensional therapeutic library of potent chemotherapeutic drugs' nanoformulations. We have studied several molecular mechanisms of these nanoformulations that impart better therapeutic effect and help control cancer cells' growth *in vitro* and *in vivo* model of several solid cancer types.

The apoptotic mechanism and epigenetic regulations contributing to cancer development and progression are addressed and support the advancement of currently available clinical practices like transarterial chemoembolization (TACE). We have addressed the post-surgical wound healing issues, developed after surgical resection of the tumour and adjuvant radio and chemotherapies. A hydrogel matrix is prepared using natural polymer and pigmented protein C-phycocyanin to improve and accelerate wound healing in cancer patients. In addition to the therapy, promising diagnostic platforms are developed in combination with nanoformulations' therapeutic potential. These diagnostic platforms are non-invasive and provide the advantage of in situ diagnostics of disease progression and drug delivery to the body's specific organ. This thesis's prime goal is to develop highly effective cancer management platforms that could deliver the chemotherapeutic drugs at the prescribed location in the body and should be free from systemic toxicities. Therefore, all the platforms developed in the current thesis for various cancer types and post-cancer management of the cancer wounds are designed using highly biocompatible carrier molecules like albumin proteins and edible polysaccharides. The thesis provides an in-depth understanding of the synthesis chemistry and unique properties exhibited by the chemotherapeutic drugs' nanoformulation. The complete thesis is organized into five significant studies covering different aspects of cancer treatments in solid cancer. Every chapter of the thesis is a complete study showing the synthesis of individual nanoformulation and its therapeutic mechanism in the respective cancer types.

References

1. Forouzanfar, M. H.; Afshin, A.; Alexander, L. T.; Anderson, H. R.; Bhutta, Z. A.; Biryukov, e. a., Global, regional, and national comparative risk assessment of 79 behavioural, environmental and occupational, and metabolic risks or clusters of risks, 1990–2015: a systematic analysis for the Global Burden of Disease Study 2015. *The Lancet* **2016,***388* (10053), 1659-1724.
2. Plummer, M.; de Martel, C.; Vignat, J.; Ferlay, J.; Bray, F.; Franceschi, S., Global burden of cancers attributable to infections in 2012: a synthetic analysis. *The Lancet Global Health* **2016,***4* (9), e609-e616.
3. Stewart BW, W. C., World cancer report 2014*Lyon: International Agency for Research on Cancer; 2014.* **2014**.
4. Bray, F.; Ferlay, J.; Soerjomataram, I.; Siegel, R. L.; Torre, L. A.; Jemal, A., Global cancer statistics 2018: GLOBOCAN estimates of incidence and mortality worldwide for 36 cancers in 185 countries. **2018,***68* (6), 394-424.
5. Kim, T. H.; Woo, S. M.; Lee, W. J.; Oh, E. S.; Youn, S. H.; Moon, S. H.; Kim, S. S.; Han, S. S.; Park, S. J.; Kim, D. Y., Benefit of Adjuvant Chemoradiotherapy in Resected Gallbladder Carcinoma. *Scientific reports* **2019,***9* (1), 11770.
6. Bergman, P. J.; Harris, D., Radioresistance, chemoresistance, and apoptosis resistance. The past, present, and future. *Vet Clin North Am Small Anim Pract* **1997,***27* (1), 47-57.
7. Couvreur, P., Nanoparticles in drug delivery: past, present and future. *Advanced drug delivery reviews* **2013,***65* (1), 21-3.
8. Gelderblom, H.; Verweij, J.; Nooter, K.; Sparreboom, A., Cremophor EL: the drawbacks and advantages of vehicle selection for drug formulation. *European journal of cancer* **2001,***37* (13), 1590-8.
9. Probst, C. E.; Zrazhevskiy, P.; Bagalkot, V.; Gao, X., Quantum dots as a platform for nanoparticle drug delivery vehicle design. *Advanced drug delivery reviews* **2013,***65* (5), 703-18.
10. Wang, Y.; Chen, L., Quantum dots, lighting up the research and development of nanomedicine. *Nanomedicine : nanotechnology, biology, and medicine* **2011,***7* (4), 385-402.

Chapter 02

Blue light mediated photodynamic therapy for the treatment of Glioblastoma multiforme

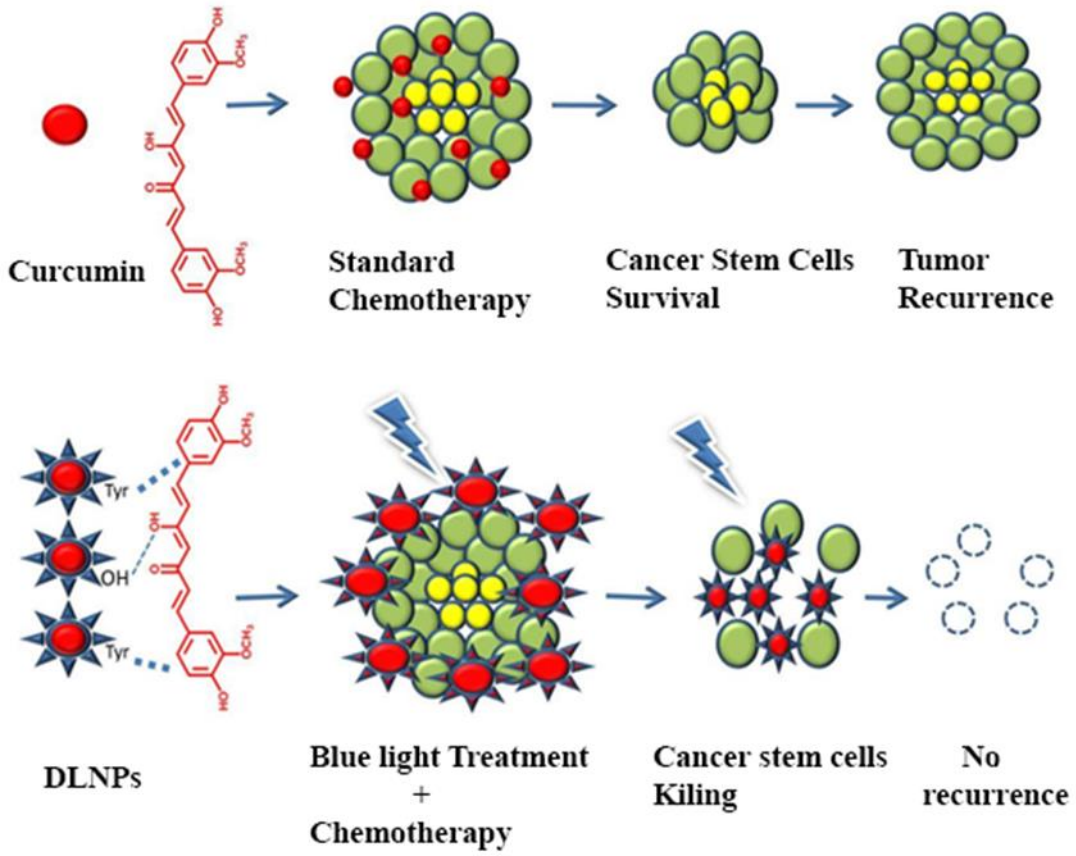

1.0 Background

1.1 Glioblastoma multiforme

Glioma is a general term given to describe a group of neoplasm of the central nervous system (CNS), which consist genetically and phenotypically heterogeneous groups of tumors.[1] The term Glioblastoma multiforme was first introduced by Percival Bailey and Harvey Cushing in the late nineteenth century. The idea was based on the tumor originating glial cells (glioblasts) and its highly variable appearance (multiform). Primary glioblastoma which contributes to more than 90% GBMs are developed *de novo* from glial cells and the remaining nearly 10 % cases are secondary neoplasm, which are developed from astrocytes. Glioblastoma multiforme term is more precisely used for primary neoplasms developed from glial cells. These primary and secondary neoplasm are very different from each other in genetic and molecular pathways.[1] Although, no such variation is found in the physical appearance of the disease except the growth rate. Primary neoplasm develops within months of initiation of tumorigenesis, while the secondary neoplasm develops in years. The first glioblastoma treatment was reported in Vienna in the early 19th century. The grading of glioblastoma is classified on the basis of WHO classification which depends on the basis of severity of disease. Glioblastoma is categorized from Grade I to Grade IV. Grade I represent, low grade tumors with less proliferative activity. These types of tumors are successfully removed using surgery and chemotherapy. Grade II to Grade IV tumors are very invasive and difficult to control. Glioblastoma multiforme is a grade IV type of tumor, which is highly invasive and highly undifferentiated in nature.

1.2 Epidemiology

The lower incidence rate of GBM (10 in 100000) across the globe makes it a rare tumor but its poor diagnosis and prognosis with survival rate of 14-15 months makes it a crucial public health concern.[2] GBM accounts more than 50% of all gliomas in all age groups.[3] The occurrence of GBM is unpredictable, although it has been found that the peak incidence is between 55 to 60 years.[4] It is also reported in children and neonates with very less frequency (1.1 to 3.6 in 100000). No morphological differences are reported in GBMs developed in adults and children except the proliferation activity. The proliferation rate of GBM development is much higher in children. Worldwide, Men are more prone than women against the development of GBM.[4, 5] As such there is not much known about the genetic

susceptibility of a particular genetic condition for GBM. Although, the Han Chinese population with EGF +61 AA genotype was found somewhere related to such conditions.[6]

1.3 Etiology

No clear-cut evidence for the etiology of GBMs so far is established. GBMs are considered as spontaneous. Its development is related to the genetic disturbances and deregulation of cell cycle at G1/S checkpoint in glioma cells.[7] Human cytomegalovirus (HCMV) is also among the etiologic agents for glioma development. The virus encoded proteins (IE1, US28, GB) activate intracellular signalling and dysregulate the key signalling pathways (including PDGFR, Akt, STAT3). It is also believed to induce disturbances in monocyte and glial cell functions.[8, 9] Granulocyte-colony stimulating factor (G-CSF) is one of the contributing glycoproteins in GBMs development. Increased expression of this glycoprotein and its receptor (G-CSFR) was found in different grades of malignancy in GBMs. Except these factors, certain potentially harmful chemicals (pesticides, polycyclic aromatic compounds and solvents) and electromagnetic fields are also considered to be involved in glioma development.[10] Certain genetic diseases like tuberous sclerosis[11], Turcot syndrome [12], multiple endocrine neoplasia type IIA [13] and neurofibromatosis type I, NF1 [14] are also found related to the GBMs development. In addition, acquired head injuries, which occurred as a result of a brain contusion, may predispose to the onset of glioblastoma [15, 16].

1.4 Morphological features

Glioblastoma multiforme develops in various parts of the brain. Although, its presence is majorly reported in hemispheres,[17] brain stem,[18] and cerebellum.[19] Tumor mass is not clearly distinguishable from the normal tissue due to its infiltrating growth.[1, 15] Its Invasiveness, short course of disease and cerebral meninges barrier results in its low metastatic potential.[20] Cerebrospinal fluid [21] and blood [22] mediated metastasis is rare.

GBM consists of small polymorphic cells with acidophilic cytoplasm and indistinct cellular borders. Anaplasia and anisokaryosis are other significant features of GBMs. GBM cells show increased nuclear to cytoplasmic ratio and show nuclear pleomorphism. Extensive vascularization is the signature pattern of GBMs.[23] The newly developed vessels have phenotypically different endothelial cells which are focally overlapped, hyperplastic and heterogeneous in size and shape. Vascular thrombi formation in GBMs lead to endothelial

cell damage and extensive proliferation which result in vascular damage and red blood cells extravasation.[24]

Higher multiplication rate of GBM cells result in insufficient blood supply, which causes characteristic necrotic foci formation in large areas of all primary glioblastomas. Some small irregular shaped necrotic foci were also reported in both primary and secondary glioblastomas. These necrotic foci were covered with pseudopalisading areas. These areas consist of rapidly proliferating, apoptosis resistance, blood supply outgrown neoplastic cells population. Cell density in these areas is almost twice as high, but proliferation activity is from 5 to 50% lower than in other tumor zones.[25] The increased malignancy of GBMs accompanied by an increase of degree of atypia, nuclear hyperchromatosis, increased mitotic index, presence of necrotic areas and atypical blood vessels.[24]

1.5 Clinical symptoms

The clinical symptoms of GBMs are diverse. These symptoms majorly depend upon the localization and clinical stage of tumor. The most common symptoms include headaches, ataxia, dizziness, vision disturbances (blurred vision, diplopia), and frequent syncope.[18 26] Due to these unspecific symptoms, glioma is often misdiagnosed as infections, inflammatory processes and circulatory and immunological diseases.[18]

1.6 Diagnosis

Initial Diagnostic tools for GBMs detection include sophisticated imaging techniques like computed tomography (CT or CAT scan) and magnetic resonance imaging (MRI), which precisely provides tumor locations in the brain. MRI scan is the primary diagnostic tool for GBM, it diagnoses tumors as small as 4 cm in diameter. Final diagnosis of tumor is based on histopathological examination through cytological and histochemical methods.[27] Additionally, Magnetic resonance spectroscopy (MRS) is used during surgery to examine the chemical profile of tumor. Positron emission tomography (PET scan) found helpful in detecting tumor recurrence.

1.7 Treatments

GBMs is comprises of highly proliferative, ratio resistance and chemo resistant cell population. Its infiltration property makes it difficult to operate tumor and presence of blood-

brain barrier makes treatment even more difficult.[28] Currently, a combined strategy, which includes Surgical resection to the feasible extent, followed by chemotherapy and radiotherapy is the mainstay of GBM treatment, it prolongs the survival time in young people up to 202 weeks.[29, 30] The best results are obtained when radiotherapy is performed after the surgery, with the doses of 5000–6000 cGy. Dose escalation over 6000 cGy has resulted in increased toxicity without a survival benefit.[28] The standard treatment scheme for glioma most frequently in comparison to the other chemotherapeutics includes temozolomide. [31] It is known that the survival advantage among patients treated with temozolomide and radiotherapy is longer compared with radiotherapy alone.[32]

Increased vascularization in GBMs inspired the development of an anti-angiogenic gene therapy to block the VEGF-dependent pathway. [33] Bevacizumab, a humanized IgG1 monoclonal antibody which selectively binds with high affinity to human VEGF and neutralizes its biologic activity.[34] Bevacizumab has been shown to improve patient outcomes in combination with chemotherapy and was granted accelerated approval as a single agent in recurrent GBM.[35]

RNA interference (RNAi) is another treatment modality leading to a total or partial silencing of gene expression. RNAi therapy can be used in combination with other methods, improving patient outcomes.[36] This technique targets GBP1 –a binding protein which participates in the regulation of metalloproteinases and decreases the capacity of glioma cells for invasion into normal brain tissue.[37] Immunotherapy, consisting of vaccines prepared from autologic dendritic cells, is also used for treatment of patients with GBM. Adjuvant therapy using the lysate prepared from whole dendritic cells improves the short-term survival in patients with GBM.[38] Hormone treatment is another therapeutic method for patients with GBM. It blocks, among others, the c-Jun N-terminal kinase (JNK)-dependent signalling pathway, which further blocks pro-apoptotic action of estradiol in glioblastoma cells. This method indicates a key role of the JNK pathway in growth inhibition of GBM and induction of the apoptotic pathway.[39]

1.8 GBMs and high rate of recurrence

Current available treatments improve survival time of patients suffering from GBMs but fail to cure it completely. The median survival without treatment is only a few months, which could be increased to only one year after treatment. The five-year survival rate still stands to

roughly 5.0%. In maximal possible surgical resection cases along with chemotherapy and radiotherapy the overall median survival is only 14 months along with median recurrence time of 9.5 months.[40] In case of paediatric glioblastoma this 5-year median survival time is more optimistic and stands at 17%.[41] It is very important to understand the cause of GBM recurrences. There are many hypotheses which explain the GBMs recurrence, among which cancer stem cells hypothesis is the most accepted till date. The concept of CSCs was originated in 1994 during *in vivo* xenotransplantation of human acute myeloid leukaemia cells. During the experiment a fraction of cells was found which showed self-renewal ability along with reconstituting hierarchy of leukemic cells and maintaining the clinical state of disease *in vivo*.[42-45] The CSC hypothesis proposes that there is a cellular hierarchy in each individual tumor and CSCs reside at the top of this hierarchy, with self-renewal and differentiation ability. CSCs show G0 phase arrest which result in drug resistance, radiation resistance and cancer relapse, giving rise to new tumors.[46]

1.9 How CSCs differ from normal stem cells?

CSCs hypothesis raised so many questions regarding the origin of cancer. One of the very important questions arose after the discovery of CSCs, whether cancer is a disease of stem cells? Do normal stem cells get mutated into cancer stem cells? Are they different? The answer to all these questions is that cancer stem cells do differ from normal stem cells. One of the differences between normal stem cells and cancer stem cells is their degree of dependence on the stem cell niche, a specialized microenvironment in which stem cells reside.[47] Chromosomally normal SCs are stable containing a normal diploid genome but CSCs are aneuploid with chromosomal rearrangements. In addition, normal stem cells are generally quiescent or very slow growing, reside in a specific niche, and have relatively long telomeres. Contrariwise, cancer cells expressing stem cell markers are not completely quiescent, and importantly, cancer stem/initiating cells have short telomeres which may reflect the multistep nature of cancer initiation and progression.[48]

1.10 Time delay between surgical resection and adjuvant chemotherapy and radiotherapy

The time delay between surgery of glioblastoma and initiation of chemo and radiotherapy is utmost crucial. It is well established that surgery cannot remove all cancerous cells from the tumor site. There are microscopic remains of tumor at the surgery site which could initiate

tumor relapse. Even after complete feasible resection followed by concomitant chemo radiotherapy the rate of glioblastoma relapse is not going down. It possesses a new challenge for clinicians to treat relapsed tumors. It raises a concern why cancer relapses even after multiple stages of therapy. The answer lies in the unique properties of cancer stem cells which show abnormal behaviour after radio and chemotherapy. Radio resistance and chemoresistance make CSCs very difficult to treat cells. It is important to understand that time delay between the surgery and initiation of radiotherapy and chemotherapy is of utmost important. The remains of the tumor after surgery grow rapidly and initiate new tumor formation at the same site. According to few reports in more than 90% cases the relapse was at the same site of the primary tumor.[49] [50] The average time lapse between surgery and initiation of radio chemotherapy is 4-5 weeks, to allow wound recovery. In a study it was found that nearly 78% of patient with Glioblastoma with surgical resection developed new tumors within 4 weeks of resection.[51] This data possesses a new challenge to look into the therapies to minimize this window of no treatment post-surgery.

1.11 Curcumin and Cancer stem cells

Glioblastoma recurrence is universal and CSCs play a major role in this relapse. Chemoresistance and radio resistance make this relapse even more difficult to treat. This relapse could be controlled by controlling or eliminating the CSCs. We need a therapy that could specifically kill these CSCs and help restore the therapeutic potential. Curcumin is a known anticancer molecule which has immense properties to fight against various cancers including glioblastoma[52-55] but what really amazed the medical researchers is its property to effectively target cancer stem cells.[56-60] Curcumin is a highly lipophilic curcuminoid of turmeric which absorb light at 420nm. There are many mechanisms by which curcumin target various molecular pathways to induce cell death of cancer cells. The main mechanisms by which it targets CSCs is the generation of ROS and suppression of the release of cytokines, particularly interleukin IL-6, IL-8 and IL-1, which stimulate CSCs. It is very interesting to note that curcumin has asymmetrical effect on CSCs and normal stem cells. This property further makes it a molecule of choice during second line treatment post-surgery of glioblastoma.[61]

Despite been the plethora of valuable activities, this molecule suffers significantly at the therapeutic stage because of its poor bioavailability at the treatment site. Curcumin is highly

metabolized in liver and intestine if given orally, which becomes impossible to maintain its good plasma and tissue levels.[62, 63] Nanotherapeutic approaches could be utilized to achieve good bioavailability and improved therapeutic potential of curcumin.

1.12 Chemistry of curcumin

Curcumin (IUPAC name: (1E,6E)-1,7-bis(4-hydroxy-3-methoxyphenyl)-1,6-heptadiene-3,5-dione) is, practically insoluble in water at a neutral and lower pH, but is soluble in acetone, dichloromethane, methanol, ethanol, alkali and oils. The water solubility of curcumin may be increased by its incorporation into various surfactants, such as sodium dodecyl sulfate, polysaccharides, polyethylene glycol and cyclodextrins.[64, 65] In addition, in aqueous solutions and at an alkaline pH, the acidic phenol group in curcumin dissociates its hydrogen, forming the phenolate ion(s) that render the solubility of curcumin in water somewhat possible.[66-68] Curcumin is a natural polyphenol that is responsible for the yellow color of turmeric and exhibits *keto-enol* tautomerism. The *enol* form is more energetically stable in the solid phase and, depending on the solvent, up to 95% can be in the *enol* form.[69] Three reactive functional groups, namely diketone moiety and two phenolic groups determine the activity of curcumin. The biologically important chemical reactions of curcumin are the following: the hydrogen donation leading to oxidation, reversible and irreversible nucleophilic addition (Michael reaction), hydrolysis, degradation and enzymatic reactions.[70] The anticancer properties of curcuminoids depend on the presence of OH groups in the phenolic ring. These groups are an electron donor to free radicals. The methoxy group at position 3 and 3' increases the antioxidant properties of curcuminoids; substitution in the 2 and 2' positions increases all activities than the unsubstituted analogs; cyclization in the central part of the compound and the introduction of heteroatoms (oxygen and nitrogen) leads to the formation of compounds with enhanced antitumor and anti-angiogenic activities; attaching solubilizing groups to the OH group in position 4 and 4' is responsible for the cytotoxicity of curcuminoids; conversion of methoxy groups to hydroxyl increases the anti-HIV activity. [71]

1.13 Curcumin and its degradation product

Wang *et al.* incubated curcumin in 0.1 M phosphate buffer, pH 7.2 at 37°C, and found that 90% was degraded in 30 min.Trans-6-(4-hydroxy-3-methoxyphenyl)-2,4-dioxo-5-hexenal, vanillin, ferulic acid and feruloyl methane were identified as degradation products. [64] This is a plausible explanation of the biological activity of curcumin. However, intermediates of the

curcumin oxidation pathway increased the level of DNA cleavage by both enzymes ~4-5-fold. Moreover, under conditions that promote oxidation, curcumin enhanced topoisomerase II-mediated DNA cleavage even further.[72] They concluded that oxidative metabolites may be responsible for the biological effects of curcumin.[73] Exposure to visible light inflicts more degradation than UV light; the irradiation of curcumin in 254-nm in methanol has been shown to produce three unspecified degradation products, whereas irradiation with daylight produces five unspecified degradation chemicals products.[74] The exposure of curcumin to visible light is solvent-dependent. Irradiation with light (400-750 nm) for 4 h was shown to be associated with cyclization at one of the o-methoxyphenyl groups, producing 7-hydroxy-1-[(2E)-3-(4-hydroxy-3-methoxyphenyl)prop-2-enoyl]-6-methoxy-naphthalen-2(1H)-one in isopropanol, methanol and chloroform, but not in acetonitrile and ethyl acetate.[75] It has also been reported that the photodegradation of curcumin involves the formation of the excited states and generation of singlet oxygen that is responsible for the photobiological and photodynamic activity of curcumin.[76] Thus, it was postulated that the degradation of curcumin following photoexcitation must proceed though the triplet excited state of curcumin. [70]

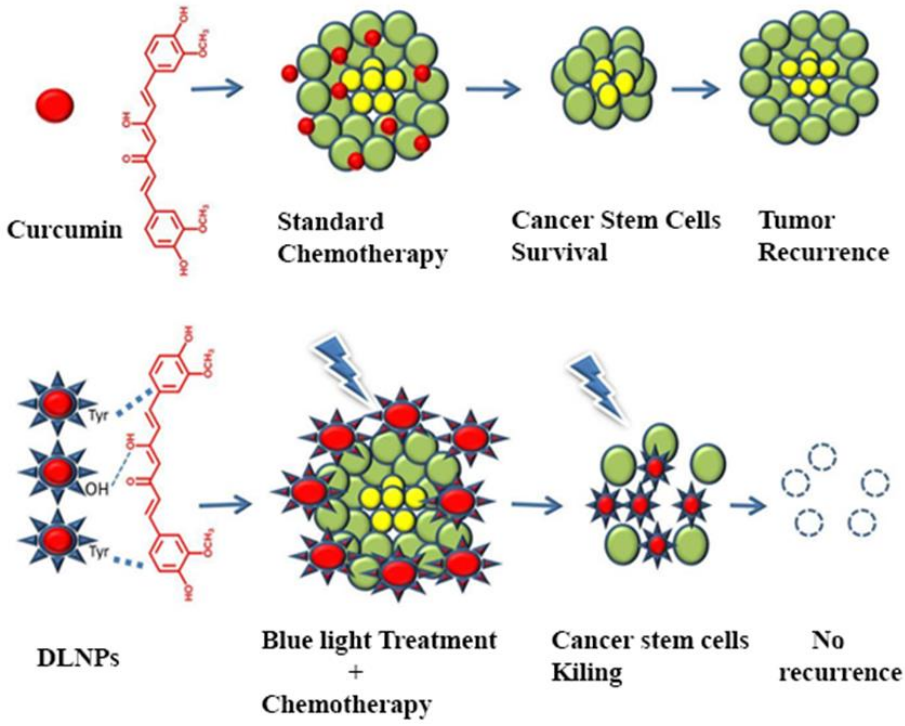

Schematic 1: Nanocurcumin (DLNPs) mediated Blue light photodynamic therapy to restrict growth of glioma stem cells

Our approach is to develop a nano-therapy which could be utilized post-surgery to keep CSCs in check without affecting the growth of normal healthy cells. To address this concern, we have developed blue light mediated therapy which utilizes a potential anticancer molecule curcumin in very low doses to selectively kill CSCs. The concept of nanocurcumin mediated photodynamic therapy is summarized in schematic 1.

2.0 Materials and methods

2.1 Chemicals

Bovine Serum Albumin (BSA) was purchased from sigma life science (cat# A2153), Ethanol molecular grade was purchased from (Merck 1.00983.0511). MTT dye (cat#TC191), Glutaraldehyde 25% w/v solution (cat #RM5927), streptomycin-penicillin solution and MANNITOL were procured from Hi-media. DMEM, FBS, Trypsin EDTA, Curcumin and dialysis membrane were purchased from Sigma Aldrich.

2.2 Characterization

X-ray diffractograms (XRD) were recorded on a Bruker powder XRD D8 X-ray diffractometer. Transmission electron microscopy (TEM) images were obtained with a JSM 2100 operated at 120 kV. Scanning electron microscopy (SEM) images were obtained with JSM IT 300 at 5kV. Fourier transform infrared (FTIR) spectra were recorded on the Cary Agilent 660 IR spectrophotometer. For each spectrum, 256 scans and 4 cm^{-1} resolution were applied over the range of 400–4000cm^{-1}. Micro titter plate reader BioTek synergy 2, Finland was used to record the absorbance and fluorescence change of BSA and curcumin interactions. CD spectra were recorded using JASCO J-1500 Circular dichroism spectrophotometer, Easton, MD, USA using demountable cells (0.1 mm path length, Hellma). Size and zeta potential measurements were performed using Malvern particle size analyzer with the backscattering angle of 173°. UV-Vis spectrophotometer Shimadzu UV-2600 was used to prepare a standard curve of drug and to analyze the amount of drug left in supernatants. Samples were freeze dried using lyophilizer model no. at -140°C and 10mT.

2.3 Synthesis of Placebo BSA Nanoparticles

BSA nanoparticles were prepared by using desolvation method. 20mg/ml of BSA was dissolved in milliQ water. Drop wise addition of 90% ethanol was done under constant stirring of 700rpm at room temperature (25°C). The pH of the solution was maintained at 8.0.

Addition of ethanol causes protein precipitation marked by presence of turbidity as soon as protein gets phase separated. Protein nanoparticles are further crosslinked by 8% Glutaraldehyde solution in water and the solution kept on a rotary shaker overnight. After overnight shaking of nanoparticles with glutaraldehyde, ethanol was vaporized using rotavapor which allowed the nanoparticles to remain suspended in the water phase. Nanoparticle solution was centrifuged at 30,000X g for 30 min to separate the particles. Nanoparticles were resuspended in water using bath sonicator and again centrifuged. This step repeated three times to remove excess of glutaraldehyde and unconverted BSA molecules. After washing particles were freeze dried using 5% mannitol as a cryoprotectant.[77]

2.4 Effect of pH change on size of nanoparticles

Effect of pH was studied on the size of nanoparticles. A wide range of pH from pH 2.0 to pH 12.0 was selected to monitor the size change of BSA nanoparticles. The pH was adjusted using 1N HCl and 1N NaOH. After completion of reaction, a small sample was taken and size was monitored using DLS in distilled water.

2.5 Effect of concentration change in size of nanoparticles

Concentration of the reactant significantly affects the size of nanoparticles. To understand the effect of concentration, change on particles size, different concentrations of BSA (1, 2, 4, 8, 10 mg/ml) was used to prepare BSA nanoparticles in different concentrations at pH8.0 After completion of reaction, a small sample was taken and size was monitored using DLS.

2.6 Drug encapsulation and loading

Curcumin was dissolved in a minimal amount of ethanol and added dropwise to the 2% BSA solution in the mass ratio of 1:5. This reaction allowed to stir for 2 hrs. in the dark condition. After 2 hrs., the same amount of ethanol was added dropwise as in the placebo BSA nanoparticles. Reaction of Curcumin loading was performed in dark condition to avoid the degradation of curcumin in presence of light. After washing, drug loaded nanoparticles were freeze dried using 5% mannitol as a cryoprotectant.

2.7 Drug loading efficiency and Drug encapsulation efficiency

Drug loading efficiency and encapsulation efficiency was calculated using UV-Vis spectroscopy. Supernatant collected after centrifugation was analyzed to check the

availability of the drug in the nanoparticles. Absorbance of curcumin was checked after diluting the supernatant in ethanol and calculation of the presence was done using standard curve of curcumin prepared in ethanol. After freeze drying, nanoformulation was weighed and loading efficiency was calculated as follows.

$$\text{Drug encapsulation efficiency} = \frac{\text{Amount of the drug added} - \text{Amount of drug in supernatant}}{\text{Amount of Drug added}} \times 100$$

$$\text{Drug loading efficiency} = \frac{\text{Amount of drug added- Amount of drug in supernatant}}{\text{Weight of Nanoparticles}} \times 100$$

2.8 CD analysis

CD spectra of BSA, BSA nanoparticle and drug loaded nanoparticles were recorded with a CD spectrophotometer. A quartz cell with a path length of (0.1 cm) was used in the nitrogen atmosphere for measurements in the far-UV region (195-260 nm). BSA concentration was kept constant (2.5 µM), while concentration of BSA nanoparticles (20 µM) and drug loaded nanoparticles (45 µM) was used. An accumulation of three scans with a scan speed of 50 nm/min was performed, and data were collected for each nm from 260 to 195 nm. Sample temperature was maintained at 25 °C using a Neslab RTE-111 circulating water bath connected to the water-jacketed quartz cuvettes. Secondary structure analysis was done using JASCO secondary structure analysis software.

2.9 Spectral studies of BSA and Curcumin interaction

Curcumin interaction with BSA was studied using UV-Vis spectrophotometer. BSA (10 µM) was prepared in milliQ water while curcumin stock was initially prepared in ethanol which was later diluted in milliQ water for interaction studies. Curcumin in different concentrations (5, 10, 20, 40 µM) was treated with 10 µM BSA in 96 well plates and spectra were recorded using a microtiter plate reader. Interaction of curcumin was further confirmed by observing fluorescence of BSA in the presence of different concentrations of curcumin. All the Fluorescence studies were performed in dark color 96 well plates.

2.10 XRD analysis

Powder XRD analysis, samples were lyophilized and put to analysis. XRD analysis was performed from 2θ values of 2 to 80° with a scan rate of 0.2 scan per minute using powder

XRD. Curcumin, BSANPs, drug loaded BSANPs and Physical mixture of BSANPs and curcumin was analyzed and comparative analysis was carried out for the crystallinity of the materials.

2.11 *In vitro* drug release studies

In vitro drug release studies were performed in 20% Ethanolic solution of PBS pH 7.2 using 12KD cut-off dialysis membrane. A solution of 1 mg/ml of curcumin was with prepared 20% Ethanolic solution of PBS pH 7.4, respective amount of drug loaded nanoparticles and physical mixture of BSANPs and curcumin was dissolved in the same solvent. Drug release was analyzed in 9ml 20% Ethanolic solution of PBS pH 7.4 as a releasing media at 37° C with stirring @ 150 rpm. One ml of aliquot was taken at different time intervals and the sink was replaced with the same amount of solvent; aliquot was analyzed using UV-Vis spectrophotometer after taking absorbance at 450nm.

2.12 Photodynamic therapy

Photodynamic therapy was performed using blue led light. Blue light setup was created at INST Mohali lab. Cells were seeded in 24 well plates at the density of 1.5X 10^4 on the prior day to the experiment. Once cells formed the monolayer, treated with different concentrations of drug loaded nanoparticles, BSA nanoparticles, and drug for 2 to 6 hrs in incomplete media. After treatment cells were washed thrice with PBS pH 7.4 and incomplete media was added. Blue light was exposed at different time intervals at a fixed distance of 17mm for a variable time period starting from 2.5 min to 10 min exposure. After exposure, cells were supplemented with 2%FBS DMEM media and incubated overnight. MTT assay was performed at 24hrs with the control that was untreated with blue light.

2.13 ROS generation in presence and absence of light

ROS generation is common phenomena in Photodynamic therapy. The effect of Blue light therapy on ROS generation was studied using DCFDA which produces fluorescence once in contact with free radicles. The C6 cells were seeded in 96 well plates at a density of 1x10^4 cells per well. The cells were treated with various concentrations of drug and drug loaded nanoparticles in presence and absence of light. The generation of ROS was estimated after

taking fluorescence measurements at 562 nm. Hydrogen peroxide was taken as positive control.

2.14 Calculation of Dose for photodynamic therapy

To make photodynamic therapy more appropriate and successful, calculation of effective dose is very important. A comparative analysis of different concentrations (2.5 µM, 5.0 µM, 10.0 µM, 20 µM) of drug, blank nanoparticles and Drug loaded nanoparticles was performed. To calculate the effective dose for therapy the cells were incubated with various concentrations in presence and absence of light followed by MTT assay.

2.15 Time of exposure of light for photodynamic therapy

Exposure time of light is very important to provide sufficient energy to the drug activity. The time of exposure is also dependent on the light intensity of the source. We initially calculated the heat density of the assembly and accordingly calculated different time intervals to provide a fixed does of light. The cells were exposed to blue light for 2.5 min, 5 min and 10 min time with controls of no light exposure. The MTT assay was performed to calculate cell viability in different conditions and to decide the best effective time for exposure.

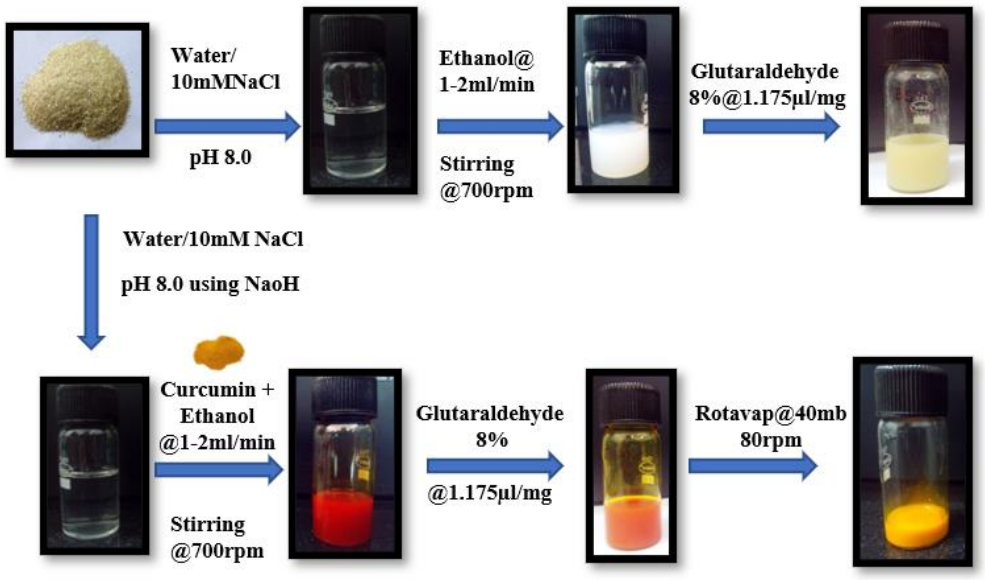

Schematic 2. Methodology of the synthesis of BSA nanoparticles (BSANPs) and curcumin loaded BSA nanoparticles (DLNPs).

2.16 Time delay between drug delivery and exposure of light

Time delay between drug delivery and photodynamic light is equally important. To understand the best time delay between drug delivery and onset of photodynamic therapy three different time intervals which includes 2 hr. 4 hr and 6 hrs. were selected. The cells were treated with drug, blank nanoparticles and drug loaded nanoparticles and exposed to the blue light therapy for 2.5 min after specific time intervals. The MTT assay was performed to calculate the best time delay between drug delivery and photodynamic therapy.

2.17 Western blotting

The western blot analysis was performed to analyze the molecular fate of light exposure on C6 cells. The cells were incubated with 2.5 µM concentration of drug, drug loaded nanoparticles and blank nanoparticles for 4 hrs in presence and absence of light. After exposure, the cells were lysed and protein was isolated. The expression of caspase 3 was estimated using caspase 3 specific antibodies. The western analysis was performed using PVDF membrane.

3.0 Results and discussion

3.1 Nanoparticle Characterization

The size of the BSA nanoparticles were tuned initially in the size range of 80-100nm using various combinations of pH and protein concentrations. The best hydrodynamic size and zeta potential of BSANPs was obtained at a concentration of 2% (w/v) and pH 8.2. The size of the BSA nanoparticle decreases as we move away from the isoelectric point of BSA, although using too low or too high pH is not recommended, because it affects the stability of the loaded drug. After initial optimization of size, zeta and polydispersity the particles were synthesized for drug delivery application in i*n vitro* model of cancer stem cells. The method of nanoparticle synthesis is described in schematic 2**.**

Dynamic light scattering measurements showed an Average hydrodynamic size of 80nm (PDI=0.048) (Fig. 1a) and 90 nm (PDI=0.119) (Fig. 1e) for BSANPs and Drug loaded BSANPs respectively. The zeta potential value of -45mV and -39mV was reported for BSANPs (Fig. 1b) and DLNPs (Fig. 1f) respectively**.** Scanning electron

microscopy (SEM) and transmission electron microscopy (TEM) reveal near to spherical nature of BSANPs (Fig. 1c, 1d) and DLNPs (Fig. 1g, 1h) which lies in the size range of 70-80 nm.

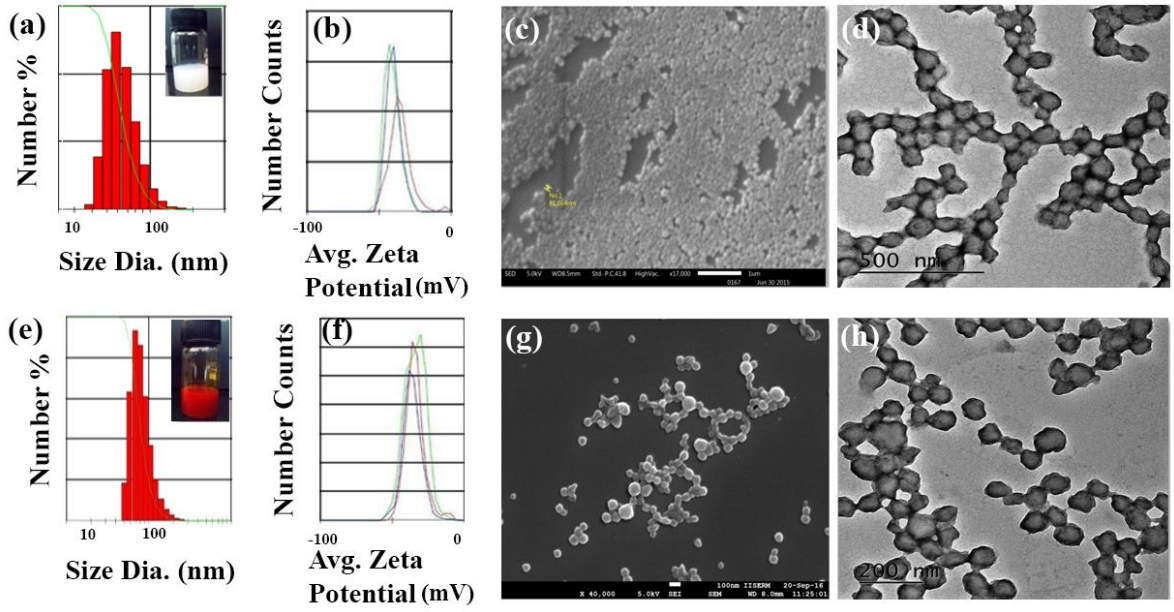

Fig 1.Nanoparticles characterization of BSANPs showing hydrodynamic diameter size (a) ,Average Zeta potential (b), Morphological characteristic through Scanning electron microscopy image (c), Transmission electron microscopy image (d), DLNPs showing Hydrodynamic diameter size (e), average zeta potential (f), and morphological characteristic through field emission scanning electron microscopy image (g), Transmission electron microscopy image showing near spherical shape morphology of nanoparticles (h) .

Fourier transformation infrared (FTIR) analysis was performed to study the interaction between BSANPs and Curcumin and simultaneously to explore the presence of drug inside the nanoformulation. For analysis point of view, only the region of interest is shown (Fig.2a-c). BSANPs exhibit a peak at 1656 cm^{-1} which is the characteristic peak of amide I bond, present in all the three-sample including BSANPs, DLNPs, PM of BSANPs and curcumin. Curcumin displays a characteristic peak at 3507 cm^{-1} (-OH vibrations) which were also present in all three-sample including curcumin, the physical mixture of curcumin and BSANPs and curcumin loaded BSANPs, the peak at 1628cm^{-1} 1604cm^{-1} 1427 cm^{-1} and 1281cm^{-1} represent (-C=O), (aromatic C=C), (phenol C-O), (Enol C-O) respectively. Except these peaks, some additional peaks were also present in DLBSANPs, a broad peak at 3283 cm^{-1} (intermolecular hydrogen bonding) and a small and sharp peak at 3175 cm^{-1} indicating some interaction between curcumin and BSANPs. Additionally, DLBSANPs contain most of the characteristic

peaks of curcumin and only some characteristic peaks of BSANP indicating presence of curcumin inside the BSANPs and a minor change in the secondary structure of BSA during nanoparticle formation which was further confirmed by CD spectroscopy analysis. It has been found that BSA lost its secondary structure through formation of beta sheets and random coils during formation of nanoparticles (Fig.2d. 2e)

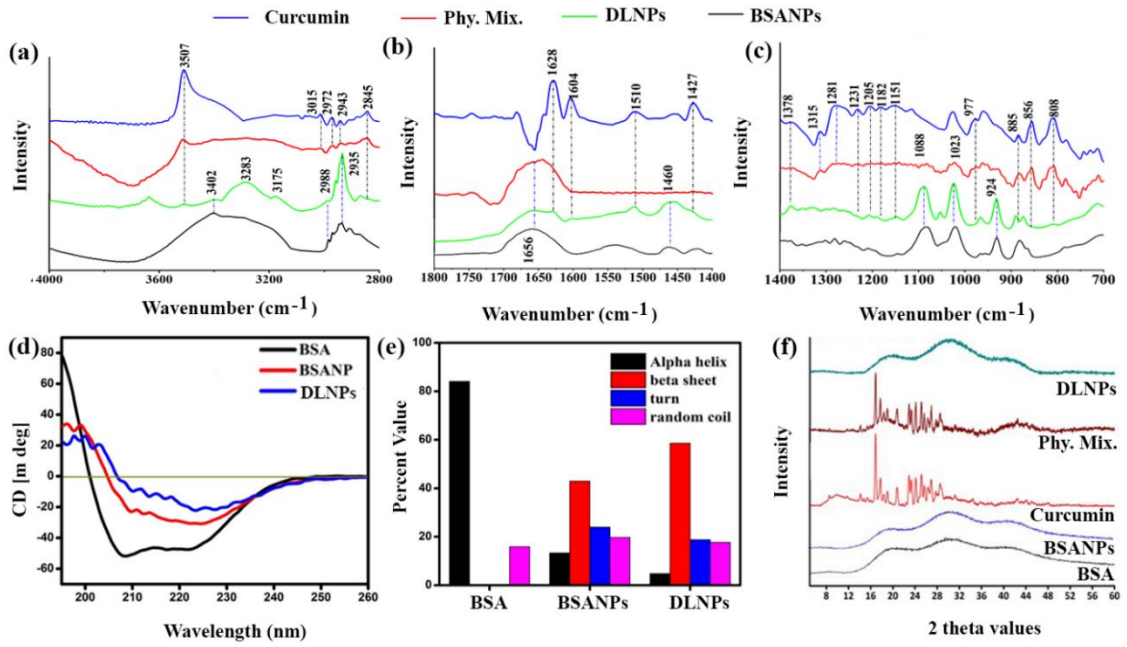

Fig 2. FTIR studies showing presence of various functional groups in Curcumin, BLNPs, DLNPs and physical mixture (a), (b), (c), CD spectroscopy analysis showing change in secondary structure of the BSA during nanoparticles synthesis (d), (e) and PXRD analysis showing crystallinity of the curcumin, BSA, BSANPs, DLNPs and Physical Mix (f).

X-ray diffraction studies were performed to analyze the crystallinity of the drug molecules. The diffraction pattern of BSANPs, curcumin, curcumin loaded BSANPs, and PM were compared (Fig.2f). Curcumin shows diffraction peak at 2θ value of 16.82, 17.72, 20.78, 24.07 and 24.22, although no such diffraction peaks of crystalline curcumin were found in DLNPs, which indicate that curcumin is entirely entrapped inside the BSANPs. The diffraction peaks of curcumin were present in PM of BSANP and curcumin showing crystallinity of the drug (Fig. 4f). We have further studied the solubility of the curcumin as a bare drug and in the form of drug loaded nanoparticles in PBS pH7.4 at 25°C. A saturated solution of the curcumin and equivalent dose in the form of drug loaded nanoparticles along with the PM were subjected to dissolution in

PBS7.4. We have found that Curcumin solubility was increased nearly by two-fold in drug loaded nanoparticles (Fig. 3d). The enhanced solubility of curcumin in DLBSANPs is because of the interaction with BSA. The interaction of the BSA and curcumin was further studied using the change in absorbance and fluorescence of the tryptophan residue (Fig. 3a. 3b).

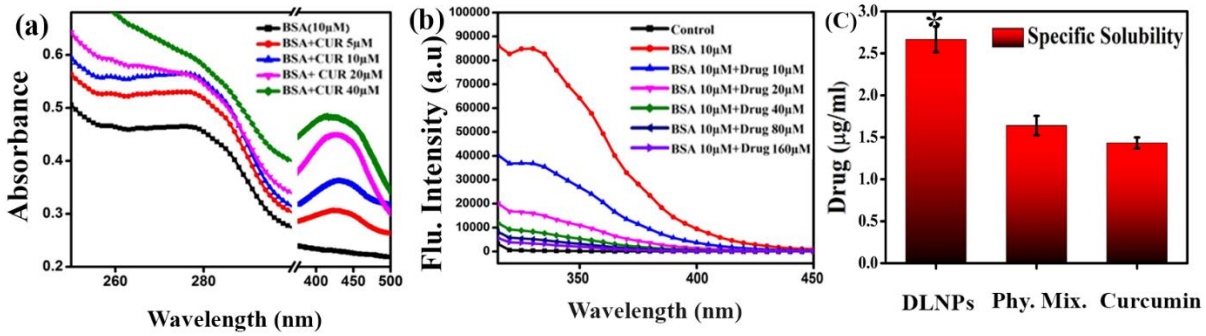

Fig 3. Interaction studies between BSA and curcumin showing change in absorbance (a) and fluorescence of tryptophan residue(b), specific solubility of drug in DLNPs, Phy. Mix. and bare curcumin(c), *p<0.05 is considered as significant.

It is a proven notion that tryptophan is kept buried inside the protein core and its changing absorption pattern helps detect the state of the protein molecule. The interaction studies performed with the fixed concentration of the BSA and varying concentration of curcumin revealed that absorbance of tryptophan changes with change in concentration of the curcumin, similar changes were observed in the fluorescence pattern of the tryptophan. These interactions validate the role of tryptophan in the interaction with curcumin which help buffer the curcumin and improve its solubility in the medium. Along with the interaction studies the data of increased solubility is well supported by *in vitro* drug release profile of DLNPs, where improved drug release pattern was obtained (Fig. 4d).

3.2 Photodynamic therapy and glioma cancer stem cells

The cancer stem cells exhibit drug resistance and radioresistance through some of the very well-defined mechanisms such as ATP-binding cassette (ABC) transporters. [78] [79] Different phytochemicals can overcome this medication resistance. In the present study, we have developed a novel combination therapy to prevent glioblastoma using nano-curcumin and blue light chemo-phototherapy to prevent growth of C6 cells.

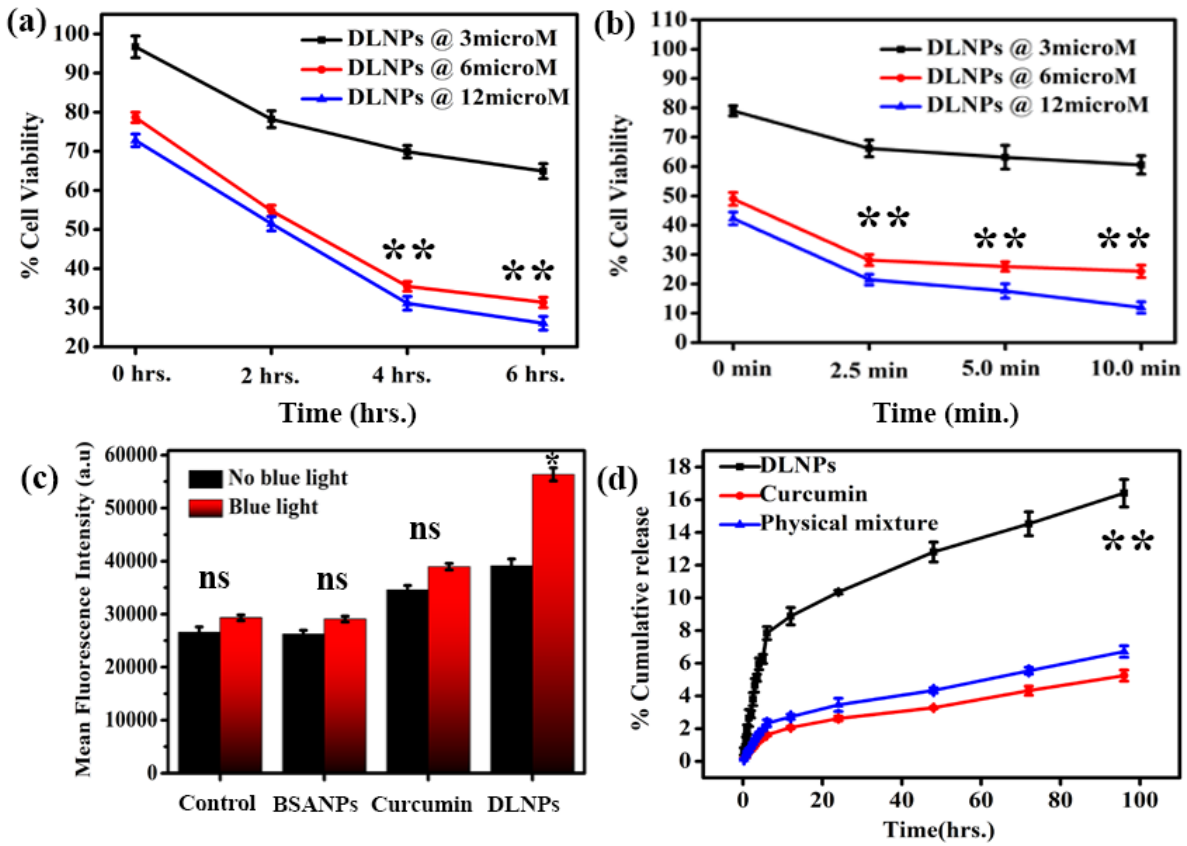

Fig 4. Effect of time delay between DLNPs treatment and exposure of blue light on percent cell viability (a), effect of blue light exposure time on the percent cell viability (b), estimation of ROS activity in the presence and absence of blue light at 6µM dose of DLNPs (c), and In vitro drug release profile for DLNPs, curcumin and Physical mixture, n=3 (d), **p<0.01 is considered as significant, ns= non-significant.

The majority of the population of the C6 cell line are stem cells. [80] Studies on C6 glioma stem cells suggest that they can proliferate in a serum-free medium, indicating that they are very difficult to control. Curcumin is an effective phytochemical that has shown the potential to target cancer stem cells and simultaneously provide neuroprotection. It has proved to reduce the viability of several glioma cell lines over time at concentrations as low as 10-15mM [51]. At the same time, curcumin was also shown to be non-toxic to astrocytes and cortical neurons at low levels. It sensitises radioresistant human glioma cells to radiation-induced cytotoxicity; the same effect was observed with chemotherapeutic drugs. Dietary consumption of curcumin hardly allows reaching effective concentrations in the blood. When orally administered, 8 g of curcumin per day produced 2 mM of curcumin in patients' blood, [81] which is not enough to make any visible changes. nanoparticles of limited dimensions provided a better formulation, which also showed better pharmacokinetics than curcumin administered as a free drug. Several nanoformulations of curcumin comprised metal oxides,[82, 83] liposomes,[84] artificial

liposomes,[85] dendrimers,[86] polymers,[87 88] and cyclodextrins [89] are available but most of them suffer from complex synthesis and toxicity constraints and cannot be used in critical biological organs such as the brain after surgery.

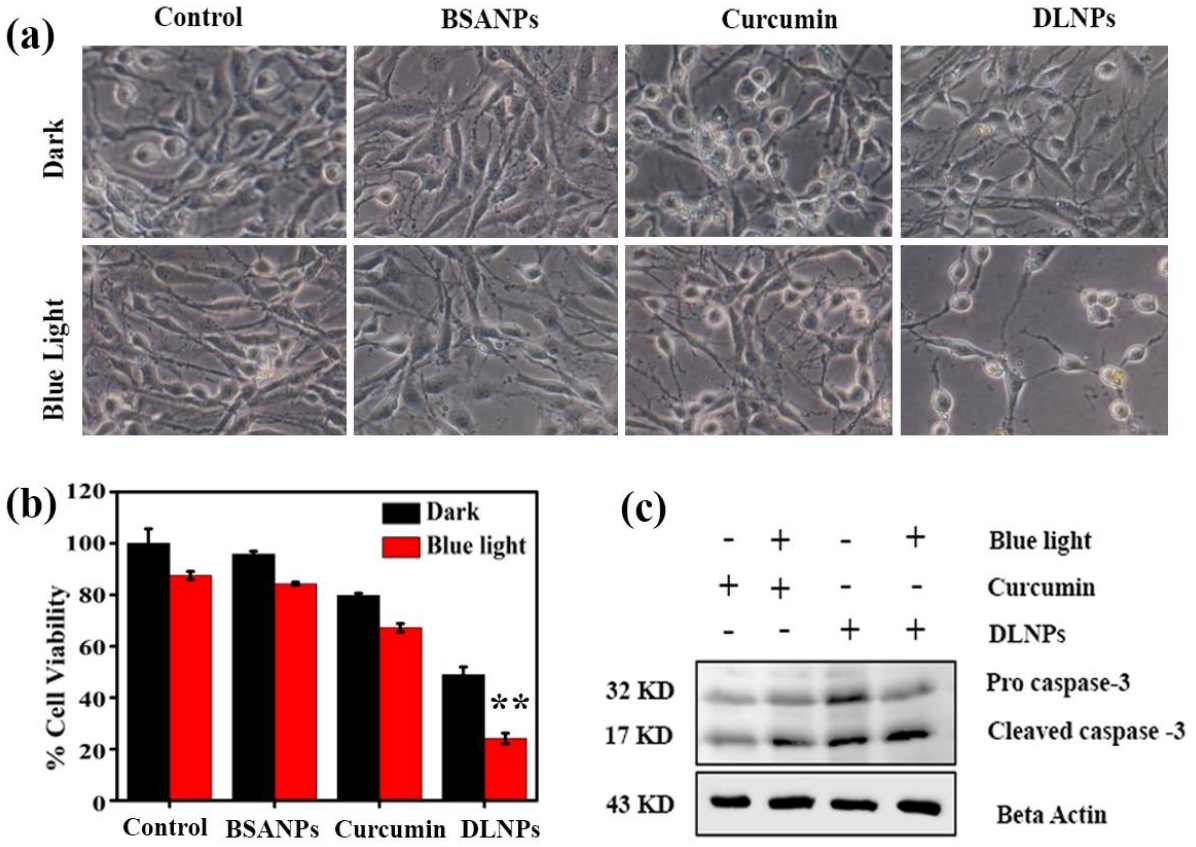

Fig 5. Bright field microscope image of the cells under treatment in absence and presence of the light (a), percent cell viability of the C6 under treatment condition with 6µM equivalent dose of curcumin, DLNPs, BSANPs in presence and absence of the light (b), Western blot analysis of the DLNPs treated C-6 cells showing caspase-3 activation (c), **p<0.01 is considered as significant.

PDT is a growing field with several limitations of therapy and procedures. Delivering light to deep tissues such as the brain is one of the major challenges in PDT, but implantable optical probes have changed the scenario for light mediated therapy in recent years. It is now possible to deliver different wavelengths of light, even to specific regions of the brain, without affecting brain functionality.[90] Curcumin PDT has been effectively used in microorganisms[91-93] but nano-curcumin PDT in cancer stem cells has received little attention. In the current study, bovine serum albumin was used to synthesize curcumin-loaded BSA nanoparticles, which are considered as highly biocompatible and non-toxic. BSA is also utilized in incorporation of photosensitizers using a heat denaturation method; [94] however, the current method is based on glutaraldehyde mediated protein crosslinking, which allows better

packaging of curcumin inside BSANPs. To estimate the best combination of drug dose and blue light exposure time, cells were treated with different concentrations of the drug in combination with blue light.

The effect of Photodynamic therapy was studied through cytotoxicity studies using MTT assay on C6 cancer stem cells. The experiment was conducted in the presence and absence of blue light. In an initial experiment, toxicity of BSANPS were studied in C6 cell line in absence and presence of blue light for various exposure time. The particles were well tolerated by cells and no measurable cytotoxicity was reported in both the conditions at various tested concentrations of the BSANPs. These results are well supported by earlier study, which confirms the biocompatibility of the BSANPs as drug carrier system.[6] Further studying the effect of bare curcumin and Drug loaded BSANPS on cellular toxicity, the cells were treated with various concentrations of the material. We have studied three important parameters during the cellular treatment to obtain the maximum killing of the cancer cells under blue light treatment. The first parameter was the concentration of the drug in DLNPs, second parameter was time of exposure of blue light and the last parameter was the time delay between treatment of the materials and blue light exposure to the cells.

The blue light treatment device was designed indigenously in the lab to give maximum blue light exposure to the cultured cells in 96 well format. The heat energy output of the device was calculated and it was found to be 400 J/ cm^{-2} per minute at a minimum distance of 17mm. Keeping in mind the heat energy factor we have decided three time period of 2.5min, 5 min and 10 min with a complete exposure of 1000 J/ cm^{-2}, 2000 J/ cm^{-2} and 4000 J/ cm^{-2}. The best time delay between treatment and light exposure was calculated depending upon the cellular internalization of the material. We have exposed blue light to the treated cells after 2hrs. 4hrs. and 6 hrs. of treatment. The result confirms that 4 hrs. time delay between treatment and blur light exposure provide better cellular killing, although no advantage in cellular killing was observed after 6 hrs. of internalization (Fig.4a). The best condition of maximum cellular killing was found at 6µM concentration of DLNPs with heat energy output of 1000 J/ cm^{-2} i.e. 2.5 min exposure time (Fig. 4b) after 4hrs of internalization. DLNPs reported best cytotoxicity at the 6µM concentration compared to the curcumin drug. The images were captured using bright field microscope to see the morphological changes of the

cells during cytotoxicity. The cells lost its morphological characteristic after blue light exposure indicating onset of the killing mechanism. Although the morphology was retained in the curcumin and BSANPs treatment group, which indicated their biocompatibility at the treatment concentration (Fig.5a).

The superior cytotoxicity of DLNPs could be attributed to enhanced and sustained release of curcumin from the nanoparticles as demonstrated in the *in vitro* dissolution studies (Fig.3d) and *in vitro* drug release studies (Fig.4d). Spectroscopic properties of BSA and curcumin interaction indicate a strong interaction (Fig. 3a, 3b**)** which allow sustained release of drugs and allow for a prolonged period of drug exposure. Curcumin-loaded BSANPs significantly inhibited the growth of C6 cancer stem cells at a very low dose of curcumin (6µM) following blue light PDT, which is strikingly considered as non-lethal for the healthy cell growth.[95] The combination of chemotherapy with phototherapy induced more cell death in comparative to the chemotherapy alone (Fig. 5b). We have found that nano-curcumin mediates improved solubility, bioavailability and release of curcumin. In combination with blue light PDT therapy, nano-curcumin showed a promising efficacy to inhibit glioblastoma C6 stem cells, which could be difficult to achieve by conventional treatments.

3.3 Mechanism of Enhanced killing of cancer stem cells

Curcumin is a multi-action drug that targets different cellular pathways inside the body. Increased solubility and better bioavailability provided by DLNPs allow improved therapeutic efficacy of the drug at a very small dose of 6µM. The introduction of blue light further elevated the therapeutic potential of the molecule in its nanoform. Blue light in combination with DLNPs induced increased ROS production in the cancer cells compared to the DLNPs alone (Fig. 4c), this could be due to the photo degradation product of curcumin, formed after the blue light exposure. These products, which includes ferulic aldehyde, ferulic acid, feruloyl methane and vanillin are considered as more toxic than parent curcumin leading to increased ROS production. The increased production of ROS in cancer stem cells further onset the proteolytic cascades of molecular events resulting in the caspase activation and cellular apoptosis (Fig. 5c). This increased toxicity of DLNPs is conclusively due to the increased endocytosis of the curcumin-loaded BSANPs and

could be due to the better intracellular distribution of the drug. Current formulation was studied for the C6 glioma cancer stem cells only, but this could be evenly adequate for other kinds of cancer stem cells. Contrary to cancer stem cells, which shows high metabolism rate leading to accumulation of high ROS after nanoparticles delivery, non-cancerous cells metabolize the drug and nanoparticles product very slow causing reversible damage by ROS and induce less toxicity. This could result in specificity of the treatment for cancer cells.

4.0 Conclusions

In summary, we have successfully synthesized curcumin loaded BSANPs with an improved solubility and bioavailability of the curcumin inside the tumor cells. The addition of blue light has further improved the therapeutic potential of the nanocurcumin. This study is designed as a possible treatment method, which could be utilized during the time lag between glioma resection and onset of chemoradiotherapy. Curcumin-loaded BSANs formulation in combination with blue light mediated phototherapy can provide prolonged prevention towards recurrence of tumour through diminishing tumour stem cells and may fasten the wound healing process following craniotomy.

5.0 References

1. Karcher, S.; Steiner, H. H.; Ahmadi, R.; Zoubaa, S.; Vasvari, G.; Bauer, H.; Unterberg, A.; Herold-Mende, C., Different angiogenic phenotypes in primary and secondary glioblastomas. *International journal of cancer* **2006,** *118* (9), 2182-9.
2. Iacob, G.; Dinca, E. B., Current data and strategy in glioblastoma multiforme. *Journal of medicine and life* **2009,** *2* (4), 386-93.
3. Rock, K.; McArdle, O.; Forde, P.; Dunne, M.; Fitzpatrick, D.; O'Neill, B.; Faul, C., A clinical review of treatment outcomes in glioblastoma multiforme--the validation in a non-trial population of the results of a randomised Phase III clinical trial: has a more radical approach improved survival? *The British journal of radiology* **2012,** *85* (1017), e729-33.
4. Ohgaki, H.; Kleihues, P., Epidemiology and etiology of gliomas. *Acta neuropathologica* **2005,** *109* (1), 93-108.
5. Thakkar, J. P.; Dolecek, T. A.; Horbinski, C.; Ostrom, Q. T.; Lightner, D. D.; Barnholtz-Sloan, J. S.; Villano, J. L., Epidemiologic and molecular prognostic review of glioblastoma. *Cancer epidemiology, biomarkers & prevention : a publication of the American Association for Cancer Research, cosponsored by the American Society of Preventive Oncology* **2014,** *23* (10), 1985-96.

6. Schwartzbaum, J. A.; Fisher, J. L.; Aldape, K. D.; Wrensch, M., Epidemiology and molecular pathology of glioma. *Nature clinical practice. Neurology* **2006,** *2* (9), 494-503; quiz 1 p following 516.

7. Lam, P. Y.; Di Tomaso, E.; Ng, H. K.; Pang, J. C.; Roussel, M. F.; Hjelm, N. M., Expression of p19INK4d, CDK4, CDK6 in glioblastoma multiforme. *British journal of neurosurgery* **2000,** *14* (1), 28-32.

8. Cobbs, C. S., Evolving evidence implicates cytomegalovirus as a promoter of malignant glioma pathogenesis. *Herpesviridae* **2011,** *2* (1), 10.

9. Cobbs, C. S.; Harkins, L.; Samanta, M.; Gillespie, G. Y.; Bharara, S.; King, P. H.; Nabors, L. B.; Cobbs, C. G.; Britt, W. J., Human cytomegalovirus infection and expression in human malignant glioma. *Cancer research* **2002,** *62* (12), 3347-50.

10. Spinelli, V.; Chinot, O.; Cabaniols, C.; Giorgi, R.; Alla, P.; Lehucher-Michel, M. P., Occupational and environmental risk factors for brain cancer: a pilot case-control study in France. *Presse medicale* **2010,** *39* (2), e35-44.

11. Padmalatha, C.; Harruff, R. C.; Ganick, D.; Hafez, G. B., Glioblastoma multiforme with tuberous sclerosis. Report of a case. *Archives of pathology & laboratory medicine* **1980,** *104* (12), 649-50.

12. Grips, E.; Wentzensen, N.; Sutter, C.; Sedlaczek, O.; Gebert, J.; Weigel, R.; Schwartz, A.; von Knebel-Doeberitz, M.; Hennerici, M., [Glioblastoma multiforme as a manifestation of Turcot syndrome]. *Der Nervenarzt* **2002,** *73* (2), 177-82.

13. Sanchez-Ortiga, R.; Boix Carreno, E.; Moreno-Perez, O.; Pico Alfonso, A., [Glioblastoma multiforme and multiple endocrine neoplasic type 2 A]. *Medicina clinica* **2009,** *133* (5), 196-7.

14. Broekman, M. L.; Risselada, R.; Engelen-Lee, J.; Spliet, W. G.; Verweij, B. H., Glioblastoma multiforme in the posterior cranial fossa in a patient with neurofibromatosis type I. *Case reports in medicine* **2009,** *2009*, 757898.

15. Zhen, L.; Yufeng, C.; Zhenyu, S.; Lei, X., Multiple extracranial metastases from secondary glioblastoma multiforme: a case report and review of the literature. *Journal of neuro-oncology* **2010,** *97* (3), 451-7.

16. Moorthy, R. K.; Rajshekhar, V., Development of glioblastoma multiforme following traumatic cerebral contusion: case report and review of literature. *Surgical neurology* **2004,** *61* (2), 180-4; discussion 184.

17. Krex, D.; Klink, B.; Hartmann, C.; von Deimling, A.; Pietsch, T.; Simon, M.; Sabel, M.; Steinbach, J. P.; Heese, O.; Reifenberger, G.; Weller, M.; Schackert, G.; German Glioma, N., Long-term survival with glioblastoma multiforme. *Brain : a journal of neurology* **2007,** *130* (Pt 10), 2596-606.

18. Lakhan, S. E.; Harle, L., Difficult diagnosis of brainstem glioblastoma multiforme in a woman: a case report and review of the literature. *Journal of medical case reports* **2009,** *3*, 87.

19. Hur, H.; Jung, S.; Jung, T. Y.; Kim, I. Y., Cerebellar glioblastoma multiforme in an adult. *Journal of Korean Neurosurgical Society* **2008,** *43* (4), 194-7.

20. Tysnes, B. B.; Mahesparan, R., Biological mechanisms of glioma invasion and potential therapeutic targets. *Journal of neuro-oncology* **2001,** *53* (2), 129-47.

21. Birbilis, T. A.; Matis, G. K.; Eleftheriadis, S. G.; Theodoropoulou, E. N.; Sivridis, E., Spinal metastasis of glioblastoma multiforme: an uncommon suspect? *Spine* **2010,** *35* (7), E264-9.
22. Lun, M.; Lok, E.; Gautam, S.; Wu, E.; Wong, E. T., The natural history of extracranial metastasis from glioblastoma multiforme. *Journal of neuro-oncology* **2011,** *105* (2), 261-73.
23. Linkous, A. G.; Yazlovitskaya, E. M., Angiogenesis in glioblastoma multiforme: navigating the maze. *Anti-cancer agents in medicinal chemistry* **2011,** *11* (8), 712-8.
24. Urbanska, K.; Sokolowska, J.; Szmidt, M.; Sysa, P., Glioblastoma multiforme - an overview. *Contemporary oncology* **2014,** *18* (5), 307-12.
25. Brat, D. J.; Castellano-Sanchez, A. A.; Hunter, S. B.; Pecot, M.; Cohen, C.; Hammond, E. H.; Devi, S. N.; Kaur, B.; Van Meir, E. G., Pseudopalisades in glioblastoma are hypoxic, express extracellular matrix proteases, and are formed by an actively migrating cell population. *Cancer research* **2004,** *64* (3), 920-7.
26. Levine, S. A.; McKeever, P. E.; Greenberg, H. S., Primary cerebellar glioblastoma multiforme. *Journal of neuro-oncology* **1987,** *5* (3), 231-6.
27. Katsetos, C. D.; Draberova, E.; Legido, A.; Dumontet, C.; Draber, P., Tubulin targets in the pathobiology and therapy of glioblastoma multiforme. I. Class III beta-tubulin. *Journal of cellular physiology* **2009,** *221* (3), 505-13.
28. Chang, J. E.; Khuntia, D.; Robins, H. I.; Mehta, M. P., Radiotherapy and radiosensitizers in the treatment of glioblastoma multiforme. *Clinical advances in hematology & oncology : H&O* **2007,** *5* (11), 894-902, 907-15.
29. Simpson, J. R.; Horton, J.; Scott, C.; Curran, W. J.; Rubin, P.; Fischbach, J.; Isaacson, S.; Rotman, M.; Asbell, S. O.; Nelson, J. S.; et al., Influence of location and extent of surgical resection on survival of patients with glioblastoma multiforme: results of three consecutive Radiation Therapy Oncology Group (RTOG) clinical trials. *International journal of radiation oncology, biology, physics* **1993,** *26* (2), 239-44.
30. Mahvash, M.; Hugo, H. H.; Maslehaty, H.; Mehdorn, H. M.; Stark, A. M., Glioblastoma multiforme in children: report of 13 cases and review of the literature. *Pediatric neurology* **2011,** *45* (3), 178-80.
31. Kislin, K. L.; McDonough, W. S.; Eschbacher, J. M.; Armstrong, B. A.; Berens, M. E., NHERF-1: modulator of glioblastoma cell migration and invasion. *Neoplasia* **2009,** *11* (4), 377-87.
32. Hegi, M. E.; Diserens, A. C.; Gorlia, T.; Hamou, M. F.; de Tribolet, N.; Weller, M.; Kros, J. M.; Hainfellner, J. A.; Mason, W.; Mariani, L.; Bromberg, J. E.; Hau, P.; Mirimanoff, R. O.; Cairncross, J. G.; Janzer, R. C.; Stupp, R., MGMT gene silencing and benefit from temozolomide in glioblastoma. *The New England journal of medicine* **2005,** *352* (10), 997-1003.
33. Gerstner, E. R.; Batchelor, T. T., Antiangiogenic therapy for glioblastoma. *Cancer journal* **2012,** *18* (1), 45-50.
34. Specenier, P., Bevacizumab in glioblastoma multiforme. *Expert review of anticancer therapy* **2012,** *12* (1), 9-18.
35. Chamberlain, M. C., Bevacizumab for the treatment of recurrent glioblastoma. *Clinical Medicine Insights. Oncology* **2011,** *5*, 117-29.

36. Guo, D.; Wang, B.; Han, F.; Lei, T., RNA interference therapy for glioblastoma. *Expert opinion on biological therapy* **2010,** *10* (6), 927-36.

37. Li, M.; Mukasa, A.; Inda, M. M.; Zhang, J.; Chin, L.; Cavenee, W.; Furnari, F., Guanylate binding protein 1 is a novel effector of EGFR-driven invasion in glioblastoma. *The Journal of experimental medicine* **2011,** *208* (13), 2657-73.

38. Cho, D. Y.; Yang, W. K.; Lee, H. C.; Hsu, D. M.; Lin, H. L.; Lin, S. Z.; Chen, C. C.; Harn, H. J.; Liu, C. L.; Lee, W. Y.; Ho, L. H., Adjuvant immunotherapy with whole-cell lysate dendritic cells vaccine for glioblastoma multiforme: a phase II clinical trial. *World neurosurgery* **2012,** *77* (5-6), 736-44.

39. Altiok, N.; Ersoz, M.; Koyuturk, M., Estradiol induces JNK-dependent apoptosis in glioblastoma cells. *Oncology letters* **2011,** *2* (6), 1281-1285.

40. Delgado-Lopez, P. D.; Corrales-Garcia, E. M., Survival in glioblastoma: a review on the impact of treatment modalities. *Clinical & translational oncology : official publication of the Federation of Spanish Oncology Societies and of the National Cancer Institute of Mexico* **2016,** *18* (11), 1062-1071.

41. Liu, M.; Thakkar, J. P.; Garcia, C. R.; Dolecek, T. A.; Wagner, L. M.; Dressler, E. V. M.; Villano, J. L., National cancer database analysis of outcomes in pediatric glioblastoma. *Cancer medicine* **2018,** *7* (4), 1151-1159.

42. Al-Hajj, M.; Wicha, M. S.; Benito-Hernandez, A.; Morrison, S. J.; Clarke, M. F., Prospective identification of tumorigenic breast cancer cells. *Proceedings of the National Academy of Sciences of the United States of America* **2003,** *100* (7), 3983-8.

43. Bonnet, D.; Dick, J. E., Human acute myeloid leukemia is organized as a hierarchy that originates from a primitive hematopoietic cell. *Nature medicine* **1997,** *3* (7), 730-7.

44. Lapidot, T.; Sirard, C.; Vormoor, J.; Murdoch, B.; Hoang, T.; Caceres-Cortes, J.; Minden, M.; Paterson, B.; Caligiuri, M. A.; Dick, J. E., A cell initiating human acute myeloid leukaemia after transplantation into SCID mice. *Nature* **1994,** *367* (6464), 645-8.

45. Visvader, J. E.; Lindeman, G. J., Cancer stem cells in solid tumours: accumulating evidence and unresolved questions. *Nature reviews. Cancer* **2008,** *8* (10), 755-68.

46. Stopschinski, B. E.; Beier, C. P.; Beier, D., Glioblastoma cancer stem cells--from concept to clinical application. *Cancer letters* **2013,** *338* (1), 32-40.

47. Li, L.; Neaves, W. B., Normal stem cells and cancer stem cells: the niche matters. *Cancer research* **2006,** *66* (9), 4553-7.

48. Shay, J. W.; Wright, W. E., Telomeres and telomerase in normal and cancer stem cells. *FEBS letters* **2010,** *584* (17), 3819-25.

49. Sherriff, J.; Tamangani, J.; Senthil, L.; Cruickshank, G.; Spooner, D.; Jones, B.; Brookes, C.; Sanghera, P., Patterns of relapse in glioblastoma multiforme following concomitant chemoradiotherapy with temozolomide. *The British journal of radiology* **2013,** *86* (1022), 20120414.

50. Loeffler, J. S.; Alexander, E., 3rd; Hochberg, F. H.; Wen, P. Y.; Morris, J. H.; Schoene, W. C.; Siddon, R. L.; Morse, R. H.; Black, P. M., Clinical patterns of failure following stereotactic interstitial irradiation for malignant gliomas. *International journal of radiation oncology, biology, physics* **1990,** *19* (6), 1455-62.

51. Pirzkall, A.; McGue, C.; Saraswathy, S.; Cha, S.; Liu, R.; Vandenberg, S.; Lamborn, K. R.; Berger, M. S.; Chang, S. M.; Nelson, S. J., Tumor regrowth between surgery and initiation of adjuvant therapy in patients with newly diagnosed glioblastoma. *Neuro-oncology* **2009,** *11* (6), 842-52.

52. Perry, M. C.; Demeule, M.; Regina, A.; Moumdjian, R.; Beliveau, R., Curcumin inhibits tumor growth and angiogenesis in glioblastoma xenografts. *Molecular nutrition & food research* **2010,** *54* (8), 1192-201.

53. Liao, H.; Wang, Z.; Deng, Z.; Ren, H.; Li, X., Curcumin inhibits lung cancer invasion and metastasis by attenuating GLUT1/MT1-MMP/MMP2 pathway. *International journal of clinical and experimental medicine* **2015,** *8* (6), 8948-57.

54. Sobolewski, C.; Muller, F.; Cerella, C.; Dicato, M.; Diederich, M., Celecoxib prevents curcumin-induced apoptosis in a hematopoietic cancer cell model. *Molecular carcinogenesis* **2015,** *54* (10), 999-1013.

55. Zhang, X.; Wang, R.; Chen, G.; Dejean, L.; Chen, Q. H., The Effects of Curcumin-based Compounds on Proliferation and Cell Death in Cervical Cancer Cells. *Anticancer research* **2015,** *35* (10), 5293-8.

56. Hossain, M.; Banik, N. L.; Ray, S. K., Synergistic anti-cancer mechanisms of curcumin and paclitaxel for growth inhibition of human brain tumor stem cells and LN18 and U138MG cells. *Neurochemistry international* **2012,** *61* (7), 1102-13.

57. Almanaa, T. N.; Geusz, M. E.; Jamasbi, R. J., Effects of curcumin on stem-like cells in human esophageal squamous carcinoma cell lines. *BMC complementary and alternative medicine* **2012,** *12*, 195.

58. Lin, L.; Liu, Y.; Li, H.; Li, P. K.; Fuchs, J.; Shibata, H.; Iwabuchi, Y.; Lin, J., Targeting colon cancer stem cells using a new curcumin analogue, GO-Y030. *British journal of cancer* **2011,** *105* (2), 212-20.

59. Charpentier, M. S.; Whipple, R. A.; Vitolo, M. I.; Boggs, A. E.; Slovic, J.; Thompson, K. N.; Bhandary, L.; Martin, S. S., Curcumin targets breast cancer stem-like cells with microtentacles that persist in mammospheres and promote reattachment. *Cancer research* **2014,** *74* (4), 1250-60.

60. Rodriguez, G. A.; Shah, A. H.; Gersey, Z. C.; Shah, S. S.; Bregy, A.; Komotar, R. J.; Graham, R. M., Investigating the therapeutic role and molecular biology of curcumin as a treatment for glioblastoma. *Therapeutic advances in medical oncology* **2016,** *8* (4), 248-60.

61. Peter P. Sordillo, L. H., Curcumin and Cancer Stem Cells: Curcumin Has Asymmetrical Effects on Cancer and Normal Stem Cells. *Anticancer research* **2015,** *35*, 599-614.

62. Christopher Ireson, S. O., Don J. L. Jones, Richard Verschoyle, Chang-Kee Lim, Jin-Li Luo,; Lynne Howells, S. P., Rebekah Jukes, Marion Williams, William P. Steward, and Andreas Gescher, Characterization of Metabolites of the Chemopreventive Agent Curcumin in Human

and Rat Hepatocytes and in the Rat in Vivo, and Evaluation of Their Ability to Inhibit Phorbol Ester-induced Prostaglandin E2 Production. *Cancer research* **2001,** *61*, 1058–1064.

63. Ireson, C. R.; Jones, D. J.; Orr, S.; Coughtrie, M. W.; Boocock, D. J.; Williams, M. L.; Farmer, P. B.; Steward, W. P.; Gescher, A. J., Metabolism of the cancer

chemopreventive agent curcumin in human and rat intestine. *Cancer epidemiology, biomarkers & prevention : a publication of the American Association for Cancer Research, cosponsored by the American Society of Preventive Oncology* **2002,** *11* (1), 105-11.

64. Wang, Y. J.; Pan, M. H.; Cheng, A. L.; Lin, L. I.; Ho, Y. S.; Hsieh, C. Y.; Lin, J. K., Stability of curcumin in buffer solutions and characterization of its degradation products. *Journal of pharmaceutical and biomedical analysis* **1997,** *15* (12), 1867-76.
65. Tonnesen, H. H., Solubility, chemical and photochemical stability of curcumin in surfactant solutions. Studies of curcumin and curcuminoids, XXVIII. *Die Pharmazie* **2002,** *57* (12), 820-4.
66. Schneider, C.; Gordon, O. N.; Edwards, R. L.; Luis, P. B., Degradation of Curcumin: From Mechanism to Biological Implications. *Journal of agricultural and food chemistry* **2015,** *63* (35), 7606-14.
67. Metzler, M.; Pfeiffer, E.; Schulz, S. I.; Dempe, J. S., Curcumin uptake and metabolism. *BioFactors* **2013,** *39* (1), 14-20.
68. Mohanty, C.; Sahoo, S. K., The in vitro stability and in vivo pharmacokinetics of curcumin prepared as an aqueous nanoparticulate formulation. *Biomaterials* **2010,** *31* (25), 6597-611.
69. Manolova, Y.; Deneva, V.; Antonov, L.; Drakalska, E.; Momekova, D.; Lambov, N., The effect of the water on the curcumin tautomerism: a quantitative approach. *Spectrochimica acta. Part A, Molecular and biomolecular spectroscopy* **2014,** *132*, 815-20.
70. Priyadarsini, K. I., The chemistry of curcumin: from extraction to therapeutic agent. *Molecules* **2014,** *19* (12), 20091-112.
71. Mazumder, A.; Neamati, N.; Sunder, S.; Schulz, J.; Pertz, H.; Eich, E.; Pommier, Y., Curcumin analogs with altered potencies against HIV-1 integrase as probes for biochemical mechanisms of drug action. *Journal of medicinal chemistry* **1997,** *40* (19), 3057-63.
72. Ketron, A. C.; Gordon, O. N.; Schneider, C.; Osheroff, N., Oxidative metabolites of curcumin poison human type II topoisomerases. *Biochemistry* **2013,** *52* (1), 221-7.
73. Gordon, O. N.; Luis, P. B.; Ashley, R. E.; Osheroff, N.; Schneider, C., Oxidative Transformation of Demethoxy- and Bisdemethoxycurcumin: Products, Mechanism of Formation, and Poisoning of Human Topoisomerase IIalpha. *Chemical research in toxicology* **2015,** *28* (5), 989-96.
74. Ansari, M. J.; Ahmad, S.; Kohli, K.; Ali, J.; Khar, R. K., Stability-indicating HPTLC determination of curcumin in bulk drug and pharmaceutical formulations. *Journal of pharmaceutical and biomedical analysis* **2005,** *39* (1-2), 132-8.
75. Heger, M.; van Golen, R. F.; Broekgaarden, M.; Michel, M. C., The molecular basis for the pharmacokinetics and pharmacodynamics of curcumin and its metabolites in relation to cancer. *Pharmacological reviews* **2014,** *66* (1), 222-307.
76. Tonnesen, H. H.; de Vries, H.; Karlsen, J.; Beijersbergen van Henegouwen, G., Studies on curcumin and curcuminoids. IX: Investigation of the photobiological activity of curcumin using bacterial indicator systems. *Journal of pharmaceutical sciences* **1987,** *76* (5), 371-3.

77. Zhao, D.; Zhao, X.; Zu, Y.; Li, J.; Zhang, Y.; Jiang, R.; Zhang, Z., Preparation, characterization, and in vitro targeted delivery of folate-decorated paclitaxel-loaded bovine serum albumin nanoparticles. *International journal of nanomedicine* **2010,** *5*, 669-77.

78. Kratz, F., Albumin as a drug carrier: design of prodrugs, drug conjugates and nanoparticles. *Journal of controlled release : official journal of the Controlled Release Society* **2008,** *132* (3), 171-83.

79. Agostinis, P.; Berg, K.; Cengel, K. A.; Foster, T. H.; Girotti, A. W.; Gollnick, S. O.; Hahn, S. M.; Hamblin, M. R.; Juzeniene, A.; Kessel, D.; Korbelik, M.; Moan, J.; Mroz, P.; Nowis, D.; Piette, J.; Wilson, B. C.; Golab, J., Photodynamic therapy of cancer: an update. *CA: a cancer journal for clinicians* **2011,** *61* (4), 250-81.

80. Brown, P. D.; Maurer, M. J.; Rummans, T. A.; Pollock, B. E.; Ballman, K. V.; Sloan, J. A.; Boeve, B. F.; Arusell, R. M.; Clark, M. M.; Buckner, J. C., A prospective study of quality of life in adults with newly diagnosed high-grade gliomas: the impact of the extent of resection on quality of life and survival. *Neurosurgery* **2005,** *57* (3), 495-504; discussion 495-504.

81. Cheng, A. L.; Hsu, C. H.; Lin, J. K.; Hsu, M. M.; Ho, Y. F.; Shen, T. S.; Ko, J. Y.; Lin, J. T.; Lin, B. R.; Ming-Shiang, W.; Yu, H. S.; Jee, S. H.; Chen, G. S.; Chen, T. M.; Chen, C. A.; Lai, M. K.; Pu, Y. S.; Pan, M. H.; Wang, Y. J.; Tsai, C. C.; Hsieh, C. Y., Phase I clinical trial of curcumin, a chemopreventive agent, in patients with high-risk or pre-malignant lesions. *Anticancer research* **2001,** *21* (4B), 2895-900.

82. Abbaraju, P. L.; Meka, A. K.; Jambhrunkar, S.; Zhang, J.; Xu, C.; Popat, A.; Yu, C., Floating tablets from mesoporous silica nanoparticles. *Journal of materials chemistry. B* **2014,** *2* (47), 8298-8302.

83. Jambhrunkar, S.; Karmakar, S.; Popat, A.; Yu, M.; Yu, C., Mesoporous silica nanoparticles enhance the cytotoxicity of curcumin. *RSC advances* **2014,** *4* (2), 709-712.

84. Mourtas, S.; Lazar, A. N.; Markoutsa, E.; Duyckaerts, C.; Antimisiaris, S. G., Multifunctional nanoliposomes with curcumin-lipid derivative and brain targeting functionality with potential applications for Alzheimer disease. *European journal of medicinal chemistry* **2014,** *80*, 175-83.

85. Pawar, N.; Rawat, K.; Bohidar, H. B., Self-assembly of synthetic liposome-like curcumin nanoparticles. *RSC advances* **2016,** *6* (77), 73677-73682.

86. Shi, W.; Dolai, S.; Rizk, S.; Hussain, A.; Tariq, H.; Averick, S.; L'Amoreaux, W.; El ldrissi, A.; Banerjee, P.; Raja, K., Synthesis of monofunctional curcumin derivatives, clicked curcumin dimer, and a PAMAM dendrimer curcumin conjugate for therapeutic applications. *Organic letters* **2007,** *9* (26), 5461-4.

87. Shaikh, J.; Ankola, D. D.; Beniwal, V.; Singh, D.; Kumar, M. N., Nanoparticle encapsulation improves oral bioavailability of curcumin by at least 9-fold when compared to curcumin administered with piperine as absorption enhancer. *European journal of pharmaceutical sciences : official journal of the European Federation for Pharmaceutical Sciences* **2009,** *37* (3-4), 223-30.

88. Song, Z.; Feng, R.; Sun, M.; Guo, C.; Gao, Y.; Li, L.; Zhai, G., Curcumin-loaded PLGA-PEG-PLGA triblock copolymeric micelles: Preparation, pharmacokinetics and distribution in vivo. *Journal of colloid and interface science* **2011,** *354* (1), 116-23.

89. Yallapu, M. M.; Jaggi, M.; Chauhan, S. C., beta-Cyclodextrin-curcumin self-assembly enhances curcumin delivery in prostate cancer cells. *Colloids and surfaces. B, Biointerfaces* **2010,** *79* (1), 113-25.

90. Zorzos, A. N.; Boyden, E. S.; Fonstad, C. G., Multiwaveguide implantable probe for light delivery to sets of distributed brain targets. *Opt Lett* **2010,** *35* (24), 4133-5.

91. Leite, D. P.; Paolillo, F. R.; Parmesano, T. N.; Fontana, C. R.; Bagnato, V. S., Effects of photodynamic therapy with blue light and curcumin as mouth rinse for oral disinfection: a randomized controlled trial. *Photomed Laser Surg* **2014,** *32* (11), 627-32.

92. Dovigo, L. N.; Pavarina, A. C.; Ribeiro, A. P.; Brunetti, I. L.; Costa, C. A.; Jacomassi, D. P.; Bagnato, V. S.; Kurachi, C., Investigation of the photodynamic effects of curcumin against Candida albicans. *Photochemistry and photobiology* **2011,** *87* (4), 895-903.

93. Andrade, M. C.; Ribeiro, A. P.; Dovigo, L. N.; Brunetti, I. L.; Giampaolo, E. T.; Bagnato, V. S.; Pavarina, A. C., Effect of different pre-irradiation times on curcumin-mediated photodynamic therapy against planktonic cultures and biofilms of Candida spp. *Archives of oral biology* **2013,** *58* (2), 200-10.

94. Rodrigues, M. M. A.; Simioni, A. R.; Primo, F. L.; Siqueira-Moura, M. P.; Morais, P. C.; Tedesco, A. C., Preparation, characterization and in vitro cytotoxicity of BSA-based nanospheres containing nanosized magnetic particles and/or photosensitizer. *Journal of magnetism and magnetic materials* **2009,** *321* (10), 1600-1603.

95. Fong, D.; Yeh, A.; Naftalovich, R.; Choi, T. H.; Chan, M. M., Curcumin inhibits the side population (SP) phenotype of the rat C6 glioma cell line: towards targeting of cancer stem cells with phytochemicals. *Cancer letters* **2010,** *293* (1), 65-72.

Note:

- The due permission has been obtained from authors and corresponding author of the following published paper before adopting in the present thesis.
- **Dev, A**.; Srivastava, A. K.; Choudhury, S. R.; Karmakar, S., Nano-curcumin influences blue light photodynamic therapy for restraining glioblastoma stem cells growth. *RSC advances* 2016, 6 (97), 95165-95168.

Chapter 03

Acetyl modified 4HPR loaded HSA nanoparticles for the treatment of paediatric Neuroblastoma

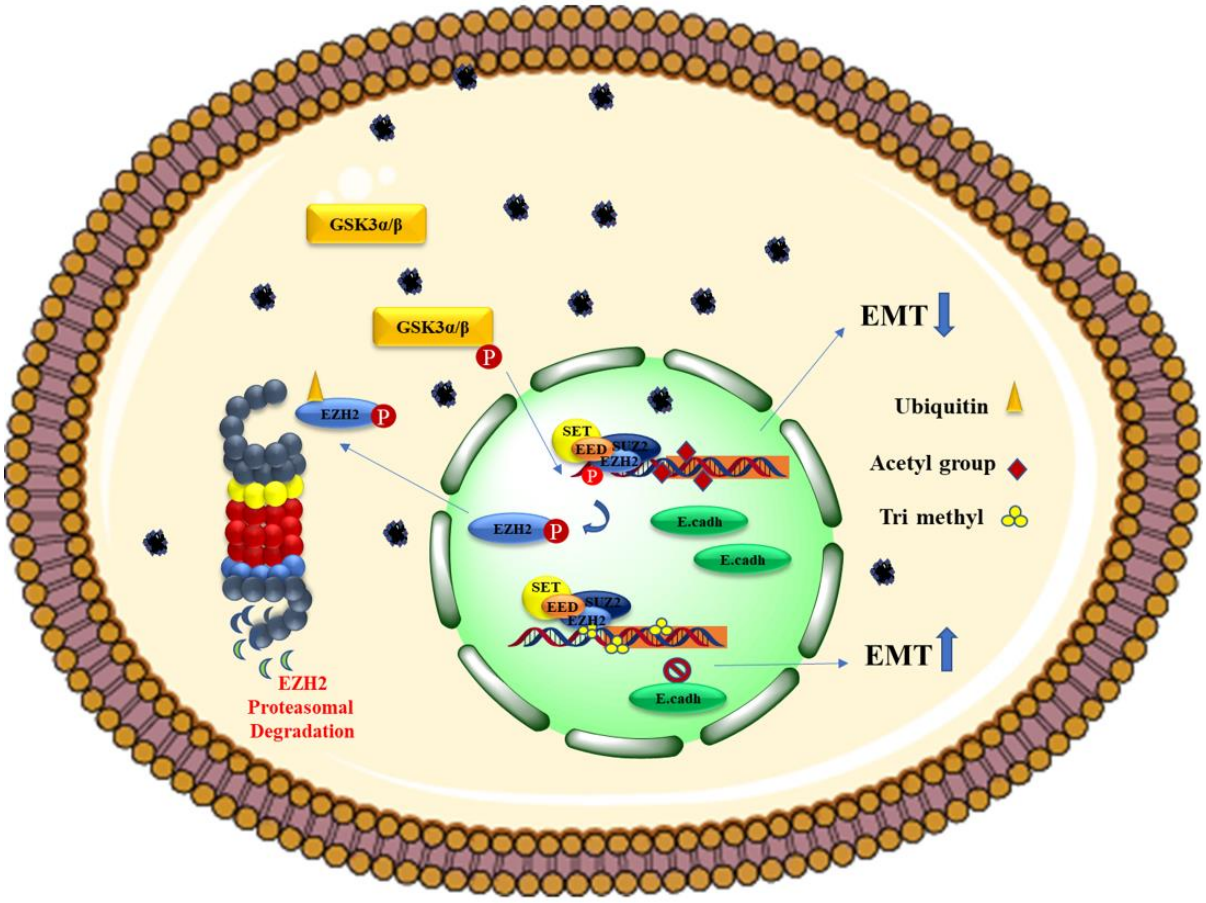

1.0 Background

Neuroblastoma (NB) is a form of extracranial solid tumour that develops in young children. It is prominent in the age group of 0-14 years with a median age of 19 months at the time of diagnosis.[1]The historical medical data suggest that boys are more prone compared to girls for Neuroblastoma. Biological heterogeneity and range of clinical behaviour distinguish Neuroblastoma from other solid tumours. The clinical behaviour of NB spans from spontaneous regression to cases of highly aggressive metastatic disease, which are highly unresponsive to standard anticancer treatment.

Depending on historical overall and event-free survival (EFS) rates and histological and biological characteristics, the clinician categorized NB patients into low-, intermediate-, and high-risk groups. In general, the low-risk category has excellent EFS and overall survival (OS) rates with minimal therapeutic interventions. The patients with the intermediate-risk disease receive surgery and chemotherapy, after initial improvement due to surgery and chemotherapy, the focus is shifted to biologic markers to monitor the progress of the treatment further.[2] Patients with high-risk disease contribute heavily to the new NB cases each year. The patient with high-risk groups requires multimodal therapies, including chemotherapy, surgery, radiotherapy, biologic and immunotherapeutic maintenance therapy to improve their survival odds. A Four-year EFS of 59%±5% is reported using these multimodal therapies in the NB patients treated with ch14.18 immunotherapy in phase III clinical trial.[3]A higher incidence of cancer relapse and associated deaths has raised concern on the currently available treatments' therapeutic potential. It remains essential to better understand the origins and pathophysiology of the disease to develop new therapeutic platforms.

Neuroblastoma is anembryonic malignancy which arises in the neuronal ganglia of the peripheral sympathetic nervous system. The neuronal structures are derived from ventrolateral neural crest cells in the early developmental stages of the embryo.[4] Neuroblastoma can develop anywhere in the body along with the sympathetic nervous system. Thirty percent of NB cases report development in the adrenal medulla, while ~60% arises in the abdominal paraspinal ganglia. The remainder cases report development in the sympathetic ganglia in the chest, head/neck, and pelvis. The clinical behaviour and therapeutic outcome of NB are highly variable. Long term survival depends primarily on the

differentiation of the tumour. The more primitive type of tumour has a less favourable outcome compared to the well-differentiated tumours.[5]

The extensive heterogeneity in the malignancy of NB is the reflection of complex developmental biology of the neural crest.[6] The biology of neural crest development in the embryogenesis holds the key to understand the pathogenesis of NB. Understanding the pathophysiology of the disease help identify the novel molecular pathways for the new targeted interventions. Neural tube formation in vertebrates requires a maturation process which occurs within the neural crest. This maturation process control by several complex transcriptional and epigenetic regulatory factors[7, 8]. This process, help gain the multipotent differentiation potential in the earliest neural crest precursors. These precursors obtain self-renewal phenotype of embryonic stem cells. A cascade of signalling molecules involving BMP, Wnt, Notch, and other ligands helps drive these precursors' differentiation into epithelial, mesenchymal and endothelial components[9, 10] the development of peripheral sympathetic ganglia and neuroendocrine adrenal medulla.[11]Any alteration in this maturation process directs the multipotent neural crest precursors into malignant transformation.

Development of neural crest requires the programmed epithelial to mesenchymal transition. This process is guard by several transcriptional factors, including ZIC1, PAX3, TPAP2a, Notch, and PRDM1A, which transform the neural ectoderm into the neural crest. Subsequent expression of the several new transcription factors like SOXE family and ZEB2 drives mesenchymal transformation, marked by loss of E-cadherins, cell contacts, and activation of metalloproteinases. Activation of new molecules in the microenvironment further derives the differentiation of these mesenchymal migratory neural crest cells. These early precursor cells are pluripotent and have self-renewal capacity. Expression of several pro-survival factors such as C-Myc and MYCN makes these cells highly proliferative and resistant to apoptosis.[12] Neuroblastoma cancer stem cells (CSCs) may yield distinct tumour phenotypes depending on the developmental stage of the neural crest precursor cells.[13, 14]

The development of NB was thought to be controlled by allowing the differentiation of the neuroblastoma stem cells responsible for NB development. The same strategy found to be successful in the last decades using retinoids for NB patients. However, the success rate was higher in the patient with minimal residual disease. The toxicity and development of resistance against retinoids have limited the clinical practice using retinoic acid. After the

limited success of currently available therapies, alternative approaches, including epigenetic regulatory drugs, are in high demand to counter the aggressiveness and drug resistance of NB. Epigenetic changes can be transmitted through mitosis and meiosis without changing the nucleotide sequence of the genes. These changes include DNA methylation and histone modifications which contribute to the development of NB. Histone methylation and acetylation in the promoter region of tumour suppressors are among the hallmarks of NB. Targeting histone methylation and acetylation by targeting the methyltransferases EZH2, along with delivering the derivative of retinoic acid could solve the problem of therapeutic inefficacy and resistance against NB. The current work precisely addresses this hypothesis. Here we have synthesized HSA based nanoformulation of 4-HPR (fenretinide), a retinoic acid derivative to improve its bioavailability and minimize toxicities. We have further modified the same 4HPR loaded HSA nanoparticles with acetyl group modification on the surface. The idea here is to deliver the acetyl pool inside the cancer cells and improve the acetyl: methyl equilibrium at the histones and simultaneously provide retinoic acid to induce the differentiation and slow the tumour's growth. The prime reason of histone methylation is removing acetyl pool from the macromolecules to feed highly proliferative cancer cells' energy demand. It has been reported that cancer cells use the acetyl-CoA pool to fulfil its energy demands and upgrade fat metabolism for the synthesis of new cells.[15, 16] We hypothesized that by simultaneously delivering acetyl pool locally inside the cancer cells and retinoic acid would allow epigenetic reversal at tumour suppressors' promoter sites and improve NB treatment efficacy.

2.0 Materials and methods

2.1 Materials

Human serum albumin 20% solution was purchased from AlbuRel™.4HPR (fenretinideH7779) was purchased from Sigma Aldrich. MTT dye (TC191), Glutaraldehyde 25% w/v solution (RM5927), Propidium Iodide (TC252), streptomycin penicillin solution (A018), Mannitol (PCT0604), High glutamax (AL007G), FBS (RM9955), Trypsin EDTA (TCL144), were purchased from Hi-media. Primary antibodies Beta-actin (SC-47778), Caspase 3 (SC-56053), ENX1 (SC-16609), pSer (SC-81514), SOX2(SC-365823), Oct3/4(SC-5279), Nanog (SC-293121) Fibronectin (SC-271098) E-cadherin (SC-71007), pGSK3α/β (SC-81496), Ac-H3 (SC-56616), Ub (SC-8017) were purchased from SCBT.

Histone 3[17], H3K27me3 [18] were purchased from CST. HPR tagged secondary anti-mouse antibody (SC-516102), and TRITC labelled secondary anti-mouse antibody (SC-516140) were purchased from Santa Cruz Biotechnology. Primary antibodies H3K27me3 (9733) were purchased from Cell Signaling Technology. Neuroblastoma cells SH-SY5Y was procured from national cell repository, NCCS, Pune, India. The nude mice strain of the mice was procured from ACTREC, Pune.

2.2 Characterization

Size and zeta potential measurement were performed using Malvern particle size analyzer with the backscattering angle of 173 Transmission electron microscopy (TEM) images were obtained with a JSM 2100 operated at 120 kV. UV-Vis spectrophotometer Shimadzu UV-2600 was used to prepare a standard curve of 4HPR in ethanol and analyze the amount of 4HPR left in the supernatant. Flow cytometry analysis was performed on BD FACS Calibur (BD Biosciences, San Jose, CA, USA) and Confocal Laser scanning microscope (Leica microsystems) was used for fluorescence imaging.

2.3 Synthesis of HSA nanoparticles (HSANP)

HSANP were prepared by using the antisolvent precipitation method. Briefly, 20 mg/ml of Human serum albumin (HSA) was precipitated using an ethanolic solution. The crosslinking of the newly synthesized nanoparticles was performed by 8% solution of glutaraldehyde. The process was followed as described in the earlier report[19].

2.4 4HPR drug loading

4HPR loading efficiency and encapsulation efficiency were calculated using UV-Vis spectroscopy at 362 nm. Unbound 4HPR was removed using ten kDa Amicon tubes centrifuged at 4000 rpm. The quantification of encapsulated 4HPR was calculated from the standard curve ranging from 10-100 μg/mL. The following equation was used to calculate the drug loading and entrapment efficiency of HSA nanoparticles.

$$\text{Entrapment efficiency (EE)} = \frac{\text{amount of the 4HPR added - Amount of 4HPR in supernatant X 100}}{\text{Amount of GEN added}}$$

$$\text{Drug Loading efficiency} = \frac{\text{amount of 4HPR added - Amount of 4HPR in supernatant X 100}}{\text{Weight of Nanoparticles}}$$

2.5 Acetyl modification of 4HPR loaded HSA nanoparticles

The acetyl modification of the 4HPR loaded nanoparticle is performed using two different acetylating agents like acetylsalicylic acid (Aspirin) and acetic anhydride. Briefly, newly synthesized 4HPR loaded HSA nanoparticles were incubated with the acetylating agent's variable concentration at pH7.4 in the PBS. The addition of acetylating agents to the 4HPR loaded HSA nanoparticles solution resulted in a significant pH drop, maintained by the addition of 1N NaOH and 1N HCl. The reaction was performed overnight at the room temperature (25°C). After completing the reaction, the 4HPR loaded HSA nanoparticles were purified using multiple washing with 1X PBS at 4°C. The purified samples were lyophilized and stored at 4°C for further use.

2.6 Studying percent acetyl modification in 4HPRANP

The percent acetyl modification of 4HPRANP was calculated using Fluorescamine. A fluorescence-based standard curve of Fluorescamine was briefly prepared using HSA as a source of free NH_2 group. Initially, the reaction was setup, and 4HPRNP were synthesized, the reaction volume was equally divided into two halves. Half was taken to monitor the free amino group's presence in the reaction; the second half of the reaction was modified using 20microM acetylsalicylic acid in 1XPBS. The fluorescence 4HPRNP and modified 4HPRANP was recorded using standard protocols. The fluorescence quenching in 4HPRANP indicates the modification of the amine group using Aspirin. The percent free amine group was calculated concerning unmodified 4HPRNP.

2.7 TEM analysis

TEM samples were prepared on the carbon-coated grid 300 meshes after dilution in distilled water and bath sonication for 30 min. The samples' negative staining was performed using 0.5 % phosphor tungstic acid (PTA) for 2 min. Furthermore, kept in a desiccator overnight to remove moisture before analysis.

2.8 *In vitro* 4HPR release studies

In vitro drug release studies were performed in 20% ethanolic solution of PBS pH 7.4 using 12KD cut off dialysis membrane. Ten mg of 4HPRNP and 4HPRANP (acetyl modified 4HPR loaded HSANP) was weighed and suspended in 1 ml of 20% ethanolic solution of PBS pH 7.4. 4HPR release was analyzed in 50 ml of 20% methanolic solution of PBS pH 7.4 as a releasing medium at 37° C with stirring @ 150rpm. One ml of aliquot was taken at a different

time interval, and the sink was replaced with the same amount of solvent; an aliquot was analyzed using UV-Vis spectrophotometer after taking absorbance at 362 nm.

2.9 Cell Culture

Neuroblastoma cells SH-SY5Y was purchased from NCCS Pune (passage number 24) and sub-cultured at 50-60% confluency. According to standard cell culture protocols, the cells were cultured in Higlutamx medium supplemented with 10% FBS and 1% antibiotic solution and culture were maintained at 37°C under 5% CO_2 atmosphere. The cells were maintained in log phase before every experiment.[36]

2.10 Cytotoxicity assay

Proliferation of SH-SY5Y cells under various treatment conditions was evaluated using the colorimetric MTT assay. Briefly, $1x10^4$ cells per well were seeded in 96-well plates. After 24 hrs. Culture media was replaced with fresh media containing 2% FBS, and the cells were treated with different concentrations of 4HPR drug, 4HPRNPs and 4HPRANPs for different time points (48 and 72hrs.). MTT solution (5mg/ml in phosphate-buffered saline (PBS) was added to each well and incubated for 2 hrs. at 37 °C and 5% CO_2. The insoluble formazan crystals were dissolved by adding DMSO to each well, and the absorbance of each well was read at 570 nm using a microplate reader. The results were presented as a percent value to the control. The percent cell viability was calculated using the following equation: cell viability= (ODexp/ODcon)×100 in which ODexp and ODcon represent the optical densities of experimental and control cells, respectively. GEN concentration that inhibited cell proliferation to 50% (IC50) in comparison to the control was determined using curve fitting method from at least three independent experiments in a triplicate format for each treatment.

2.11 Cell cycle distribution analysis

PI staining was used to determine cells' distribution in different cell cycle phases by flow cytometry analysis. Briefly, cells were seeded into 6-well plates at a density of $1×10^5$ cells/well. The cells were treated with HSA nanoparticles, IC50 of 4HPR and 4HPRNP and 4HPRANP. Cells were collected by trypsinization, fixed and stained with a PI solution at 4°C for 30 min in the dark to analyze cell cycle distribution based on DNA content of cells by flow cytometer. Data analysis was performed using FlowJoV10 software.

2.12 Determination of Cellular Uptake by Confocal Laser Scanning Microscopy

The cells were trypsinized and seeded in a 6-well plate on coverslips in a density of 5×10^4 cells per well in 2 ml of culture medium. SH-SY5Y cells were incubated with free Rhodamine B tagged nanoparticles at a concentration of 50 μg mL^{-1} for 4hrs. The cellular uptake and distribution of HSANP were investigated by a confocal laser scanning microscope (Leica microsystems).

2.13 Real-time polymerase chain reaction

About $2.0x10^6$ cells/ml were seeded in T25 flask followed by incubation for 24 hrs. Next, the cells were treated with HSANP, 4HPR, 4HPRNP, 4HPRANP for 48 hrs. After treatment, cells were washed with chilled PBS. The RNA isolation kit was used to isolate mRNA from the treated cells. The isolated mRNA was quantified by a TECAN plate reader using Nanoquant assembly. The cDNA was synthesized using a cDNA synthesis kit (Thermofisher). The purified RNA (1 μg) was taken as a template, and the genes of interest were amplified using specific primer sets with SYBR green dye. A 10 μL of PCR reaction containing cDNA template (1 μL), SYBR green dye (5 μL) and gene-specific primers (1 μL each of forwarding and reverse primers) was performed using Quant qRT-PCR (QuantStudio™ 5System, Thermo Fischer). The relative expression levels of each gene were calculated considering comparative CT values, normalized with the CT value of GAPDH. The details of the primers are given in table 1.

2.14 Western blotting

The harvested tumour samples and *in vitro* treated cells were washed thrice with chilled PBS, followed by lysis with RIPA buffer containing PMSF. The samples were probe sonicated at 35% amplitude (10 sec. 'on', 3sec. 'off') for 3 min followed by centrifugation at 15000 rpm for 30 min at 4°C. The supernatant was collected, and the concentration of protein for each sample was quantified using Bradford assay. A 4-15% gradient SDS polyacrylamide gel was considered to resolve the isolated protein and later transferred onto a polyvinylidene difluoride (PVDF) membrane using trans blot turbo standard transfer protocol. The protein-containing membrane was blocked using 5% BSA in TBST (tween-tris buffer saline) buffer for 1 hr at room temperature followed by washing thrice using TBST (10 min wash cycle). The blots were further incubated with protein-specific primary antibodies (1:1000) overnight at 4°C. Next, the blots were washed thrice (10 min each) with TBST followed by incubation with the suitable secondary antibody (1:2000 dilution) for 2 hr at room temperature. Finally, the blots were washed thrice (10 min each) with TBST and developed using ECL western

substrate (Bio-Rad). Finally, the obtained protein bands were quantified using the densitometry function of ImageJ and relative expression.

2.15 *In vivo* whole-body biodistribution of the nanoparticles

In-vivo whole-body biodistribution experiments on six-weeks-old male Balb/c mice were performed after due ethical clearance from the institutional animal ethics committee. To assess the tissue distribution and clearance studies in a pre-clinical model, Indocyanine green conjugated HSANP and HSAANP were dispersed in PBS pH 7.4 and injected intravenously Balb/c mice (n = 3) at a concentration of 2.0 mg/kg body weight. For the negative control group, 100 µL of sterile PBS was administered through the tail vein. The mice were imaged at the various time points till 24 hrs. The images were acquired using the IVIS Spectrum (Perkin Elmer) animal imager measuring quantitative estimation of the fluorescence intensity. After completing the experiment, significant organs such as liver, spleen, kidney, heart, and brain were harvested for *ex vivo* imaging and histological analysis.

2.16 *In vivo* therapeutic efficacy in Xenograft mice model of Neuroblastoma

The therapeutic efficacy of the nanoformulation was evaluated in the *in vivo* xenograft nude mice model of Neuroblastoma. The xenograft mice model of Neuroblastoma was developed in the nude mice. Briefly, the mice were acclimatized for 10 days in the day: night cycle of 16:8hrs. Once the mice get acclimatized to the conditions, xenograft model development was started. The neuroblastoma cells SH-SY5Y were cultured *in vitro* and collected in concentration of $1X10^7$ cells per ml. Briefly, $1X10^6$ cells per 100 µl were subcutaneously injected into the flank region of the mice. Once the tumour reached a minimum size of 500mm3, the dosing of nanoformulation was performed. The nanoparticles and drug were intraperitoneally administered at an equivalent dose of 5mg/kg/day for 14 consecutive days, including a 1-day break period on the seventh day of treatment. After completing the treatment, the tumours and all body parts of the mice were harvested and snap-frozen in liquid nitrogen for further analysis.

2.17 Histopathological studies

The snap-frozen samples of the tumours and significant body organs were processed with OCT, and 10-15-micron sections were cut using cryostat assembly. The sections were fixed using 4% formaldehyde solution overnight at 4°C. Histochemistry was performed on fixed

tissue and tumour samples using H and E stain. The section was processed and permanently mounted onto glass slides using DP for further analysis.

2.18 Immunohistochemistry

The heat-induced antigen retrieval was performed in sodium citrate buffers on fixed tumour tissue and organs sections. After antigen retrieval, the section was permeabilized using 0.1% TritonX-100 in the PBS. The Blocking of the section was performed at room temperature for 30 min using 2%. BSA solution. Furthermore, the sections were incubated with primary antibody (1:200) overnight at 4°C. The sections were incubated with secondary antibody (1:500) in 2% BSA for 1 hr in dark condition at room temperature after washing. After completing the incubation, the sections were washed thrice with PBS and mounted on a glass slide for fluorescence analysis.

2.19 Statistical Analysis

All data were analyzed using the statistical package of origin 8.5 SR1 version of the software from origin lab corporation with the License number GF3S4-9089-7123456. One-way ANOVA was applied to evaluate the data from different groups followed by Tukey test for further comparison among the groups, a p-value of <0.05*, <0.01**, <0.001*** was considered as statistically significant.

3.0 Result and Discussion

3.1 Synthesis and characterization of Nanoparticles

HSA nanoparticles were synthesized using a well-established ethanol precipitation method. The ethanol precipitation and glutaraldehyde crosslinking of HSA protein molecules result in spherical shape protein nanoparticles. Here we have kept the size of nanoparticles in the 80-100nm range to impart better drug loading and effective targeting in the tumour through EPR effects. The synthesis method resulted in the average hydrodynamic diameter of 72nm, 84nm and 78nm for HSANP, 4HPRNP and 4HPRANP, respectively (Fig. 1a). The hydrophobic interaction and hydrogen bonding of 4HPR drug and Protein molecule HSA result in a mere increase in the size of 4HPRNP and 4HPRNP. All the nanoformulations have shown excellent PDI values of <0.1, which is very impressive for a polymeric molecule. The nano formulation's zeta potential was recorded to be -41mV, -39mV and -37mV for HSANP, 4HPRNP and 4HPRANP, respectively (Fig. 1b). These zeta values indicated excellent

stability of the nanoparticles in the solvent system. The mere change in the zeta values could be due to drug molecules' occupancy on the surface of 4HPRNP and 4HPRANP. The TEM images were captured to see the morphology and actual size of the nanoparticles. The images revealed that all three nanoparticles exhibit nearly similar size and spherical morphology (Fig. 1c-e).

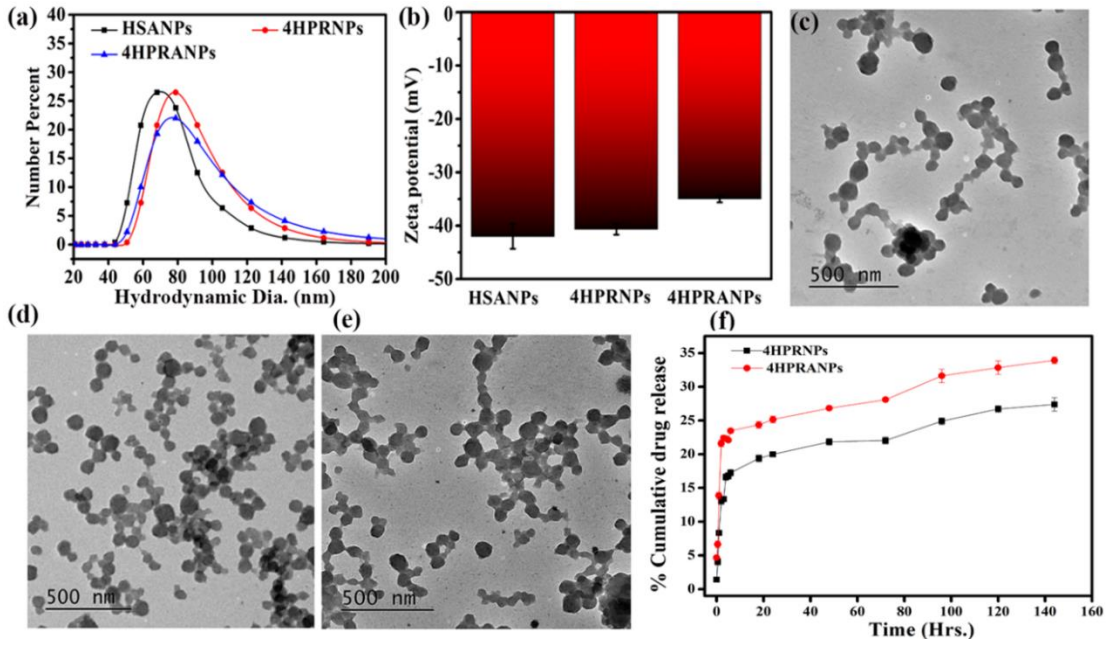

Fig. 1 Hydrodynamic Size of Nanoparticles (a), Zeta Potential (b), TEM image of HSANP (c),4HPR loaded HSANP (d), 4HPR acetylated HSANPs (e), Percent cumulative release (f).

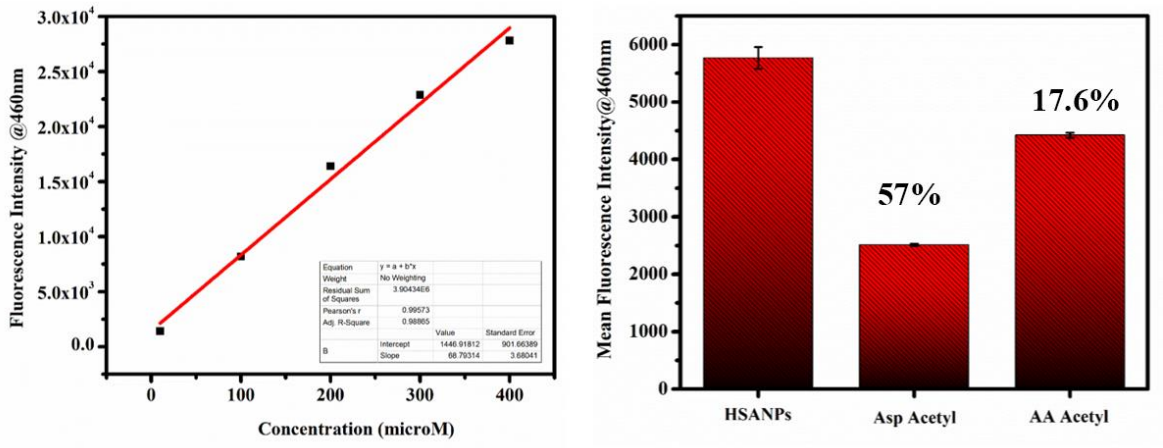

Fig 2. Standard curve of Fluorescamine with HSA (a) Different methods showing percent Acetyl modification (b)

The synthesized 4HPRNP and 4HPRANPs were further subjected to the *in vitro* drug release analysis. The drug release patterns of both the formulations show initial burst release of the drug for a few hours, which could be due to the swelling effect and leaching of surface-bound

drug molecules. After the initial burst release, 4HPRNP and 4HPRANP have shown sustained release patterns. Surprisingly, the acetyl variant 4HPRANP has shown a better release profile compared to the 4HPRNP alone. This improved drug release behaviour could be due to the hydrogen bonding of the acetyl group to the water molecules which may result in better wettability of the nanoformulation and so as the better drug release from the nanoparticles (Fig. 1f).

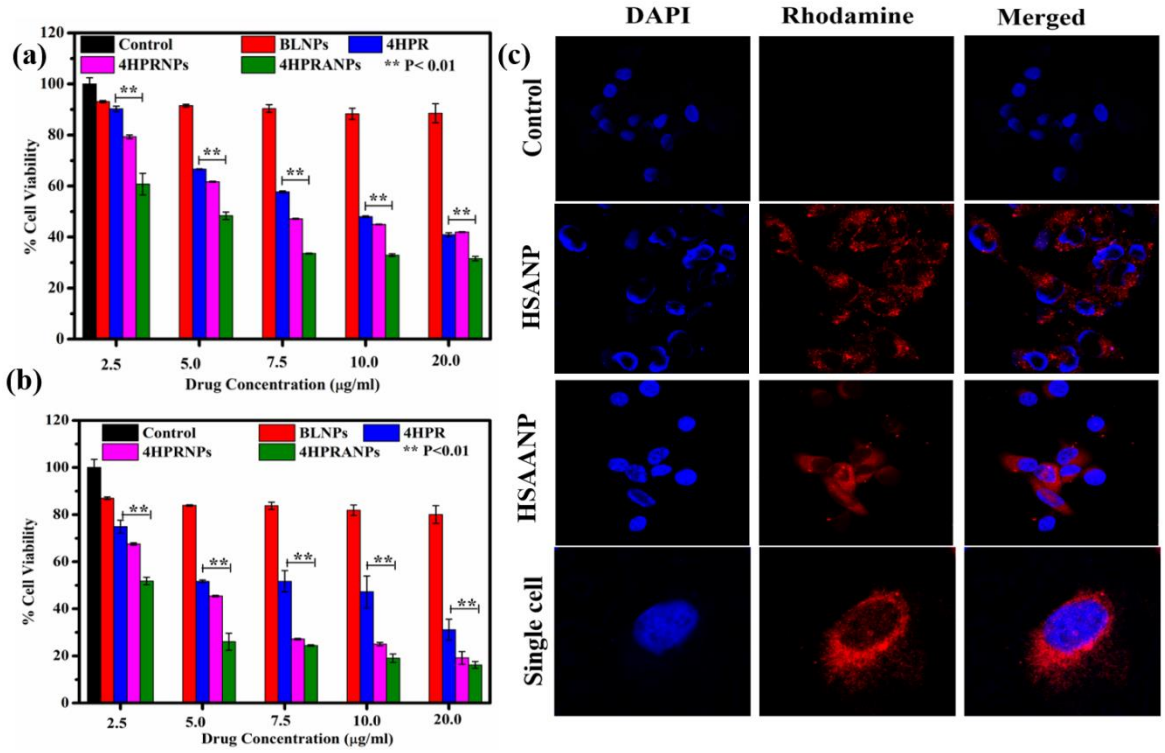

Fig 3. *In vitro* cytotoxicity analysis showing MTT at 48 hrs (a), 72 hrs. (b) Cellular uptake studies of HSANP and HSAANP in monolayer cells (c). **p<0.01 is considered significant.

The presence of acetyl group on the surface of 4HPRNP was calculated using Fluorescamine which itself is non-fluorescent but forms a fluorescent complex in the presence of free amine groups. Therefore, the fluorescence is directly proportional to the presence of free amine groups. Acetyl modification, which usually occurs at the free amine groups, results in decreased an amine group on the surface, causing subsequent fluorescence quenching. The Aspirin mediated acetylation of the 4HPRNP resulted in 57% modification of the available amine groups, while in the case of acetic anhydride this percentage was deficient at 17.6%. (Fig. 2a-b). This result indicates that Aspirin is a better acetylating agent resulting in stable acetyl modification at the free amine residue.

3.2 *In vitro* cytotoxicity, cellular uptake and cell cycle arrest analysis

The prepared nanoparticles are evaluated for their cytotoxicity in SH-SY5Y *in vitro* model of Neuroblastoma. All the formulations, including, HSANP, 4HPR, 4HPRANP and 4HPRANP were screened for their IC50 value at 48 and 72hrs of the treatment (Fig.3a, b). The neuroblastoma cells showed variable response with variable treatment groups. The IC50 value of 4HPR was 10.15±0.8µg/ml at the 48hrs. of treatment which significantly improved to 5.2±0.32 µg/ml at 72 hrs. 4HPRNP and 4HPRANP have shown better therapeutic efficacy at 48 and 72 hrs of treatment compared to the 4HPR drug.

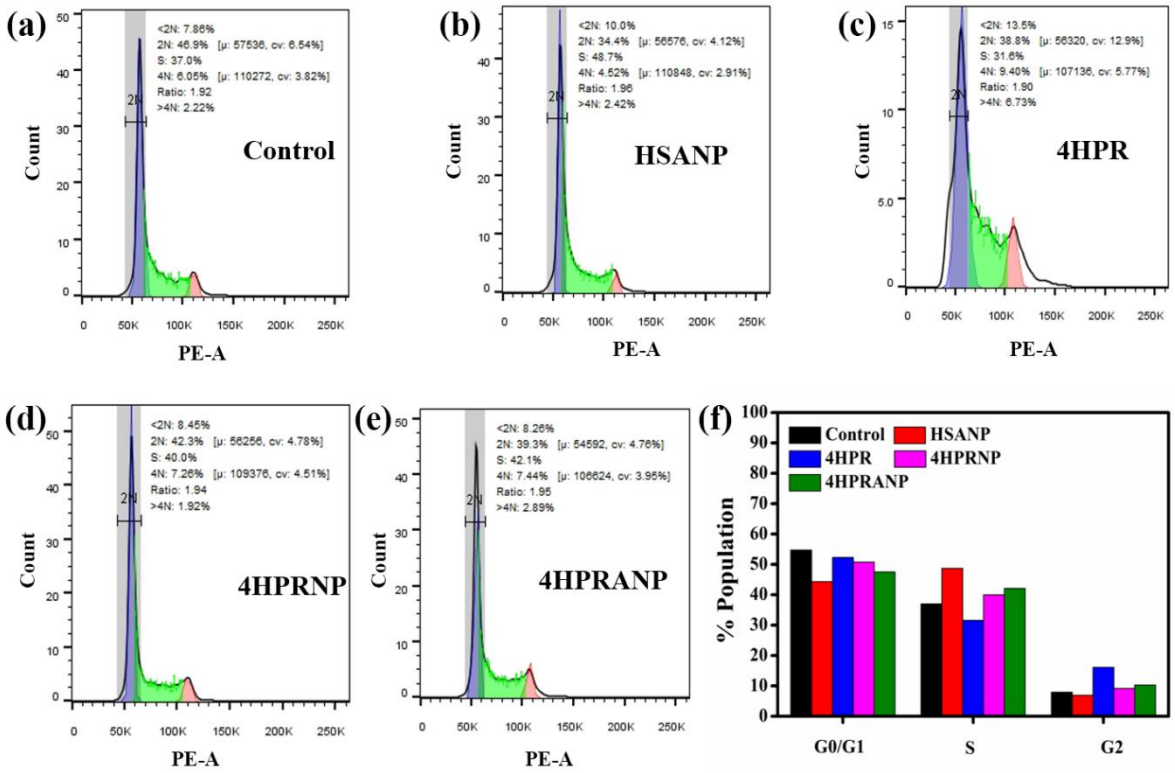

Fig 4. Cell Cycle Analysis showing effect of various treatment groups on cell cycle phases (a-f).

The IC50 value of 4HPRNP and 4HPRANP significantly dropped to 7.63±0.41 µg/ml and 5.14±0.13 µg/ml respectively at 48 hrs. of treatment. At 72 hrs of treatment, the IC50 value of 4HPRNP and 4HPRANP was further improved to 4.8±0.2 µg/ml and 2.6±0.16 µg/ml. The available reports support the therapeutic potential of the 4HPR drug at the microM doses, except pleiotropic effect on several neuroblastoma cell lines *in vitro*, which shows high resistance depending on Myc positive and Myc negative phenotypic features. The cellular uptake studies were performed to study cancer cells' ability to uptake the HSANP and acetylated HSANP(HSAANP). Several uptake mechanisms very well internalize both types of particles. The in-depth analysis of results confirmed the nuclear uptake of HSAANP (Fig.3c) The cellular uptake result showing nuclear uptake further strengthens our hypothesis

of delivering acetyl moieties inside the nuclear compartment to re-establish the histone methylation and acetylation equilibrium.

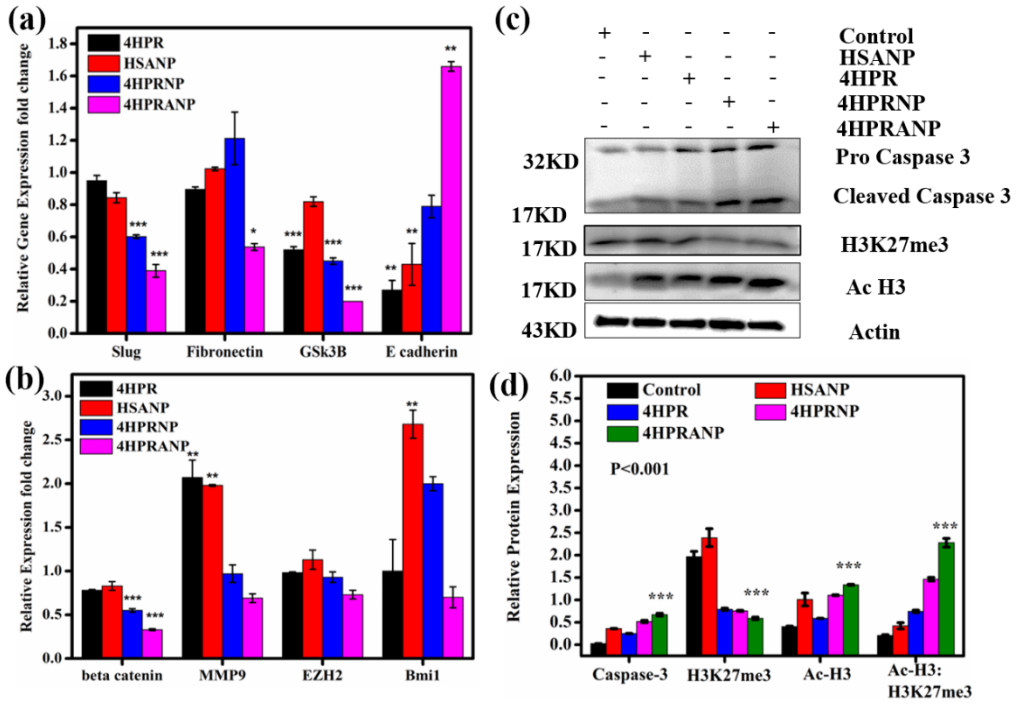

Fig 5. Relative mRNA expression (a, b) relative protein expression (c, d) of several molecular markers in different treatment groups of SH-SY5Y cells. ***p<0.001 is considered significant.

The cancer cells utilize acetyl moieties of the cellular component as a preferred source to feed their energy requirement, resulting in excessive methylation on histone and DNA residues.[20] We have further studied the mechanism of therapeutic action by monitoring the effect on cell cycle arrest. Interestingly, no cell cycle arrest was reported in the SH-SY5Y cells (Fig 4a-f), which supports earlier reports, where similar results were obtained. [21]

3.3 *In vitro* gene expression analysis using qPCR and Western blotting

The *in vitro* therapeutic potential of the nanoformulation was evaluated at the transcriptional and translational level of expression. Neuroblastoma is a highly metastatic and invasive form of concrete cancer. We were interested in studying whether the newly synthesized nanoformulation could provide better therapeutic efficacy at the molecular level and restrict the metastasis potential of NB by regulating the apoptotic and epigenetic pathways. The mRNA expression analysis of the SH-SY5Y cells after treatment of 4HPR, HSANP, 4HPRNP and 4HPRANP has shown variable gene expression (Fig. 5a, b).

The results indicate that 4HPRNP and 4HPRANP are potentially very useful in regulating the metastasis-related genes like Slug, E-cadherin, Fibronectin, MMP9, GSK3β, β-catenin, and

epigenetic regulatory markers like EZH2 and Bmi-1. E-cadherin is the prime molecular marker which controls the EMT transition of the cells.

A significant lower expression of E cadherin is the hallmark of the mesenchymal phenotype that shows high metastasis potential. Fibronectin is another critical protein expressed in the mesenchymal phenotype of the cells and represent metastasis niche of cancer cells.[22] The mRNA expression analysis reveals that 4HPRNP and 4HPRANP have significantly increased E-cadherin's expression, ensuring epithelial characteristics of the cells. Fibronectin expression is found to be reduced in 4HPRANP treatment group only, showing the better therapeutic potential of the nanoformulation in controlling the metastasis phenotype of SH-SY5Y. In addition to these vital molecular markers, reduced expression of slug, Gsk3β, β-catenin and MMP-9 strongly support the therapeutic potential of 4HPRANP in restricting the metastatic. These molecular markers are highly expressed in metastatic cancer cells and regulate several molecular pathways to induce invasiveness and resistance to therapies. [23-26] Except these metastatic pathways, we have studied the expression of epigenetic regulators EZH2 and Bmi1. EZH2 has methyltransferase activity and results in gene silencing by promoting histone H3 trimethylation at several tumour suppressor genes' promoter site.

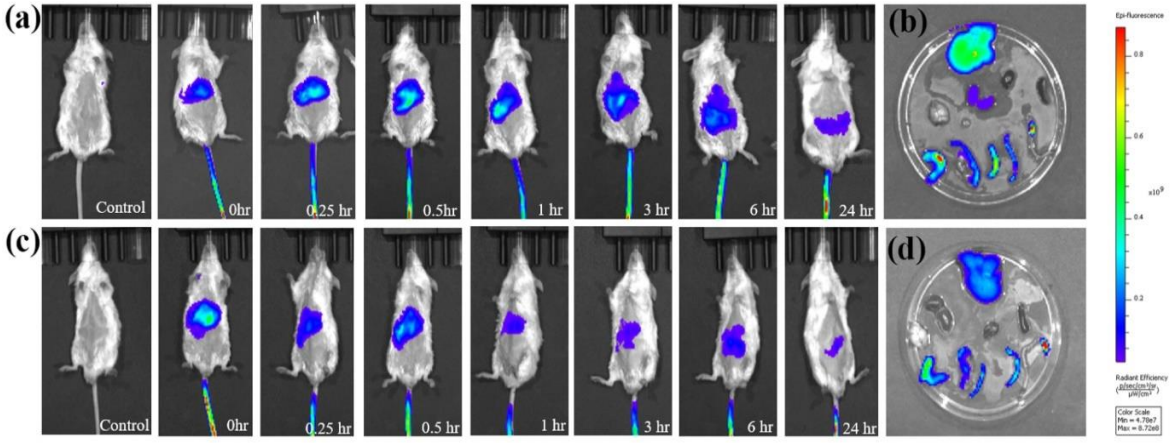

Fig 6. Time dependent *In vivo* biodistribution of HSANP (a) ex vivo distribution in organs (b) *In vivo* biodistribution of acetylated HSANP (c) ex vivo distribution in organs (d).

The qPCR and western blot result confirm that 4HPRANP has successfully downregulated the expression of EZH2 and H3K27me3, along with inducing the acetylation of histone 3. Increase in the expression of H3 acetylation indicates a highly active chromatin state which could positively regulate anticancer activity and epigenetic changes in the cancer cells. We

have seen that 4HPRNP and 4HPRANP have induced caspase 3 activation in the cancer cells (Fig.5c, d) showing active apoptotic machinery which result in cellular apoptosis.

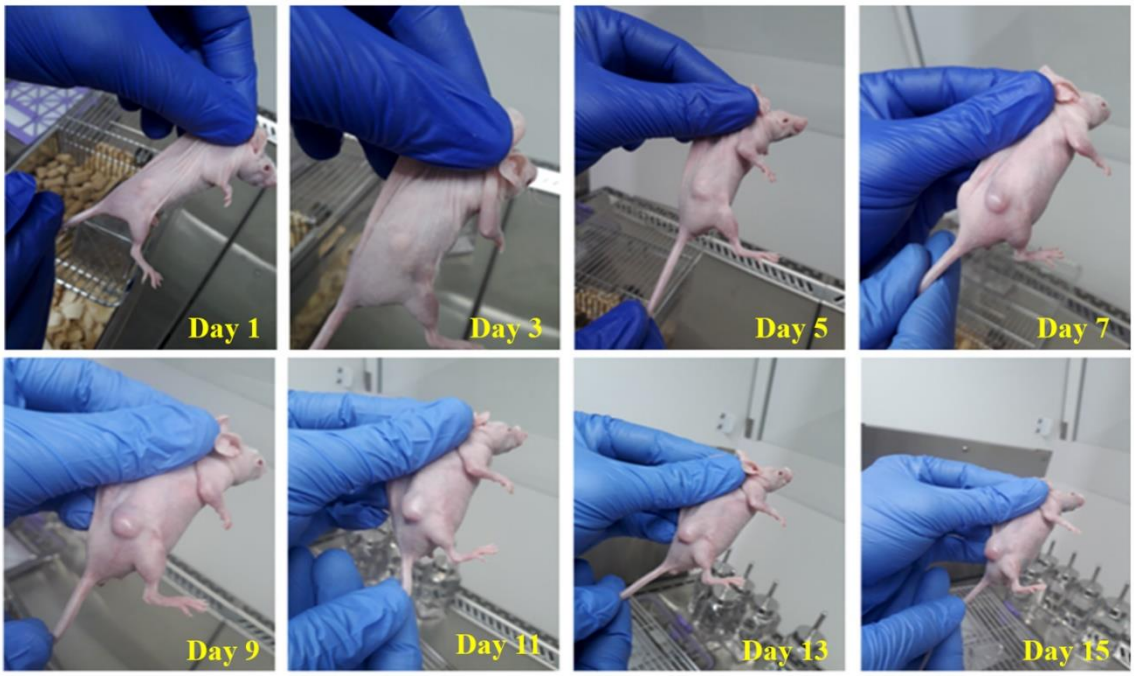

Fig 7. Time dependent development of SH-SY5Y neuroblastoma xenograft model in nude mice

3.4 *In vivo* whole-body distribution of nanoparticles

The HSA nanoparticles (HSANP) and acetyl modified HSA nanoparticles (HSAANP) were tagged with NIR dye ICG. The whole-body biodistribution of nanoparticles was studied in the *in vivo* mice model system. The tagged particles were injected through the mice's tail vein, and time-dependent animal imaging was performed to monitor the whole body biodistribution. The biodistribution result showed that HSANP and HSAANP are very well distributed in the mice's whole body; no specific accumulation of nanoparticles is reported in any of the major organs. The particles showed adequate clearance from the system after 24hrs of treatment (Fig. 6a, c). Acetyl modified HSA nanoparticles has shown better clearance compare to the HSA nanoparticles. After completion of treatment, the *ex-vivo* imaging of harvested organs showed very little accumulation of nanoparticles in highly complex and fibrous organs like liver, kidney and intestine (Fig. 6b, d). This accumulation could be due to the complex excretory machinery of the organs.

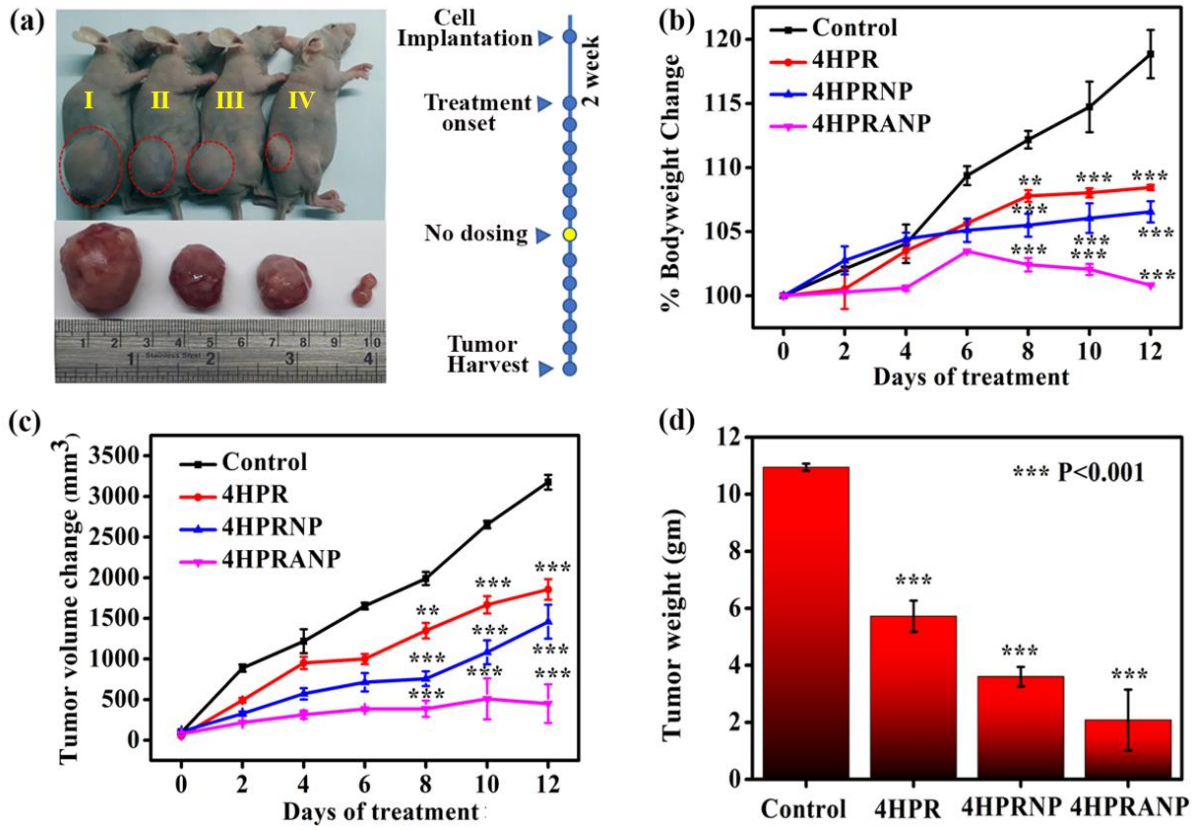

Fig 8. ***In vivo*** **therapeutic efficacy of nanoformulation in xenograft nude mice model of Control (I), 4HPR(II), 4HPRNP (III), 4HPRANP (IV) (a) percent bodyweight change during days of treatment (b), Tumor volume change during days of treatment (c), tumor weight after completion of treatment (d). **p<0.01, ***p<0.001 is considered as significant.**

3.5 *In vivo* therapeutic efficacy of nanoformulation in xenograft mice model

The initial *in vitro* therapeutic results of the nanoformulations are further evaluated for their potential in the *in vivo* mice model of Neuroblastoma. The subcutaneous xenograft mice model of Neuroblastoma is developed in the nude mice (Fig. 7). Initially, the SH-SY5Y cells were injected in the flank region of the mice. The cells multiplied vigorously at the injection site and developed into the mass of visible tumour within a few days. The tumours were subjected to dosing of the nanoformulation after reaching a tumour volume of 500mm^3. The animal dose of 4HPR was calculated using LD50 estimation. Briefly, three different concentration of the 4HPR (5mg/kg/day, 7mg/kg/day, 9mg/kg/day) was administered intraperitoneally for 30 days or development of any significant toxicity. Depending upon the toxicity of doses, a least toxic dose of 5mg/kg/day was selected for the treatment. Finally, the xenograft bearing mice were treated with 5mg/kg/day equivalent doses of 4HPR, 4HPRNP and 4HPRANP. A daily dose of the formulation was given for 14 days, keeping a day off

after six consecutive dosings. The body weight of the treatment groups was monitored after every alternative day. The nanoformulation has shown a significant decrease in tumour volume after the treatment. The change in tumour volume was significantly highest in 4HPRANP groups, followed by 4HPRNP and 4HPR groups (Fig 9a, c). The percent bodyweight of the 4HPRANP group was significantly found constant throughout the treatment phase, showing good sign of the formulation's treatment efficacy and biocompatibility. 4HPRNP and 4HPR group also showed per cent body weight maintenance compared to the control groups (Fig 9b). The tumours were harvested after completing the treatment and weighed for the actual change in weight compared to the control (Fig. 8d). The result indicates a successful reduction of tumour weight compared to the control group. These results show that 4HPRANP has maximum therapeutic potential in treating Neuroblastoma in the *in vivo* model system.

3.6 Molecular mechanism of therapeutic efficacy

The molecular mechanism of the therapeutic efficacy was studied using protein expression of various vital molecular markers. The tumour tissue was lysed in the protein isolation buffer, and relative protein expression was studied using western blot analysis. The apoptotic pathways, metastasis pathways and epigenetic regulatory pathways focus on studying molecular changes during the treatment phase. We have hypothesized that we could address metastasis and cancer growth of NB by simultaneously targeting the apoptotic and epigenetic pathways. 4HPR is a vitamin A derivative which is known to induce apoptosis and cellular differentiation of neuroblastoma cells. [27, 28] The nanoformulation of 4HPR shows better bioavailability of the drug inside the tumour, therefore impart better therapeutic potential. The acetyl variant of the same nanoformulation has acetyl groups attached to the surface, which could provide better epigenetic control on the histone's trimethylation and acetylation profile. Western blot analysis (Fig 10a-g) revealed that 4HPRNP and 4HPRANP have significantly induced apoptosis in the tumour tissues by activating caspase 3 protease. Besides, to induce apoptosis in the neuroblastoma tumours, this nanoformulation has significantly altered the expression of gene silencing signature H3K27me3 and simultaneously induced acetylation of histone 3.

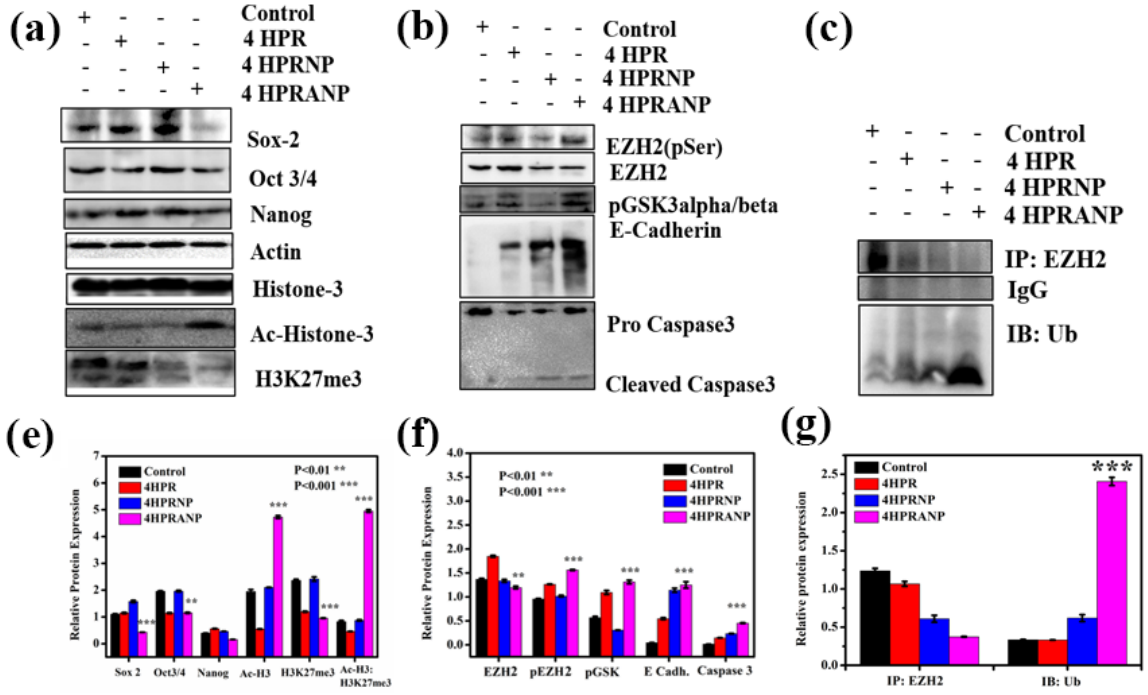

Fig 9. Relative protein expression of key molecular markers in different treatment groups (a, b), pool down assay showing EZH2 and Ub interaction (c) quantitative estimation of the relative protein expression of the molecular markers (e-g). **p<0.01, ***p<0.001 is considered as significant.

These results confirm that by re-establishing the acetyl and methyl equilibrium, we may control the regulation of the drug molecules' gene expression and therapeutic efficacy. We have further studied the effect of these nanoformulations on the methyltransferase EZH2 known to foul play in the metastasis regulations. The expression of EZH2 is highly upregulated in several cancer types resulting in the vigorous and invasive phenotype of cancer. [29, 30] Increased expressions of EZH2 is known to silence E-cadherin expression and therefore induce metastasis.[31] The treatments results have shown that 4HPRANP has successfully downregulated the EZH2 expression in the tumours and reestablishment of E-cadherin's protein expression. The 4HPR and 4HPRNP groups have shown a mere change in the expression profile of EZH2 and E-cadherin. This result suggests that 4HPRANP has improved therapeutic potential to address NB. In addition to these molecular pathways, we have studied whether these nanoformulations have a specific role in expressing key transcriptional factors (SOX2, Nanog, and Oct3/4).[32-34] These transcriptional factors are involved in regulating E-cadherin protein expression through distinct molecular pathways. The protein expression analysis confirms that 4HPRANP also downregulate the expression of SOX2, which is highly elevated in the cancer condition. Although the expression of Nanog

and Oct3/4 remain unchanged in all the treatment groups. The 4HPRNP and 4HPRANP resulted in reduced expression of EZH2, which consecutively causes increased expression of E-cadherin. We were interested to understand how this nanoformulation is regulating the expression of EZH2. Therefore, in the series of the molecular cascade, we study the expression of upstream molecule pGSK3α/β. As pGSK3α/β is known to interact with the EZH2 and induce phosphorylation of the molecule at serine and threonine residue.[35] The phosphorylation of EZH2 at serine and threonine residue causes conformational changes in the molecule and directs it to the ubiquitin-mediated proteasomal degradation. We have found that increased level of pGSK3α/β coincides with the phospho-EZH2(pSerEZH2) expression in the 4HPRANP treatment groups. These results further validated by studying the ubiquitin expression in the pool down assay of the EZH2. Increased expression of ubiquitin in 4HPRANP treatment groups confirms that 4HPRANP treatment is inducing the phosphorylation of EZH2 at the serine residues through pGSK3α/β and inducing its proteasomal mediated degradation.

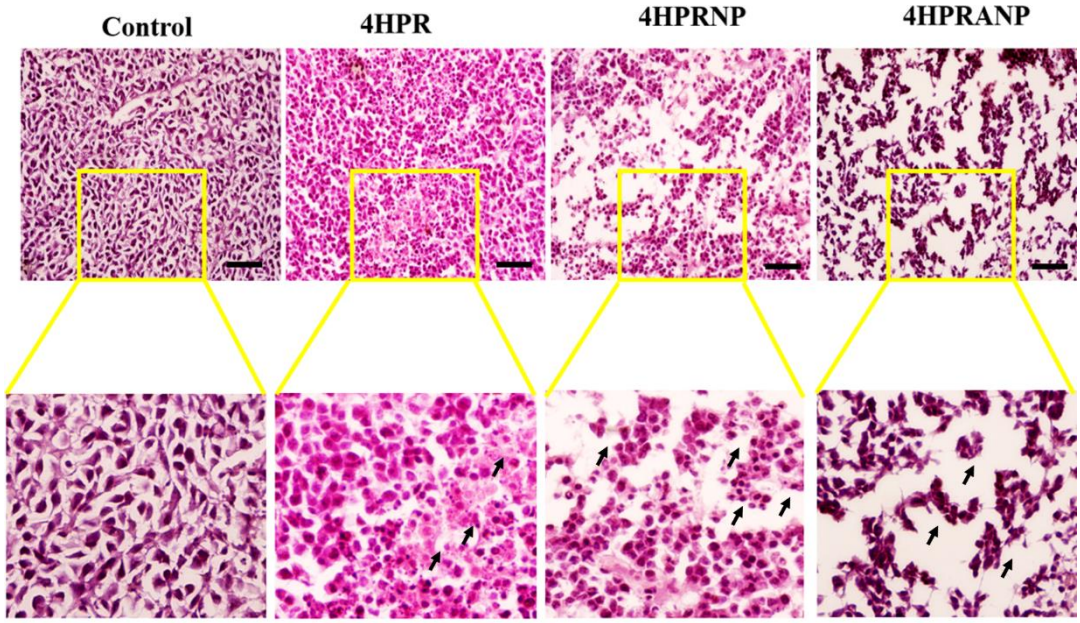

Fig 10. Histopathological evaluation using H&E staining showing changes in tumor tissues during treatment. Scale bar represent 200 microns. Changes in cell morphology is marked with bold arrows.

3.7 Histopathology and immunohistochemistry Analysis

All the treatment groups were subjected to the histopathological evaluation of harvested tumours (Fig.10) and major organs (Fig.11) to study physiological changes. The histology of the tumour section confirmed that induction of killing off cancer cells. Treatment groups

showing a significant loss of cellular morphology with gradient loss of cytoplasm and nuclear condensation. The histological sections of significant organs confirm that 4HPR shows mild liver toxicity at the treatment dose of 5mg/kg/day, marked with bold arrows.

This toxicity is probably due to the drug accumulation in the liver tissues. The nanoformulation treatment groups have not shown any associated liver toxicities; showing highly biocompatible and therapeutically potential candidates for treating NB. All other major organs, including brain, kidney, spleen, and heart, show no observable toxicity of any kind in any treatment group. The immunohistochemistry was performed on the tumour tissue harvested after completion of the treatment. The results of IHC (Fig 12a-f) were as per the protein expression results obtained in western blot analysis. The 4HPRANP treatment group has successfully shown caspase3 activation, downregulation of fibronectin and increased expression of E-cadherin.

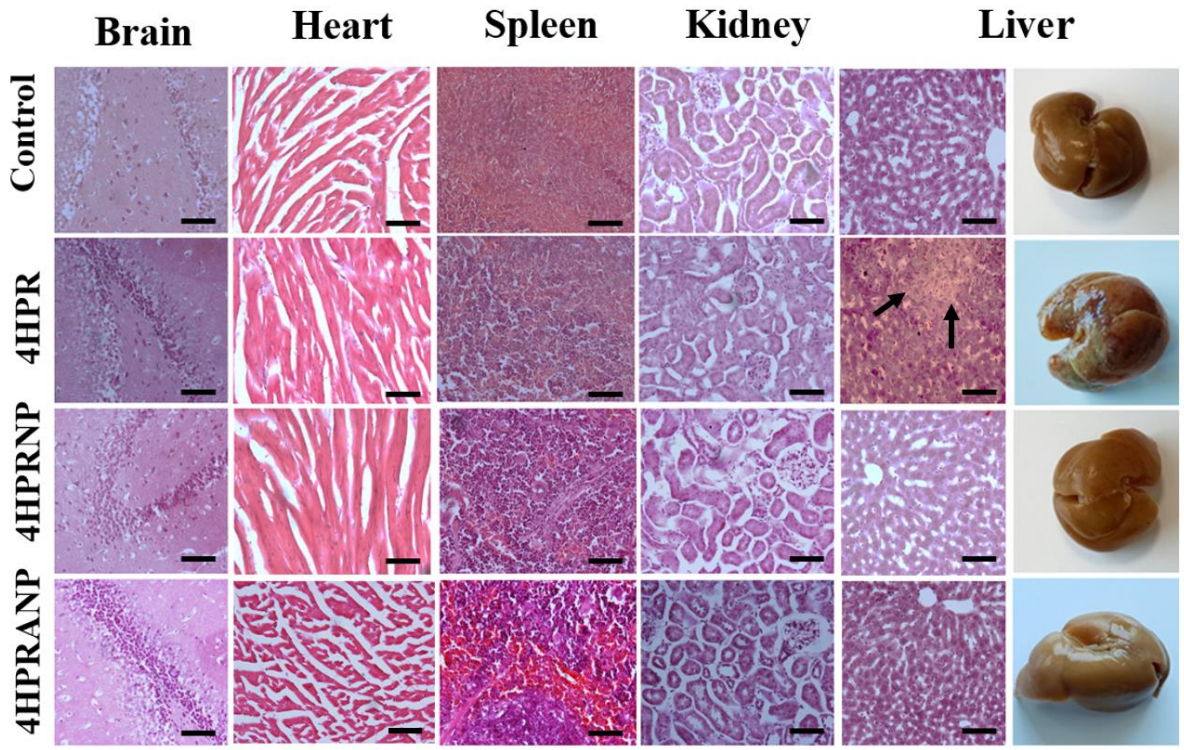

Fig 11. Histopathological evaluation of Major body organs showing effect of different treatment groups, scale bar represents 400µm. bold arrows marked showing liver toxicity.

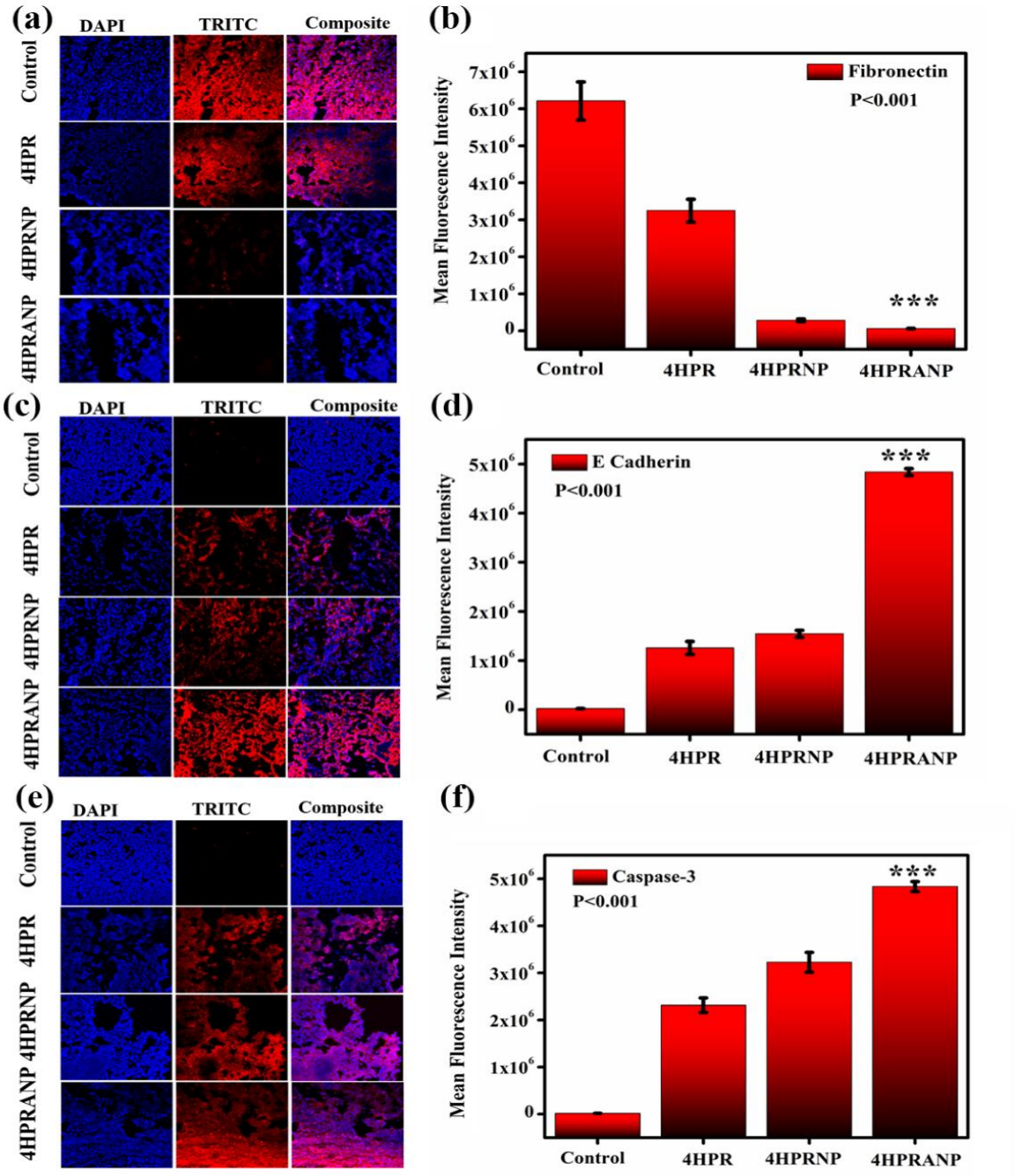

Fig. 12 Immunohistochemistry of Tumor section showing expression of fibronectin (a, b) E-Cadherin (c, d) and Caspase 3 (e, f). ***p<0.001 is considered as significant.

4.0 Conclusion

In summary, we have synthesized 4HPR loaded HSANP formulation along with its acetyl variant 4HPRANP. Both the formulations have shown significant therapeutic efficacy in the *in vitro* and *in vivo* tumour xenograft model of Neuroblastoma. The 4HPRANP variant was

more potent than other treatment groups in imparting therapeutic effect on NB. The nanoformulation has shown the potential to curve the cancer cells' metastatic potential by regulating epigenetic changes and inducing apoptosis. This nanoformulation overcame the observed cytotoxicity of the drug with improved therapeutic efficacy *in vitro* and *in vivo.* Molecular mechanism reveals that nanoformulation (4HPRANP) imparts therapeutic efficacy by downregulating EZH2 expression. Scheme 1 shows the complete molecular mechanism of the nanoformulation inside cancer cells.

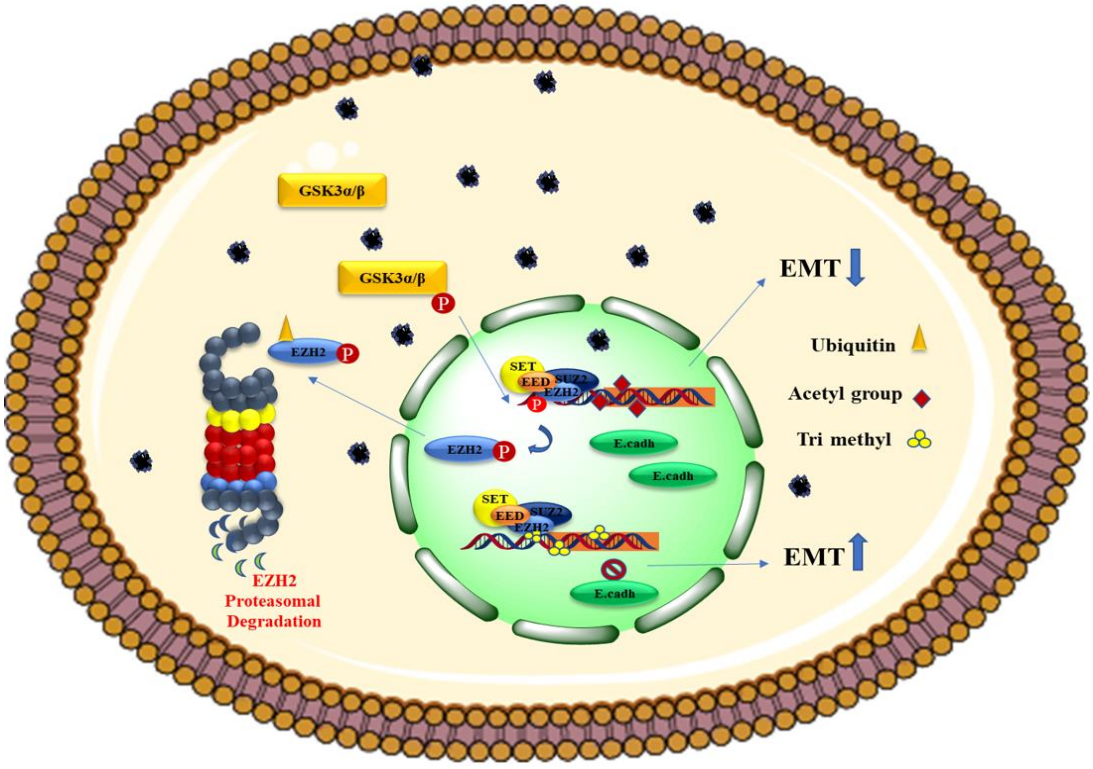

Scheme 1. Molecular mechanism showing therapeutic efficacy of 4HPRANP inside cancer cell

5.0 References

1. London, W. B.; Castleberry, R. P.; Matthay, K. K.; Look, A. T.; Seeger, R. C.; Shimada, H.; Thorner, P.; Brodeur, G.; Maris, J. M.; Reynolds, C. P.; Cohn, S. L., Evidence for an age cutoff greater than 365 days for neuroblastoma risk group stratification in the Children's Oncology Group. *Journal of clinical oncology : official journal of the American Society of Clinical Oncology* **2005,** *23* (27), 6459-65.

2. Park, J. R.; Bagatell, R.; London, W. B.; Maris, J. M.; Cohn, S. L.; Mattay, K. K.; Hogarty, M.; Committee, C. O. G. N., Children's Oncology Group's 2013 blueprint for research: neuroblastoma. *Pediatric blood & cancer* **2013,** *60* (6), 985-93.
3. Ozkaynak, M. F.; Gilman, A. L.; London, W. B.; Naranjo, A.; Diccianni, M. B.; Tenney, S. C.; Smith, M.; Messer, K. S.; Seeger, R.; Reynolds, C. P.; Smith, L. M.; Shulkin, B. L.; Parisi, M.; Maris, J. M.; Park, J. R.; Sondel, P. M.; Yu, A. L., A Comprehensive Safety Trial of Chimeric Antibody 14.18 With GM-CSF, IL-2, and Isotretinoin in High-Risk Neuroblastoma Patients Following Myeloablative Therapy: Children's Oncology Group Study ANBL0931. *Frontiers in immunology* **2018,** *9*, 1355.
4. Betters, E.; Liu, Y.; Kjaeldgaard, A.; Sundstrom, E.; Garcia-Castro, M. I., Analysis of early human neural crest development. *Developmental biology* **2010,** *344* (2), 578-92.
5. Fredlund, E.; Ringner, M.; Maris, J. M.; Pahlman, S., High Myc pathway activity and low stage of neuronal differentiation associate with poor outcome in neuroblastoma. *Proceedings of the National Academy of Sciences of the United States of America* **2008,** *105* (37), 14094-9.
6. Takahashi, Y.; Sipp, D.; Enomoto, H., Tissue interactions in neural crest cell development and disease. *Science* **2013,** *341* (6148), 860-3.
7. Prasad, M. S.; Sauka-Spengler, T.; LaBonne, C., Induction of the neural crest state: control of stem cell attributes by gene regulatory, post-transcriptional and epigenetic interactions. *Developmental biology* **2012,** *366* (1), 10-21.
8. Mayanil, C. S., Transcriptional and epigenetic regulation of neural crest induction during neurulation. *Dev Neurosci* **2013,** *35* (5), 361-72.
9. Strobl-Mazzulla, P. H.; Bronner, M. E., Epithelial to mesenchymal transition: new and old insights from the classical neural crest model. *Seminars in cancer biology* **2012,** *22* (5-6), 411-6.
10. Pegoraro, C.; Monsoro-Burq, A. H., Signaling and transcriptional regulation in neural crest specification and migration: lessons from xenopus embryos. *Wiley interdisciplinary reviews. Developmental biology* **2013,** *2* (2), 247-59.
11. Shtukmaster, S.; Schier, M. C.; Huber, K.; Krispin, S.; Kalcheim, C.; Unsicker, K., Sympathetic neurons and chromaffin cells share a common progenitor in the neural crest in vivo. *Neural Dev* **2013,** *8*, 12.
12. Rogers, C. D.; Saxena, A.; Bronner, M. E., Sip1 mediates an E-cadherin-to-N-cadherin switch during cranial neural crest EMT. *The Journal of cell biology* **2013,** *203* (5), 835-47.
13. Beck, B.; Blanpain, C., Unravelling cancer stem cell potential. *Nature reviews. Cancer* **2013,** *13* (10), 727-38.
14. Howk, C. L.; Voller, Z.; Beck, B. B.; Dai, D., Genetic Diversity in Normal Cell Populations is the Earliest Stage of Oncogenesis Leading to Intra-Tumor Heterogeneity. *Frontiers in oncology* **2013,** *3*, 61.
15. Lee, J. V.; Shah, S. A.; Wellen, K. E., Obesity, cancer, and acetyl-CoA metabolism. *Drug Discov Today Dis Mech* **2013,** *10* (1-2), e55-e61.
16. Koundouros, N.; Poulogiannis, G., Reprogramming of fatty acid metabolism in cancer. *British journal of cancer* **2020,** *122* (1), 4-22.
17. Gupta, N.; Cruz, M. A.; Nasser, P.; Rosenberg, J. D.; Iatridis, J. C., Fibrin-Genipin Hydrogel for Cartilage Tissue Engineering in Nasal Reconstruction. *The Annals of otology, rhinology, and laryngology* **2019**, 3489419836667.

18. Jiang, T.; Xu, G.; Chen, X.; Huang, X.; Zhao, J.; Zheng, L., Impact of Hydrogel Elasticity and Adherence on Osteosarcoma Cells and Osteoblasts. *Advanced healthcare materials* **2019**, e1801587.
19. Dev, A.; Srivastava, A. K.; Choudhury, S. R.; Karmakar, S., Nano-curcumin influences blue light photodynamic therapy for restraining glioblastoma stem cells growth. *RSC advances* **2016,** *6* (97), 95165-95168.
20. Martinez-Reyes, I.; Chandel, N. S., Acetyl-CoA-directed gene transcription in cancer cells. *Genes & development* **2018,** *32* (7-8), 463-465.
21. Cuperus, R.; Tytgat, G. A.; Leen, R.; Brites, P.; Bras, J.; Caron, H. N.; Van Kuilenburg, A. B., Pleiotropic effects of fenretinide in neuroblastoma cell lines and multicellular tumor spheroids. *International journal of oncology* **2008,** *32* (5), 1011-9.
22. Wang, J. P.; Hielscher, A., Fibronectin: How Its Aberrant Expression in Tumors May Improve Therapeutic Targeting. *Journal of Cancer* **2017,** *8* (4), 674-682.
23. Kim, S.; Yao, J.; Suyama, K.; Qian, X.; Qian, B. Z.; Bandyopadhyay, S.; Loudig, O.; De Leon-Rodriguez, C.; Zhou, Z. N.; Segall, J.; Macian, F.; Norton, L.; Hazan, R. B., Slug promotes survival during metastasis through suppression of Puma-mediated apoptosis. *Cancer research* **2014,** *74* (14), 3695-706.
24. Zhang, D.; Fei, F.; Li, S.; Zhao, Y.; Yang, Z.; Qu, J.; Zhang, X.; Yin, Y.; Zhang, S., The role of beta-catenin in the initiation and metastasis of TA2 mice spontaneous breast cancer. *Journal of Cancer* **2017,** *8* (11), 2114-2123.
25. Kao, S. H.; Wang, W. L.; Chen, C. Y.; Chang, Y. L.; Wu, Y. Y.; Wang, Y. T.; Wang, S. P.; Nesvizhskii, A. I.; Chen, Y. J.; Hong, T. M.; Yang, P. C., GSK3beta controls epithelial-mesenchymal transition and tumor metastasis by CHIP-mediated degradation of Slug. *Oncogene* **2014,** *33* (24), 3172-82.
26. Bhoopathi, P.; Pradhan, A. K.; Bacolod, M. D.; Emdad, L.; Sarkar, D.; Das, S. K.; Fisher, P. B., Regulation of neuroblastoma migration, invasion, and in vivo metastasis by genetic and pharmacological manipulation of MDA-9/Syntenin. *Oncogene* **2019,** *38* (41), 6781-6793.
27. Hewson, Q. D.; Lovat, P. E.; Corazzari, M.; Catterall, J. B.; Redfern, C. P., The NF-kappaB pathway mediates fenretinide-induced apoptosis in SH-SY5Y neuroblastoma cells. *Apoptosis : an international journal on programmed cell death* **2005,** *10* (3), 493-8.
28. Chen, S.; Samuel, W.; Fariss, R. N.; Duncan, T.; Kutty, R. K.; Wiggert, B., Differentiation of human retinal pigment epithelial cells into neuronal phenotype by N-(4-hydroxyphenyl)retinamide. *Journal of neurochemistry* **2003,** *84* (5), 972-81.
29. Wang, C.; Liu, Z.; Woo, C. W.; Li, Z.; Wang, L.; Wei, J. S.; Marquez, V. E.; Bates, S. E.; Jin, Q.; Khan, J.; Ge, K.; Thiele, C. J., EZH2 Mediates epigenetic silencing of neuroblastoma suppressor genes CASZ1, CLU, RUNX3, and NGFR. *Cancer research* **2012,** *72* (1), 315-24.
30. Li, Z.; Takenobu, H.; Setyawati, A. N.; Akita, N.; Haruta, M.; Satoh, S.; Shinno, Y.; Chikaraishi, K.; Mukae, K.; Akter, J.; Sugino, R. P.; Nakazawa, A.; Nakagawara, A.; Aburatani, H.; Ohira, M.; Kamijo, T., EZH2 regulates neuroblastoma cell differentiation via NTRK1 promoter epigenetic modifications. *Oncogene* **2018,** *37* (20), 2714-2727.
31. Cao, Q.; Yu, J.; Dhanasekaran, S. M.; Kim, J. H.; Mani, R. S.; Tomlins, S. A.; Mehra, R.; Laxman, B.; Cao, X.; Yu, J.; Kleer, C. G.; Varambally, S.; Chinnaiyan, A. M.,

Repression of E-cadherin by the polycomb group protein EZH2 in cancer. *Oncogene* **2008,** *27* (58), 7274-84.

32. Yang, N.; Hui, L.; Wang, Y.; Yang, H.; Jiang, X., Overexpression of SOX2 promotes migration, invasion, and epithelial-mesenchymal transition through the Wnt/beta-catenin pathway in laryngeal cancer Hep-2 cells. *Tumour biology : the journal of the International Society for Oncodevelopmental Biology and Medicine* **2014,** *35* (8), 7965-73.
33. Tamura, S.; Isobe, T.; Ariyama, H.; Nakano, M.; Kikushige, Y.; Takaishi, S.; Kusaba, H.; Takenaka, K.; Ueki, T.; Nakamura, M.; Akashi, K.; Baba, E., Ecadherin regulates proliferation of colorectal cancer stem cells through NANOG. *Oncology reports* **2018,** *40* (2), 693-703.
34. Sancakli Usta, C.; Turan, G.; Bulbul, C. B.; Usta, A.; Adali, E., Differential expression of Oct-4, CD44, and E-cadherin in eutopic and ectopic endometrium in ovarian endometriomas and their correlations with clinicopathological variables. *Reproductive biology and endocrinology : RB&E* **2020,** *18* (1), 116.
35. Ko, H. W.; Lee, H. H.; Huo, L.; Xia, W.; Yang, C. C.; Hsu, J. L.; Li, L. Y.; Lai, C. C.; Chan, L. C.; Cheng, C. C.; Labaff, A. M.; Liao, H. W.; Lim, S. O.; Li, C. W.; Wei, Y.; Nie, L.; Yamaguchi, H.; Hung, M. C., GSK3beta inactivation promotes the oncogenic functions of EZH2 and enhances methylation of H3K27 in human breast cancers. *Oncotarget* **2016,** *7* (35), 57131-57144.
36. Sardoiwala, M. N.; Srivastava, A. K.; Kaundal, B.; Karmakar, S.; Choudhury, S. R. Recuperative effect of metformin loaded polydopamine nanoformulation promoting EZH2 mediated proteasomal degradation of phospho-alpha-synuclein in Parkinson's disease model. *Nanomedicine : nanotechnology, biology, and medicine* **2020,** *24*, 102088, DOI: 10.1016/j.nano.2019.102088.

Table 1.

The sequence of primers used in qPCR analysis

Sr. No.	Molecular Marker	Sequence (5'-3')
1.	**EzH2 Forward** **EzH2_Reverse**	GCCAGACTGGGAAGAAATCTG TGTGCTGGAAAATCCAAGTCA
2.	**Bmi-1 Forward** **Bmi-1 Reverse**	CTGGTTGCCCATTGACAGC CAGAAAATGAATGCGAGCCA
3.	**E-cadherin Forward** **E-cadherin Reverse**	GAACAGCACGTACACAGCCCT GCAGAAGTGTCCCTGTTCCAG
4.	**GAPDH Forward** **GAPDH Reverse**	GACTCATGACCACAGTCCATGC AGAGGCAGGGATGATGTTCTG
5.	**MMP9 Forward** **MMP9 Reverse**	AAGGCAAACCCT GTGTGTTC GTGGTTCAGTTGTGGTGGTG
6.	**β-Catenin Forward** **β-Catenin Reverse**	CCAGCGTGGACAATGGCTAC CTCTGAGCTCGAGTCATTGC
7.	**Fibronectin Forward** **Fibronectin Reverse**	GTGCCTGGGCAACGGA CCCGACCCTGACCGAAG
8.	**Slug Forward** **Slug Reverse**	CAAGATGCCGCGCTCCTTCC TGGCATGGGGGTCTGAAAGCT
9.	**GSK3Beta Forward** **GSK3Beta_Reverse**	CATGCCATCACTGCCACTCA GCGGCAT GT CAGATCCACAA

Chapter 04

Genistein and Lactalbumin based nano nutraceuticals for the treatment of Oral squamous cell carcinoma (OSCC)

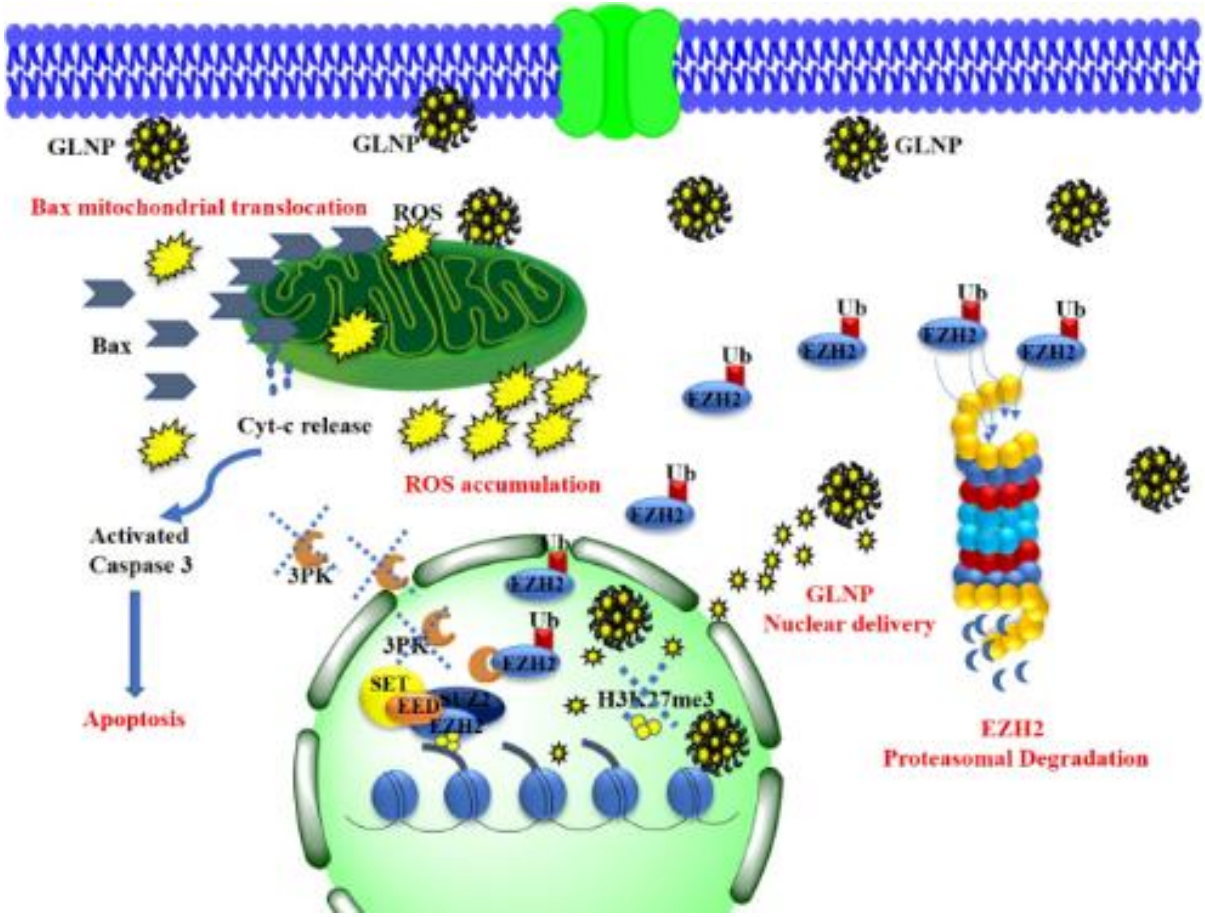

1.0 Background

Oral squamous cell carcinoma (OSCC) is a group of highly malignant tumors that may appear in different parts of the oral cavity which includes larynx, pharynx, nasal cavity, paranasal sinuses, salivary glands and thyroid. OSCC represents up to 80-90% of all malignant neoplasms of the oral cavity, leading more than 550,000 new cases worldwide in 2016.[1] In Indian scenario this disease is very common; with an estimate of nearly 1% population having oral premalignant lesions. India shares nearly 20% worldwide burden of oral cancer. The major etiological factors include the tobacco consumption along with the infection of Human papillomavirus. These factors contribute significantly to the incidence and mortality rates of OSCC worldwide [2]. Oral leukoplakia (OL) which is considered as an early precancerous lesion, believed to develop into OSCC due to some unregulated genetic and epigenetic changes. The most common epigenetic changes reported are histone methylation through histone methyltransferases. OL disease conditions show unregulated overexpression of EzH2. The successive development of OSCC from OL found it to be very provocative. Among the OL patients, nearly 80% of patients with high EZH2 expression have developed OSCC in no time. Although, patients with moderate or weak expressions of EZH2 had not developed OSCC[3]. In addition to the overexpression of EZH2, another key member of PRC-1 complex, Bmi-1, has been linked to the OSCC development. Overexpression of Bmi-1 in the oral squamous cell carcinomas (OSCC) compared to the normal human oral keratinocytes (NHOK) influenced the proliferation and survival of cancerous cells[4]. Bmi-1 is a core subunit of Polycomb repressive complex 1 (PRC1) that mediates gene silencing by regulating chromatin structure while EZH2, member of Polycomb repressive complex 2 (PRC2) catalyze the formation of H3K27me3. This signature is further involved in DNA methylation and gene silencing [5]. Prognostic significance of global histone modifications in OSCC is not investigated so far. Although relative levels of modified histones like H3K4ac, H3K18ac, H3K4me3, H3K9me3, and H3K27me3 were examined, among them H3K27me3 found to be a promising therapeutic target for OSCC [6]. The inhibition of EzH2 and Bmi-1 overexpression restricted the proliferation of cancer cells by inducing cell-cycle arrest and reducing invasiveness [4, 7]. Although the precise mechanism through which Bmi-1 and EzH2 contribute to these malignancies is not fully understood.

Currently available treatments of OSCC involve extensive tumor resection through surgery or a concurrent dose of chemoradiotherapy. Although recurrence of cancer, development of

metastasis and inadequate response to concurrent chemoradiotherapy have restricted the therapeutics options in OSCC treatments [8]. The conventional highly potent chemotherapeutic drugs suffer poor water solubility and limited systemic stability [9], therefore are not suitable for the treatment of the disease. The undesired side effects, high dose requirements, short half-life in plasma and development of drug resistance, prevented their clinical usage [10]. The therapeutic potential of these drugs could be enhanced by providing the new drug delivery options and agents. Development of newer therapeutics with fewer limitations having promising antitumor efficacy and increasing survival rates are highly warranted to treat OSCC. Use of nutraceutical compounds as chemotherapeutics is gaining more interest in recent time for their ability to fight against cancer progression. These molecules are relatively nontoxic and Generally Recognized As Safe (GRAS) nature.

The Nutraceuticals are the isolates of medicinal plants and dietary products that mediate positive health benefits. These molecules directly affect the several molecular pathways along with their targets. The therapeutic potential of nutraceuticals is not high enough to impart effective results in its original bulk, therefore development of the nanotechnology based platforms could help improve the therapeutic potential of these molecules [11].

The present study is focussed on development of the nanotherapeutic platform of Genistein and Lactalbumin (LA). LA is a well-known protein supplement which is highly consumed by the peoples and better known as Whey protein. In LA, resides bioactive peptides and high cysteine content that gives nutritional and therapeutic potential to the molecule.[12] These peptides and cysteine contents stimulate the synthesis of cellular antioxidants which, in turn, modulate the redox state of the cells and provide antiproliferative effect on the development of several types of tumors [13]. How LA imposes these anticancer activities are not yet well known. The LA being a member of the albumin family of proteins have tremendous potential to transport several drugs. Its highly biocompatible chemistry along with anticancer activity has drawn our attention to use this molecule as drug a delivery carrier. Another nutraceutical molecule that is indirectly consumed by the people is Genistein (GEN). Genistein is an isoflavonoid which is present in soybeans, another high source of protein diets. Genistein is a poorly water-soluble compound which has immense anticancer potential but suffers low bioavailability in the tumor sites. GEN targets various molecular pathways to execute their anticancer activities and is well tolerated with no known toxicities.[14, 15] In recent time, several clinical trials of GEN for bladder cancer (NCT00118040), breast cancer (NCT00290758) and

prostate cancer (NCT01126879) are completed or in continuation, indicating the importance of the GEN as a potent anticancer molecule for the treatment of variety of cancer.

The study is designed to synthesize the nanotherapeutic platforms using lactalbumin and GEN to improve the chemotherapeutic potential of the molecules along with studying their molecular mechanisms. Here we have focussed on how the nanoformulation will impart its therapeutic potential in eliminating the OSCC. The study will evaluate the nanoformulations compared to their counter bulk in terms of anti-cancer activity and compatibility for the treatment and management of OSCC. In another aspect, the developed nanotherapeutic platforms will be screened for their ability in reversing the epigenetic changes which contribute heavily to the development and poor prognosis of the disease.

2.0 Materials and methods

2.1 Materials

Lactalbumin (A0196) and Genistein (G0272) were purchased from TCI chemicals. Methanol molecular grade was purchased from Merck (106009). MTT dye (TC191), Glutaraldehyde 25% w/v solution (RM5927), Propidium Iodide (TC252), streptomycin penicillin solution (A018), Mannitol (PCT0604), RPMI1640 (AL162S), FBS (RM9955), Trypsin EDTA (TCL144), were purchased from Hi-media. 2′,7′-Dichlorofluorescin diacetate (D6883) and dialysis membrane (D6191) were purchased from Sigma Aldrich. Cell inserts were purchased from Millipore (MCEP12H48). Primary antibodies Beta-actin (SC-47778), Bax (SC-20067), Bcl-2 (SC-492), 3PK (SC-376626), PP2A-Cα/β (SC-80665), Bmi1 (SC-390443), Caspase 3 (SC-56053), ENX1 (SC-16609), HPR tagged secondary anti-mouse antibody (SC-516102), and FITC labelled secondary anti-mouse antibody (SC-516140) were purchased from Santa Cruze Biotechnology. Primary antibodies UbH2AK119 (8240) and H3K27me3 (9733) were purchased from Cell Signaling Technology. 5,5’,6,6’-tetrachloro-1,1’,3,3’-tetraethylbenzimidazolylcarbocyanine iodide (JC-1) (551302) mitochondrial membrane potential dye was obtained from BD biosciences. Oral Squamous cell carcinoma cell line JHU011 was purchased from Genetic Resources Core Facility, Johns Hopkins University, USA. L929 fibroblast cell line was obtained from the National Centre for Cell Science, Pune, India.

2.2 Characterization

Size and zeta potential measurement were performed using Malvern particle size analyzer with the backscattering angle of 173 Transmission electron microscopy (TEM) images were obtained with a JSM 2100 operated at 120 kV. CD spectra were recorded using JASCO J-1500 Circular dichroism spectrophotometer, Easton, MD, the USA using demountable cells (0.1 mm path length, Hellma). UV-Vis spectrophotometer Shimadzu UV-2600 was used to prepare a standard curve of GEN and to analyze the amount of GEN left in the supernatant. Fourier transform infrared (FTIR) spectra were recorded on the Cary Agilent 660 IR spectrophotometer. For each spectrum, 256 scans and 4 cm^{-1} resolution were applied over the range of 400–4000cm^{-1}. X-ray diffractograms (XRD) were recorded on a Bruker powder XRD D8 X-ray diffractometer. Microtiter plate reader BioTek synergy 2 Finland was used to record the absorbance and fluorescence change of lactalbumin and Genistein interactions. Flow cytometry analysis was performed on BD FACS Calibur (BD Biosciences, San Jose, CA, USA) and Confocal Laser scanning microscope (Leica microsystems) was used for fluorescence imaging.

2.3 Synthesis of Genistein loaded lactalbumin nanoparticles (GLNPs)

GLNPs were prepared by using the antisolvent precipitation method. 20 mg/ml of Lactalbumin (LA) was precipitated using a methanolic solution of GEN in 5:1 ratio. The process was followed as described in the earlier report [16].

2.4 GEN loading efficiency and GEN encapsulation efficiency

GEN loading efficiency and encapsulation efficiency were calculated using UV-Vis spectroscopy at 261 nm. Unbound GEN was removed using 10 kDa Amicon tubes centrifuged at 4000 rpm. The quantification of encapsulated GEN was calculated from the standard curve ranging from 10-100 μg/mL.

$$\text{GEN EE} = \frac{\text{Amount of the GEN added - Amount of GEN in supernatant X 100}}{\text{Amount of GEN added}}$$

$$\text{GEN loading efficiency} = \frac{\text{Amount of GEN added - Amount of GEN in supernatant X 100}}{\text{Weight of Nanoparticles}}$$

2.5 TEM analysis

TEM samples were prepared on the carbon-coated grid 300 meshes after dilution in distilled water and bath sonication for 30 min. Negative staining of the samples was performed using 0.5 % phosphor tungstic acid (PTA) for 2 min. and kept in a desiccator overnight to remove out moisture before analysis.

2.6 Structural and interaction studies of GEN and Lactalbumin

Genistein (GEN) interaction with Lactalbumin (LA) was studied using UV-Vis spectrophotometer. LA (10 µM) was prepared in milliQ water while Genistein stock was initially prepared in methanol which was later diluted in milliQ water for interaction studies. Genistein in different concentrations (1, 2, 4, 6, 8, 10 µM) was treated with 10 µM LA in 96 well plates and spectra were recorded using a microtiter plate reader. The change in absorption peaks value between 215-320 nm is monitored as a parameter of GEN protein interaction, this change in absorption peaks is attributed to the hydrogen bonding of tryptophan and tyrosine residues to the neighbouring atoms and transfer of the aromatic chromophore from a hydrophobic interior of a protein into the hydrophilic environment during denaturation and aggregation of the protein. Increasing concentrations of Genistein causes larger shifts in the peak area, indicating protein aggregation and involvement of hydrogen bonding.

2.7 FTIR analysis

FTIR samples were prepared using classical KBr pellet method. An equal amount of lactalbumin, lactalbumin nanoparticles, Genistein (GEN), GLNPs and physical mixture of GEN and lactalbumin nanoparticles were mixed with KBr and grind to a fine powder before making the pellets.

2.8 CD analysis

CD spectra of Lactalbumin, Lactalbumin nanoparticles (LANPs) and GEN lactalbumin nanoparticles (GLNPs), were recorded with a CD spectrophotometer. A quartz cell with a path length of (0.1 cm) was used in a nitrogen atmosphere for measurements in the far-UV region (195-260 nm). LA concentration was kept constant (2.5 µM), while concentration of LA nanoparticles (20 µM) and GLNPs (45 µM) were used as mentioned. An accumulation of three scans with a scan speed of 50 nm/min was performed, and data were collected for each nm from 260 to 195 nm. Sample temperature was maintained at 25 °C using a Neslab RTE-

111 circulating water bath connected to the water-jacketed quartz cuvettes. Secondary structure analysis was done using JASCO secondary structure analysis software.

2.9 XRD analysis

In powder XRD analysis, samples were lyophilized and put to analysis. XRD analysis was performed from 2θ values of 2 to 80° with a scan rate of 0.2 scans per minute using powder XRD. Genistein, LANPs, GLNPs and Physical mixture of LANPs and Genistein were analyzed, and comparative analysis we carried out for the crystallinity of the materials.

2.10 Specific Solubility Determination

The PBS solubility of the free Genistein or in the form of GLNPs was determined by a shake-flask method. An excess amount of Genistein and GLNPs was added to 2.0 mL of PBS pH 7.4 and incubated at 37 °C. The suspended solution was continuously shaken with 150 rpm for 24 h. Once equilibrium attained, the supernatant liquid was held still for 2 h and filtered through a 0.45μm membrane and analyzed by UV spectroscopy. Each measurement was repeated three times. Specific solubility result indicates the increased solubility of GEN in GLNPs as compared to pure GEN. This increased solubility could be the result of nano compartmentalization of the GEN with carrier protein lactalbumin.

2.11 *In vitro* GEN release studies

In vitro GEN, release studies were performed in 20% methanolic solution of PBS pH 7.2 using 12KD cut off dialysis membrane. 1 mg of GEN was weighed and suspended in 1 ml of 20% methanolic solution of PBS pH 7.2, the respective amount of GEN loaded nanoparticles was dissolved in the same solvent. GEN release was analyzed in 9ml of 20% methanolic solution of PBS pH 7.2 as a releasing media at 37° C with stirring @ 150rpm. One ml of aliquot was taken at different time intervals and sink was replaced with the same amount of solvent; an aliquot was analyzed using UV-Vis spectrophotometer after taking absorbance at 261 nm.

2.12 Cell Culture

Oral Squamous cell carcinoma cell lines JHU011 was purchased from Genetic Resources Core Facility, Johns Hopkins University, USA. The cells were cultured in RPMI-1640 supplemented with 10% FBS and 1% antibiotic solution and maintained at 37°C under 5% CO2 atmosphere according to standard cell culture protocols. L929 fibroblast cell line was

purchased from The National Centre for Cell Science, Pune, India and maintained in DMEM supplemented with 10% FBS and 1% antibiotic solution.

2.13 3D raft generations

JHU011 cells were grown in RPMI 1640 with 20% FBS and 1% Streptomycin and seeded at the density of $3x10^6$ cells in Cell insert (Millipore) with the pore volume of 8 µM. Media was replaced after every 24 hrs of incubation at 37°C. After seven days of incubation or raft generation, cell inserts were taken out and washed with chilled PBS before fixing with 4% formaldehyde. The membrane was cut and frozen into the optimal cutting temperature (OCT) tissue freezing media for cryo-sectioning and further analysis.

2.14 Cytotoxicity assay

Proliferation of JHU011 cells under various treatment conditions was evaluated by using the colorimetric MTT assay. Briefly, $1x10^4$ cells per well were seeded in 96-well plates. After 24 hrs. Culture media was replaced with fresh media containing 2% FBS, and the cells were treated with different concentrations of blank nanoparticles, pure GEN and GLNPs for different time points (48 and 72hrs.). MTT solution (5mg/ml in phosphate-buffered saline (PBS) was added to each well and incubated for 2 hrs. at 37 °C and 5% CO_2. The insoluble formazan crystals were dissolved by adding DMSO to each well, and the absorbance of each well was read at 570 nm using a microplate reader. The results were presented as a percent value to the control. The percent cell viability was calculated using the following equation: cell viability = (ODexp/ODcon)×100 in which ODexp and ODcon represent the optical densities of experimental and control cells, respectively. GEN concentration that inhibited cell proliferation to 50% (IC50) in comparison to the control was determined using curve fitting method from at least three independent experiments in a triplicate format for each treatment.

2.15 Cell cycle distribution analysis

PI staining was used to determine the distribution of cells in different phases of the cell cycle by flow cytometry analysis. Briefly, cells were seeded into 6-well plates at a density of $1×10^5$ cells/well. The cells were treated with blank nanoparticles, IC50 of Genistein and GLNPs. Cells were collected by trypsinization, fixed and stained with a PI solution at 4°C for 30 min in the dark to analyze cell cycle distribution based on DNA content of cells by flow cytometer. Data analysis was performed using FlowJoV10 software.

2.16 Determination of Cellular Uptake by Confocal Laser Scanning Microscopy

The cells were trypsinized and seeded in a 6-well plate on coverslips in a density of 5×10^4 cells per well in 2 ml of culture medium. JHU011 cells were incubated with free Rhodamine B tagged nanoparticles at a concentration of 50 μg mL^{-1} for 4hrs. The cellular uptake and distribution of LANPs were investigated by a confocal laser scanning microscope (Leica microsystems).

2.17 Intracellular estimation of ROS

Intracellular ROS levels were estimated using a cell-permeable non-fluorescent probe 2′,7′-Dichlorofluorescin diacetate, which de-esterified intracellularly and turns to highly fluorescent 2′,7′-dichlorofluorescein upon oxidation. Cells were cultured in 96 well plates and allowed to attach overnight. After attachment overnight, cells were washed with PBS and stained with DCFDA in a final concentration of 10μM for 45min at 37°C. Cells were washed to remove excess DCFDA and incubated with 40 μM dose of GEN, GEN lactalbumin nanoparticles (GLNPs) and blank lactalbumin nanoparticles (LANPs) for 6 hrs. at 37°C in reduced serum media. Finally, fluorescence intensity was recorded using a plate reader (Ex/Em = 485/535 nm). ROS level was estimated as percentage change concerning control after background subtraction.

2.18 Bax mitochondrial Translocation

Bax is a pro-apoptotic protein present in cytoplasm. Bax mitochondrial translocation was studied using Mito-tracker Green probe and Bax specific antibodies. Initially cells were cultured on coverslip in 6 well plates in a density of $1x10^5$ cells per well. The cells were treated with 40μM GEN equivalent GLNPs for 4 hrs. After treatment, cells were washed thrice with PBS and treated with Mito-tracker green (Invitrogen) (100nM) for 15 min followed by 30 min fixation in 4% formaldehyde. After fixation standard immunofluorescence staining protocols were followed. Finally, the cells were analyzed using a Confocal laser scanning microscope.

2.19 Immunofluorescence studies

Treated cells and fixed raft sections were washed thrice in PBS. Cells were permeabilized using 100 % methanol (-20ºC) for five minutes at room temperature and successively fixed using 4% paraformaldehyde for 10 min at 4ºC. Cells and raft washed thrice before adding a blocking agent (2% BSA). Blocking was performed at room temperature for 30 min to rule

out nonspecific binding sites of antibodies. Cells and raft were incubated with primary antibody in (1:200) 2% BSA for 1 hr at room temperature. The solution was decent with successive washing with PBS. After washing, cells and raft are further incubated with secondary antibody (1:500) in 2% BSA for 1 hr in dark condition at room temperature. After incubation cells and raft washed thrice with PBS and mounted on a glass slide for fluorescence analysis.

2.20 Real-time polymerase chain reaction

About $2.0x10^6$ cells/ml were seeded in T25 flask followed by incubation for 24 hrs. Next, the cells were treated with GEN, GLNPs, LANPs for 48 hrs. After treatment, cells were washed with chilled PBS. The RNA isolation kit was used to isolate mRNA from the treated cells. The isolated mRNA was quantified by the TECAN plate reader using Nanoquant assembly. The cDNA was synthesized using a cDNA synthesis kit (Thermo Fisher). The purified RNA (1 μg) was taken as a template, and the genes of interest were amplified using specific primer sets with SYBR green dye. A 10 μL of PCR reaction containing cDNA template (1 μL), SYBR green dye (5 μL) and gene-specific primers (1 μL each of forward and reverse primers) was performed using Quant qRT-PCR (QuantStudio™ 5System, Thermo Fischer). The relative expression levels of each gene were calculated considering comparative CT values, normalized with the CT value of GAPDH.

2.21 Western blotting

In a T25 cell culture flask, about 2.0×10^6 cells were seeded and incubated overnight. Next day, the cells were exposed to GEN, GLNPs and LANPs (equivalent dose of 40 μM GEN) for 48 hrs After completion of treatment, the cells were washed thrice with chilled PBS, followed by lysis with RIPA buffer containing PMSF. Further, the cells were broken down by sonication at 35% amplitude (10 sec. ‘on’, 3sec. ‘off’) for 3 min followed by centrifugation at 15000 rpm for 30 min at 4°C. The supernatant was collected, and the concentration of protein for each sample was quantified using Bradford assay. A 4-15% gradient SDS polyacrylamide gel was considered to resolve the isolated protein and later transferred onto a polyvinylidene difluoride (PVDF) membrane using trans blot turbo standard transfer protocol. The protein-containing membrane was blocked by using 5% BSA in TBST (tween-tris buffer saline) buffer for 1 hr at room temperature followed by washing thrice using TBST (10 min wash cycle). The blots were further incubated with protein-specific primary antibodies (1:1000)

overnight at 4°C. Next, the blots were washed thrice (10 min each) with TBST followed by incubation with the suitable secondary antibody (1:2000 dilution) for 2 hr at room temperature. Finally, the blots were washed thrice (10 min each) with TBST and developed using ECL western substrate (Bio-Rad). Finally, the obtained protein bands were quantified by using the densitometry function of Image-J and relative expression was calculated.

2.22 Chromatin Immunoprecipitation assay

The cells were crosslinked with 4% formaldehyde in culture media after completion of treatment. The crosslinked cells further lysed and sonicated to obtain Chromatin. Chromatin DNA was immunoprecipitated with 3PK antibody and normal IgG. The complex was washed, and reverse crosslinking was performed overnight. After reverse crosslinking, the DNA was recovered and purified using phenol/chloroform/isoamyl alcohol extraction method. Recovered DNA was analyzed using qPCR against EZH2 promoter sequences (Forward 5′-GACACGTGCTTAGAACTACGAACAG-3′ and Reverse 5′-TTTGGCTGGCCGAGCTT-3′), (Forward 5’-GAACTGGTTCAAACTTGGCTTC-3’, Reverse 5’-CCAATCGCCATCGCTTTTAT-3’). The relative amount of immunoprecipitated DNA was evaluated and normalized against the Input (lysate) and negative control (IgG).

2.23 Animal experimentation

In-vivo experiments on six-weeks-old male Balb/c mice soy-derived after due ethical clearance from the institutional animal ethics committee. To assess the tissue distribution and clearance studies in a pre-clinical model, Indocyanine green conjugated LANP was dispersed in PBS pH 7.4 and injected intravenously in Balb/c mice (n = 3) at a concentration of 2.0 mg/kg body weight. For the negative control group, 100 µL of sterile PBS was administered through the tail vein. The mice were imaged at the various time point for 4 hrs. The images were acquired using the IVIS Spectrum (Perkin Elmer) animal imager measuring quantitative estimation of the fluorescence intensity. For probing any potential *in vivo* toxicity of the LANPs, mice were given a random higher I.V dose of (5mg/kg/day) for seven days, after seven days the mice were anaesthetized and sacrificed. Major organs such as liver, spleen, kidney, heart, and brain were harvested for further histological analysis.

2.24 Statistical Analysis

All data were analyzed using the statistical package of origin 8.5 SR1 version of the software from origin lab corporation with the License number GF3S4-9089-7123456. One-way

ANOVA was applied to evaluate the data from different groups followed by Tukey test for further comparison among the groups, a p-value of <0.05 was considered as statistically significant.

3.0 Results and Discussion

3.1 Synthesis and Characterization of GLNPs

Protein-based nanoparticles have shown tremendous success in cancer drug delivery application on account of improved drug loading ability, minimum systemic toxicities, better cellular uptake and improved pharmacokinetics and pharmacodynamics properties. Several protein-based strategies loaded with poorly water-soluble drugs are already approved or in an advanced stage of clinical trials.[17, 18]

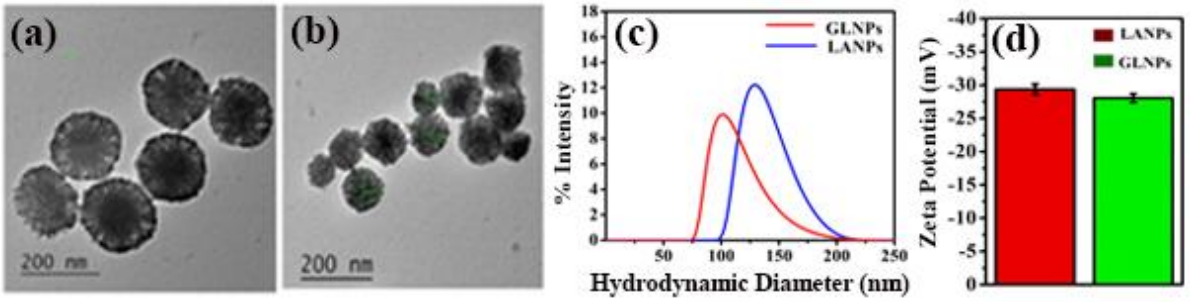

Fig 1. Nano formulation characterization showing (a)TEM images of LANPs (b) GLNPs (c) hydrodynamic diameters (d) Zeta potentials

In this study, we have prepared a genistein loaded lactalbumin nanoparticles system in which a nutraceutical carrier protein and chemotherapeutic drug are used in combination, which selectively kills cancer cells without negatively affecting the health of fibroblast cells. The NPs were characterized using TEM (Fig 1a, b), DLS (Fig 1c, d) which suggest that the morphology of LANPs and GLNPs are spherical in shape with average particle size distribution 150 and 100 nm, respectively. The XRD pattern of GLNPs indicate the amorphous state of GEN in GLNPs, as no GEN specific XRD peaks were observed in XRD scan (Fig 2f). The average particle size distribution pattern predicts that the incorporation of GEN offers a decrease in the size of GLNPs, which could be due to the alteration in hydrophobic pockets of the protein molecules during protein and GEN Interaction, as evident in CD spectroscopy (Fig 2d, e) and FTIR studies (Fig 2a-c). FTIR spectra of GLNPs show blue shift and broadening in phenolic peak (3200-3550 cm^{-1}) which is attributed to the development of a conjugate system and hydrogen bonding. It indicates that hydrophobic interactions and hydrogen bonding are the major forces responsible for the interaction of

GEN and lactalbumin in GLNPs. Interaction studies performed to confirm the role of hydrophobic interaction using tryptophan absorbance change revealed that with change in GEN concentration, the tryptophan absorbance changes significantly (Fig 3a).

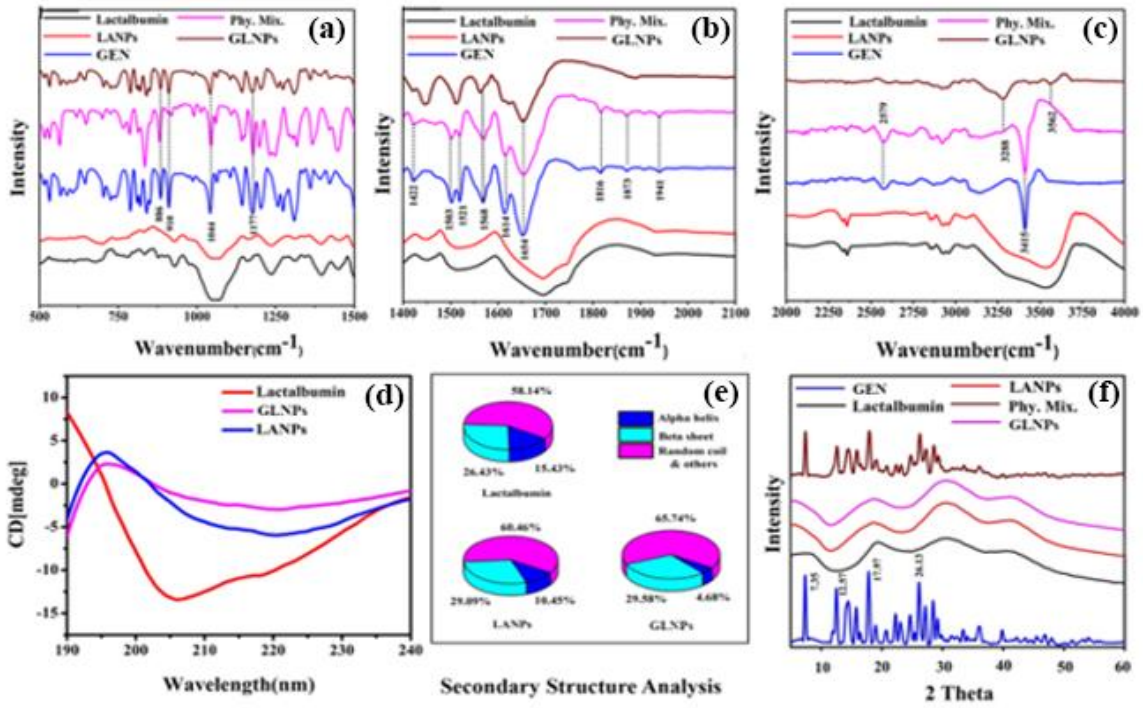

Fig 2. FTIR spectra (a) 500-1500nm (b) 1400-2100nm (c) 2000-4000 nm (d) CD spectra (e) secondary structure estimation from CD spectra (f) powder XRD analysis of GEN, Lactalbumin, Lactalbumin nanoparticles (LANPs), Physical Mix., GEN lactalbumin nanoparticles (GLNPs)

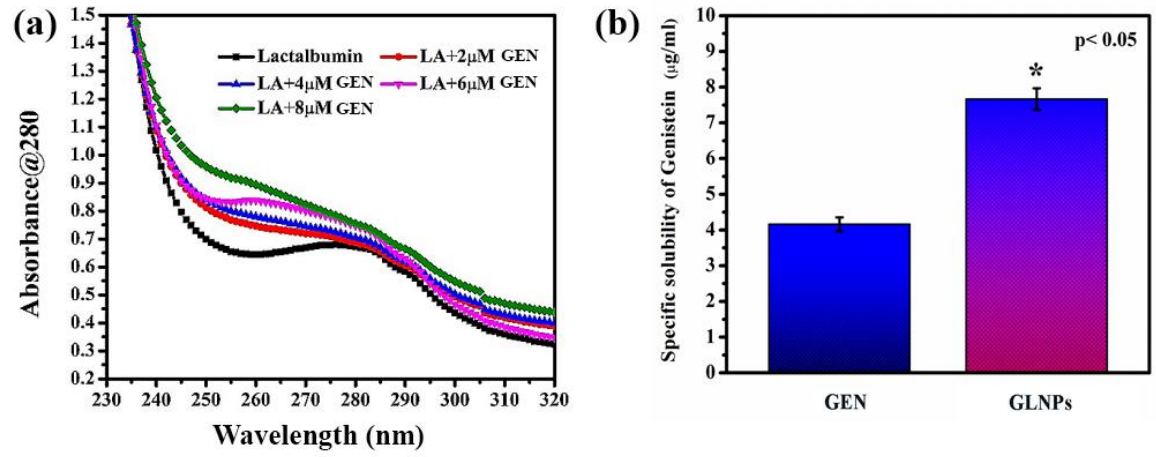

Fig 3. UV spectra for the Lactalbumin (LA) showing the impact of different concentrations of Genistein (GEN) on tryptophan absorbance (a) Specific solubility of Genistein (GEN) and GLNPs in PBS pH 7.4 at 37 °C (b).

This observation change validates our hypothesis of hydrophobic interaction between GEN and LA. These interactions help in better dispersibility of the GEN from GLNPs in the

aqueous solvent (Fig 3b) and facilitate improved GEN release from the nanoparticles without any alteration in the activity.

3.2 *In vitro* cytotoxicity, cellular uptake and cell cycle studies

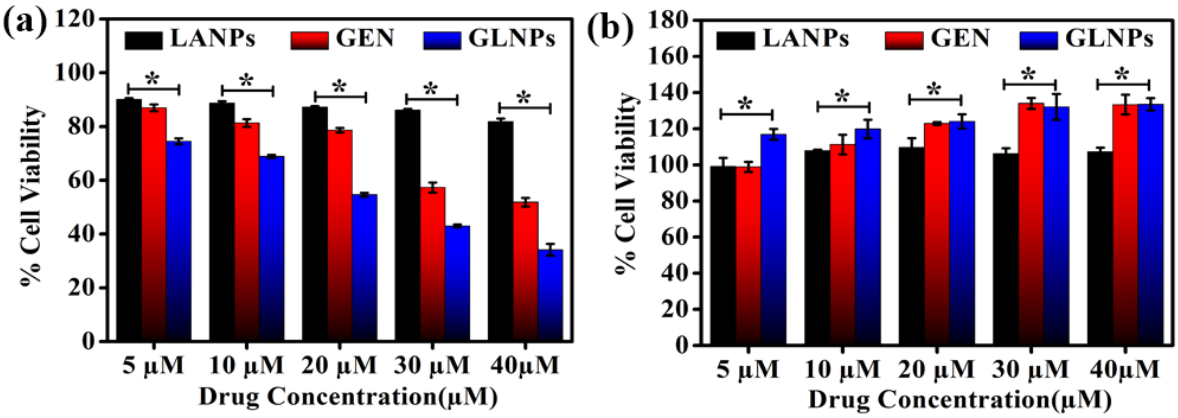

Fig 4. ***In vitro*** **cytotoxicity analysis (a) JHU011 cells at 48 hrs. (b) Fibroblast L929 cells at 48hrs of treatment**

One of the major reasons for the development of drug resistance and side effects associated with the use of anticancer agents is the requirement of high concentration of the drugs. It is well established that anticancer drugs alter signalling pathways needed for cancer cell proliferation. In this context, it becomes vital that if multiple therapeutic molecules are combined, could target multiple key pathways simultaneously to inhibit the progression of cancer cells efficiently. Therefore, to demonstrate that, we have developed a nano combination which selectively inhibits the cancer cell proliferation. It is evident from cell viability assay that GLNPs at 40µM dose induces ~60% decrease in JHU011 cells viability, however respective concentration of GEN and LANPs induced ~40%, ~15% decrease in viability respectively when exposed to 48 hrs (Fig 4a). Further incubation of GLNPs, GEN and LANPs till 72hrs did not induce any significant improvement in cell viability. Considering the release kinetics of GEN from GLNPs (Fig 5c), it can be concluded that GEN maintains sufficient concentrations in the medium, which is enough to inhibit the viability of the JHU011 cells for a prolonged period. We have also investigated the effect of LNPs, GEN, and LANPs on viability of L929 fibroblast cells. The exposure for 48hrs did not show any decrease in cell viability from a 5-40 µM dose of GEN and respective GLNPs (Fig 4b). Although, nutritional values of the formulation supported fibroblast cell growth in dose dependent manner. This observation suggests that the GLNPs selectively are more effective against cancerous cells and impart no toxic effect on normal fibroblast.

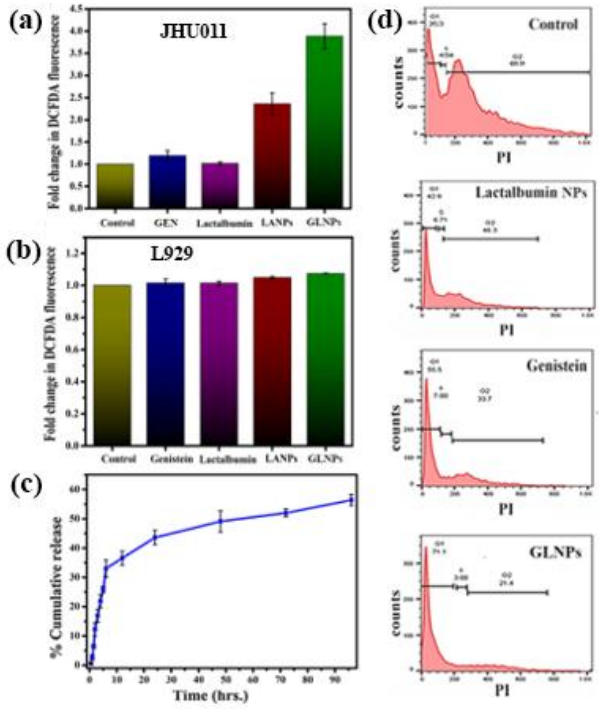

Fig 5. *In vitro* studies on cell lines showing (a) Fold change in DCFDA fluorescence in JHU011 (b) Fold change in DCFDA fluorescence in L929 (c) *In vitro* percent cumulative release of GEN from GLNPs at different time interval (d) Cell cycle analysis showing PI staining of JHU011 cell line in Control, Lactalbumin, GEN and GLNPs

Cell cycle analysis through flow cytometric has revealed that LANPs, GLNPs and GEN had delayed the progression of OSCC JHU011 cells at the G0/G1 phase and arrest cell cycle at 40 µM dose of GEN. GLNPs has resulted in accumulation of 71.1 percent of the cell population in the G0/G1 phase while LANPs and GEN show 42.9%, 55.5% accumulation in a cell population, respectively. This percent of the arrested cell population is significantly higher than the 25.3% of control (Fig 5d). GEN is known to produce G2/M phase arrest in various cancer models [19]. In the present study, the majority of the cell population was found accumulated in G0/G1 phase after GLNPs treatment. There is no conclusive evidence of LANPs activity on cancer cell cycle regulation so far, the accumulation of cell population in G0/G1 phase confirms its potential to modulate the early phase of the cell cycle. These results validate the improved anticancer properties of GLNPs in comparison to GEN and LANPs monotherapy to inhibit the cancer cell progression at the early stage of the cell cycle. Rhodamine B doped GLNPs have shown that it can efficiently bypass the cellular pumps and deliver the carrier to the cell nucleus of the 2D monolayer (Fig 6a) and 3D multi-layer ex vivo tissue culture system, and this could be one of the prime reasons for better anticancer therapeutic results of nanoformulations in a complex tissue system (Fig 6b). A Z-stack image further confirm delivery of nanoparticles in multilayer structures (Fig 7).

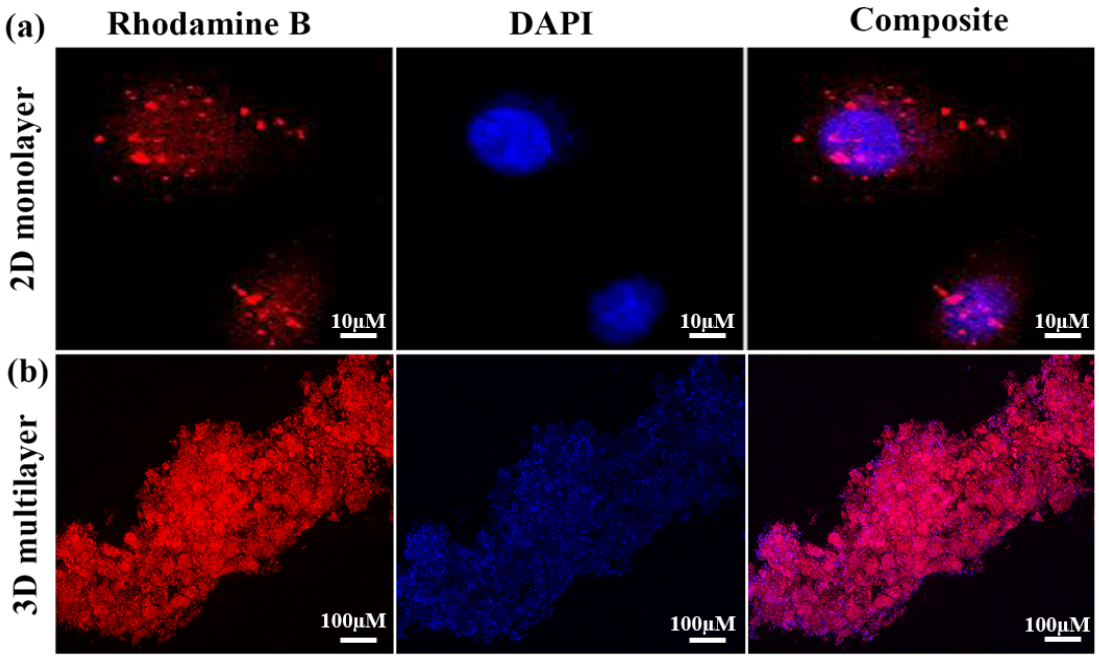

Fig 6. Cellular uptake studies in JHU011 cell line showing nanoparticle uptake in (a) 2D monolayer culture (b) 3D multilayer culture

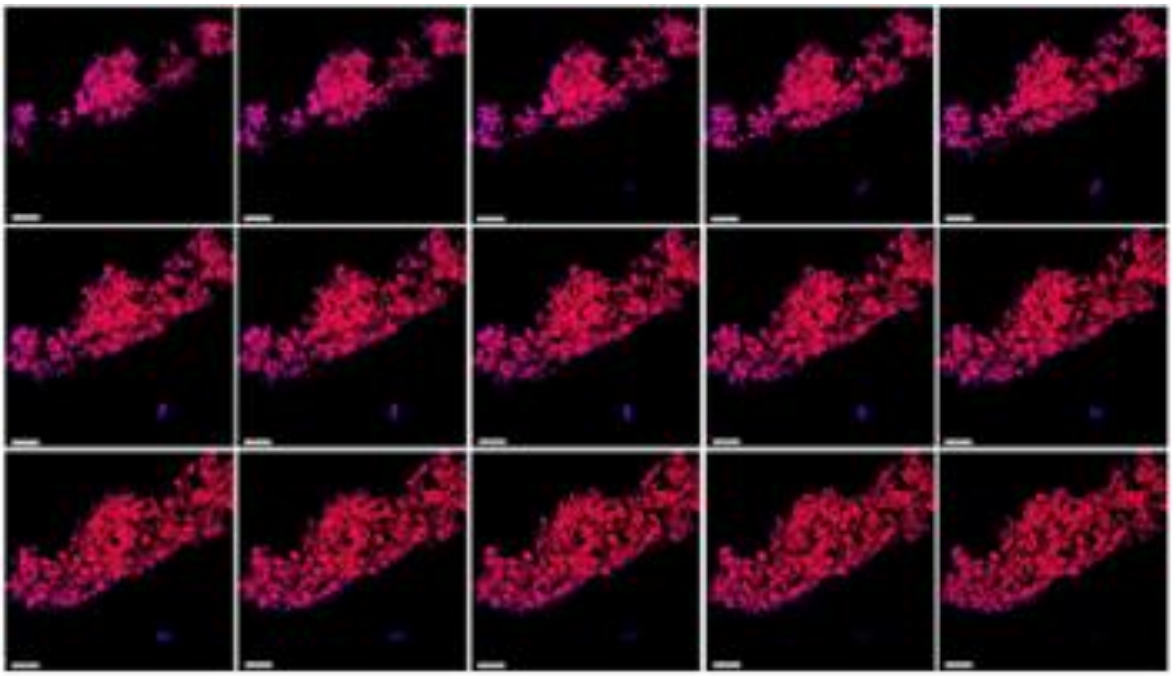

Fig 7. Z stacked images of 3D raft multilayer cultures of JHU011 cells showing cellular uptake

3.3 GLNPs selectively Induce apoptosis through ROS mediated Bax mitochondrial translocation and activation of Caspase 3

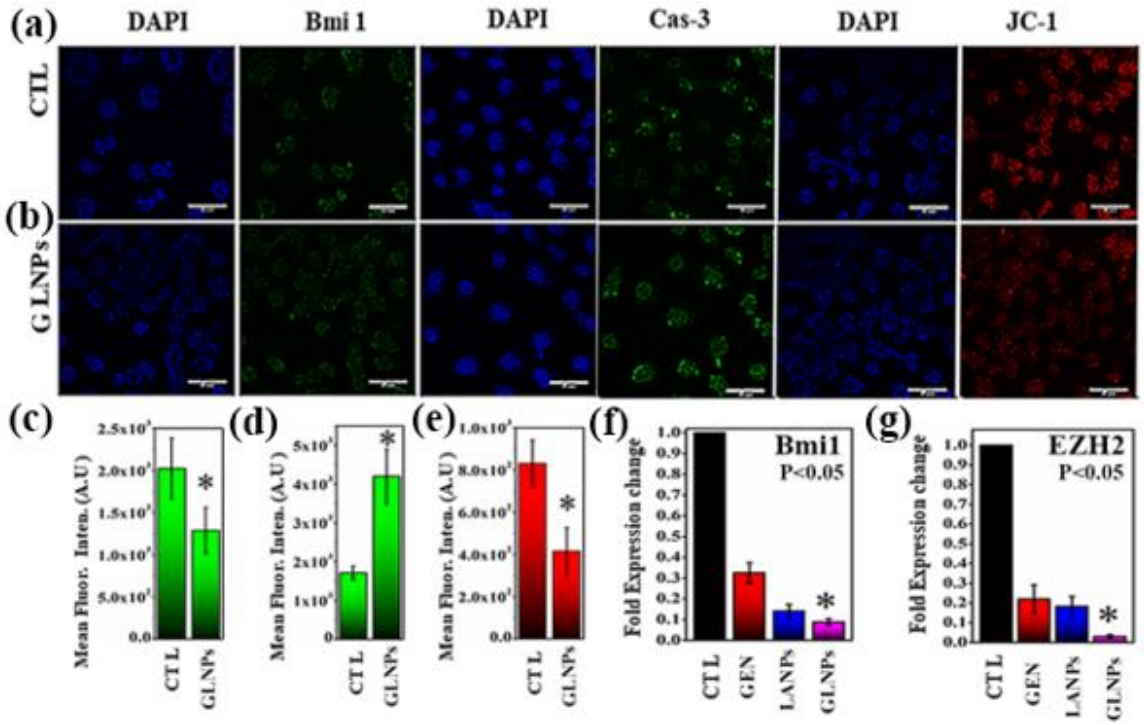

Fig 8. 2D monolayer JHU011 cell line showing (scale bar 40µm) immunofluorescence-based expression of Bmi-1, Caspase-3 (Cas-3), and JC-1 in (a) Control (CTL) (b) GEN lactalbumin nanoparticles (GLNPs) treated cells (c) Quantitative estimation of Bmi-1 expression in immunofluorescence (d) quantitative estimation of Cas-3 expression (e) quantitative estimation of JC-1 (f) mRNA based quantitative relative expression of Bmi-1 (g) EZH2.

It is well established that cancer cells are more sensitive for the cellular accumulation of excessive ROS. This strategy has been well exploited to selectively kill cancer cells without affecting normal cells [20]. Genistein, a potential anticancer drug and lactalbumin, a known protein supplement, scavenge ROS through a distinct mechanism in their bulk state [21]. Their cellular effect in nano form is not established so far. Therefore, we have incubated GEN, GLNPs, LANPs with OSCC cells along with fibroblast cells for initial 6 hrs and examined ROS production at a respective 40µM dose of GEN, GLNPs, LANPs. As hypothesized, GEN has not induced significant ROS production in initial 6 hrs incubation, surprisingly GLNPs and LANPs increased the ROS production to ~3.5 fold and ~3 fold respectively in JHU011 cells (Fig 5a). The developed GLNPs showed better inhibition in JHU011 cells, which is in agreement with our ROS generation data, suggesting that ROS play a significant role in GLNPs mediated killing of OSCC cells.

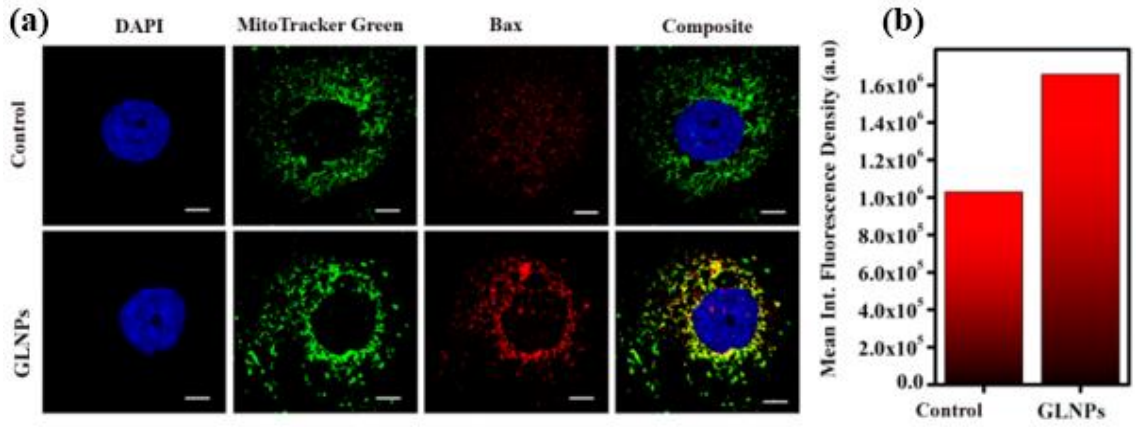

Fig 9. Bax mitochondrial translocation studies showing (a) colocalization of mitochondria (Mitotracker green) and Bax (TRITC) (b) quantitative Mean Integrated Fluorescence Density of Bax in Control, and GLNPs. Scale bar represents 5µm.

Additionally, we studied the effect of these NPs over the normal cells, considering fibroblasts as in vitro model systems. The results showed that GEN, GLNPs, LANPs did not induce any significant enhancement in ROS generation in fibroblasts compared to control (Fig 5b). This observation suggests that GEN and Lactalbumin in its bulk form did not induce any significant inhibition in OSCC and normal fibroblasts cells, however, when combined (in GLNPs), cause substantial killing to OSCC cells without altering the proliferation of fibroblasts cells. This could be further hypothesized that the GLNPs target selective signalling pathways expressed in cancer cells but not in normal cells, which lead to this targeted action. Our Immunofluorescence and western blot results are in support of this hypothesis. GLNPs treatment causes cytoplasmic accumulation of ROS, which results in mitochondrial membrane damage as evident from the decrease in JC-1 monomers fluorescence (Fig 8 a, b). Compromised mitochondrial membranes become permeable for various pro-apoptotic protein viz. Bax and Bak which trigger the translocation of cytochrome c (Cyt-c) from mitochondria into the cytosol. This cytosolic release of Cyt-c in a cell makes the point of no return in apoptotic signalling pathway. In the current study we observed that GLNPs have successfully activated Bax and induced its mitochondrial translocation (Fig 9) which directs cells to caspase mediated apoptotic pathways. Overexpression of cleaved caspase 3 in GLNPs treated cells confirms our mechanistic hypothesis of Apoptosis (Fig 8.a, b). Beyond these classical apoptotic pathways there are many other mechanisms which regulate the apoptotic pathways in cancer cells, among which polycomb repressor complex (PRC1 and PRC2) mediated epigenetic repression of transcription of various tumor

suppressor and proapoptotic genes are frequent. These epigenetic repressors are the potential targets of cancer therapy.

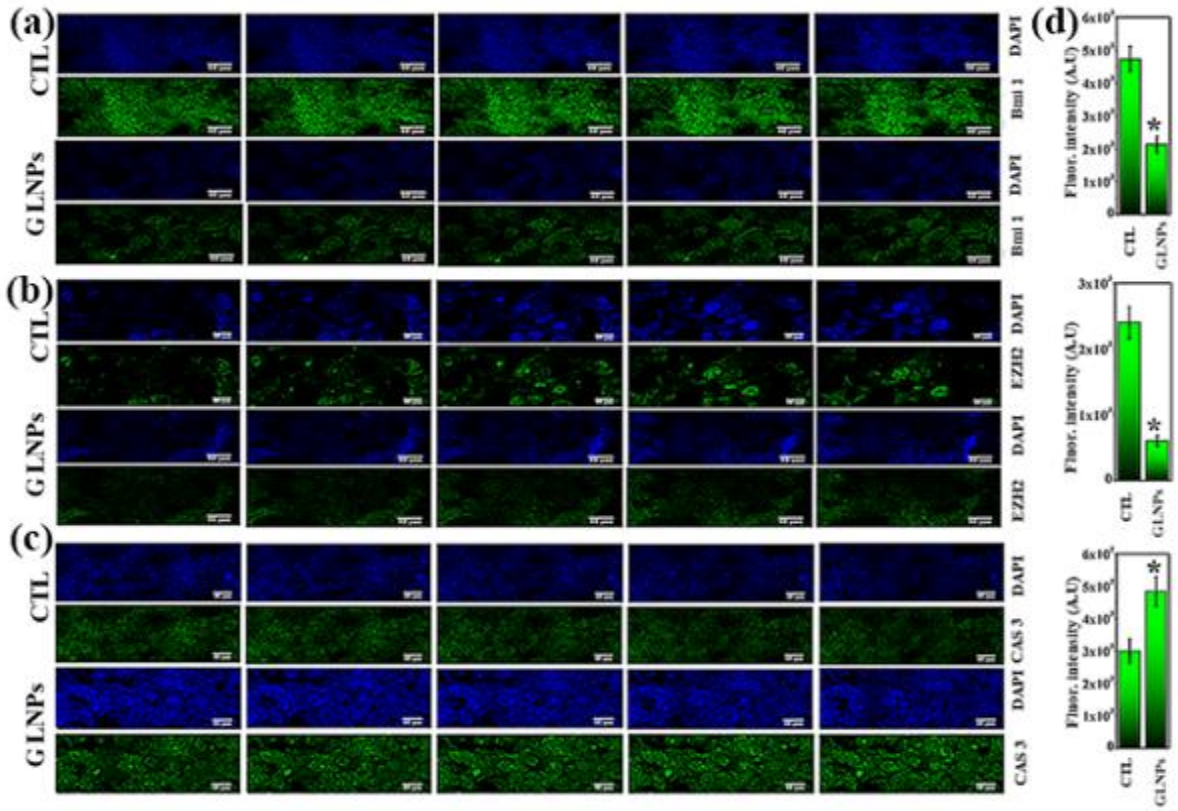

Fig 10. Immunofluorescence analysis showing (scale bare 40µm) Expression in Z stacked images of JHU011 3D ex vivo raft (a) Bmi-1 Expression (b) EzH2 Expression (c) Caspase-3 Expression (d) Quantitative estimation profile of expression of Bmi-1, EzH2 and Caspase-3.

3.4 Concurrent downregulation of epigenetic repressors

GEN is a known potential regulator of expression of epigenetic repressors [22]. Therefore, we have further investigated the possibility of GEN, LANPs and GLNPs in regulating the epigenetic modulation of histones along with epigenetic repression signatures of H3K27me3 and UbH2AK119 proteins in OSCC progression. The GLNPs has shown a dramatic reduction in the expression level of Bmi 1 and EZH2 (Fig 10), (Fig 9) as evident in immunofluorescence studies. In the current study, we have found that GLNPs treatment has resulted in significant decrease in EZH2 expression at transcription and translational level (Fig 8g, Fig 11a, b). EZH2 has methyltransferase activity and tri-methylate histone 3 at lysine 27 residue which serves as a hallmark of epigenetic repression. Downregulation of EZH2 expression in GEN treated cells has not resulted in successive downregulation of H3K27me3, although GLNPs and LANPs treated cells show reduced H3K27me3 expression (Fig 11a, b).

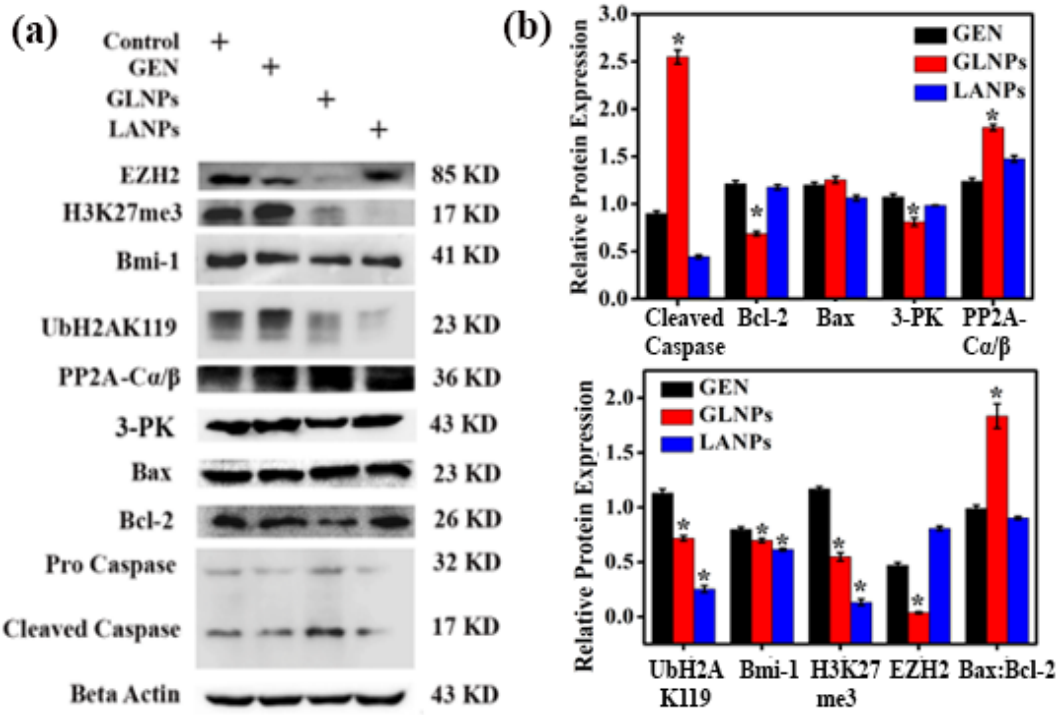

Fig 11. (a) Western blot analysis of various protein targets after 48 hrs of treatment GEN, GLNPs and LANPs (b) quantitative estimation of expression.

Interestingly, LANPs alone has resulted in complete removal of the H3K27me3 mark without affecting the expression of EZH2, which could be attributed to the activation of various histone demethylases as a consequence of LANPs treatment. There are reports which support this hypothesis where H3K27me3 signature modulated independently of the EZH2 expression [23]. In addition to EZH2, another key repressor Bmi-1, which is upregulated in various human cancers, including OSCC, stabilizes RING1A/B, leading to increased H2A ubiquitination activity and result in transcription repression [24]. Targeting Bmi-1 in cancer therapeutics seems very difficult as it does not have any enzymatic activity [25]. In the current study, GLNPs and LANPs treatment have resulted in downregulation of Bmi-1 protein, followed by reduced UbH2AK119 expression. The relative mRNA expression (Fig 8f) is well supported through immunofluorescence studies and western blot analysis in GLNPs treated JHU011 cells. It could be hypothesized that the GLNPs have laid the foundation of cellular apoptosis in OSCC, which is well supported through ROS production, Bax mitochondrial translocation and concurrent downregulation of these key repressors. Certain reports support the role of ROS accumulation in epigenetic regulation [26] and vice versa where inhibitors of epigenetic repressors sensitize cancer cells for ROS accumulation followed by apoptosis [27]. In the present study, the hallmarks of epigenetic repression are well targeted by GLNPs and

LANPs in OSCC without affecting the normal fibroblast cells; this supports their selective combinatorial potential as an anticancer molecule.

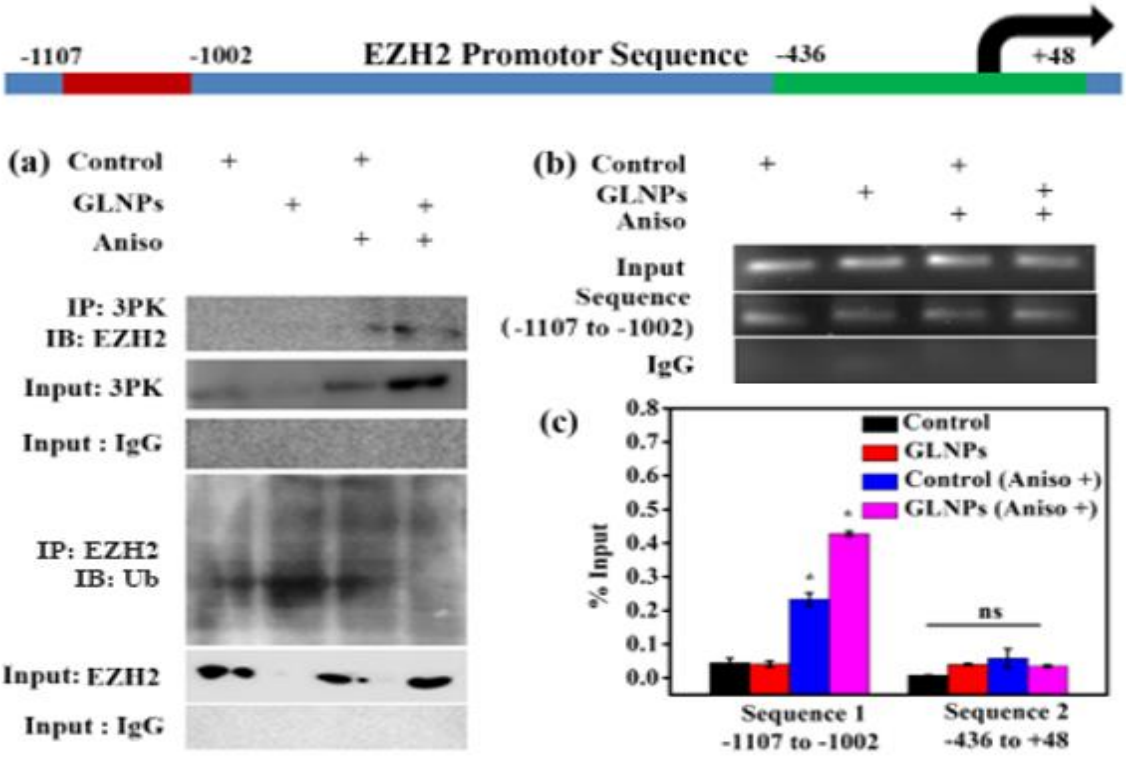

Fig 12. Co-IP studies showing (a) effect of Anisomycin (Aniso) on 3PK, EZH2 and Ub expression, (b) ChIP-qPCR % Input analysis of sequence 1 and Sequence 2 (c) Sequence 1 amplified product.

3.5 GLNPs regulate EZH2 expression through proteasomal degradation and 3PK inhibition

PcG proteins phosphorylation play a major role in their chromatin association and gene silencing. The nature of PcG kinase remained unknown for a long time, but slowly it is beginning to unravel. MAPKAP kinases are the key molecules discovered which play a crucial role in regulating the PcG [28]. These molecules work downstream to the MAP kinase pathways, which play a significant role in cancer development and are the direct targets of many therapeutic drugs [29]. In the current study we found that GLNPs are actively downregulating the expression of MAPKAPK3 (3PK) and EZH2, known to be highly expressed in OSCC. In the series of events, we have found that Protein phosphatase 2 (PP2A-Cα/β) which is silenced in many cancer types, is upregulated in GLNPs treatment group. The kinases and phosphatases expression pattern in relation with EZH2 and 3PK relation with another PcG protein Bmi-1driven us to look into 3PK and EZH2 interaction. To establish the 3PK and EZH2 relation and to understand the effect of GLNPs in OSCC epigenetics, we studied the expression pattern in normal treatment condition of GLNPs and in the presence of

anisomycin using Co-immunoprecipitation method. Anisomycin works as a stress inducer and is known to activate 3PK [29]. We have found that GLNPs downregulate the 3PK and EZH2 expression in OSCC, which was restored in the presence of anisomycin (Fig 12a). This indicates that 3PK has some role in altering EZH2 expression. To further understand the role of GLNPs play in this cascade, we have studied the EZH2 degradation mechanism using co-immunoprecipitation of EZH2 and ubiquitination under similar treatment conditions. We have found that under normal treatment conditions GLNPs induce proteasomes mediated degradation of EZH2, as evident from increased ubiquitination (Fig 12a). Restored EZH2 expression in anisomycin treatment condition is most probably due to the inability of GLNPs to bring down the 3PK expression along with inhibited proteasomal pathways.

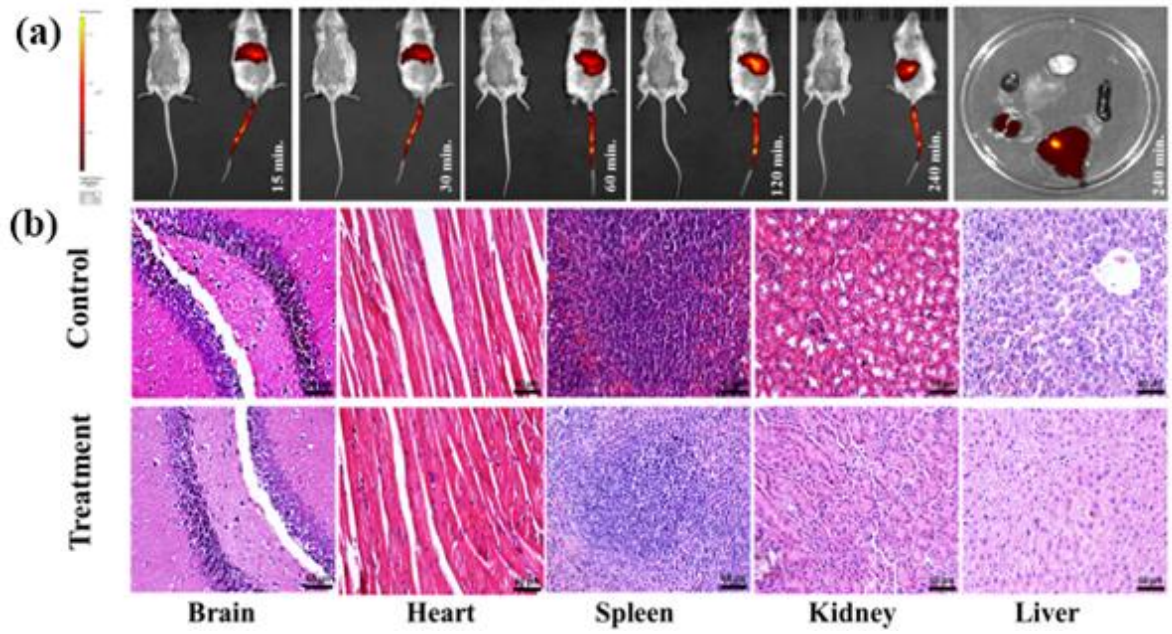

Fig 13. ***In vivo*** **biodistribution of (a) LANPs at various time point (b) Histopathological sections of various organs.**

3.6 GLNPs inhibit 3PK and its direct target EZH2 collaboration to inhibit OSCC

We further studied whether there is any direct relation between 3PK and EZH2 expression. To validate our hypothesis, we performed ChIP-qPCR assay using 3PK specific antibodies and two different primers sets from the EZH2 promoter region. We found that region (-1107 to -1002) was amplified in qPCR analysis (Fig 12 b, c), showing a physical interaction of 3PK with EZH2 promoter region. Anisomycin treatment groups has shown increased amplification activity in the region (-1107 to -1002), while no specific amplification was observed from region (-436 to +48). These findings indicate that EZH2 is the direct target of 3PK.

3.7 *In vivo* biodistribution and cytotoxicity studies

Biodistribution profile of the LANP in Balb/c mice has shown that the majority of the injected dose accumulated in the highly perfused organs, such as liver, while spleen and kidney showed minimum accumulation, no accumulation was observed in the brain and heart. can uptake the particles and retain them longer. The images captured at various time points indicate that fluorescence intensity in the liver increased initially from 60 min to 120 min and finally decreased from 120 to 240 min. These organs have an active reticuloendothelial system (RES), which shows the distribution and clearance of the particles from the system. Ex vivo imaging of harvested organs after 4 hr. of administration confirms the presence of particles in the liver and kidney (Fig 14). We have further studied In-vivo toxicological studies with a random higher I.V dose of LANPs (5mg/kg/day). No acute toxicities were observed in the biochemical assay and histopathological sections of various organs, which assures their biocompatibility in the animal system (Fig 14).

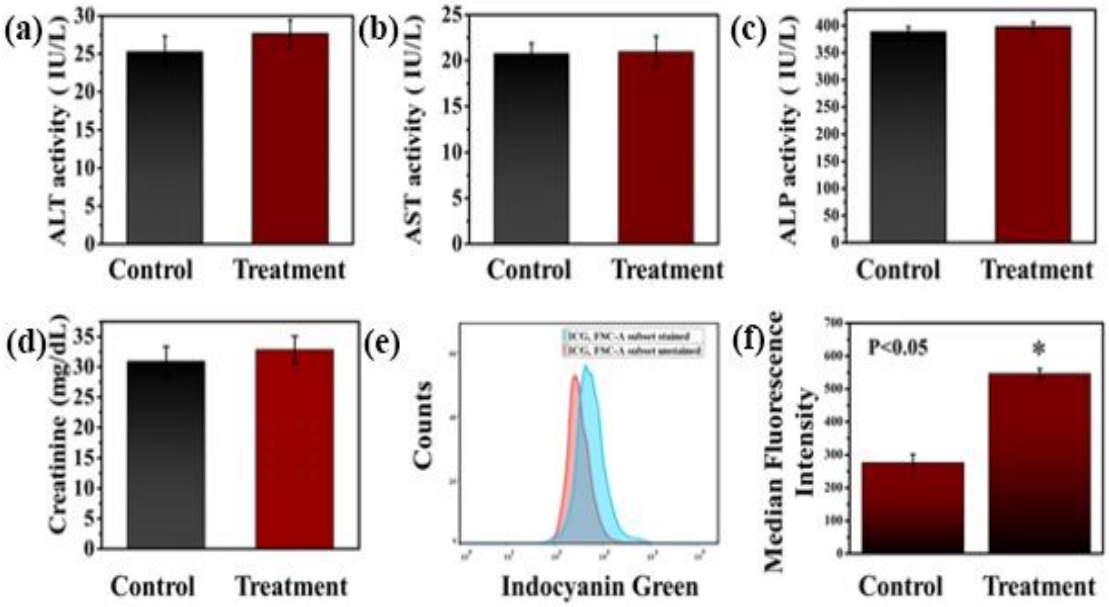

Fig 14. Quantitative estimation of various biochemical markers in liver, kidney (a-d), Kidney samples from control and treated groups showing the presence of ICG (e, f).

4.0 Conclusions

In summary, we have synthesized Genistein loaded lactalbumin nanoparticles, which has improved the bioavailability of genistein, which result in higher drug doses at the treatment site and thus possess the anticancer and epigenetic regulation ability and can overturn the

genetic repression marks in OSCC without affecting the normal fibroblast cells. We have studied the molecular mechanism of apoptosis and epigenetic regulation and established that GLNPs activate proapoptotic protein Bax and induce its mitochondrial translocation to activate caspase 3 which results in cancer cell apoptosis. We have established mechanisms that GLNPs regulate epigenetic repression through EZH2 proteasomal degradation and 3PK inhibition. EZH2 was found physically related to 3PK at transcription and translational level. GLNPs show the unique ability to simultaneously target Bmi 1 and EZH2 activity along with activation of apoptotic pathways in OSCC. These simultaneously provide a potent anti-cancer activity in comparison to its natural bulk counterparts. It shows ready uptake of the nanomaterials in the cells and tissue-layer with better distribution in the nucleus, required for optimal drug delivery. Ability to downregulate key molecule 3PK, which plays a crucial role in PcG protein EZH2 regulation, opens a new window for understanding critical events of OSCC regulation and improvement in currently available treatment. We believe that this nanomaterial can provide a better understanding of the therapeutic abilities of these molecules in its nanoforms along with bulk counterparts, which would further boost their application in the translational arena.

5.0 References

1. Anonymous, headandneck, Home page. Home and Neck Cancer Alliance website (2017). http://www.headandneck.org/. Accessed March 1, 2017., (2017). **2017**.
2. Zhu, C.; Ling, Y.; Dong, C.; Zhou, X.; Wang, F., The relationship between oral squamous cell carcinoma and human papillomavirus: a meta-analysis of a Chinese population (1994-2011). *PloS one* **2012,** *7* (5), e36294.
3. Cao, W.; Younis, R. H.; Li, J.; Chen, H.; Xia, R.; Mao, L.; Chen, W.; Ren, H., EZH2 promotes malignant phenotypes and is a predictor of oral cancer development in patients with oral leukoplakia. *Cancer prevention research* **2011,** *4* (11), 1816-24.
4. Kang, M. K.; Kim, R. H.; Kim, S. J.; Yip, F. K.; Shin, K. H.; Dimri, G. P.; Christensen, R.; Han, T.; Park, N. H., Elevated Bmi-1 expression is associated with dysplastic cell transformation during oral carcinogenesis and is required for cancer cell replication and survival. *British journal of cancer* **2007,** *96* (1), 126-33.
5. Ho, L.; Crabtree, G. R., An EZ mark to miss. *Cell stem cell* **2008,** *3* (6), 577-8.
6. Chen, Y. W.; Kao, S. Y.; Wang, H. J.; Yang, M. H., Histone modification patterns correlate with patient outcome in oral squamous cell carcinoma. *Cancer* **2013,** *119* (24), 4259-67.
7. Bryant, R. J.; Cross, N. A.; Eaton, C. L.; Hamdy, F. C.; Cunliffe, V. T., EZH2 promotes proliferation and invasiveness of prostate cancer cells. *The Prostate* **2007,** *67* (5), 547-56.
8. Kamangar, F.; Dores, G. M.; Anderson, W. F., Patterns of cancer incidence, mortality, and prevalence across five continents: defining priorities to reduce cancer disparities in

different geographic regions of the world. *Journal of clinical oncology : official journal of the American Society of Clinical Oncology* **2006,** *24* (14), 2137-50.

9. Chen, S. F.; Nieh, S.; Jao, S. W.; Liu, C. L.; Wu, C. H.; Chang, Y. C.; Yang, C. Y.; Lin, Y. S., Quercetin suppresses drug-resistant spheres via the p38 MAPK-Hsp27 apoptotic pathway in oral cancer cells. *PloS one* **2012,** *7* (11), e49275.
10. Zhang, P.; Zhang, Z.; Zhou, X.; Qiu, W.; Chen, F.; Chen, W., Identification of genes associated with cisplatin resistance in human oral squamous cell carcinoma cell line. *BMC cancer* **2006,** *6*, 224.
11. Kelloff, G. J.; Crowell, J. A.; Steele, V. E.; Lubet, R. A.; Malone, W. A.; Boone, C. W.; Kopelovich, L.; Hawk, E. T.; Lieberman, R.; Lawrence, J. A.; Ali, I.; Viner, J. L.; Sigman, C. C., Progress in cancer chemoprevention: development of diet-derived chemopreventive agents. *The Journal of nutrition* **2000,** *130* (2S Suppl), 467S-471S.
12. Bounous, G., Whey protein concentrate (WPC) and glutathione modulation in cancer treatment. *Anticancer research* **2000,** *20* (6C), 4785-92.
13. Sternhagen, L. G.; Allen, J. C., Growth rates of a human colon adenocarcinoma cell line are regulated by the milk protein alpha-lactalbumin. *Advances in experimental medicine and biology* **2001,** *501*, 115-20.
14. Wang, S. D.; Chen, B. C.; Kao, S. T.; Liu, C. J.; Yeh, C. C., Genistein inhibits tumor invasion by suppressing multiple signal transduction pathways in human hepatocellular carcinoma cells. *BMC complementary and alternative medicine* **2014,** *14*, 26.
15. Gardner, C. D.; Oelrich, B.; Liu, J. P.; Feldman, D.; Franke, A. A.; Brooks, J. D., Prostatic soy isoflavone concentrations exceed serum levels after dietary supplementation. *The Prostate* **2009,** *69* (7), 719-26.
16. Dev, A.; Srivastava, A. K.; Choudhury, S. R.; Karmakar, S., Nano-curcumin influences blue light photodynamic therapy for restraining glioblastoma stem cells growth. *RSC advances* **2016,** *6* (97), 95165-95168.
17. Foss, F. M.; Sjak-Shie, N.; Goy, A.; Jacobsen, E.; Advani, R.; Smith, M. R.; Komrokji, R.; Pendergrass, K.; Bolejack, V., A multicenter phase II trial to determine the safety and efficacy of combination therapy with denileukin diftitox and cyclophosphamide, doxorubicin, vincristine and prednisone in untreated peripheral T-cell lymphoma: the CONCEPT study. *Leukemia & lymphoma* **2013,** *54* (7), 1373-9.
18. Fuentes, A. C.; Szwed, E.; Spears, C. D.; Thaper, S.; Dang, L. H.; Dang, N. H., Denileukin Diftitox (Ontak) as Maintenance Therapy for Peripheral T-Cell Lymphomas: Three Cases with Sustained Remission. *Case reports in oncological medicine* **2015,** *2015*, 123756.
19. Zhang, Z.; Wang, C. Z.; Du, G. J.; Qi, L. W.; Calway, T.; He, T. C.; Du, W.; Yuan, C. S., Genistein induces G2/M cell cycle arrest and apoptosis via ATM/p53-dependent pathway in human colon cancer cells. *International journal of oncology* **2013,** *43* (1), 289-96.
20. Yokoyama, C.; Sueyoshi, Y.; Ema, M.; Mori, Y.; Takaishi, K.; Hisatomi, H., Induction of oxidative stress by anticancer drugs in the presence and absence of cells. *Oncology letters* **2017,** *14* (5), 6066-6070.
21. Joubran, Y.; Moscovici, A.; Lesmes, U., Antioxidant activity of bovine alpha lactalbumin Maillard products and evaluation of their in vitro gastro-duodenal digestive proteolysis. *Food & function* **2015,** *6* (4), 1229-40.

22. Li, Y.; Chen, H.; Hardy, T. M.; Tollefsbol, T. O., Epigenetic regulation of multiple tumor-related genes leads to suppression of breast tumorigenesis by dietary genistein. *PloS one* **2013,** *8* (1), e54369.
23. Shen, Y.; Guo, X.; Wang, Y.; Qiu, W.; Chang, Y.; Zhang, A.; Duan, X., Expression and significance of histone H3K27 demethylases in renal cell carcinoma. *BMC cancer* **2012,** *12*, 470.
24. Ben-Saadon, R.; Zaaroor, D.; Ziv, T.; Ciechanover, A., The polycomb protein Ring1B generates self atypical mixed ubiquitin chains required for its in vitro histone H2A ligase activity. *Molecular cell* **2006,** *24* (5), 701-711.
25. Cao, L.; Bombard, J.; Cintron, K.; Sheedy, J.; Weetall, M. L.; Davis, T. W., BMI1 as a novel target for drug discovery in cancer. *Journal of cellular biochemistry* **2011,** *112* (10), 2729-41.
26. Wu, Q.; Ni, X., ROS-mediated DNA methylation pattern alterations in carcinogenesis. *Current drug targets* **2015,** *16* (1), 13-9.
27. Zhou, J.; Bi, C.; Cheong, L. L.; Mahara, S.; Liu, S. C.; Tay, K. G.; Koh, T. L.; Yu, Q.; Chng, W. J., The histone methyltransferase inhibitor, DZNep, up-regulates TXNIP, increases ROS production, and targets leukemia cells in AML. *Blood* **2011,** *118* (10), 2830-9.
28. Voncken, J. W.; Niessen, H.; Neufeld, B.; Rennefahrt, U.; Dahlmans, V.; Kubben, N.; Holzer, B.; Ludwig, S.; Rapp, U. R., MAPKAP kinase 3pK phosphorylates and regulates chromatin association of the polycomb group protein Bmi1. *The Journal of biological chemistry* **2005,** *280* (7), 5178-87.
29. Ludwig, S.; Engel, K.; Hoffmeyer, A.; Sithanandam, G.; Neufeld, B.; Palm, D.; Gaestel, M.; Rapp, U. R., 3pK, a novel mitogen-activated protein (MAP) kinase-activated protein kinase, is targeted by three MAP kinase pathways. *Molecular and cellular biology* **1996,** *16* (12), 6687-97.

Note:

- The due permission has been obtained from authors and corresponding author of the following published paper before adopting in the present thesis.

- **Dev, A**.; Sardoiwala, M. N.; Kushwaha, A. C.; Karmakar, S.; Choudhury, S. R., Genistein nanoformulation promotes selective apoptosis in oral squamous cell carcinoma through repression of 3PK-EZH2 signalling pathway. *Phytomedicine: international journal of phytotherapy and phytopharmacology* 2021, 80, 153386.

Chapter 05

Paclitaxel nanocrystalline assemblies as a potential Transcatheter arterial chemoembolization (TACE) candidate for unresectable hepatocellular carcinoma

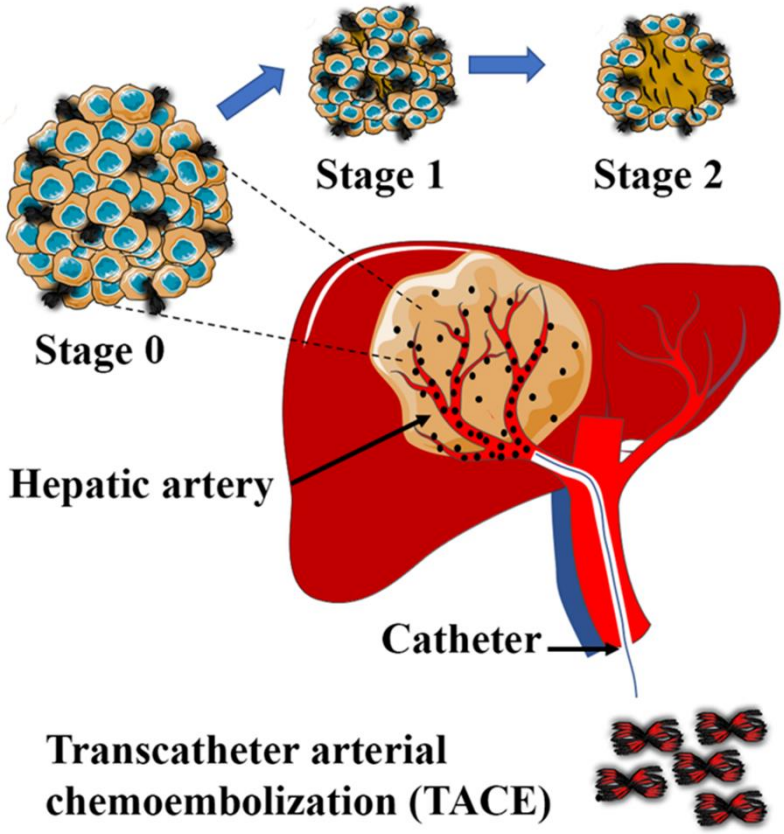

1.0 Background

Liver cancer is one of the leading causes of cancer-related death worldwide. It comprises various hepatic neoplasms viz; hepatocellular carcinoma [1], intrahepatic bile duct carcinoma, hepatoblastoma. Among these primary malignancies, HCC is the most common type of liver cancer, which accounts for more than 80% of cases of liver cancer.[2] The pathophysiology of HCC is an evolving concept which seems to be multifactorial, although the prime cause of HCC is mostly unknown. Long-persisting chronic liver disease, chronic hepatitis B, C and alcoholic liver disease are considered as the most influencing factors in the development of HCC.[3] The worldwide prevalence of HCC is non-uniform depending upon the burden of underlying liver diseases. China is the most affected country in the world, with the highest incidence rate of nearly 1%.[4] The prime reason for such a higher incidence rate in chronic hepatitis B, which contribute 40 to 90% to the HCC related malignancies.[5] The second most affected country in Africa, where chronic hepatitis B contributes to the higher HCC incidence rate. Among all the HCC reported cases, hepatitis infection is the primary cause of HCC along with alcoholism, which contributes nearly 45% cases in HCC. Currently, there is an increasing trend of HCC in the Low incidence regions like USA, France, Japan, Scotland, Australia, Italy. Among all the rising cases worldwide, hepatitis C is considered as the prime suspect.[6] Besides, to the other essential factors, the gender of the patient also influence the risk of development of HCC, currently available worldwide patient data indicates that males are accounting for a larger fraction of cases in HCC compared to the females.[7]

Several advancements in terms of surveillance, diagnosis and disease management of HCC has been made over the past decade, which resulted in decreased incidence rates of the disease. Although the HCC specific mortality rates remain very high. [8] Timely detection of HCC progression is still vital to improve disease outcomes. [9]. Development of HCC believed to be initiated with Chronic hepatitis leading to the liver cirrhosis. Increased proliferation of hepatocytes in the Cirrhotic livers develops regenerative nodules. These nodules vary in size and develop into HCC. For the detection of nodules under ultrasound (US), it should be minimum of 1 cm in size. Nodules larger than 1 cm should have radiologic investigation through CT or MRI imaging. The meta-analysis diagnostic data indicated better sensitivity of MRI compared to the CT for evaluating HCC. [10] In the case of equivocal results in radiologic tests; a different technique is used to reconfirm the presence of HCC. The malignancy of

HCC could be confirmed by measuring the HCC biomarker in the serum. The higher serum level (>400 ng/mL) of alpha-fetoprotein (AFP) indicates positive predictive value. [11].

The treatment of HCC is very diverse, which primarily depends upon the stage of HCC progression. The disease development of HCC is categorized depending upon its severity and spread. Barcelona clinic liver cancer (BCLC) staging uses a set of criteria for the treatment of HCC. This classification uses multiple variables viz; tumour stage, liver function, cancer-related symptoms and links multiple stages with a treatment algorithm. According to the BCLC staging, HCC is categorized in stage 0 (very early stage), stage A (early stage), stage B (intermediate stage), stage C (advanced stage) and stage D (End stage). In stage 0 and stage A, where the size of the nodule is <3cm with less than 3 numbers of nodules; tumour resection, liver transplant, and radiotherapy are the safest option to treat HCC with a highest 5year survival percentage. In stage B of the disease Chemoembolization, is the safest option with a higher survival rate. Stage C includes treatment with new chemo agents like sorafenib, Regorafenib while in stage D, there is only symptomatic treatment available. [12]

1.1 Transcatheter arterial chemoembolization (TACE)

Chemoembolization is an excellent treatment option in BCLC stage B. In Chemoembolization, a chemotherapeutic drug is given near the tumour site through the blood supply along with an embolizing agent, to block the blood flow into the tumour. This treatment is possible in the HCC due to the unique dual blood supply system of the liver. HCC receives its nutrition through the hepatic artery while normal liver cells receive blood through the portal vein. Therefore, embolizing the hepatic artery helps restrict the growth of HCC, however causing no effect on the growth of normal cells of the liver. This procedure of embolization is precisely known as TAE (Transarterial embolization). When chemotherapeutic drugs are given in addition to the embolization, TAE becomes TACE (Transarterial chemoembolization).[13] TACE is highly recommended in the patients of HCC with preserved liver function. While TACE is the first line treatment option for BCLC stage B, it is a highly effective option in patients with BCLC stage 0 and stages A, especially for the patients who are not suitable for surgical resection due to the location of the tumour or to bridge the time gap for the patients awaiting liver transplantation.[1] Today, TACE comes under minimally invasive image-guided therapies for HCC. Generally, there is no standard protocol for doing TACE, use of chemotherapeutic agents, its dosage, rate of injection,

choice of embolizing agent and optimal retreatment strategy are variable and depends on the physicians performing TACE.[14]. The number of TACE sessions highly depends on the response of the treatment and associated toxicity in the patients. In recent time, there are continuous efforts to improve the chemotherapeutic delivery in TACE procedure. Drug-eluting beads were designed to improve the localization of the drug inside the tumour, minimizing its systemic exposure to curb post-operative toxicities of the drug embolizing agent lipiodol [15, 16]. There are two different types of drug-eluting particles: polyvinyl alcohol microspheres and superabsorbent polymer microspheres. These particles provide sustained release of the drugs at the tumour site and restrict the growth of HCC. Currently, the common anticancer drug used in TACE is doxorubicin (36%), cisplatin (31%), epirubicin/doxorubicin (12%), mitoxantrone (8%) and mitomycin C (8%). Additionally, a chemical conjugate of a synthetic copolymer of styrene-maleic acid (SMA) and the proteinaceous anticancer agent neocarzinostatin (NCS) which are termed as SMANCS (5%) is also reported in TACE.[17]

1.2 Paclitaxel and Drug Nanocrystals

Paclitaxel (PTX) is a potent microtubule-stabilizing agent, which is one of the most effective and widely used drugs against several cancer types, including lung, ovarian, and breast cancer.[18] Despite its regular usage in cancer malignancies, so far there is little or no reported use of it in the TACE procedure. The prime reason could be the commercial formulation of PTX, which includes organic solvents polyoxyethylated castor oil (Cremophor EL) and dehydrated ethanol (1:1, v/v). These components are known to induce severe toxic effects including neurotoxicity, hypersensitivity, cardio-toxicity, anaphylaxis and nephrotoxicity. [19] To address this concern, there is the development of several alternative nanoplatforms like drug nanocrystals,[20] polymers, [21] and drug conjugates[22]. Among these several formulations, nanocrystals have shown tremendous development for the usage in the chemotherapy. Currently, there are numerous nanocrystal forms of poorly water-soluble drugs in advanced stages of clinical trials; few of them are available in the market. [23] The prime reason for such developmental form is the unique properties provided by the drug nanocrystals. Nanocrystals (NCs) are carrier free solid drug particles with at least one dimension in the nanometer scale. The most significant advantage of NCs is the nearly 100% drug loading potential, which makes it highly attractive in treating various types of diseases. [24] The high drug loading in NCs compared to other nanotherapeutic platforms provides an increased payload of the drug at the treatment site, which produced desirable pharmacological results. Nanocrystallization

of the drugs improves their bioavailability along with the pharmacokinetics, biodistribution and treatment efficacy [25] The nanosize of the drug allows increased dissolution pressure and dissolution rate which solve various problems associated with the drug solubility and release.

This work reports the synthesis of the nanocrystalline structural assembly of paclitaxel using an antisolvent precipitation method producing highly stable Cremophor EL®-free PTX formulations. Several studies on PTX nanocrystals have been carried out for the treatment of various cancer, which signifies its potential use in chemotherapy.[26, 27] Nanocrystal allow increased drug load at the treatment site, their extension into nanocrystalline assemblies could further enhance the drug payload at the tumour site and impart improved therapeutic effect. Additionally, the structure's uniqueness and size could allow embolization of the blood flow creating minimum hypoxia effect at the embolization site. These assemblies are designed for their introduction into the TACE procedures as potent TACE agents. The astral structural advantage of present drug formulation over currently available TACE formulation promises prolonged retention inside the tumour with minimum passive diffusion to the nearby healthy tissues. Current hierarchical self-assembled PTX structures closely resemble earlier reported structures [28], but the method of synthesis, morphology and development of inherent fluorescence property makes it a different structural entity. The simplicity of the method of synthesis allows structural integrity, uniformity and ease of scaleup during large scale production.

We hypothesize that paclitaxel nanocrystalline assemblies show higher retention in the tumour due to their unique astral structure, which imparts the highly desirable therapeutic effect in solid tumours. The synthesized nanomaterial could be utilized as a potent TACE agent to treat HCC.

2.0 Materials and Methods

2.1 Materials

Paclitaxel (PTX) was purchased from Clear synth. Sodium lauryl sulfate (SLS), Ethanol molecular grade was purchased from Merck. Glutaraldehyde 25% w/v solution, Dulbecco's Modified Eagle Medium (DMEM), streptomycin penicillin solution, Fetal Bovine Serum (FBS) and Trypsin EDTA were procured from HI-media. DAPI(4′,6-diamidino-2-phenylindole), Glycerol, and 12KD dialysis membrane were purchased from Sigma Aldrich.

Human liver carcinoma cell line (HepG2) was purchased from National Centre for Cell Science, Pune.

2.2 Synthesis of PTX nanocrystal assemblies

Paclitaxel nanocrystal assemblies were synthesized using the antisolvent precipitation method. Briefly, the paclitaxel powder form was dissolved in ethanol to prepare the concentration of 2mg/ml. The ethanolic solution of PTX was added dropwise to the antisolvent (water) at pH 7.4, maintaining the final solvent and antisolvent ratio of 3:7. During precipitation reaction, the system was continuously stirred to provide homogeneous conditions to the reaction. Once complete addition of PTX solution, the reaction was kept on stirring further for 15 min at 1000 rpm. After completion of the reaction period of 15 min., the glutaraldehyde solution of (1%) was slowly added to the reaction mixture and reaction was kept under continuous stirring for a period of 10 hrs. at 4°C. After completion of the process, the reaction mixture was purified by multiple washing of mil1liQ water and performing repeated centrifugation at 10000 g for 30min. Finally, the nanocrystalline assemblies were lyophilized and stored at 4°C for further use.

2.3 Characterization

The size of the Nanocrystalline assemblies of PTX was analyzed using Scanning electron microscopy (SEM). The PTX nanocrystalline assemblies were dispersed in water and air-dried onto the silicon wafer. The air-dried samples were sputter-coated with gold for 45 sec before performing SEM(JEOL) analysis at 10-20kV. The ethanolic solution of PTX was taken as the control to observe the morphological variation among structures. The fluorescence properties of the molecules were imaged using confocal microscopy. The water-dispersed solution was air-dried onto the glass coverslip before performing CLSM analysis. The fluorescence was observed in all three fluorescence channels, including DAPI, FITC and TRITC. Characterizing the crystallinity of newly formed PTX assemblies, X-ray diffractograms (XRD) were recorded on a Bruker powder XRD D8 X-ray diffractometer over 2θ range of 5°–40° using Cu Kα X-rays of wavelength 1.54 Å operated at 30 mA & 40 kV. The variation of the functional groups due to formation of Nanocrystals assemblies was analyzed by recording Fourier transform infrared (FTIR) spectra using Cary Agilent 660 IR spectrophotometer. The samples were mixed with potassium bromide, KBr pellets were

formed to record the spectra. The spectra were recorded by performing 256 scans at 4 cm^{-1} resolution over the range of 400–4000cm^{-1}.

2.4 1H NMR studies

The mechanism of formation of Nanocrystalline assemblies was studied using Proton (1H)-NMR studies. The reaction intermediates were collected at a different time interval and stored at 4°C for further analysis. The 1HNMR studies were carried out on anhydrous PTX (P1), reaction intermediates (P2 and P3) and PTX astral assemblies (P4) respectively. The samples under investigation were dissolved in D-6 DMSO and spectra were recorded using Bruker Av III HD at 400 MHz and 25 °C. The chemical shift values of components are reported in ppm scale using tetramethyl silane (TMS) as an internal standard.

2.5 *In-vitro* drug release studies

In vitro, drug release studies of PTX nano assemblies were performed in PBS pH 7.4 using 12KD cut-off dialysis membrane. A fixed amount of one mg of PTX and PTX nano-assemblies were weighed separately and suspended in 1 ml of PBS solution containing 0.1% of SLS. The Drug release was analyzed in 20ml of 1X PBS solution at 37° C with continuous stirring at 150 rpm. One ml sample was drawn at different time intervals, and the sink was replaced with the same volume release medium. The aliquots were analyzed using UV-Vis spectrophotometer after preparing a standard curve of PTX in methanol.

2.6 Spheroid generation, uptake studies and therapeutic efficacy of Nanocrystalline assemblies

The 3D Spheroids was generated using a hanging drop culture technique. Briefly, HepG2 cells were cultured in DMEM media supplemented with 10% FBS maintaining 2000 cells per hanging drop. After 7 days of culture at 37°C and 5% CO_2, the cells were developed into 3D spheroids. The development of spheroids was observed under a brightfield microscope for intactness and morphology. The spheroids were collected and further cultured in 48 well plates with minimum orbital shaking at 37°C and 5% CO_2. The delivery of Nanocrystalline assemblies in spheroids was observed along with monitoring the therapeutic potential. The spheroids were treated with a clinically relevant concentration of PTX (10nM), and time-lapse images were captured to monitor the growth patterns. The spheroid uptake of assemblies was further verified using SEM imaging of the nano assemblies treated spheroids.

Briefly, 5-day treated HepG2 spheroids were taken for uptake studies. The treated spheroids were washed 3-4 times with chilled PBS and fixed overnight in paraformaldehyde at 4° C. After overnight fixation the spheroids were washed three times with chilled PBS and subsequently treated with gradient series of ethanol. The spheroids were fractured to expose the internal morphology and presence of PTX astral assemblies. Finally, the spheroids were sputter-coated with gold and imaged at 10kV. The delivery of PTX nanocrystalline assemblies in spheroid was also verified using confocal imaging. Briefly, seven-day old HepG2 spheroids were seeded in 24-well plates and incubated with PTX nanocrystalline assemblies for 6 hrs. After completion of the treatment, spheroids were washed three times with chilled PBS and fixed using 4% formaldehyde for 30 min at 4°C. Multiple washing was performed after fixation to remove extra fixative. Spheroids were mounted on glass slides using 90% glycerol and coverslip. Control spheroids were stained with DAPI nuclear stain before mounting to the glass slides.

2.7 Statistical analysis

Statistical analyses were accomplished using the Origin 8.5 software (serial number GF3S4-9089-7123456). The data were statistically analyzed using a one-way analysis of variance (ANOVA) at $p < 0.01$ level of significance.

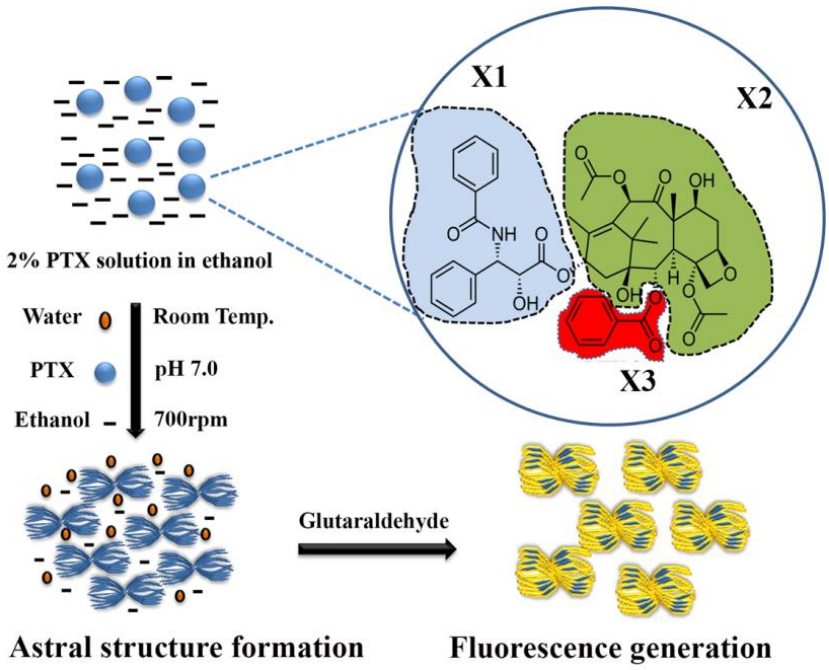

Scheme 1. General procedure of PTX astral structure synthesis from PTX solution and fluorescence generation after glutaraldehyde mediated crosslinking. X1, X2 and X3 represent different structural parts of paclitaxel molecule

3.0 Result and Discussion

3.1 Synthesis and Characterization of Nanocrystalline assemblies

The mechanism of formation of Nanocrystalline nano assemblies was studied by analyzing the molecular structure of PTX. Depending upon the presence and nature of various functional groups, PTX molecular structure is divided into three parts (Fig 1), among which X1 part of the molecule believed to constitute the core of the fibre structure of PTX due to the high repulsive forces between X2 and X3.[29] Surprisingly no further report on the self-assembly of these PTX fibres is available. The prime reason for the formation of PTX nanocrystalline self-assemblies is the presence of particular stereochemistry of the PTX molecule. The key feature lies in the structure of PTX itself due to its impressive molecular arrangement. The general procedure of supramolecular synthesis for the self-assembly of PTX molecules through antisolvent precipitation method is well described in scheme 1. The Scanning electron microscopy and confocal microscopy results revealed the morphology of air-dried samples of self-assembled PTX structures, which form long astral-like assembly with the multichannel fluorescence emission.

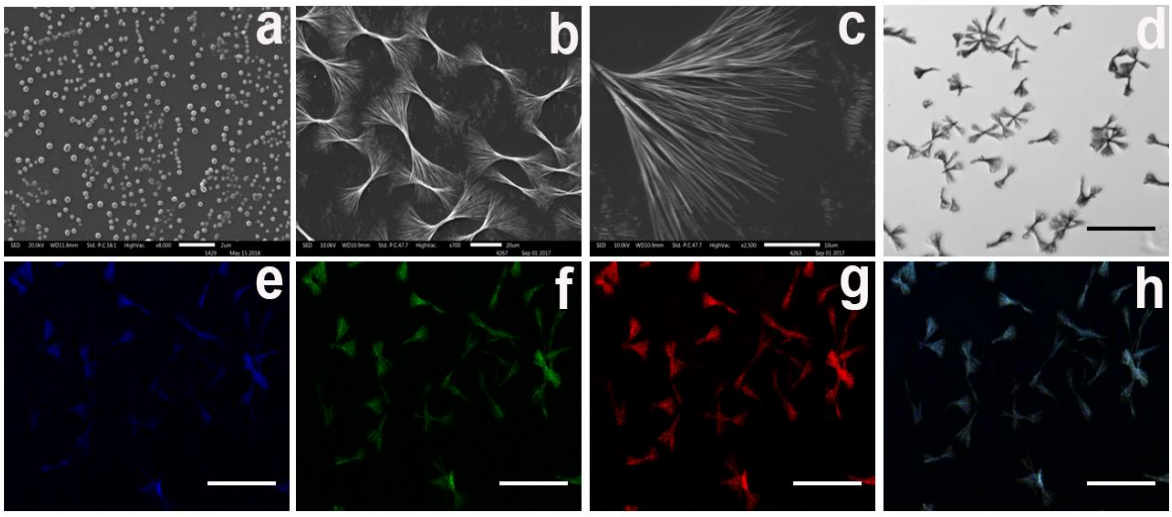

Fig.2. SEM image of air-dried paclitaxel solution (scale bar:2µm, x8000) (a), PTX astral structure (scale bar :20µm, x700) (b), filaments of PTX astral structure (scale bar: 10µm, x2500) (c), bright field image of PTX astral structure (scale bar:80µm) (d) fluorescence confocal images of PTX astral structure in blue channel (e) green channel (f) red channel (g) merged image (scale bar: 40µm) (h).

The dimensions of the astral structure were recorded to be ~20µm in diameter, and ~40µm in length. At the same time, the individual fibre was ~200 nm in diameter. The ethanolic solution of PTX gives a circular morphology (Fig.2) with a diameter of approximately 200

nm. The orientation of the PTX molecule is well projected and established in the presence of water and organic solvent. It was computationally predicted and shown that PTX molecules self-assemble into long ribbon-like or hollow fibrous structures in the presence of water and organic solvent. [29] There are several variables in the reaction mixture which favourably affect the self-assembly process of PTX nanocrystals. Among these variables, the concentration of PTX and solvent to antisolvent ratio was found very crucial. The morphological variations were observed in the PTX nanocrystalline assemblies while changing the concentration of PTX. This observation is in complete agreement with the earlier reports where similar morphology is reported in the presence of copolymers.[28] We have found that the nanocrystalline assemblies are achieved at the PTX concentration of 2mg/ml. Altering the solvent: antisolvent ratio may affect the morphology of the assemblies. The SEM result of various samples with variable ratio showed morphological variation (Fig. 3a, b).

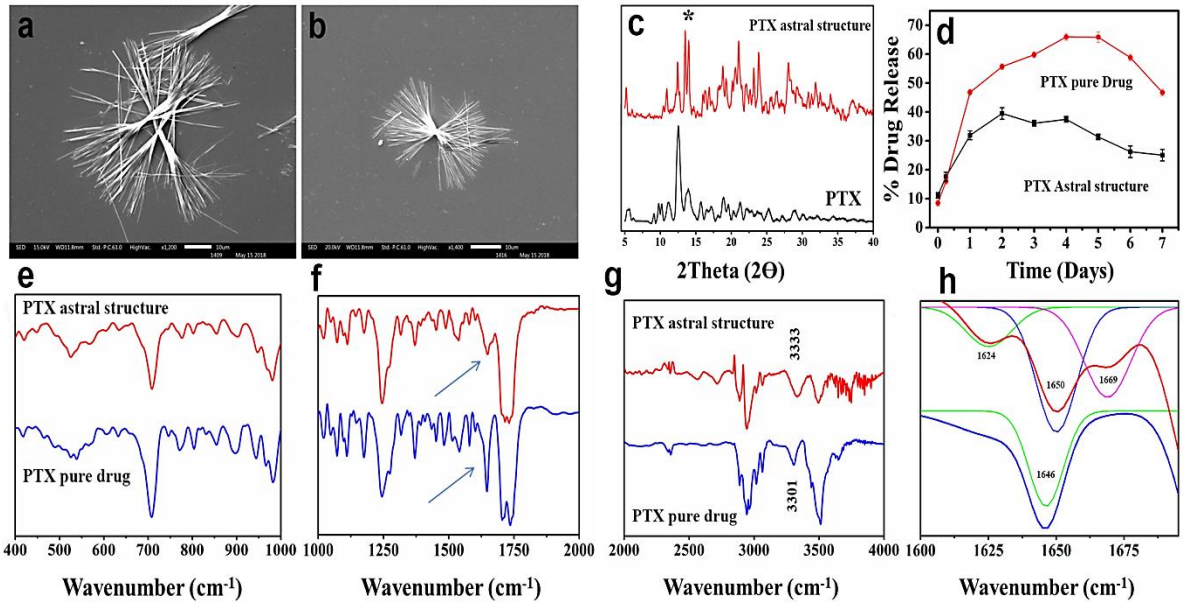

Fig. 3. SEM image of PTX astral structure prepared in solvent : antisolvent ration (3:7) scale bar:10µm, x1200(a) ratio (3:9), scale bar: 1010µm, x1400 (b) powder X-Ray diffraction (PXRD) of PTX microstructure and PTX Drug(c) Invitro percent drug release profile of PTX Astral structure and PTX drug (d) FTIR analysis of PTX astral structure and PTX pure drug showing various region of spectra from 400-1000cm^{-1} (e) 1000-2000 cm^{-1} (f) 2000-4000 cm^{-1} (g) deconvoluted peaks of 1620-1695 cm^{-1} marked as two arrows in figure f, showing N-H stretching at 1646 cm^{-1} and C=O stretching at 1669cm^{-1}(h) .

The decrease in the solvent: antisolvent ratio from 3:7 to 3:9 resulted in the overall size reduction of the molecule. This size reduction reduced the central stalk and increased the number of fibres. In the supernatant, no significant appearance of PTX nanoparticles was

observed, clearly predicting the complete conversion of the pure PTX drug into the nanocrystalline assemblies. The PTX molecules are very reactive, which is known to interact among each other and the microenvironment surrounding the solvent ions. The PTX molecules form an extensive network of inter and intramolecular hydrogen bonding.[30] To further validate the process of self-assemblies during the formation of nanocrystals, we have performed the 1HNMR studies of several reaction intermediates.

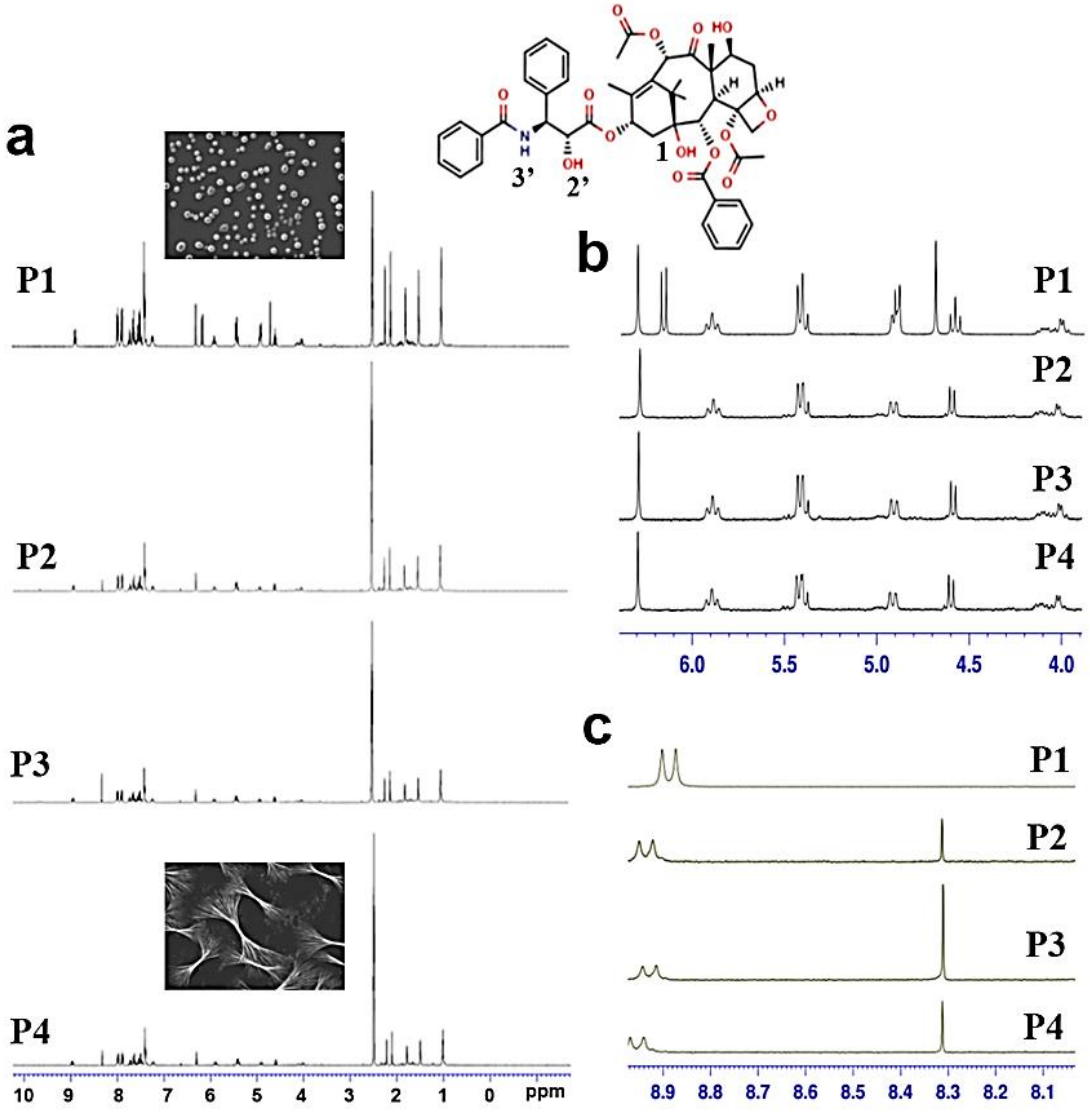

Fig.4 1H NMR spectra of paclitaxel (P1), reaction intermediates (P2, P3), astral structure (P4) in DMSO solvent (a) enlarged view from chemical shift 4.0 to 6.5 (b) enlarged view from chemical shift 8.1 to 9.0 (c).

The results of 1HNMR presented significant changes in the values of the chemical shift of reaction intermediates (P2, P3) of nanocrystalline assemblies and reaction product (P4) compared to the parent drug molecule (P1). Alteration in chemical shift values could be of

significant importance in predicting the environment of the proton atoms that are contributing to the information of self-assembly of the molecule during synthesis. Fig. 4 shows the 1H NMR spectra of PTX in D6-DMSO at 298K for P1, P2, P3 and P4 respectively. Significant changes in the chemical shift values were observed at 4.69 ppm 6.16 ppm and 8.89 ppm assigned to the proton involvement of OH1, OH2'and 3'NH moieties. The proton peaks at 4.69 ppm and 6.16 ppm of OH1 and OH2' moieties were found missing in case of the reaction intermediates (P2, P3) and final product of PTX self-assembled structure (P4). It could be speculated that the OH of C2' and C1 position of P1 might be involved in glutaraldehyde mediated cross-linking. The Appearance of the additional peak at 8.310 ppm further validates our hypothesis. The downfield shift of 3'NH from 8.89 to 8.94 in P3 and 8.96 in case of P4 specifies structural alteration, associated with intermolecular hydrogen bonding.[31] This alteration in chemical shift values strongly indicates the presence of intermolecular hydrogen bonding as a significant factor contributing to the nanocrystalline assembly formation of PTX.

The current method of synthesis utilizes glutaraldehyde as a crosslinking agent to stabilize the assemblies, which could have further provided the unique fluorescence properties to the molecule. In the current synthesis, fluorescence property of the self-assembled structure of PTX could be attributed to the electronic transitions such as π-π^* transition of C=C bond and n-π^* transition of the partial double bond characteristic of C=N bond associated with amide bonding.[32] Interestingly, we have found that the fluorescence property of structure is lost in the absence of the glutaraldehyde, signifying the importance of the molecule in the fluorescence generation. PTX nanocrystal doped with fluorescent guest molecules has been used earlier for the delivery and imaging application.[33] External introduction of fluorescence guest molecule into the structures, through ionic and physical adsorption method, makes it vulnerable to leaching process, thereby reducing the efficacy of the method. In the current synthesis method, no external fluorescent molecule is introduced to the structure which nullifies the leaching phenomenon. The fluorescent property is the inbuilt character of the molecule.

We have studied the crystal structure of the PTX molecule and nanocrystalline self-assemblies using powder XRD. The X-ray diffraction (XRD) patterns of PTX nanocrystalline assembly and pure PTX were recorded to study the crystal state of PTX. As shown in Fig. 3c, pure PTX shows prominent peaks at 2θ value of 5.22, 12.58 and 13.93 respectively, which

are in coherence to the peaks present in PTX astral structure. The 13.93 2θ peak of PTX astral structure is split into two, thereby indicating the hydrated form of the PTX crystal. No further significant changes were observed in the XRD pattern of both the structures. This depicts the negligible difference in the crystalline arrangement of PTX, thus confirming the molecular integrity of the PTX molecule during synthesis.

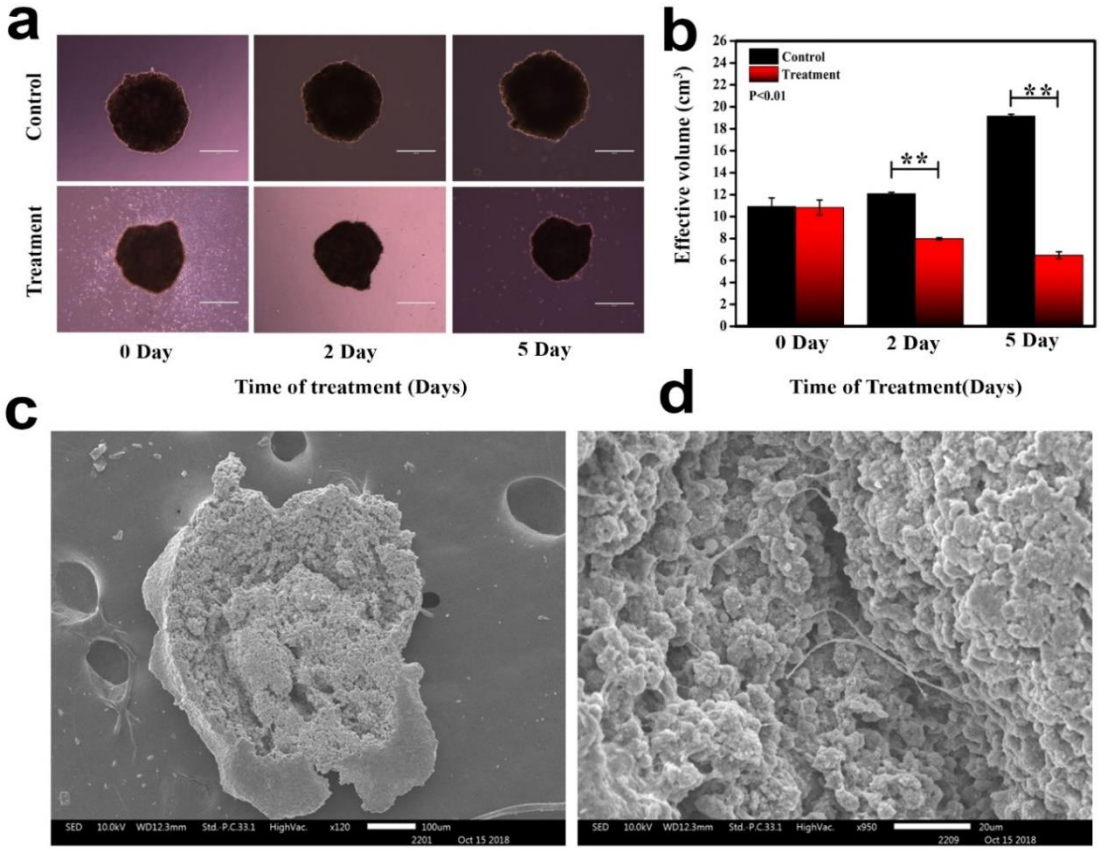

Fig.5. Time dependent brightfield images of Control (treated with PBS) and treatment (PTX astral assemblies) (a) quantification of effective volume change (b) SEM images of treated spheroid; scale bar :100µm, x120 (c) PTX astral structure inside spheroid; scale bar: 20 µm, x950 (d).

The change in functional groups of pure PTX during self-assembly was studied using FTIR spectrophotometer. FTIR spectra of pure PTX and PTX nanocrystalline assemblies (Fig. 3e-h) was recorded to analyze further the possible mechanism associated with the formation of such unique structures. IR spectra of PTX and PTX astral structure presented a strong peak at 1646 cm^{-1} which could be assigned to C=O stretching vibration of amide bonding (-CONH-) present in PTX. The presence of 1624cm^{-1} and 1669 cm^{-1} peaks could be accounted to the N-H stretching and C=O stretching respectively in the PTX astral structure. The region from 2900-3000 cm^{-1} represents the sp^3 hybridized C-H bonds, while the region from 3000-3100 cm^{-1} predicts the presence of sp^2 hybridized C-H bonds in the case of PTX and PTX astral

structure respectively. PTX pure drug shows sharp peaks at 3300 cm^{-1} and 3500 $cm^{-1,}$ which could be due to the presence of N-H stretching and O-H stretching respectively. The PTX astral structure also presents a broad peak of hydrogen-bonded O-H at 3333 cm^{-1} and free O-H at 3500 cm^{-1} respectively. This interaction indicated the remarkable role of hydrogen bonding in the formation of this unique assembly.

3.2 In vitro studies

The Drug nanocrystals are known to provide sustained release of the drug compared to its bulk form. We have studied the *in-vitro* release pattern of PTX nanocrystalline nano assemblies along with the bulk form of pure PTX drug. The drug release profile indicated sustained drug release from the nanocrystalline nano assemblies (Fig. 3d). This difference in the drug release profile could be attributed to the hydrated form of PTX, which further supported our notion of sequestration of drug nanocrystal into one assembly. This could assist in the slow release of the drug and further help in providing increased payload at the

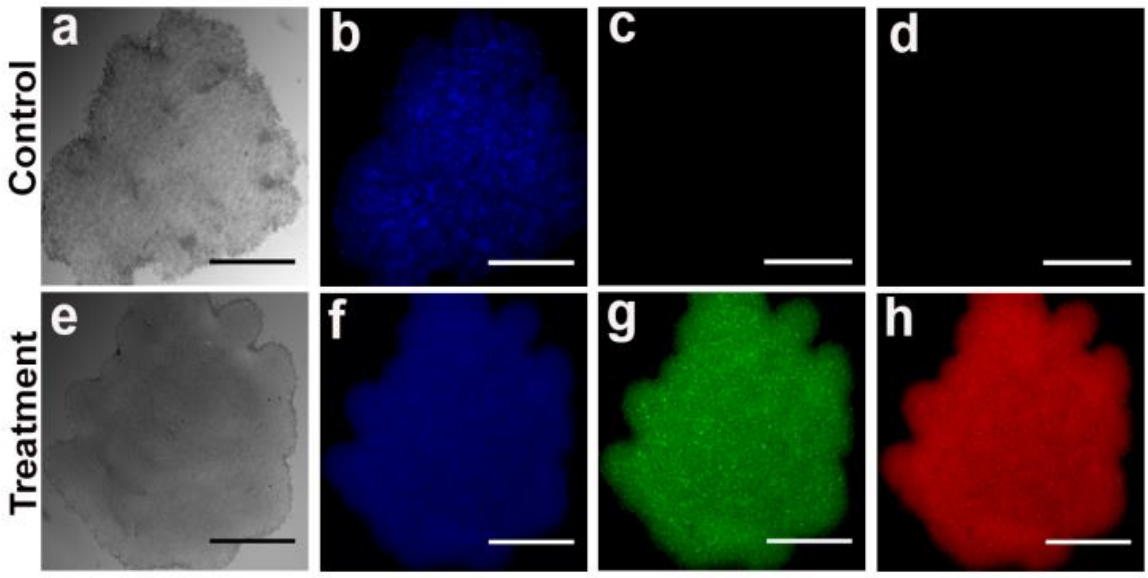

Fig. 6. Confocal images of Control HepG2 spheroids stained with DAPI in brightfield channel (a), DAPI channel (b), FITC channel (c), TRITC channel (d), PTX astral structure treated HepG2 spheroids without DAPI staining in bright field (e), DAPI channel (f), FITC channel (g), TRITC channel (h). All images showing scale bar of 200micron. (Note: The fluorescence in Treatment group (f, g, h) is due to the autofluorescence property of PTX astral assemblies penetrated inside the spheroids)

administration site with minimal dispersion to the surrounding. PTX has been successfully used independently or in combination with other chemotherapeutic drugs in systemic deliveries to treat HCC.[34, 35] Although, its use in local delivery therapies like TACE is not

much explored. Currently, PTX is in Phase I/II clinical trial (NCT03812874) in patients with non-resectable hepatocellular carcinoma following TACE treatment.

In the current study therapeutic efficacy of the PTX nanocrystalline assemblies was evaluated in 3D spheroids model of HepG2 cell. 3D spheroid culture could provide a better therapeutic reality of molecules in comparison to the 2D monolayer model. The therapeutic response of the PTX nanocrystalline assemblies at a clinically significant dose of 10nM for 5 days, is shown in Fig. 5a, b. The Spheroid volume started reducing significantly from the 3rd day of treatment which improved further till the 5th day. The significant reduction in spheroid volume when compared to the control validates the therapeutic efficacy of the molecule in complex systems like solid tumours. SEM images of PTX astral structure treated spheroid (Fig. 5c, d) further confirms the presence of the PTX assembly inside the spheroid on the 5th day of treatment, which justify the structural advantage associated with the astral structure of PTX in enhancing the accumulation of molecules inside the tumour during treatment. Fluorescence-based imaging abilities of the astral assemblies of PTX were further explored after treating the 3D spheroid cultures of HepG2 liver carcinoma cell line (Fig. 6). The

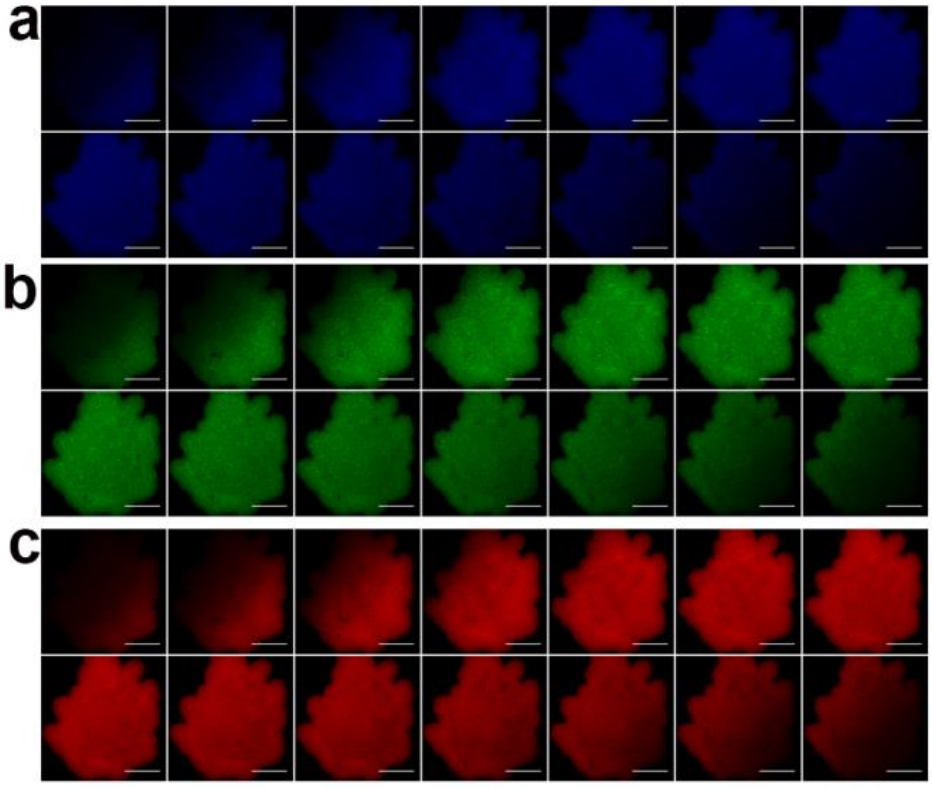

Fig 7. Z stack confocal images of astral PTX structure treated spheroids in DAPI (a) FITC (b) TRITC (c) channel. All images showing scale bar of 200 micron.

nucleus of the control HepG2 spheroids was stained using DAPI, while there was no fluorescent dye used in PTX astral structure treated spheroids. Confocal z stack images (Fig. 7) affirmed the in-depth distribution of fluorescence in spheroids. This event could strengthen the significance of using PTX astral assemblies in TACE as it could allow anatomical fluorescence imaging in various surgical complications.

4.0 Conclusion

In summary, we have synthesized a nanoscale hierarchical PTX astral structure through nanoprecipitation and self-assembly approach. The unique morphology of the nanocrystalline assemblies could be readily utilized for enhanced penetrance effect and localized application in solid tumours to overcome MDR and systemic toxicity related problems (scheme 2). The simple synthetic approach, fluorescence ability, higher therapeutic efficacy in the solid tumour, longer retention time at the tumour site and cent per cent loading makes it promising in its category of localized implantable chemotherapeutics. It could provide a structural advantage to the TACE procedures and can help in advancement against several disadvantages like MDR, hypoxia, and tumour recurrence.

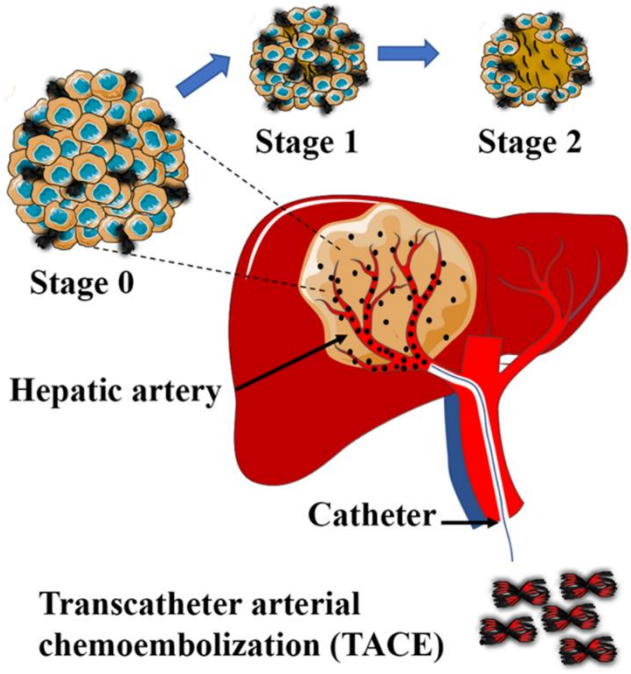

Scheme 2. Transcatheter arterial chemoembolization (TACE) therapy using PTX astral structures showing different stages of recovery in Hepatocellular carcinoma post TACE procedure

5.0 References

1. Clavien, P. A.; Lesurtel, M.; Bossuyt, P. M.; Gores, G. J.; Langer, B.; Perrier, A.; Group, O. L. T. f. H. C., Recommendations for liver transplantation for hepatocellular carcinoma: an international consensus conference report. *The Lancet. Oncology* **2012,** *13* (1), e11-22.
2. Perz, J. F.; Armstrong, G. L.; Farrington, L. A.; Hutin, Y. J.; Bell, B. P., The contributions of hepatitis B virus and hepatitis C virus infections to cirrhosis and primary liver cancer worldwide. *Journal of hepatology* **2006,** *45* (4), 529-38.
3. Farazi, P. A.; DePinho, R. A., Hepatocellular carcinoma pathogenesis: from genes to environment. *Nature reviews. Cancer* **2006,** *6* (9), 674-87.
4. Parkin, D. M.; Bray, F.; Ferlay, J.; Pisani, P., Estimating the world cancer burden: Globocan 2000. *International journal of cancer* **2001,** *94* (2), 153-6.
5. Bosch, F. X.; Ribes, J.; Diaz, M.; Cleries, R., Primary liver cancer: worldwide incidence and trends. *Gastroenterology* **2004,** *127* (5 Suppl 1), S5-S16.
6. McGlynn, K. A.; Tsao, L.; Hsing, A. W.; Devesa, S. S.; Fraumeni, J. F., Jr., International trends and patterns of primary liver cancer. *International journal of cancer* **2001,** *94* (2), 290-6.
7. Sherman, M., Hepatocellular carcinoma: epidemiology, risk factors, and screening. *Seminars in liver disease* **2005,** *25* (2), 143-54.
8. Global Burden of Disease Cancer, C.; Fitzmaurice, C.; Allen, C.; Barber, R. M.; Barregard, L.; Bhutta, Z. A.; Brenner, H.; Dicker, D. J.; Chimed-Orchir, O.; Dandona, R.; Dandona, L.; Fleming, T.; Forouzanfar, M. H.; Hancock, J.; Hay, R. J.; Hunter-Merrill, R.; Huynh, C.; Hosgood, H. D.; Johnson, C. O.; Jonas, J. B.; Khubchandani, J.; Kumar, G. A.; Kutz, M.; Lan, Q.; Larson, H. J.; Liang, X.; Lim, S. S.; Lopez, A. D.; MacIntyre, M. F.; Marczak, L.; Marquez, N.; Mokdad, A. H.; Pinho, C.; Pourmalek, F.; Salomon, J. A.; Sanabria, J. R.; Sandar, L.; Sartorius, B.; Schwartz, S. M.; Shackelford, K. A.; Shibuya, K.; Stanaway, J.; Steiner, C.; Sun, J.; Takahashi, K.; Vollset, S. E.; Vos, T.; Wagner, J. A.; Wang, H.; Westerman, R.; Zeeb, H.; Zoeckler, L.; Abd-Allah, F.; Ahmed, M. B.; Alabed, S.; Alam, N. K.; Aldhahri, S. F.; Alem, G.; Alemayohu, M. A.; Ali, R.; Al-Raddadi, R.; Amare, A.; Amoako, Y.; Artaman, A.; Asayesh, H.; Atnafu, N.; Awasthi, A.; Saleem, H. B.; Barac, A.; Bedi, N.; Bensenor, I.; Berhane, A.; Bernabe, E.; Betsu, B.; Binagwaho, A.; Boneya, D.; Campos-Nonato, I.; Castaneda-Orjuela, C.; Catala-Lopez, F.; Chiang, P.; Chibueze, C.; Chitheer, A.; Choi, J. Y.; Cowie, B.; Damtew, S.; das Neves, J.; Dey, S.; Dharmaratne, S.; Dhillon, P.; Ding, E.; Driscoll, T.; Ekwueme, D.; Endries, A. Y.; Farvid, M.; Farzadfar, F.; Fernandes, J.; Fischer, F.; TT, G. H.; Gebru, A.; Gopalani, S.; Hailu, A.; Horino, M.; Horita, N.; Husseini, A.; Huybrechts, I.; Inoue, M.; Islami, F.; Jakovljevic, M.; James, S.; Javanbakht, M.; Jee, S. H.; Kasaeian, A.; Kedir, M. S.; Khader, Y. S.; Khang, Y. H.; Kim, D.; Leigh, J.; Linn, S.; Lunevicius, R.; El Razek, H. M. A.; Malekzadeh, R.; Malta, D. C.; Marcenes, W.; Markos, D.; Melaku, Y. A.; Meles, K. G.; Mendoza, W.; Mengiste, D. T.; Meretoja, T. J.; Miller, T. R.; Mohammad, K. A.; Mohammadi, A.; Mohammed, S.; Moradi-Lakeh, M.; Nagel, G.; Nand, D.; Le Nguyen, Q.; Nolte, S.; Ogbo, F. A.; Oladimeji, K. E.; Oren, E.; Pa, M.; Park, E. K.; Pereira, D. M.; Plass, D.; Qorbani, M.; Radfar, A.; Rafay, A.; Rahman, M.; Rana, S. M.; Soreide, K.; Satpathy, M.; Sawhney, M.; Sepanlou, S. G.; Shaikh, M. A.; She, J.; Shiue, I.; Shore, H. R.; Shrime, M. G.; So, S.; Soneji, S.; Stathopoulou, V.; Stroumpoulis, K.; Sufiyan, M. B.; Sykes, B. L.; Tabares-Seisdedos, R.; Tadese, F.; Tedla, B. A.; Tessema, G. A.; Thakur, J. S.; Tran, B. X.; Ukwaja, K. N.; Uzochukwu, B. S. C.; Vlassov, V. V.; Weiderpass, E.; Wubshet Terefe, M.; Yebyo, H. G.; Yimam, H. H.; Yonemoto, N.; Younis, M. Z.; Yu, C.; Zaidi, Z.; Zaki, M. E. S.;

Zenebe, Z. M.; Murray, C. J. L.; Naghavi, M., Global, Regional, and National Cancer Incidence, Mortality, Years of Life Lost, Years Lived With Disability, and Disability-Adjusted Life-years for 32 Cancer Groups, 1990 to 2015: A Systematic Analysis for the Global Burden of Disease Study. *JAMA oncology* **2017,** *3* (4), 524-548.

9. Yang, J. D.; Harmsen, W. S.; Slettedahl, S. W.; Chaiteerakij, R.; Enders, F. T.; Therneau, T. M.; Orsini, L.; Kim, W. R.; Roberts, L. R., Factors that affect risk for hepatocellular carcinoma and effects of surveillance. *Clinical gastroenterology and hepatology : the official clinical practice journal of the American Gastroenterological Association* **2011,** *9* (7), 617-23 e1.
10. Lee, Y. J.; Lee, J. M.; Lee, J. S.; Lee, H. Y.; Park, B. H.; Kim, Y. H.; Han, J. K.; Choi, B. I., Hepatocellular carcinoma: diagnostic performance of multidetector CT and MR imaging-a systematic review and meta-analysis. *Radiology* **2015,** *275* (1), 97-109.
11. El-Serag, H. B., Hepatocellular carcinoma. *The New England journal of medicine* **2011,** *365* (12), 1118-27.
12. Llovet, J. M.; Burroughs, A.; Bruix, J., Hepatocellular carcinoma. *Lancet* **2003,** *362* (9399), 1907-17.
13. Liapi, E.; Geschwind, J. F., Chemoembolization for primary and metastatic liver cancer. *Cancer journal* **2010,** *16* (2), 156-62.
14. Paul, S. B.; Gamanagatti, S.; Sreenivas, V.; Chandrashekhara, S. H.; Mukund, A.; Gulati, M. S.; Gupta, A. K.; Acharya, S. K., Trans-arterial chemoembolization (TACE) in patients with unresectable Hepatocellular carcinoma: Experience from a tertiary care centre in India. *Indian J Radiol Imaging* **2011,** *21* (2), 113-20.
15. Tam, K. Y.; Leung, K. C.; Wang, Y. X., Chemoembolization agents for cancer treatment. *European journal of pharmaceutical sciences : official journal of the European Federation for Pharmaceutical Sciences* **2011,** *44* (1-2), 1-10.
16. Hsu, K. F.; Chu, C. H.; Chan, D. C.; Yu, J. C.; Shih, M. L.; Hsieh, H. F.; Hsieh, T. Y.; Yu, C. Y.; Hsieh, C. B., Superselective transarterial Chemoembolization vs hepatic resection for resectable early-stage hepatocellular carcinoma in patients with Child-Pugh class a liver function. *European journal of radiology* **2012,** *81* (3), 466-71.
17. Llovet, J. M.; Bruix, J., Systematic review of randomized trials for unresectable hepatocellular carcinoma: Chemoembolization improves survival. *Hepatology* **2003,** *37* (2), 429-42.
18. Jordan, M. A.; Wilson, L., Microtubules as a target for anticancer drugs. *Nature reviews. Cancer* **2004,** *4* (4), 253-65.
19. Walker, F. E., Paclitaxel (TAXOL): side effects and patient education issues. *Semin Oncol Nurs* **1993,** *9* (4 Suppl 2), 6-10.
20. Lu, Y.; Wang, Z. H.; Li, T.; McNally, H.; Park, K.; Sturek, M., Development and evaluation of transferrin-stabilized paclitaxel nanocrystal formulation. *Journal of controlled release : official journal of the Controlled Release Society* **2014,** *176*, 76-85.
21. Gawde, K. A.; Sau, S.; Tatiparti, K.; Kashaw, S. K.; Mehrmohammadi, M.; Azmi, A. S.; Iyer, A. K., Paclitaxel and di-fluorinated curcumin loaded in albumin nanoparticles for targeted synergistic combination therapy of ovarian and cervical cancers. *Colloids and surfaces. B, Biointerfaces* **2018,** *167*, 8-19.
22. Zhang, D.; Zhang, J.; Li, Q.; Tian, H.; Zhang, N.; Li, Z.; Luan, Y., pH- and Enzyme-Sensitive IR820-Paclitaxel Conjugate Self-Assembled Nanovehicles for Near-Infrared Fluorescence Imaging-Guided Chemo-Photothermal Therapy. *ACS applied materials & interfaces* **2018,** *10* (36), 30092-30102.
23. Junghanns, J. U.; Muller, R. H., Nanocrystal technology, drug delivery and clinical applications. *International journal of nanomedicine* **2008,** *3* (3), 295-309.

24. Lu, Y.; Chen, Y.; Gemeinhart, R. A.; Wu, W.; Li, T., Developing nanocrystals for cancer treatment. *Nanomedicine (Lond)* **2015,** *10* (16), 2537-52.
25. Jacob, S.; Nair, A. B.; Shah, J., Emerging role of nanosuspensions in drug delivery systems. *Biomaterials research* **2020,** *24*, 3.
26. Wei, L.; Ji, Y.; Gong, W.; Kang, Z.; Meng, M.; Zheng, A.; Zhang, X.; Sun, J., Preparation, physical characterization and pharmacokinetic study of paclitaxel nanocrystals. *Drug development and industrial pharmacy* **2015,** *41* (8), 1343-52.
27. Zhang, H.; Hu, H.; Zhang, H.; Dai, W.; Wang, X.; Wang, X.; Zhang, Q., Effects of PEGylated paclitaxel nanocrystals on breast cancer and its lung metastasis. *Nanoscale* **2015,** *7* (24), 10790-800.
28. Tan, J. P.; Kim, S. H.; Nederberg, F.; Appel, E. A.; Waymouth, R. M.; Zhang, Y.; Hedrick, J. L.; Yang, Y. Y., Hierarchical supermolecular structures for sustained drug release. *Small* **2009,** *5* (13), 1504-7.
29. Guo, X. D.; Tan, J. P.; Kim, S. H.; Zhang, L. J.; Zhang, Y.; Hedrick, J. L.; Yang, Y. Y.; Qian, Y., Computational studies on self-assembled paclitaxel structures: templates for hierarchical block copolymer assemblies and sustained drug release. *Biomaterials* **2009,** *30* (33), 6556-63.
30. Mastropaolo, D.; Camerman, A.; Luo, Y.; Brayer, G. D.; Camerman, N., Crystal and molecular structure of paclitaxel (taxol). *Proceedings of the National Academy of Sciences of the United States of America* **1995,** *92* (15), 6920-4.
31. Balasubramanian, S. V.; Alderfer, J. L.; Straubinger, R. M., Solvent- and concentration-dependent molecular interactions of taxol (Paclitaxel). *Journal of pharmaceutical sciences* **1994,** *83* (10), 1470-6.
32. Ma, X.; Sun, X.; Hargrove, D.; Chen, J.; Song, D.; Dong, Q.; Lu, X.; Fan, T. H.; Fu, Y.; Lei, Y., A Biocompatible and Biodegradable Protein Hydrogel with Green and Red Autofluorescence: Preparation, Characterization and In Vivo Biodegradation Tracking and Modeling. *Scientific reports* **2016,** *6*, 19370.
33. Zhao, R.; Hollis, C. P.; Zhang, H.; Sun, L.; Gemeinhart, R. A.; Li, T., Hybrid nanocrystals: achieving concurrent therapeutic and bioimaging functionalities toward solid tumors. *Molecular pharmaceutics* **2011,** *8* (5), 1985-91.
34. Chen, L.; Liu, Y.; Wang, W.; Liu, K., Effect of integrin receptor-targeted liposomal paclitaxel for hepatocellular carcinoma targeting and therapy. *Oncology letters* **2015,** *10* (1), 77-84.
35. Jin, C.; Li, H.; He, Y.; He, M.; Bai, L.; Cao, Y.; Song, W.; Dou, K., Combination chemotherapy of doxorubicin and paclitaxel for hepatocellular carcinoma in vitro and in vivo. *Journal of cancer research and clinical oncology* **2010,** *136* (2), 267-74.

Note

- The due permission has been obtained from authors and corresponding author of the following published paper before adopting in the present thesis.

- **Dev, A**.; Sood, A.; Choudhury, S. R.; Karmakar, S., Paclitaxel nanocrystalline assemblies as a potential transcatheter arterial chemoembolization (TACE) candidate for unresectable hepatocellular carcinoma. Materials science & engineering. C, Materials for biological applications 2020, 107, 110315.

Summary

In summary, we have developed several nanotherapeutic platforms to address multiple challenges in cancer therapeutics. The emphasis was given on solid cancers due to their physiological variability and several treatment complications. We have further addressed the post-cancer treatment issues like impaired wound healing by preparing an injectable hydrogel matrix which significantly accelerates wound healing. The nanoformulation was developed using several albumin proteins as a carrier matrix, to improve the low water solubility of highly potent chemotherapeutic drugs like Curcumin, 4HPR, and Genistein. In addition to the nanocarrier based formulations of the poorly water-soluble drugs, we have developed a nanocarrier free nanocrystal-based formulation of another very potent chemotherapeutic drug paclitaxel. We have targeted Glioblastoma cancer stem cells using curcumin loaded nanoparticles and blue light therapy. The synthesized curcumin loaded BSANPs have significantly improved the curcumin's specific solubility, which helped in the better therapeutic response against cancer stem cells. The addition of blue light has further improved the therapeutic potential of the nanocurcumin. This study shows a potential treatment option, which could be utilized at the time gap of glioma resection and onset of adjuvant chemoradiotherapy. Curcumin-loaded BSANs formulation combined with blue light phototherapy could provide prolonged prevention towards a recurrence of the tumour through diminishing tumour stem cells. The CNS cancer like Glioblastoma multiforme is tough to treat through systemic administration of the chemotherapeutic drugs due to blood-brain barriers. The local therapy does provide certain advantages and help address the aggressiveness of the tumour. The currently developed nanocurcumin formulation could be a preferred choice as a local drug delivery approach in treating Glioblastoma. The next target of the research work was to address extracranial tumours like paediatric Neuroblastoma. Neuroblastoma (NB) is a highly invasive and metastatic phenotype of extracranial cancer, which usually originates in the neural crest at the time of embryogenesis and metastasizes to the adrenal gland and other peripheral ganglions. We have developed human serum albumin-based nanoformulation of highly potent drug 4HPR, which is highly recommended for NB treatment in recent time.

Although its low water solubility deteriorates the therapeutic efficacy of the molecule, even at low doses it restricts the growth of a highly metastatic form of NB. The 4HPR allows differentiation of the NB cancer cells and induce apoptosis at comparatively higher doses.

Here we have prepared 4HPR loaded HSA nanoformulation to improve its bioavailability during the treatment and prepare an acetyl variant of the same nanoformulation to target epigenetic mechanism along with apoptosis and metastasis. Both the formulations have shown significant therapeutic efficacy in the *in vitro* and *in vivo* tumour xenograft model of Neuroblastoma. The 4HPRANP variant was more potent than 4HPRNP in imparting therapeutic effect on NB. The nanoformulation has shown the potential to curve the cancer cells' metastatic potential by regulating epigenetic changes and inducing apoptosis. This nanoformulation overcame the observed cytotoxicity of the drug with improved therapeutic efficacy *in vitro* and *in vivo.* Molecular mechanism study reveals that 4HPRANP imparts therapeutic efficacy by downregulating EZH2 expression. After targeting CNS cancer and extracranial cancer, we have focused on another prevalent form of solid cancers oral squamous cell carcinoma (OSCC).

We have addressed OSCC related challenges through the development of Nano nutraceuticals. The nanoformulation (GLNPs) was developed using whey protein (Lactalbumin), and soy-derived flavonoid Genistein. Genistein is a very competent molecule in addressing cancer development and restricting its growth patterns. Lactalbumin nanocarrier has significantly improved genistein's bioavailability, so does its therapeutic potential in targeting apoptotic and epigenetic pathways in OSCC. We have further studied the molecular mechanism exhibited by GLNPs. The results indicate that GLNPs activate pro-apoptotic protein Bax and induce its mitochondrial translocation to activate caspase 3, which results in apoptosis. GLNPs regulate epigenetic repression through EZH2 proteasomal degradation and 3PK inhibition. It was found physically related to 3PK at transcription and translational level. GLNPs show the unique ability to simultaneously target Bmi 1 and EZH2 activity and activate apoptotic pathways in OSCC.

Albumin based nanocarriers provide improved drug loading and better bioavailability of the poorly water-soluble drugs. However, these nanocarriers could offer drug loading up to a specific limit; further drug loading improvement could be achieved through nanocarrier free formulations. We have developed nanocarrier free formulation of paclitaxel (PTX) based on drug nanocrystal platforms. The nanocrystalline nano assemblies of paclitaxel are synthesized through a self-assembly approach. Their unique morphology could be readily utilized for enhanced penetrance effect and localized drug delivery in hepatocellular carcinoma (HCC). The nanoformulation has simple synthetic approach and multichannel fluorescence property.

The nearest to cent percent drug loading and higher therapeutic efficacy against HCC makes it a promising molecule in its category of localized implantable chemotherapeutics. It could be used as a potent transarterial chemoembolization agent in TACE procedures to target HCC. Treatment of cancer is not side effect free. Chemotherapy and radiotherapy keep check on cancer cells' growth but badly affect the growth of normal cells. The surgical resection is very common in solid cancers which is usually followed by adjuvant chemotherapy. These adjuvant chemoradiotherapies provide survival benefit for cancer patients, but as a side effect, it leads to the impaired wounds created after tumour resection. Cancer patients' social and personal life get badly affected due to significant tissue loss and unhealed wounds after tumour resection and adjuvant chemoradiotherapy. We have developed C-phycocyanin and (-CRG based injectable hydrogel matrix that accelerate wound healing and help restore the wound cavity to address this critical issue. The current study presents a matrix with impeccable haemostatic and *In-vivo* imaging abilities. *In vivo* imaging property could be used to trace wound healing progress by taking time-lapse images of the wounds without opening its dressings. All the nanoplatforms developed in the present thesis are highly biocompatible and exhibit high potential in improving the treatment and management of solid cancers.

Vitae

Atul Dev
Ph.D. Research Scholar
Institute of Nano Science and Technology (INST), Mohali
&
Indian Institute of Science Education and Research (IISER), Mohali, Punjab, India

Mr. Atul Dev has started is a Ph.D. Research Scholar at Institute of Nano Science and Technology (INST) and Indian Institute of Science Education and Research (IISER), Mohali, Punjab, India. He started his Ph.D. as a UGC junior research fellow in INST, where he focused on development of nano therapeutic platforms for the treatment and management of solid cancer. He studied therapeutic potential of the nanoplatforms in addressing apoptosis, metastasis, epigenetics and tissue regeneration. Mr. Atul Dev completed his schooling from Lucknow. He pursued his Bachelors in Biotechnology from Punjabi University, Punjab and Masters in Biotechnology from Punjab Agricultural University, Punjab. He authored several research articles, review articles and Book chapters in peer review journals. He presented his work on several national and international platforms. His present research interest is translational nanoscience and biomaterial development for the treatment and management of solid cancer.

Appendix

κ-carrageenan-C-Phycocyanin based smart injectable hydrogels to accelerate wound healing and real-time monitoring

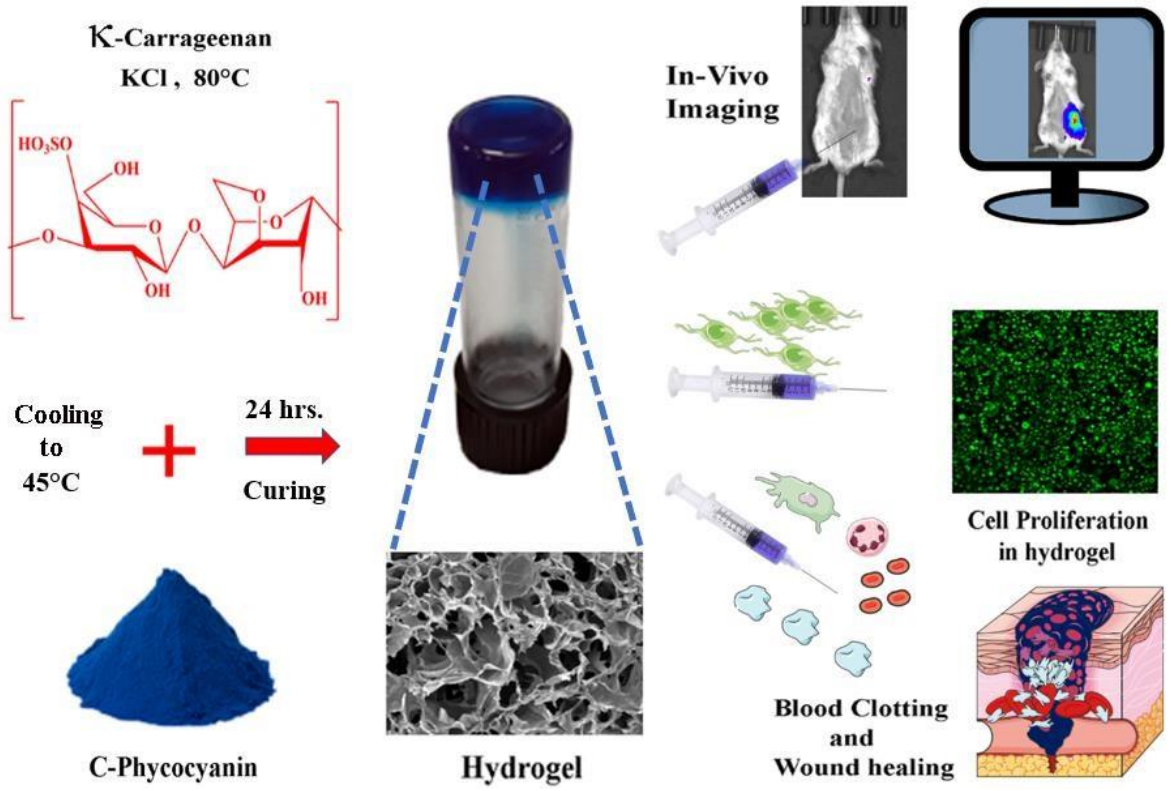

1.0 Background

Modern era of cancer management involves multiple modalities like chemotherapy, radiotherapy and surgery, among which, tumor excision surgery is very common. It is a well proven notion now, that tumor excision increases the life expectancy of the cancer patient by minimizing the burden of unnecessary growth of tumor tissues.[1] The tumor excision does provide several advantages but the quality of life significantly gets affected. The prime concern after tumor excision is the tissue loss and wound healing of the resected area. The introduction of radiotherapy after excision surgery makes things even more challenging. Although, adjuvant radiotherapy reduces the chances of cancer recurrence by eliminating the residual microscopic tumor at the excision site but , it affects the highly organized sequences of cellular interactions required in the healing of the wounds created after surgical resection.[2] It is not only radiotherapy, but the introduction of chemotherapy in later half of the disease management which adversely affect the wound healing process.

The administration of specific chemotherapeutic agents into the previously irradiated tissues may generate an inflammatory reaction which could result in erythema, blisters, oedema, and ulcer formation.[3] The most common side effect of chemotherapy is the development of Neutropenia. It is a medical condition, where number of circulating neutrophils get significantly reduced due to chemotherapeutic treatment, as chemotherapeutic agents cannot distinguish between normal and malignant cells.[4, 5] The small number of neutrophils in the circulating blood drastically affects the healing process of the wounds, and makes them susceptible for opportunistic infections. Several chemotherapy drugs cause venous irritation and are termed as vesicants. The leakage of vesicants to the wound area causes severe tissue damage causing non healing necrotic ulcers which may lead to the nerve damage, loss of limb function or even to the amputations.[6] If left untreated, advance stages of cancer may lead to the development of fungating wounds. Fungating cancer wounds are considered as the most distressing lesion in cancer patients. These wounds are strongly odorous with tissue exudates, which causes social isolation and mental trauma to the patients[7]. These wounds are developed from the extension of a malignant tumour into the structure of the skin, producing a raised or ulcerating necrotic lesion.[8] These are some very serious conditions of wound healing in cancer patients which need timely management and treatment.

Wound healing is a complex physiological process, which requires several sequential events. The healing process starts with hemostasis, which is followed by an inflammation process. Inflammation process is one of the robust and important stages. Several unhealed wounds get atrophic in this stage and fail to progress in the antiinflammation phase of the healing. During inflammation, neutrophils and monocytes initiate tissue repair by eliminating the infection and releasing several biologically active substances and growth factors necessary for tissue formation. Subsequently fibroblasts and endothelial cells proliferate simultaneously in the wound space and initiate the process of angiogenesis. Finally, reconstruction of the basement membrane is initiated owing to the differentiation of keratinocytes and follicular cells[9-11] .In case of severe burns, this process becomes more complicated due to extensive damage to the epidermis and dermis, which leads to slow healing process and scar formation. To support the wound healing process, the requirement of an ideal wound care system is of utmost importance. The wound care system should offer high humidity across the wound site, along with providing non-toxic, non-allergenic care. Additionally, it should absorb wound exudates (*e.g.*, blood, plasma), provide antimicrobial maintenance, thermally insulating and soft in mechanical support[12-16]. It should also provide proper gaseous and water exchange across the wound site and promote tissue reconstruction processes in a cost-effective way[17-19].

Hydrogels are considered as an ideal candidate to suit the requirements of wound dressing process. It often consists of a matrix of natural and chemical polymers with about 96%water content, which helps in maintaining a moist environment across wound site and further accelerated the wound healing process. The three-dimensional network system of hydrogels mimics the microarchitecture of native tissue extracellular matrix (ECM) and provide *in-vivo* niche like conditions for cell survival which further helps in the stimulation of wound healing[20, 21].

Currently, available polymer-based hydrogel systems assist in the wound healing process at individual stages viz. blood clotting, cell adhesion and migration.[56] To the best of our understanding no such system is reported till date which could offer the opportunity to empower the wound healing process at different stages along with imparting a platform for its simultaneous monitoring as well.

In this study, we have developed a gelling matrix of κ-carrageenan (κ-CRG) and natural pigment C-phycocyanin (C-Pc), which could be used as injectable wound healing hydrogels with the capabilities for *in-vivo* monitoring. Its spectroscopic properties could provide a

window for red and NIR based *in-vivo* imaging. Association with many inbuilt pharmacological properties like antimicrobial,[22] immunomodulatory,[23] anti-inflammatory, antioxidant[24, 25]and anti-tumors[26] could also be linked for its effectiveness in wound healing process. C-Phycocyanin stimulates wound healing through Urokinase-type plasminogen activator (uPA) dependent mechanism[27] although a detailed molecular mechanism is yet to be established. This κ-carrageenan-C-phycocyanin hydrogel could provide the support as wound healing matrix in damaged tissue along with real-time fluorescence imaging mediated monitoring of the wound healing.

2.0 Materials and Methods

2.1 Materials

κ-carrageenan(C1804), Phycocyanin (P2201) were purchased from TCI chemicals. Potassium Chloride (P933), Lipopolysacchardies from *Escherichia coli* (L4516) were purchased from Sigma Aldrich. MTT dye (cat# TC191), streptomycin penicillin solution (cat# A018), DMEM (cat# AL007S), FBS (cat#RM9955), Trypsin EDTA (cat#TCL144), Sucrose (cat# MB025), Sulphanilamide (cat#GRM1158) and N-(1-Naphthyl)ethylenediamine dihydrochloride (cat#RM1073) were purchased from Hi-media. Orthophosphoric acid (10057) was purchased from Merck Millipore.

2.1 Synthesis of κ-Carrageenan-C-phycocyanin Hydrogels

κ-Carrageenan-C-phycocyanin Hydrogels were obtained by taking a 1:1 ratio (wt/wt) of κ-CRG and C-Pc in 3mM KCl. Initially, κ-CRG solution was prepared and heated to 80°C for 30 min in a water bath. Once the κ-CRG was completely dissolved and formed a uniform solution, it was cooling down to 45°C and C-Pc was added. The solution was again bath sonicated to obtain uniform dispersion and incubated at room temperature (RT) for ionic crosslinking and gelation. Such prepared ionically crosslinked hydrogels were used to evaluate its physio-chemical and biological characteristics.

2.2 Rheological properties of the hydrogels

Rheological properties of the hydrogels were analyzed using a strain-controlled rheometer (Anton Parr MCR302) with 50 mm parallel plate assembly. The hydrogels samples were prepared and incubated at RT for 24hrs. before the measurement. Typical rheology measurements were done using the solvent trap at 25˚C. Initially, a strain sweep was

performed with constant frequency (1 Hz) and log ramp strain (0.1–100%) to establish the linear viscoelastic region (LVE), where the storage modulus G' and loss modulus G" are independent of the applied strain. Once, the LVE was determined for each hydrogel; frequency sweep was performed at a constant strain. Frequency sweeps were performed with a log ramp frequency (0.1–10 Hz) and constant strain (0.1%).

For self-healing behavior of the hydrogels, thixotropic studies were performed. The thixotropic nature of the hydrogels was validated with step-strain rheology experiments, putting the strain values within the LVE region. During the experiment, the gel samples were subjected to a pre-shear stress interval with 0.1% strain (equivalent to its LVE range strain) at a frequency of 1Hz, in order to obtain the initial values of modulus for 200 secs. Then high shear stress with a strain of 100% for 100 s was applied, followed by the recovering the gel state from sol state through reducing the strain to 0.1%, for 200s. Consecutive cycles were applied on the hydrogels to compare the extent of gel strength recovery.

2.3 Live Dead Assay

The hydrogel was cast into a 35mm plate before the cell seeding. Once the gel gets solidified, it was equilibrated with DMEM media supplemented with 10%FBS and 1% Penicillin-streptomycin solution for 24hrs. The cultured L929 Cells were trypsinized and seeded in the density of $1X10^5$ cells per well and allowed to grow for a various time point (1,3,5,7 days). The media was replaced after every 24 hrs. The cells were analyzed using live dead assay kit containing 3,3′-dioctadecyloxacarbocyanine (DiOC18 or "DiO"), a green fluorescent membrane stain and Propidium Iodide. The media was removed from the plate and cells were washed thrice with PBS. The cells were stained using 4ul of DiOC18 in 1ml of DMEM for 1hr. The media was removed, and the cells were washed thrice with PBS. Finally, 1X PBS was added to the cultured cells, and 2ul of Propidium Iodide was added before Imaging.

2.4 Nitric oxide assay

The nitric oxide assay was performed using RAW 264.7 cells (1.0×10^4 cells/well) in 96 well plates with LPS (1.0 µg/mL) for 24 hrs. The quantity of nitrite was measured as an indicator of NO production. Two different methods of treatment were used to detect nitrite levels during pathogenesis. In the first method, cells were pre-treated with κ-CRG-C-Pc hydrogel for 12hrs, before adding LPS. In the second method LPS was co-incubated with κ-CRG-C-Pc

hydrogel for 24 hrs. Nitrite was quantified using Griess reagent (1% sulfanilamide and 0.1% naphthylethylenediamine dihydrochloride in 2.5% phosphoric acid) and sodium nitrite standard curve. Briefly, 50 µL of culture media (treated well) was mixed with 50 µL of Griess reagent and was incubated in the dark at room temperature for 10 min. The absorbance was measured at 540 nm using a microplate reader.

2.5 Blood Coagulation Assay

Goat whole blood was collected from the local market slaughterhouse in sodium citrate (3 mg/ml blood). The hydrogel samples (κ-CRG, κ-CRG-C-Pc) were placed in 24-well plates. Subsequently, 300 µL of reactivated goat whole blood (250 µL of whole goat blood with 50 µL of a 25 mM $CaCl_2$ solution) was added to each well containing the hydrogel samples. Blood alone was used as a control. The blood clotting time was reported after the appearance of blood clotting in its first instance verified by washing of unclotted blood with saline water (0.9% NaCl).

2.6 Haemolysis Assay

The whole goat blood collected in 3.8% sodium citrate was centrifuged to collect blood cells (RBCs) and perform a haemolysis assay of the hydrogel samples. Briefly, 1 mL of RBCs was diluted with 9 mL of saline. To evaluate the hemocompatibility of the hydrogels, 500 µL of diluted RBCs were added to 100 µl of the 1% κ-CRG hydrogel, 1% κ-CRG-C-Pc hydrogel, in separate vials. 0.1 % Triton-X (100 µL) and saline (100 µL) were used as the positive and negative controls respectively. Finally, the vials were incubated at 37°C for 1hr and then centrifuged at 3500 rpm for 10 min. The resulting supernatant was collected and analyzed to measure their OD values using a microplate reader at 540 nm to determine the% haemolysis using the following equation (n=3 for each time point).

$$Haemolysis\ \% = \frac{(OD\ of\ sample - OD\ of\ negative\ control)}{(OD\ of\ positive\ control - OD\ of\ negative\ control)} X100$$

2.7 Wound healing scratch assay

Mouse fibroblast cells L929 were cultured in a 24well plate with cell density of$1x10^5$ cells per well for 24hrs. The cells were starved for next 12 hrs to minimize the proliferation. After starvation period, a scratch was made on the surface of the cell monolayer using a 200µl

pipette tip to mimic the conditions of a scratch wound. After making scratch, the cells were washed twice with 1XPBS to remove out scratched cell population followed by incubating the cells with cell culture medium along with pre-formed hydrogels. The cell layer was imaged at intervals of 0, 12, 24 hrs using phase-contrast microscopy.

2.8 In vitro fluorescence studies

In vitro Fluorescence studies of the hydrogels were performed in 96 well plates using microplate reader. Freshly prepared hydrogels were casted directly into the wells of 96 well plate in three sets namely 100 µl gel alone, 100 µl of KCl and C-Pc solution prepared in KCl respectively. An emission fluorescence intensity scan was performed from an excitation wavelength of 400 to 600nm with a step size of 20nm. The emission wavelength was recorded at 1nm interval. All the fluorescence scans were performed in triplicate.

2.9 *In-vivo* Imaging Studies

In-vivo imaging experiments were performed on six-weeks-old male Balb/c mice after due ethical clearance from the Institutional animal ethics committee. To assess the *in vivo* imaging ability of Hydrogel in the animal model, freshly prepared 100µl of κ-CRG-C-Pc hydrogel was injected subcutaneously. For the negative control group, 100 µL of sterile PBS was administered. The mice were imaged at the various time points (0.25hrs., 0.5hrs., 1hrs., 3hrs.) for 3 hrs. The images were acquired using the IVIS Spectrum (Perkin Elmer) animal imager measuring quantitative estimation of the fluorescence intensity.

2.10 *In-vivo* toxicities studies

In vivo toxicity of hydrogels was performed in six-weeks-old male Balb/c mice. The freshly prepared 100µl of sterile gels (κ-CRG, κ-CRG-C-Pc) were subcutaneously injected into the flank region of the mice. The mice were sacrificed after 24 hrs. and 7 days of injection. The skin samples were collected and fixed in paraformaldehyde for histological analysis.

2.11 Statistical Analysis

The statistical analysis was conducted in origin 8.5 SR1 version of the software from origin lab corporation with the License number GF3S4-9089-7123456. The results are expressed as mean ± standard deviation. Multiple comparisons were carried out using a one-way analysis of variance (ANOVA), $P<0.01$ or $P<0.05$ was considered statistically significant.

3.0 Results and Discussion

3.1 Physical characteristics of Hydrogels

κ-Carrageenan is a polysaccharide composed of linear chains of D-galactopyranosyl units linked via alternated (1→3)-β-D-and (1→4)-α-D-glucoside unit containing one sulphate per disaccharide unit. The hydrogels were prepared using (1%) κ-carrageenan and 1% C-Pc in 3mM KCl solution. The solution was heated to 80°C for 30 min and allowed to cool down to 45°C for the addition of C-Pc solution. The samples were incubated at room temperature for 24hrs for curing of the gel, which results in uniform gel formation[28]. The mechanism of gelation of κ-carrageenan is a multistage process, in stage one polysaccharide solution remain in random coil conformation during heating, followed by the formation of a helical dimer, aggregation of helical dimers and formation of a three-dimensional during cooling and curing at room temperature[29-32]. The transition from random coil structure to double helices conformation is a swift process whereas subsequent aggregation of double helices into small domains to form a three dimensional network is slower which take 12 to 15 hrs.[33] After curing, the gels were freeze-dried in lyophilizer and small sections were cut to analyse the interconnected network of the gel using scanning electron microscopy (SEM). The gel sections were spray-coated with gold and analyzed under vacuum condition. The SEM analysis revealed a uniform interconnected porous system of the hydrogel (Fig.1a,1b). The pore size was calculated using ImageJ software. κ-carrageenan gel results in the formation of hydrogels with 233.51 ± 45.36nm average pore size (Fig. 1c), the addition of C-phycocyanin did not result in significant variation in pore size as the average pore size of the κ-CRG-C-Pc hydrogel was reported as 214.32±45.57nm (Fig. 1c). An ideal hydrogel allows cell growth and wound healing if it permits continuous exchange of gases along with nutrients and metabolic waste products. An interconnected hydrogel network with controlled porosity and a pore size > 100 μm is typically required to meet these criteria[34, 35].

3.2 Physical interaction of κ-carrageenan and C-Phycocyanin

κ-carrageenan forms hydrogel after crosslinking with KCl. The gelation occurs due to the conformational changes from linear to coiled to the supercoiled structure. Lyophilized hydrogels of κ-CRG and κ-CRG-C-Pc were investigated along with C-Pc and κ-CRG separately using Fourier-Transform infrared spectroscopy (FTIR) (Fig.1d). In κ-CRA, a sharp peak observed at 1043 cm^{-1} was assigned to O=S=O symmetric bond (stretching).

Additionally, the sharp peaks at 926, 847 and 1236 cm^{-1} were associated with asymmetrical C-O vibration of 3,6-anhydro-D-galactose, the pseudo-symmetrical C-O-S vibration of a sulfated group of b-1,3-linked residue, and antisymmetric stretching O=S=O vibration, respectively. The smaller peak at 1644 cm^{-1} was correlated with C=O stretching of an amide. The inclusion of C-PC in hydrogels was confirmed by the presence of sharp peak of amide I band at 1648 cm-1 (C=O stretching) and amide II at 1532 cm-1 in κ-CRG- C-Pc gels. C-Pc alone shows an intense and robust peak at 3618 and 3718, which represent the free O-H (stretching) along with a broad peak from 3000-3500 cm^{-1} which represent O-H stretch of acid.

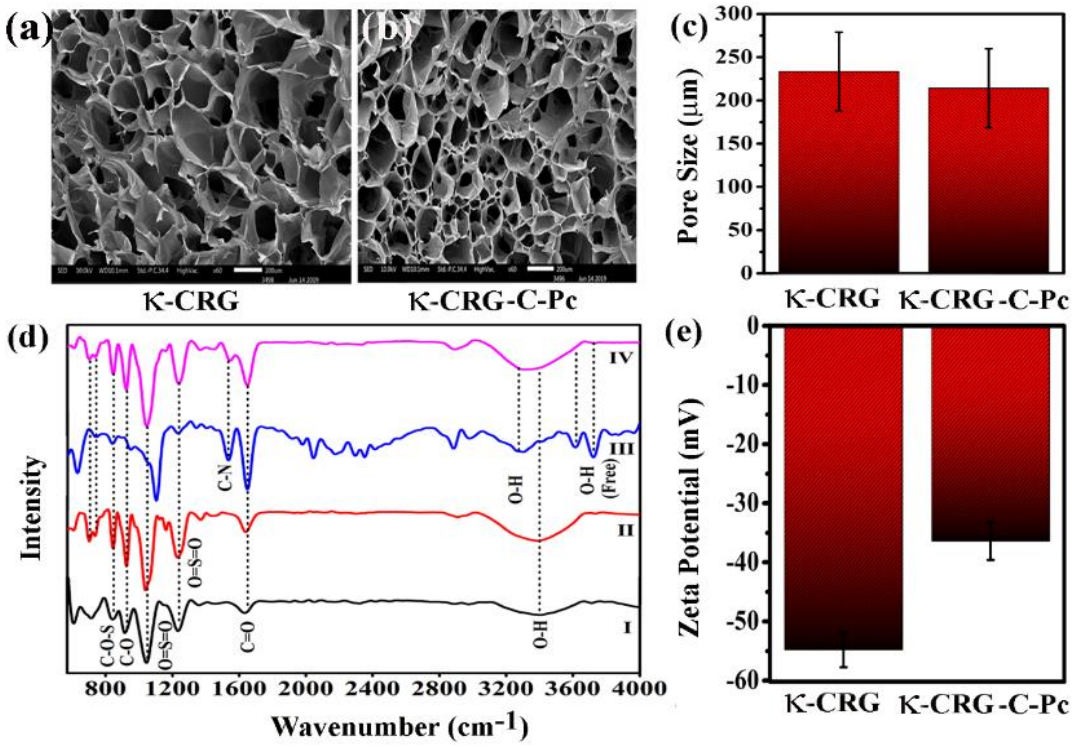

Fig.1 SEM image of κ-Carrageenan (κ-CRG) hydrogel (a) κ-Carrageenan-C-Phycocyanin(κ-CRG-C-Pc) hydrogel (b), Average Pore Diameter of hydrogels (c), FTIR spectra of κ-CRG (I), κ-CRG hydrogel (II), C-Phycocyanin (III), κ-CRG-C-Pc hydrogel (IV), Zeta potential of κ-CRG and κ-CRG-C-Pc hydrogel (e).

3.3 Rheological characteristic

Rheological experiments are utilized to access the mechanical and self-healing property of hydrogels.κ-carrageenan in the disordered conformation exhibits high sensitivity to counter ions[36, 37] the gels formed with K^+ are the strongest and most stable[30]. The viscoelastic property of κ-carrageenan highly dependent on the concentration of carrageenan and counter ion. It has been found that κ-carrageenan shows the gel-like property at 0.5%, 1% wt%

concentration with 5mM KCl. In general, the strength of the gels, expressed by G', increases with the addition of potassium chloride. For concentrations below 80mM KCl, the addition of the KCl results in a rapid increase of gel strength, whereas for concentrations above 80 mM no such increase in gel strength was found. The possible explanation for such behavior is the saturation of polysaccharide with potassium ion, reaching the maximum aggregation of the helical chain. Additionally, limiting gel strength also depends on κ-carrageenan concentration[36].

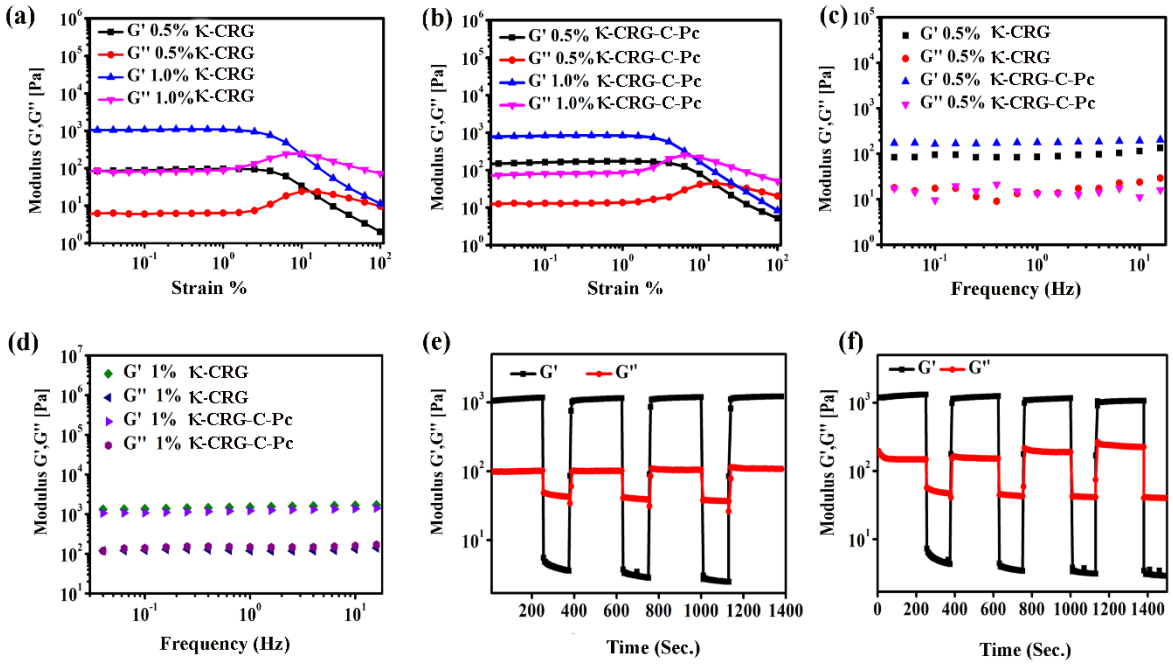

Fig. 2 Rheological characterization of Hydrogels showing amplitude sweep for κ-Carrageenan hydrogel (a),κ-Carrageenan + C-Phycocyanin hydrogel (b), Frequency sweep for κ-Carrageenan hydrogel and κ-Carrageenan+ C-Phycocyanin hydrogel at 0.5%κ-Carrageenan (c), Frequency sweep for κ-Carrageenan hydrogel and κ-Carrageenan+ C-Phycocyanin hydrogel at 1%κ-Carrageenan (d) Thixotropic behavior of 1% κ-Carrageenan hydrogel (e) Thixotropic behavior of 1%κ-Carrageenan+ C- Phycocyanin hydrogel (f).

In the current experiment, we have fixed the KCl concentration to 5mM and varied κ-carrageenan concentration from 0.5% to 1%. We have found that increasing the concentration of κ-carrageenan increases the stiffness of the gel as validated by higher G' value (Fig.2a).κ-carrageenan exhibit gel nature at both the concentrations with 5mM KCl as evident from G'>G'' values at 25°C. Addition of 1% C-phycocyanin has changed the stiffness of the gel at 0.5% Carrageenan concentration (κ-CRG G'>κ-CRG-C-Pc G'), although such results are not achieved at 1% κ-CRG concentration (Fig.2b). G' values show frequency-independent behavior for all the gels at all the concentrations, although G'' values did not show a similar pattern. G'' values at 0.5% κ-CRG and 0.5% κ-CRG+1% C-Pc changed with the change in

frequency (Fig.2c) although at 1.0% κ-CRG and 1.0% κ-CRG+1% C-Pc G'' values show frequency-independent behavior (Fig. 2d).

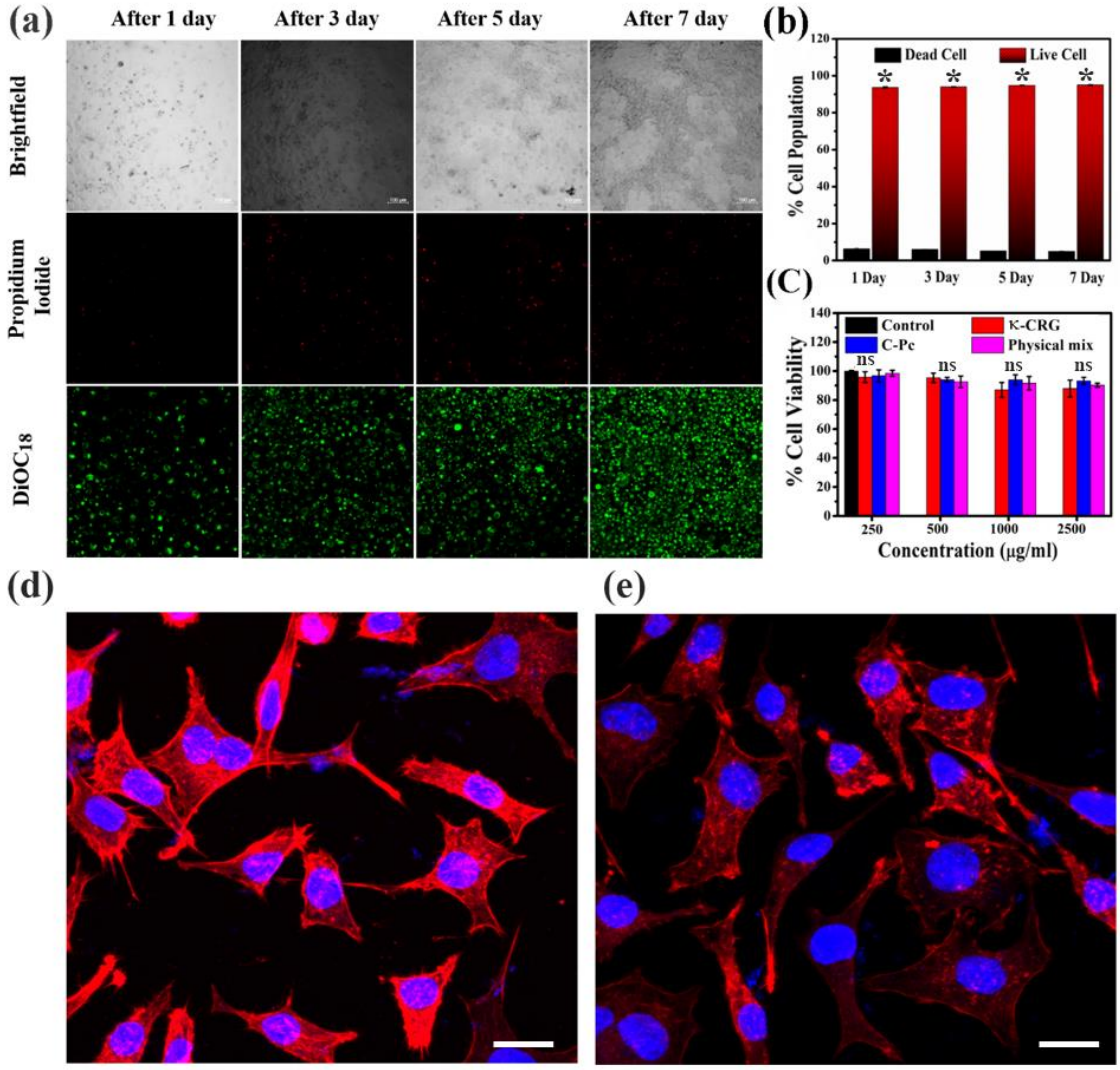

Fig.3 Time dependent Live-Dead Assay of L929 cell line growing in κ-Carrageenan hydrogel (a), Per cent survival of Cell population calculated from ImageJ using Propidium Iodide channel as Dead Cell and DIOC$_{18}$ as live Cell (b), MTT assay showing percent cell viability of L929 cells at various concentration of κ-CRG, C-Pc and physical mix. (κ-CRG+C-Pc) with respect to control (c), Morphology of Cells growing on κ-CRG gel (d) and (κ-CRG+C-Pc) gel. Scale bar represents 10µm.

Thixotropic nature of the gel was utilized by providing a cycle of high strain and low strain in the LVE region. Notably, convincing evidence about the excellent self-healing property of these gels was provided by rheological experiments. As shown in (Fig.2e,f) the G' value decreased from 1000 Pa to 0.5 Pa upon application of a large-amplitude oscillatory force (γ = 100%; frequency (1.0 Hz), resulting in a liquid state. On the contrary, G' immediately recovered its initial value, and the system recovered to a solid-state when the amplitude

decreased (γ = 0.1%) at the same frequency (1.0 Hz). The self-healing property mentioned above is one of the most amazing properties in nature[38-40] an ability of biological or artificial systems to spontaneously repair their damage and restore their original state. Different from most soft materials, which are injectable, self-healing gels can regenerate the integral network after damage. This property endows these materials vast applications in the fields of drug delivery, 3D cell proliferation, and tissue engineering[41-43].

3.4 Cell viability, proliferation, adhesion

Fibroblasts cells play a key role in the final stage of wound healing. Invasion by fibroblasts produces a fibrin matrix, which could couple with κ-CRG-C-Pc hydrogel and promote wound healing. κ-CRG-C-Pc hydrogel might provide ECM like support and play an important role in the migration of fibroblast cells, which could accelerate wound healing[44, 45].

The growth of L929 cells on hydrogel was evaluated using a Live /dead assay kit. The cells were seeded, and the growth pattern was recorded at a various time interval (1,3,5,7 days). Cells show slow growth rate initially for 1-3 days but saturated the gel on 5 and 7 days (Fig3a). This confirms the ability of the κ-CRG hydrogels to provide a matrix support for cellular adhesion and growth. Cell viability analysis revealed that >95% cell population was metabolically active throughout the incubation period (Fig. 3b). In general, bio-activity of material is significantly related to the natural attributes and their structural properties. Hydrophilic polymers with a rough surface and porous microstructure were believed more favorable for cell adhesion, migration and proliferation[46, 47]. To access the cellular toxicity, L929 cells were treated with different concentrations of κ-CRG, C-Pc, and Physical mixture for 24 hrs. It was found that the L929 cell line shows no sign of toxicity at all the concentrations tested, indicating the biocompatibility of the material for wound healing (Fig. 3c). The cellular morphology of the hydrogel in grown cells appears normal in both the hydrogel (Fig 3d, e). This indicates that hydrogels provide a good matrix support for cell spreading and proliferation.

3.5 κ-Carrageenan-C-phycocyanin hydrogel induces blood clotting

Blood clotting is the primary and most crucial stage in wound healing. Haemostatsis set the foundation for vital wound recovery process[48]. A wound-healing system should possess a substantial haemostatic ability. The blood clotting ability of hydrogels was investigated by in

vitro dynamic blood clotting assay. The coagulation active blood was incubated with κ-CRG and κ-CRG-C-Pc hydrogel along with negative control. κ-CRG-C-Pc hydrogel shows minimum blood clotting time of 171.66±10.40 sec. followed byκ-CRG hydrogel of 343.33±7.63 sec, the control group showed a maximum blood clotting time of 403.33±7.63sec. (Fig.4a, b). κ-CRG hydrogel reduces the blood clotting time to <6min, which is in line with earlier reports. This reduction in clotting time is possibly due to the anionic nature of the hydrogel[49].κ-CRG, κ-CRG-C-Pc hydrogel zeta potential values of -54.8 mV and -36.4mV shows anionic nature of the material (Fig.1e).

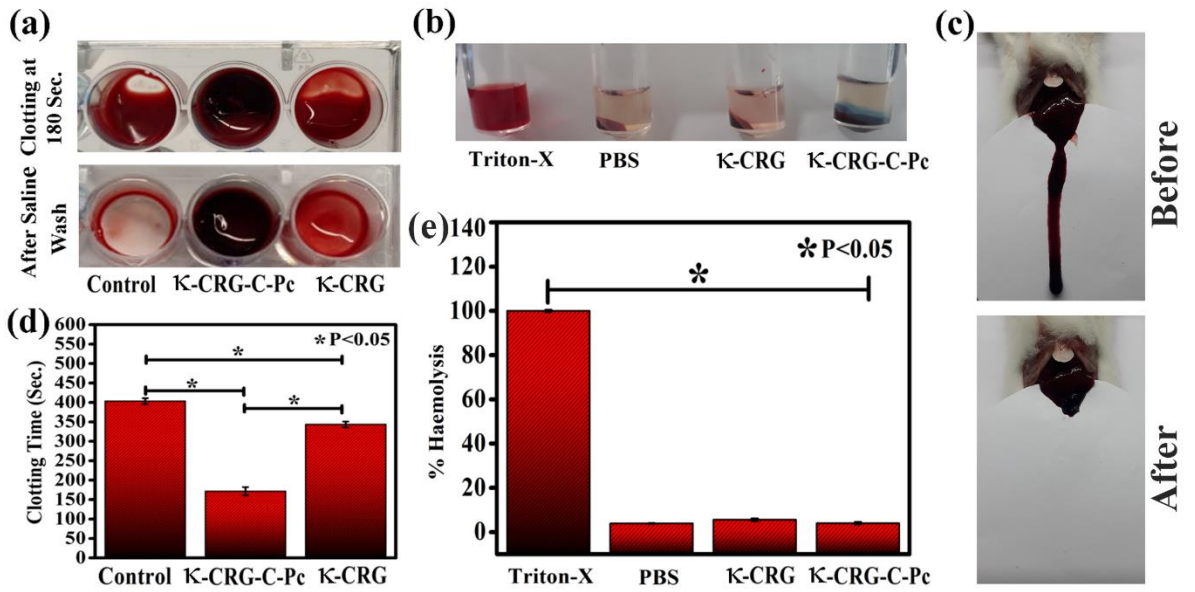

Fig.4 Blood Coagulation Assay showing ex-vivo blood clotting(a), Triton-X, PBS and Gels showing haemolysis (b), In-vivo liver shearing showing haemostasis in mice (c), Ex-vivo blood clotting time of κ-CRG, κ-CRG-C-Pc hydrogels (d), Quantitative estimation of percent haemolysis in Triton-X, PBS, κ-CRG and κ-CRG-C-Pc hydrogels (e).

The decrease in negative zeta potential values in κ-CRG-C-Pc could be associated with the presence of C-Phycocyanin protein and sequestration of K^+ ion. It is well established that anionic nature of the surface activates Hageman factor (FXII) in the intrinsic coagulation pathway of blood coagulation along with activation of the platelets[50, 51]. Addition of C-phycocyanin further reduces the clotting time to <3min (Fig 4a, d). This change in clotting time could be associated with the presence of protein molecules in κ-CRG-C-Pc hydrogel, which allows adhesion of blood protein on the hydrogel surface and further activates blood clotting machinery. Blood clotting ability of hydrogel was also performed *in vivo* to simulate the real wound conditions. The experiment was performed using liver injury as an acute

injury model to analyze the robust haemostatic capability of the κ-CRG-C-Pc hydrogel. It was observed that liver injury resulted in a large amount of blood loss, as large blood stains were seen on filter paper. However, after application of the κ-CRG-C-Pc hydrogel a physical barrier was created which results in haemostasis at injury site (Fig 4c). These results indicated that κCRG-C-Pc hydrogel possessed a superior haemostatic capability to address critical blood loss conditions in traumatic wounds. To further evaluate the blood compatibility of the material, the haemolysis assay was performed. One ml RBCs were diluted in PBS and incubated with hydrogels at 37°C for 1 hr. 0.1% Triton X-100 was used as positive control along with 1X PBS as a negative control. No significant hemolysis was reported in any of the hydrogels, validating the RBCs compatibility of the material (Fig. 4b, e).

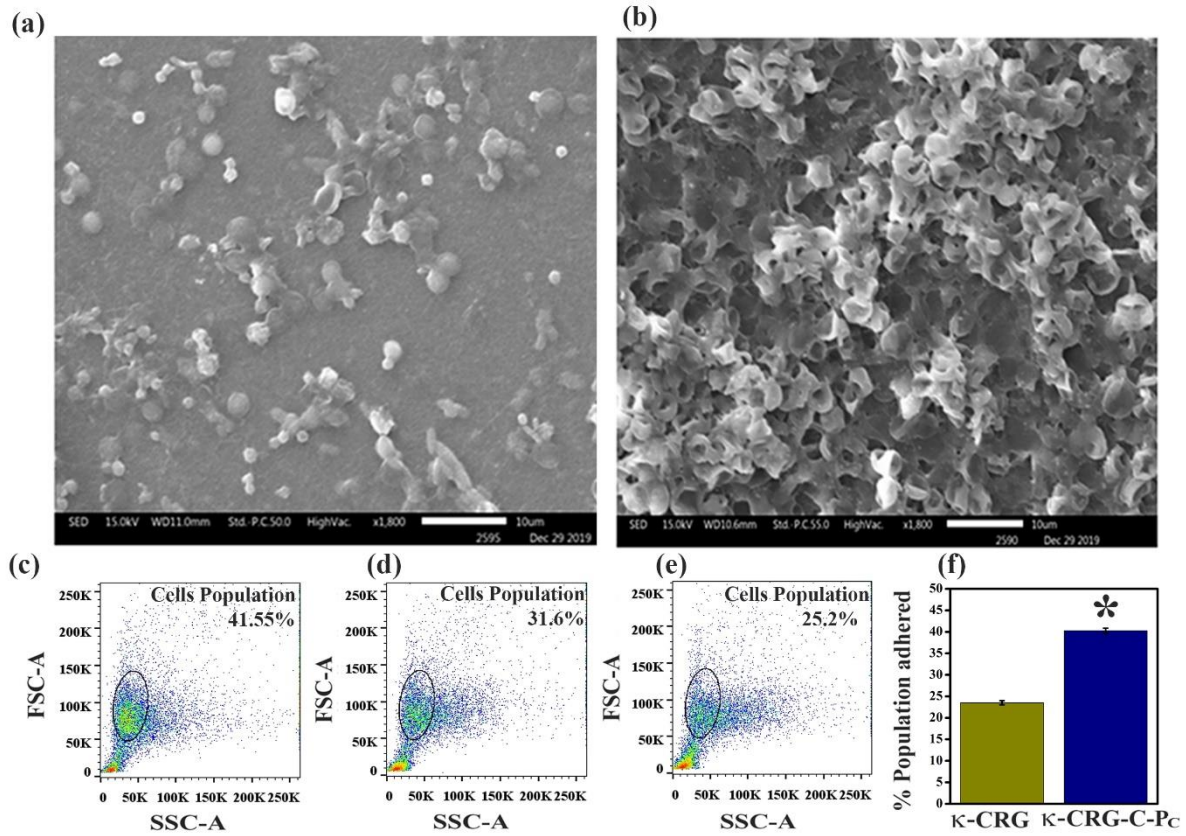

Fig.5 SEM images showing blood cells adhesion on κ-CRG hydrogel (a), κ-CRG-C-Pc hydrogel (b), FACS analysis showing a cell population in control blood wash (c), κ-CRG hydrogel treated blood wash (d), κ-CRG-C-Pc hydrogel treated blood wash (e) quantitative estimation of percent population adhered on hydrogels (f).

The κ-CRG-C-Pc hydrogel has shown improved blood clotting capabilities, to understand the mechanism of this superior blood clotting characteristic we have performed blood cells

adhesion experiment. Citrate active fresh blood was incubated with κ-CRG and κ-CRG-C-Pc hydrogel for 2 min, the gels were washed with PBS. The wash was collected and analyzed using FACS, while the gels were fixed using 4% formaldehyde overnight and imaged under SEM. We have found that κ-CRG-C-Pc hydrogel activates platelets which result in RBC adhesion and clot formation. The analysis of complete blood and hydrogel washed blood revealed that a particular type of population is adhered to the hydrogel surface, which might be the platelets or RBCs. SEM imaging confirms the presence of activated platelets and RBCs at the hydrogel surface. In comparison to complete blood control, κ-CRG result in 23.94 % of the cells adherence while κ-CRG and κ-CRG-C-Pc hydrogel shows significant increase of 39.35% in cell adherence on the surface (Fig 5).

3.6 κ-CRG-C-Pc hydrogel induces wound healing while reducing inflammation

Wound healing (WH) is a complex process which includes numbers of factors and stages. After haemostasis, the next important phase in WH is the migration of fibroblast to the wound site. The cell migration to the wound site is evaluated through in vitro scratch assay. It is a straightforward method to study cell migration in vitro[52]. A wound is created in the monolayer of the fibroblast, and percent of wound closure considered as potential parameter of wound healing. κ-CRG-C-Pc hydrogels show significant wound closure in 12hrs and 24hrs in comparison to the κ-CRG hydrogel and control (Fig.6). κ-CRG-C-Pc hydrogels filled the wound within 24 hrs of incubation, showing pronounced impact on fibroblast migration and wound recovery. These findings are in line with the earlier reports where similar results were obtained.[27] Proliferation stage is well connected to the inflammatory response in wound healing. It is the inflammation stage which decides the fate of wound healing. Cells enter proliferation and differentiation once inflammatory signals subside. Chronic wounds are one of the results of prolonged inflammation. These wounds are filled with inflammatory molecules including ROS, cytokines and many growth factors. Elimination of these pernicious factors could help restore the wound healing process [53]. Nitric oxide (NO) is a small signaling molecule that plays crucial role in the spread of inflammation[54]. C-Phycocyanin is immunomodulatory and plays important role in anti-inflammatory mechanisms. In the current study we have found that κ-CRG-C-Pc hydrogels reduced the production of nitrite, an index of NO, and iNOS expression in lipopolysaccharide (LPS) treated RAW 264.7 macrophages (Fig.6g).

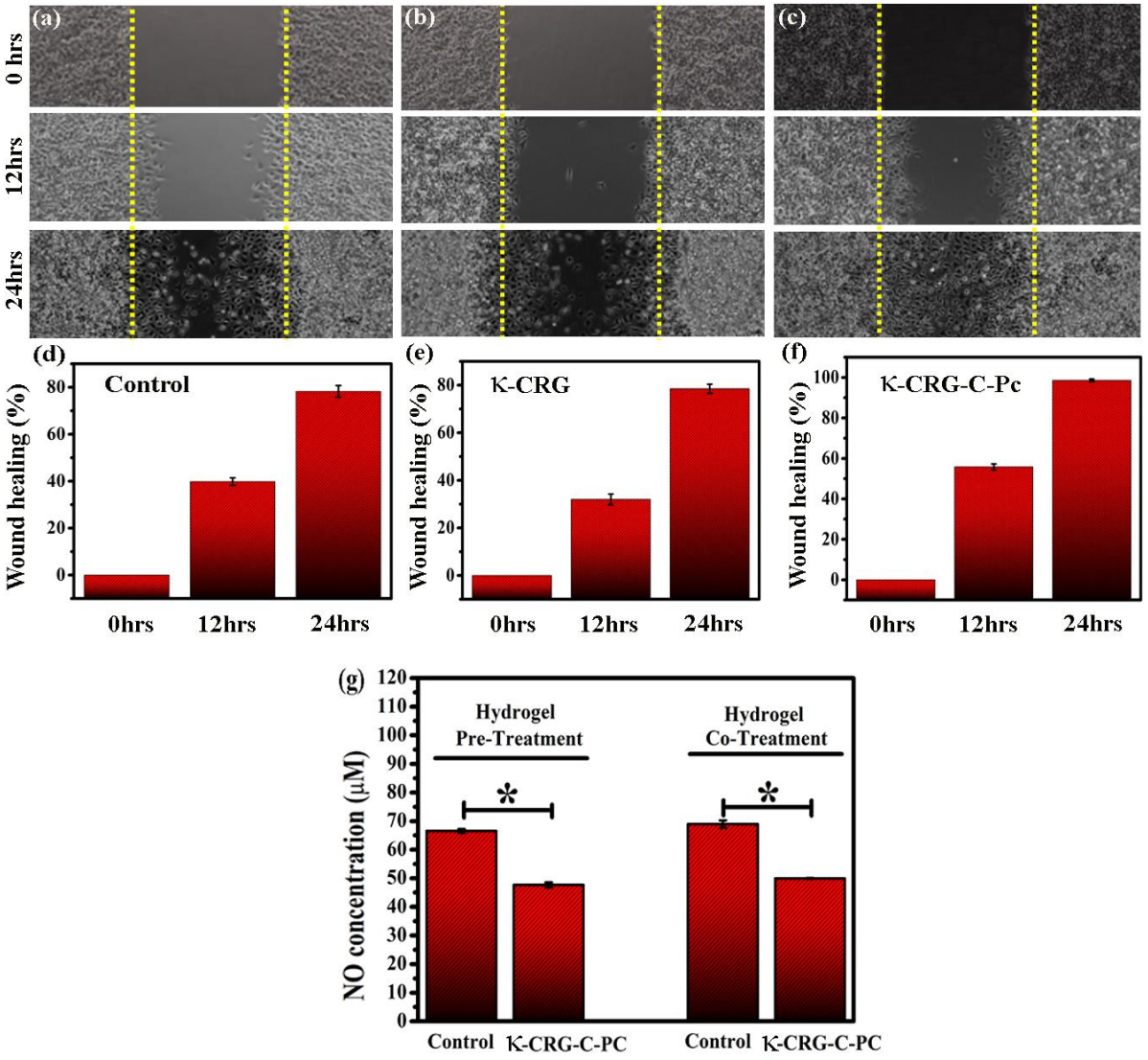

Fig.6 Wound scratch assay showing gap closure at 0hrs, 12hrs, 24hrs of Control (a), κ-CRG hydrogel (b), κ-CRG-C-Pc hydrogel (c), quantitative estimation of wound healing percentage in control (d), κ-CRG hydrogel (e), κ-CRG-C-Pc hydrogel (f) NO estimation in RAW234.7 macrophages after LPS (1μg/ml) treatment (g).

Our results indicated that κ-CRG-C-Pc hydrogels significantly inhibited the LPS-induced nitrite production in pretreatment and co-treatment of hydrogels with LPS (1μg/ml) in RAW264.7 macrophages. This study is in complete agreement of earlier study where similar results were obtained. It has been reported that C-Phycocyanin attenuates tumour necrosis factor-alpha (TNF-alpha) formation along with suppression of nuclear factor-κappaB (NF-κappa B) through preventing degradation of cytosolic Iκappa B-alpha in LPS-stimulated RAW 264.7 macrophages and thus show anti-inflammatory response[55].

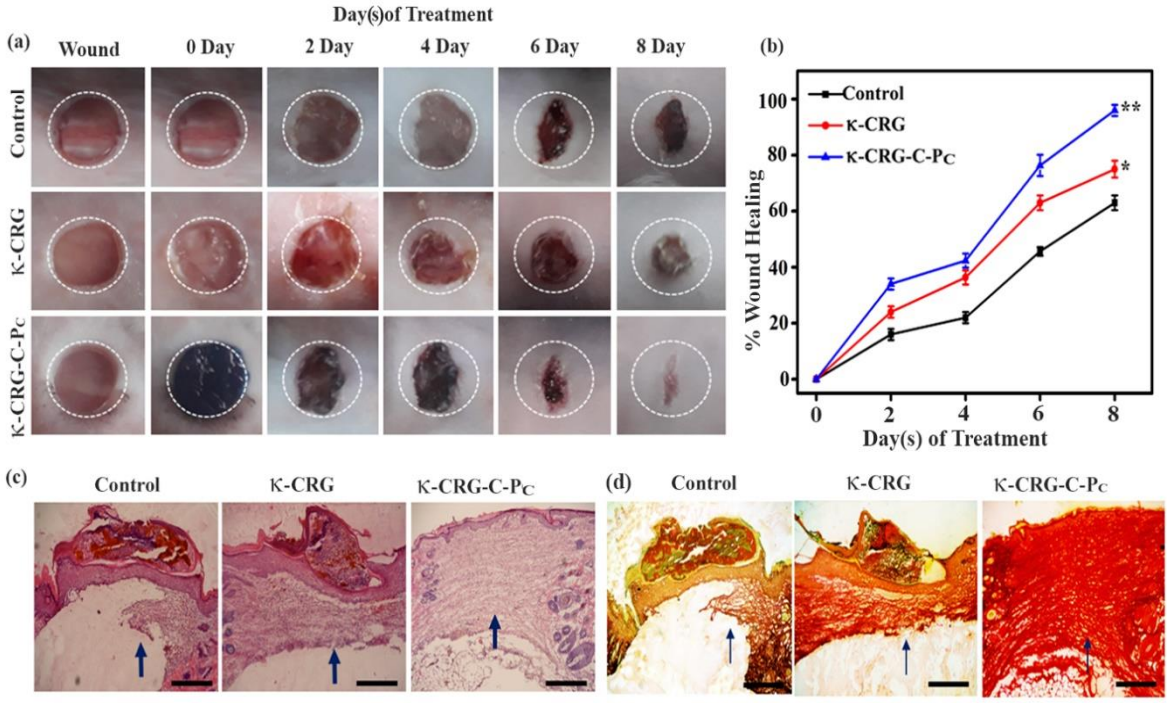

Fig.7 ***In vitro*** **wound healing showing time dependent healing in Control, κ-CRG hydrogel and κ-CRG-C-Pc hydrogel treatment (a), Time dependent percent wound healing in control, κ-CRG and κ-CRG-C-Pc hydrogel treatment (b), H&E staining of skin samples showing granulation tissue after wound recovery (c), Picrosirius red staining showing collegen development during wound recovery (d). Scale bar represent 400μm. Bold arrows showing the wound healing area, sharp arrows showing collagen restructuring at wound site.**

3.7 *In vivo* wound healing in mice

In vivo wound healing analysis was performed in cutaneous wounds. Wounds were monitored at regular time intervals to understand the wound healing efficiency of the hydrogels. We have found that κ-CRG hydrogel gets degraded within 24 hrs of application, while κ-CRG-C-Pc hydrogel remain attached in the wound till 6 days. In respect to control, both types of hydrogels provide very good support in wound recovery. Wound recovery percent was best found in κ-CRG-C-Pc hydrogel, which results in nearly 100 percent wound recovery within 8 days of treatment. While in the same time period the wound recovery percentage for κ-CRG hydrogel and control was 60 % and 40% respectively (Fig 7a, b). After treatment time of 8 days, the mice were sacrificed and skin was collected for H&E and picrosirius red staining. We have not found any remnant of the gel in the wound area, showing complete degradation. The H&E staining of wounded skin samples indicates partially healed wound in control and κ-CRG treated hydrogel, while κ-CRG-C-Pc hydrogel treatment results in complete closure and restructuring of the wound (Fig 7c). Picrosirius red

staining indicates the collagen presence in the wound. It was found that κ-CRG-C-Pc hydrogel treatment groups show maximum collagen synthesis which might help in wound closure and restructuring at the site (Fig 7d).

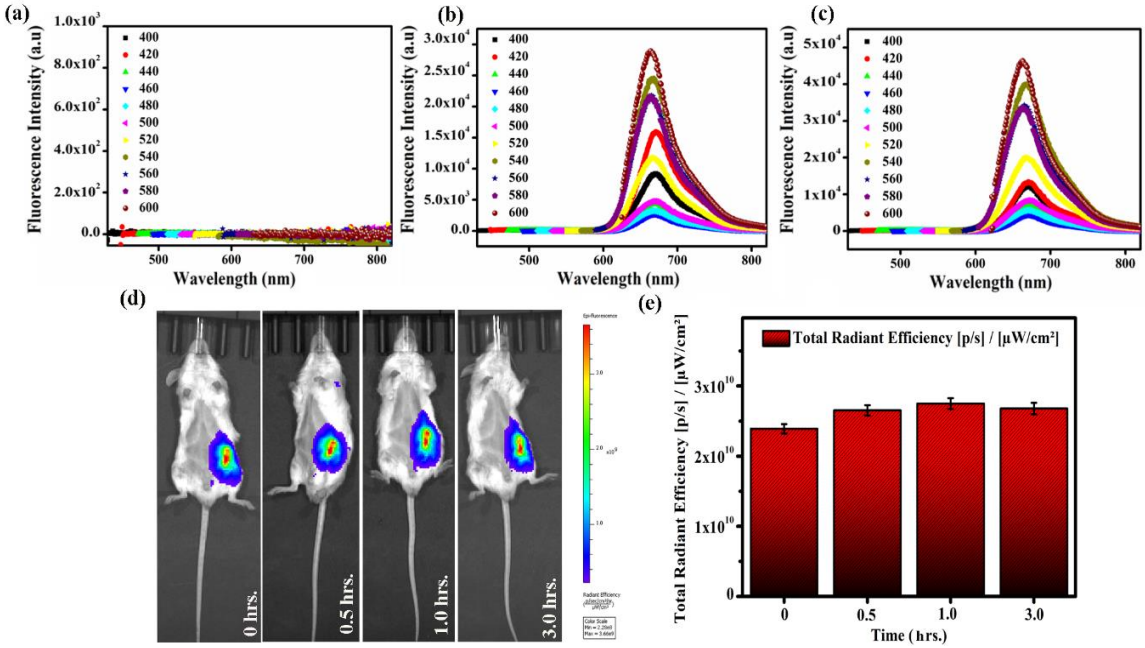

Fig. 8 Fluorescence Spectra of κ-Carrageenan hydrogel (a) C-Phycocyanin (b) κ-Carrageenan + C-Phycocyanin hydrogel (c) *In vivo* Imaging of κ-Carrageenan + C-Phycocyanin hydrogel at various time point (d) Quantitative estimation of total radiant efficiency of injected hydrogel at different time point (e).

3.8 In vitro quantitation of K-carrageenan -C-Pc hydrogel

C-Phycocyanin is a pigmented protein that has inbuilt fluorescence property in the red region. κ-carrageenan itself doesn't have any fluorescence; it enhances the fluorescence intensity of C-Pc due to the confinement of fluorophores molecules in a small area. The κ-CRG-C-Pc hydrogel shows ~150% enhancement in the fluorescence intensity in comparison to the equimolar concentration of C-Pc. The gel shows maximum emission intensity at 650nm when excited at 600nm (Fig. 8a-c). The fluorescence emission extends beyond 700 nm, providing a window of far-red and NIR imaging.

3.9 *In-Vivo* Imaging

In vivo fluorescence quantitation of κ-CRG-C-Pc hydrogel revealed the far Red and NIR imaging property, which could be exploited for the i*n vivo* imaging. Freshly prepared gel was injected subcutaneously in the Balb/C mice to monitor *in vivo* fluorescence signals from the

material. The image was captured at a different time interval after injection. The gel was excited at different wavelengths; the best emission was collected at 680nm after excitation at 600nm. Our *in-vitro* fluorescence measurements support the *in-vivo* imaging capabilities of the hydrogel. The fluorescence was quantified using Living Image® 4.5.1 Software of IVIS spectrum, Perkin Elmer. The total radiant efficiency remains substantially stable throughout the measurement from 0.25 to 3 hrs. Indicating the real time monitoring potential of the material in wound recovery (Fig. 8d, e).

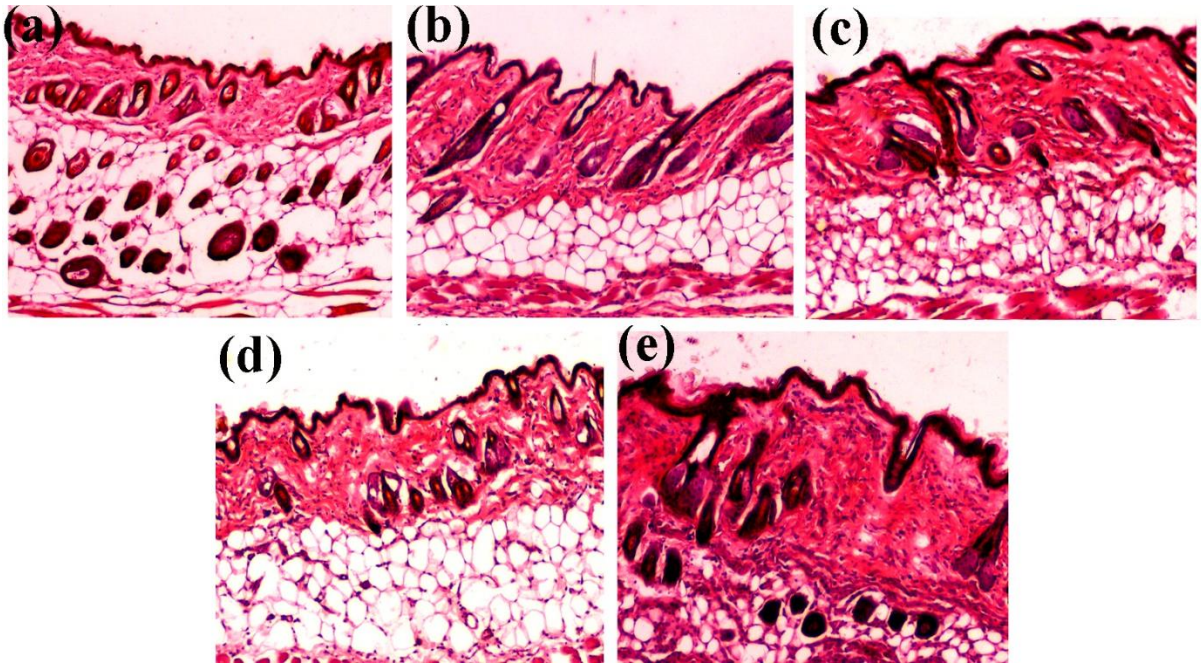

Fig.9 Histopathology of mouse skin showing sections of Control (a) 24 hrs. after implantation of κ-carrageenan hydrogel (b) 7 days after implantation of κ-carrageenan hydrogel (c) 24 hrs. after implantation of κ-carrageenan+ C-phycocyanin hydrogel (d) 7 days after implantation of κ-carrageenan+ C-phycocyanin hydrogel (e).

3.10 Histopathological studies

To investigate tissue compatibility in *in vivo* model, the κ-CRG and κ-CRG-C-Pc hydrogels were subcutaneously implanted in Balb/C mice for 7days. The mice were sacrificed, and skin tissue was collected for H&E staining after 24hrs and 7days of implantation. H&E sections revealed no infiltration of lymphocytes after 24hrs and 7days of implantation, which indicate no inflammation in the tissue. These results further assured high biocompatibility of the gels (Fig. 9 a-e).

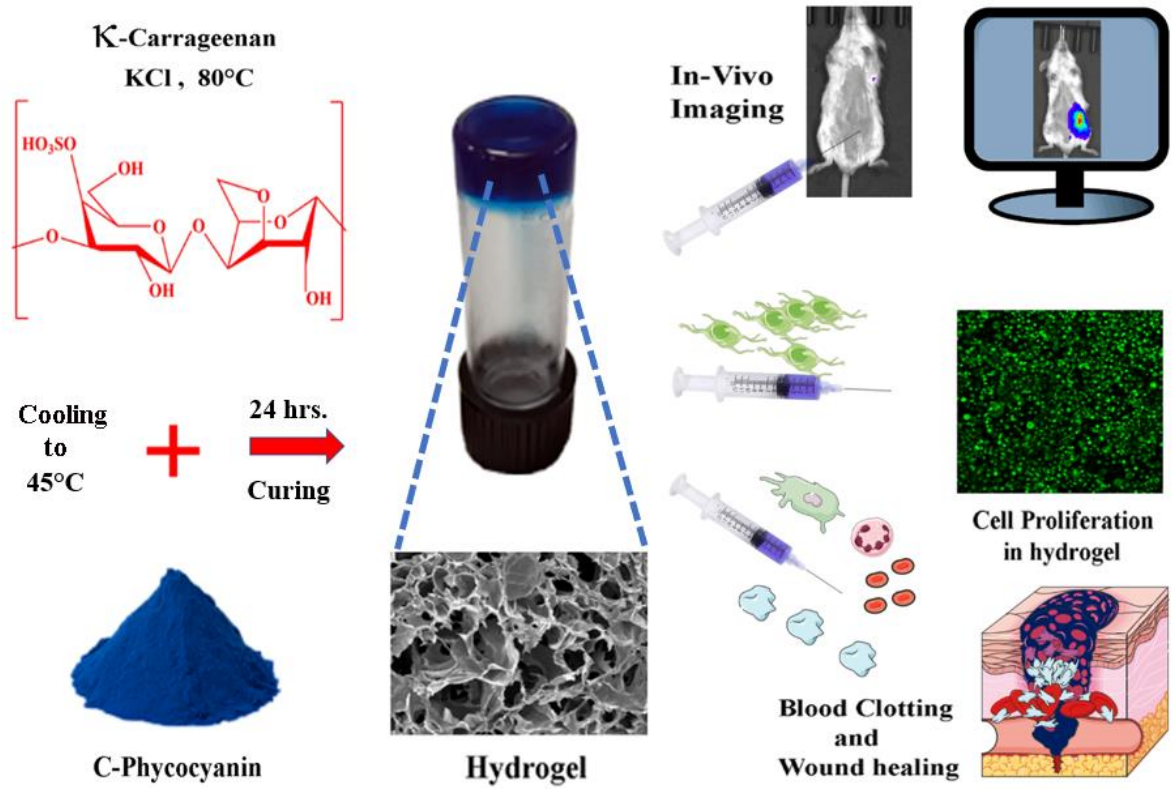

Schematic 1. Hydrogel matrix showing potential blood clotting and wound healing application along with providing cellular differentiation and *et* imaging

4.0 Conclusion

The current study presents the C-phycocyanin based κ-CRG hydrogels, which possess a high potential for blood clotting, wound healing and *In-vivo* imaging for real-time monitoring of wounds. The hydrogel exhibited an interconnected, well-distributed macroporous structure with excellent biocompatibility for advanced wound care application. It has shown superior haemostatic capabilities in traumatic injury conditions along with providing rapid wound healing and tissue restructuring in wound site (schematic 1).

5.0 References

1. Tohme, S.; Simmons, R. L.; Tsung, A., Surgery for Cancer: A Trigger for Metastases. *Cancer research* **2017,***77* (7), 1548-1552.
2. Dormand, E. L.; Banwell, P. E.; Goodacre, T. E., Radiotherapy and wound healing. *International wound journal* **2005,***2* (2), 112-27.
3. Brighton D, W. M., The Royal Marsden Hospital Handbook of Cancer Chemotherapy.Churchill Livingstone,London **2005**.
4. Kirshbaum, M., Neutropenia: more than a low neutrophil count. *European Journal of Oncology Nursing* **1998,***2* (2), 115-122.

5. Fisher DS, K. M., Durivage HJ The Cancer Chemotherapy Handbook 5th edn. Mosby Inc, Missouri. **1997,** (5th).

6. N, S., Prevention of extravasation in intravenous therapy: a review of the research evidence. In: Brighton D, Wood M (2005) The Royal Marsden Hospital Handbook of Cancer Chemotherapy. Churchill Livingstone, London. **1999**.

7. Neal, K., Treating fungating lesions. *Nurs Times* **1991,***87* (23), 84, 86.

8. Bennett G, M. M., Wound Care for Health Professionals. Chapman and Hall, London, C. A. **1995**.

9. Wang, C. C.; Su, C. H.; Chen, C. C., Water absorbing and antibacterial properties of N-isopropyl acrylamide grafted and collagen/chitosan immobilized polypropylene nonwoven fabric and its application on wound healing enhancement. *Journal of biomedical materials research. Part A* **2008,***84* (4), 1006-17.

10. Wang, C.-C.; Su, C.-H.; Chen, J.-P.; Chen, C.-C., An enhancement on healing effect of wound dressing: Acrylic acid grafted and gamma-polyglutamic acid/chitosan immobilized polypropylene non-woven. *Materials Science and Engineering: C* **2009,***29* (5), 1715-1724.

11. Diegelmann, R. F.; Evans, M. C., Wound healing: an overview of acute, fibrotic and delayed healing. *Frontiers in bioscience : a journal and virtual library* **2004,***9*, 283-9.

12. Dvir, T.; Timko, B. P.; Kohane, D. S.; Langer, R., Nanotechnological strategies for engineering complex tissues. *Nature nanotechnology* **2011,***6* (1), 13-22.

13. Wang, S. Y.; Kim, H.; Kwak, G.; Yoon, H. Y.; Jo, S. D.; Lee, J. E.; Cho, D.; Kwon, I. C.; Kim, S. H., Development of Biocompatible HA Hydrogels Embedded with a New Synthetic Peptide Promoting Cellular Migration for Advanced Wound Care Management. *Advanced science* **2018,***5* (11), 1800852.

14. Lai, B. Q.; Feng, B.; Che, M. T.; Wang, L. J.; Cai, S.; Huang, M. Y.; Gu, H. Y.; Jiang, B.; Ling, E. A.; Li, M.; Zeng, X.; Zeng, Y. S., A Modular Assembly of Spinal Cord-Like Tissue Allows Targeted Tissue Repair in the Transected Spinal Cord. *Advanced science* **2018,***5* (9), 1800261.

15. Mao, X.; Cheng, R.; Zhang, H.; Bae, J.; Cheng, L.; Zhang, L.; Deng, L.; Cui, W.; Zhang, Y.; Santos, H. A.; Sun, X., Self-Healing and Injectable Hydrogel for Matching Skin Flap Regeneration. *Advanced science* **2019,***6* (3), 1801555.

16. Darling, N. J.; Sideris, E.; Hamada, N.; Carmichael, S. T.; Segura, T., Injectable and Spatially Patterned Microporous Annealed Particle (MAP) Hydrogels for Tissue Repair Applications. *Advanced science* **2018,***5* (11), 1801046.

17. Jones, V.; Grey, J. E.; Harding, K. G., Wound dressings. *Bmj* **2006,***332* (7544), 777-80.

18. Kim, I. Y.; Yoo, M. K.; Seo, J. H.; Park, S. S.; Na, H. S.; Lee, H. C.; Kim, S. K.; Cho, C. S., Evaluation of semi-interpenetrating polymer networks composed of chitosan and poloxamer for wound dressing application. *International journal of pharmaceutics* **2007,***341* (1-2), 35-43.

19. Wittaya-areekul, S.; Prahsarn, C., Development and in vitro evaluation of chitosan-polysaccharides composite wound dressings. *International journal of pharmaceutics* **2006,***313* (1-2), 123-8.

20. Geckil, H.; Xu, F.; Zhang, X.; Moon, S.; Demirci, U., Engineering hydrogels as extracellular matrix mimics. *Nanomedicine (Lond)* **2010,***5* (3), 469-84.

21. Tibbitt, M. W.; Anseth, K. S., Hydrogels as extracellular matrix mimics for 3D cell culture. *Biotechnology and bioengineering* **2009,***103* (4), 655-63.

22. Abd El-Baky, H. H.; El-Baroty, G. S., Characterization and bioactivity of phycocyanin isolated from Spirulina maxima grown under salt stress. *Food & function* **2012,***3* (4), 381-8.

23. Cian, R. E.; Lopez-Posadas, R.; Drago, S. R.; de Medina, F. S.; Martinez-Augustin, O., Immunomodulatory properties of the protein fraction from Phorphyra columbina. *Journal of agricultural and food chemistry* **2012,***60* (33), 8146-54.

24. Romay, C.; Gonzalez, R.; Ledon, N.; Remirez, D.; Rimbau, V., C-phycocyanin: a biliprotein with antioxidant, anti-inflammatory and neuroprotective effects. *Current protein & peptide science* **2003,***4* (3), 207-16.

25. Ge, B.; Qin, S.; Han, L.; Lin, F.; Ren, Y., Antioxidant properties of recombinant allophycocyanin expressed in Escherichia coli. *Journal of photochemistry and photobiology. B, Biology* **2006,***84* (3), 175-80.

26. Li, B.; Zhang, X.; Gao, M.; Chu, X., Effects of CD59 on antitumoral activities of phycocyanin from Spirulina platensis. *Biomedicine & pharmacotherapy = Biomedecine & pharmacotherapie* **2005,***59* (10), 551-60.

27. Madhyastha, H. K.; Radha, K. S.; Nakajima, Y.; Omura, S.; Maruyama, M., uPA dependent and independent mechanisms of wound healing by C-phycocyanin. *Journal of cellular and molecular medicine* **2008,***12* (6B), 2691-703.

28. A. Tecante, J. L. D., Steady flow and viscoelastic behavior of crosslinked waxy corn starch-k-carrageenan pastes and gels. *Carbohydrate polymers* **1999,***40*, 221-231.

29. Rinaudo, C. R. a. m., Calorimetric determination of the conformationa ltransition of kappa carrageenan. *Carbohydrate research* **1982,***105*, 227-236.

30. Yu Chen, M.-L. L., Dave E. Dunstan, The rheology of K^+ - k-carrageenan as a weak gel. *Carbohydrate polymers* **2002,***50*, 109-116.

31. Chiba, M. T. a. A., Gelation Mechanism of κ- and ι-Carrageenan Investigated by Correlation between the Strain-Optical Coefficient and the Dynamic Shear Modulus. *Macromolecules* **2001,** *34*, 7427-7434.

32. Yoshiaki Yuguchi, T. T. T., Hiroshi Urakawa, Kanji Kajiwara, Structural characteristics of carrageenan gels: temperature and concentration dependence. *Food Hydrocolloids* **2002,***16* (6), 515-522.

33. Mangione, M. R.; Giacomazza, D.; Bulone, D.; Martorana, V.; San Biagio, P. L., Thermoreversible gelation of kappa-carrageenan: relation between conformational transition and aggregation. *Biophysical chemistry* **2003,***104* (1), 95-105.

34. Annabi, N.; Nichol, J. W.; Zhong, X.; Ji, C.; Koshy, S.; Khademhosseini, A.; Dehghani, F., Controlling the porosity and microarchitecture of hydrogels for tissue engineering. *Tissue engineering. Part B, Reviews* **2010,***16* (4), 371-83.

35. Karageorgiou, V.; Kaplan, D., Porosity of 3D biomaterial scaffolds and osteogenesis. *Biomaterials* **2005,***26* (27), 5474-91.

36. Núñez-Santiago, M. d. C.; Tecante, A., Rheological and calorimetric study of the sol–gel transition of κ-carrageenan. *Carbohydrate polymers* **2007,***69* (4), 763-773.

37. Núñez-Santiago, M. C.; Tecante, A.; Garnier, C.; Doublier, J. L., Rheology and microstructure of κ-carrageenan under different conformations induced by several concentrations of potassium ion. *Food Hydrocolloids* **2011,***25* (1), 32-41.

38. Hager, M. D.; Greil, P.; Leyens, C.; van der Zwaag, S.; Schubert, U. S., Self-healing materials. *Advanced materials* **2010,***22* (47), 5424-30.

39. Burattini, S.; Greenland, B. W.; Chappell, D.; Colquhoun, H. M.; Hayes, W., Healable polymeric materials: a tutorial review. *Chemical Society reviews* **2010,***39* (6), 1973-85.

40. Yang, B.; Zhang, Y.; Zhang, X.; Tao, L.; Li, S.; Wei, Y., Facilely prepared inexpensive and biocompatible self-healing hydrogel: a new injectable cell therapy carrier. *Polymer chemistry* **2012,***3* (12), 3235.

41. Park, N.; Um, S. H.; Funabashi, H.; Xu, J.; Luo, D., A cell-free protein-producing gel. *Nature materials* **2009,***8* (5), 432-7.

42. Wong Po Foo, C. T.; Lee, J. S.; Mulyasasmita, W.; Parisi-Amon, A.; Heilshorn, S. C., Two-component protein-engineered physical hydrogels for cell encapsulation. *Proceedings of the National Academy of Sciences of the United States of America* **2009,***106* (52), 22067-72.

43. Lu, H. D.; Charati, M. B.; Kim, I. L.; Burdick, J. A., Injectable shear-thinning hydrogels engineered with a self-assembling Dock-and-Lock mechanism. *Biomaterials* **2012,***33* (7), 2145-53.

44. Chen, W. Y.; Abatangelo, G., Functions of hyaluronan in wound repair. *Wound repair and regeneration : official publication of the Wound Healing Society [and] the European Tissue Repair Society* **1999,***7* (2), 79-89.

45. Aya, K. L.; Stern, R., Hyaluronan in wound healing: rediscovering a major player. *Wound repair and regeneration : official publication of the Wound Healing Society [and] the European Tissue Repair Society* **2014,***22* (5), 579-93.

46. Kumar, J. P.; Bhardwaj, N.; Mandal, B. B., Cross-linked silk sericin–gelatin 2D and 3D matrices for prospective tissue engineering applications. *RSC advances* **2016,***6* (107), 105125-105136.

47. Harley, B. A.; Kim, H. D.; Zaman, M. H.; Yannas, I. V.; Lauffenburger, D. A.; Gibson, L. J., Microarchitecture of three-dimensional scaffolds influences cell migration behavior via junction interactions. *Biophysical journal* **2008,***95* (8), 4013-24.

48. Eming, S. A.; Martin, P.; Tomic-Canic, M., Wound repair and regeneration: mechanisms, signaling, and translation. *Science translational medicine* **2014,***6* (265), 265sr6.

49. Lokhande, G.; Carrow, J. K.; Thakur, T.; Xavier, J. R.; Parani, M.; Bayless, K. J.; Gaharwar, A. K., Nanoengineered injectable hydrogels for wound healing application. *Acta biomaterialia* **2018,***70*, 35-47.

50. Davie, E. W.; Fujikawa, K.; Kisiel, W., The coagulation cascade: initiation, maintenance, and regulation. *Biochemistry* **1991,***30* (43), 10363-70.

51. Naito, K.; Fujikawa, K., Activation of human blood coagulation factor XI independent of factor XII. Factor XI is activated by thrombin and factor XIa in the presence of negatively charged surfaces. *The Journal of biological chemistry* **1991,***266* (12), 7353-8.

52. Todaro, G. J.; Lazar, G. K.; Green, H., The initiation of cell division in a contact-inhibited mammalian cell line. *Journal of cellular physiology* **1965,***66* (3), 325-33.

53. Goldman, R., Growth factors and chronic wound healing: past, present, and future. *Advances in skin & wound care* **2004,***17* (1), 24-35.

54. Sharma, J. N.; Al-Omran, A.; Parvathy, S. S., Role of nitric oxide in inflammatory diseases. *Inflammopharmacology* **2007,***15* (6), 252-9.

55. Cherng, S. C.; Cheng, S. N.; Tarn, A.; Chou, T. C., Anti-inflammatory activity of c-phycocyanin in lipopolysaccharide-stimulated RAW 264.7 macrophages. *Life sciences* **2007,***81* (19-20), 1431-5.

56. Barba, B. J. D.; Tranquilan-Aranilla, C.; Abad, L. V. Hemostatic potential of natural/synthetic polymer based hydrogels crosslinked by gamma radiation. *Radiation Physics and Chemistry* **2016,** *118*, 111-113, DOI: https://doi.org/10.1016/j.radphyschem.2015.02.022

Note:

- The due permission has been obtained from authors and corresponding author of the following published paper before adopting in the present thesis.

- **Dev, A**.; Mohanbhai, S. J.; Kushwaha, A. C.; Sood, A.; Sardoiwala, M. N.; Choudhury, S. R.; Karmakar, S., kappa-carrageenan-C-phycocyanin based smart injectable hydrogels for accelerated wound recovery and real-time monitoring. Acta biomaterialia 2020, 109, 121-131. IF:7.24